Label-Free Microfluidic Devices for Single-Cell Analysis and Liquid Biopsies

Parham Ghassemi

Dissertation submitted to the faculty of the Virginia Polytechnic Institute and State University in partial fulfillment of the requirements for the degree of

Doctor of Philosophy
In
Electrical Engineering

Masoud Agah, Chair
William T. Baumann
Liwu Li
Yang Yi
Xiaoting Jia

December 15th, 2021
Blacksburg, Virginia

Keywords: Microelectromechanical Systems (MEMS), microfluidics, impedance spectroscopy, cell deformability, cancer

Label-Free Microfluidic Devices for
Single-Cell Analysis and Liquid Biopsies

Parham Ghassemi

ABSTRACT

Mortality due to cancer is a global health issue that can be improved through further development of diagnostic and prognostic tools. Recent advancements in technologies aiding cancer research have made significant strides, however a demand for a non-invasive clinically relevant point-of-care tools exists. To accomplish this feat, the desired instrument needs to be low-cost, easy-to-operate, efficient, and have rapid processing and analysis. Microfluidic platforms in cancer research have proven to be advantageous due to its operation at the microscale, which has low costs, favorable physics, high precision, short experimentation time, and requires minimal reagent and sample sizes. Label-free technologies rely on cell biophysical characteristics to identify, evaluate, and study biological samples. Biomechanical probing of cells through deformability assays provides a label-free method of identifying cell health and monitoring response to physical and chemical stimuli. Bioimpedance analysis is an alternative versatile label-free method of evaluating cell characteristics by measuring cell response to electrical signals. Microfluidic technologies can facilitate biomechanical and bioelectrical analysis through deformability assays and impedance spectroscopy. This dissertation demonstrates scientific contributions towards single-cell analysis and liquid biopsy devices focusing on cancer research. First, cell deformability assays were improved through the introduction of multi-constriction channels, which revealed that cells have a non-linear response to deformation. Combining impedance analysis with microfluidic deformability assays

provided a large dataset of mechano-electrical information, which improved cell characterization and greatly decreased post-processing times. Next, two unique biosensors demonstrated improved throughput while maintaining sensitivity of single-cell analysis assays through parallelization and incorporating machine learning for data processing. Liquid biopsies involve studying cancer cells in patient vascular systems, called circulating tumor cells (CTCs), through blood samples. CTC tests reveal valuable information on patient prognosis, diagnosis and can aide therapy selection in a minimally invasive manner. This body of work presents two liquid biopsy devices that enrich murine and human blood samples and isolate CTCs to ease detection and analysis. Additionally, a microfluidic CTC detection biosensor is introduced to reliably count and identify cancer cells in murine blood, where an extremely low-cost version of the assay is also validated. Thus, the assays presented in this dissertation show promise of microfluidic technologies towards point-of-care systems for cancer research.

Label-Free Microfluidic Devices for
Single-Cell Analysis and Liquid Biopsies

Parham Ghassemi

GENERAL AUDIENCE ABSTRACT

Cancer is the second leading cause of death worldwide with approximately 2 million new cases each year in the just United States. Significant research development for diagnostic and prognostic tools have been conducted, however they can be expensive, invasive, time-consuming, unreliable, and not always easily accessible. Thus, a tool that is cheap, minimally invasive, easy-to-use, and robust needs to be developed to combat these issues. Typical cancer studies have primarily focused on biological and biochemical methods for evaluation; however, researchers have begun to leverage small-scale biosensors that utilize biophysical attributes. Recent studies have proven that these lab-on-a-chip technologies can produce meaningful results by exploiting these biophysical characteristics. Microfluidics is a science that consists of sub-millimeter sized channels which show a great deal of promise as they require minimal materials and can quickly and efficiently analyze biological samples. Label-free methods of studying cells rely on their physical properties, such as size, deformability, density, and electrical properties. These biophysical characteristics can be easily obtained at the single-cell level through microfluidic-based assays. Measuring and monitoring these attributes can provide valuable information to help understand cancer cell response to stimuli such as chemotherapeutic drugs or other therapies. A liquid biopsy is a non-invasive method of evaluating cancer patients by studying circulating tumor cells (CTCs) that exist in their blood. This dissertation reports a wide range of label-free microfluidic assays that evaluate and study biological samples at the single-cell level and for liquid biopsies. These assays consist of microfluidic channels with sensors that

can rapidly obtain biophysical characteristics and process blood samples for liquid biopsy applications. Uniquely modifying microfluidic channel geometries and sensor configurations improved upon previously developed single-cell and CTC-based tools. The resulting devices were low in cost, easy-to-use, efficient, and reliable methods that alleviates current issues in cancer research while showing clinical utility.

To my parents Farshid and Nazila…

Acknowledgments

I would first like to thank my academic and research advisor Dr. Masoud Agah, director of the VT MEMS Laboratory at Virginia Tech, for giving me the opportunity to work on these projects. Dr. Agah's excitement for research and exploring new ideas is infectious and his and guidance has helped me grow as a researcher and person.

Next, I would like to express gratitude to Dr. Jeannine Strobl for her valuable input on understanding the biology perspective of the work presented. Don Leber also deserves an acknowledgement for his assistance and advice in the cleanroom. I am thankful for our collaborators at the Wake Forest School of Medicine, Howard University, Georgetown University, and Virginia Tech for sharing their expertise and allowing me to further explore innovative paths of research. I would also like to thank professors Dr. William Baumann, Dr. Liwu Li, Dr. Yang Yi, and Dr. Xiaoting Jia for their role in my committee.

I am grateful for the previous and current members of the VT MEMS Lab who have helped me during my tenure including: Vaishnavi, Hesam, Kru, Ryan, Mustasihn, and Xiang. I would like to give a special thanks to my labmate and mentor Dr. Xiang Ren, whose intricate approach to research and deep knowledge has guided me to become a better researcher. I would also like to thank all my friends who have supported me and made life enjoyable.

Most importantly, I'd like to thank my loving parents, Dr. Farshid Ghassemi and Dr. Nazila Tehrani, and my siblings Pedram and Pegah for being my role models in life. Without them, I would not be where I am today academically and as an individual.

Table of Contents

1. Introduction

Cancer is one of the leading causes of death in the world and is involved in approximately 9 million deaths each year, making it a major worldwide health problem [1]. Metastasis, the spread of cancer to other regions of the body via blood and lymphatic vessels, is the main cause of deaths due to cancer [2, 3]. Researchers across the world attempt to combat cancer by developing new techniques for early detection, screening, treatment, and improving quality of life [1, 4, 5]. However, early detection, screening, and treatment can be difficult because of the heterogeneity of cancer from patient to patient. In fact, the underlying mechanisms which cause the formation and progression of cancer cells still remains largely unknown. Thus, understanding the biophysical properties of cells can help create a connection between the mechanics and biological functions of cells [6, 7].

In order to improve our insight on these biophysical properties, we developed microfluidic biosensing devices capable of revealing information about the biomechanical and bioelectrical properties of single cells. Using this information, we were able to differentiate between normal and cancer cells, as well as test the effects of chemotherapeutic drugs on such biophysical properties. In this chapter, we will examine cells modeled as mechanical and electrical objects in combination with current microfluidic platforms that combine deformability assays and impedance spectroscopy.

1.1 Cell as a Mechanical Object

A cell mainly consists of three important components: membrane, cytoskeleton, and nucleus (Figure 1.1) [8].The cytoskeleton is the structural foundation of a cell that defines the shape of the cell and plays a key role in its mechanical rigidity [9]. The cell cytoskeleton

consists of three different kinds of protein filaments (shown in Figure 1.2): actin filaments (or microfilaments), intermediate filaments, and microtubules [10, 11].

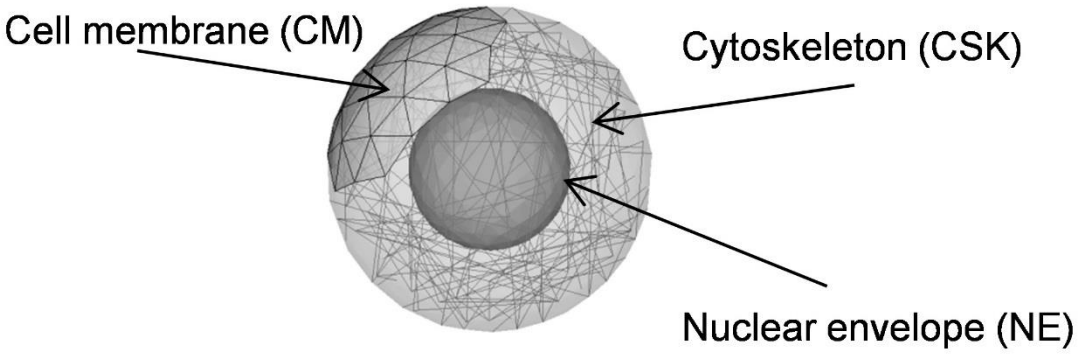

Figure 0.1: Overview of main cell components [8].

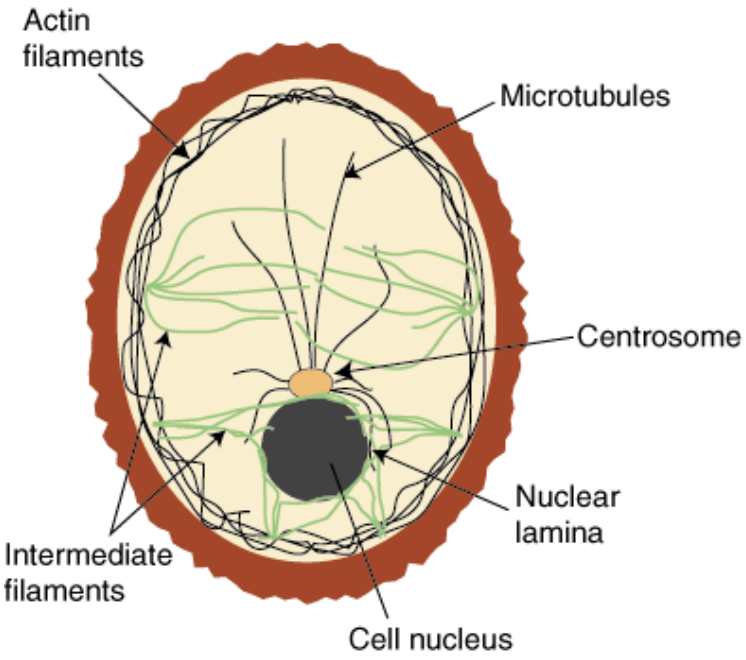

Figure 0.2: Illustration of cell with cytoskeleton components [12].

Microtubules provide the basic organization of the cytoplasm, actin filaments contribute to cell shape and are involved in cytokinesis and cell movement, and intermediate filaments

provide mechanical support for the plasma membrane [10, 13]. In general, actin filaments play a vital role in the structural integrity and deformability of the cell when it experiences lower strains. In contrast, intermediate filaments tend to deform only when the cell experiences larger strains. Microtubules are primarily responsible for providing structure to the cytoskeleton [13]. One model used to describe the role of actin filaments and microtubules is the Tensegrity Model.

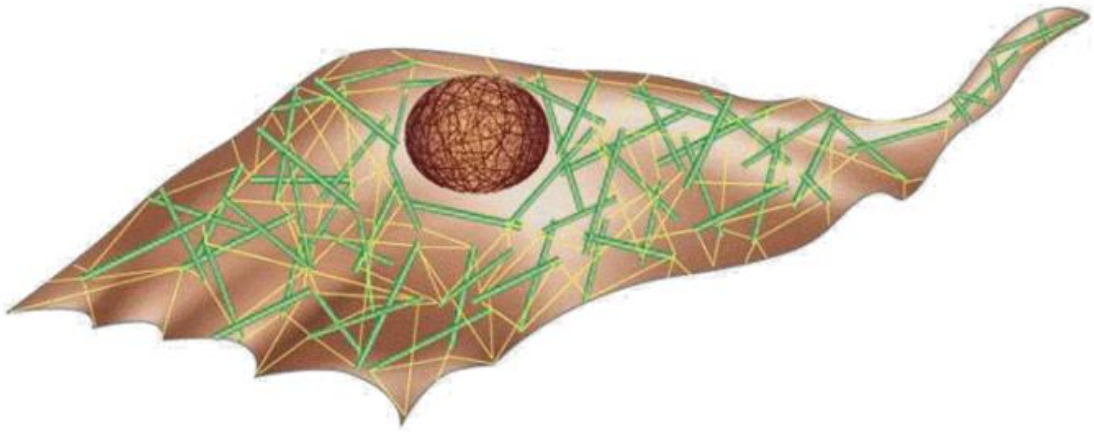

Figure 0.3: A cell and its contractile filaments and compressive elements [14].

The Tensegrity (tensional integrity) model is a method of evaluating the structure of a cell and understanding the mechanics of its behavior. The model suggests that cell structure and shape relies on preexisting tensile stresses (prestresses) in the cytoskeleton. The fibers in the cytoskeleton, primarily actin filaments, behave like muscles and create tension [15-20]. These prestresses are balanced by the internal compression from cytoskeletal components (microtubules) and adhesion forces from the extracellular matrix [18, 21]. The mechanical rigidity and stiffness of cells are correlated to these preexisting stresses, suggesting that more prestress indicates more stability and lower deformability [15-20]. Figure 1.3 illustrates a cell with prestress filaments and compressive stress elements [14]. The yellow lines are the prestress filaments and the green tube-like structures are the compressive stress elements. Cell

characterization can be then done by using biomechanical properties of the cells, such as size and deformability [22]. These characteristics can help define the metastatic potential of cells.

Cancer cell metastasis depends on its ability to deform into blood and lymphatic vessels [3]. Cell deformability can operate as a potential biomarker to differentiate diseased and healthy cells [22-25]. Benign and cancerous cells have differences in stiffness, as it is well known that cancer cells are more deformable than normal cells [22-26]. Single-cell deformability can also be used as a label-free biomarker for cell phenotyping and assessing cancer invasiveness [22]. Single-cells passing through deformation regions is used as a method to test the deformability of cells. Deformation regions are microfluidic channels that have cross-sections smaller than the cell's diameter, which essentially force the cells to deform in order to pass through the channel. The time it takes for cells to enter (entry time) and pass through (transit time) the deformation channel can be used to characterize the cells.

Cell stiffness is related to invasiveness and researchers have used these mechanical phenotypes as targets for molecular therapy of cancer. Cells that are more invasive tend to have softer mechanical characteristics, which improves its ability to deform like those in a metastatic population [27]. When comparing similarly sized cells with different metastatic potential, higher metastatic potential correlates to faster entry times in a deformability channel than cells with lower metastatic potential. Also, cells with higher metastatic potential show increases in transit times. This suggests that not only does deformability increase, but friction is possibly reduced, which could play a role in invasive cancer cells squeezing into tight spaces [28]. In general, cancer cells are associated with increasing deformability when compared to normal epithelial cells [22, 23, 25, 29].

Current developed methods for cell deformability and cell elasticity measurements include: micropipette aspiration [30-32], atomic force microscopy [33-35], optical deformability [23], magnetic bead twisting assays [36], and optical tweezers [37].

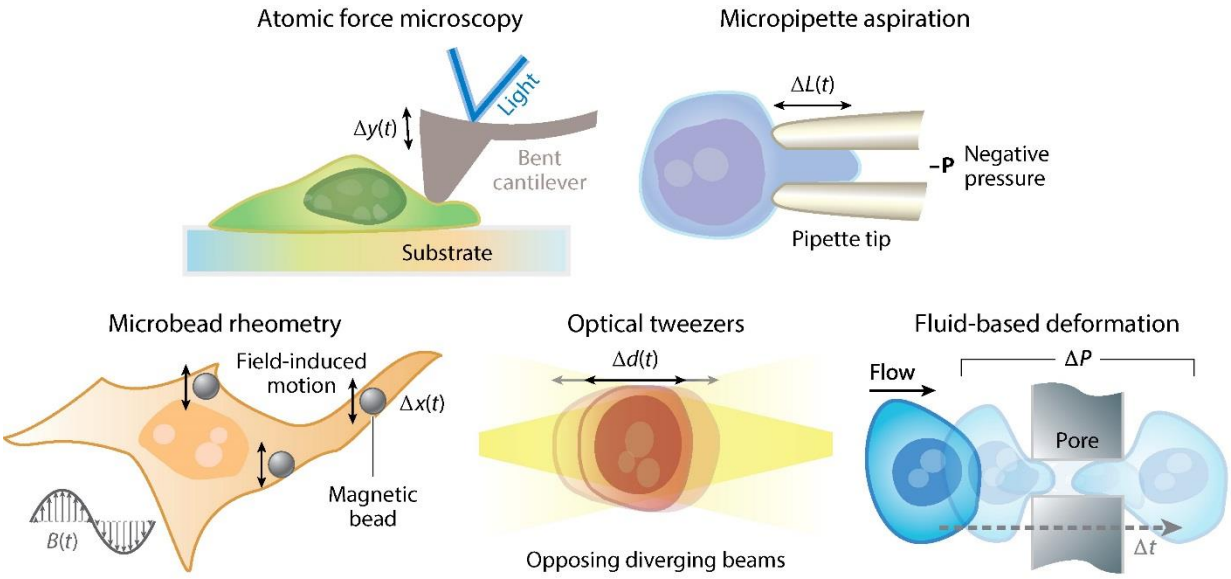

Figure 0.4: Traditional techniques used to measure mechanical properties of cells [38].

AFM is used as a method to look at cells by probing the sample with a cantilever tip to study its mechanical properties. Studies show that using AFM, relative metastatic potential of ovarian(and possibly other types of cancer cells) can by evaluated by using cell stiffness as a biomarker [39]. There are many issues involved with AFM, including extensive sample preparation, low repeatability, experimental costs, and unrealistic cell environment.

Another method of probing cell deformability is through a dual beam optical stretcher [23, 26]. Using the optical stretcher technique it was realized that cancer cells deforms 5X more than normal cells and metastatic cells deform 2X more than non-metastatic cancer cells [26]. The issue with optical stretching techniques is that forces applied on the cell from a laser is not

sufficient to completely deform the cell and is not good for simulating in vivo conditions of cell migration [24]. Dual beam optical stretchers have been improved by incorporating a microfluidic cell delivery system to look at cell biomechanical properties in a more realistic environment. By looking at the cell's response to constant stress, it was discovered that cancer cells experience higher axial strain than normal cells [25]. By utilizing a magnetic tweezer system, the mechanical stiffness of cells with varying invasiveness were compared. It was discovered that cancer cells with the lowest migratory and invasive potential are 5X stiffer than their highest migratory and invasive potential counterparts. This proves that mechanical phenotypes can be key component for determining metastatic potential of cell populations and even at the single-cell level [27].

The main disadvantages of using these techniques is that they have low throughputs [22]. To overcome this issue, researchers are looking to also improve robustness and ease-of-use of these platforms [7]. To improve the throughput of cell classification using mechanical deformability, a method that involves using deformability induced forces and inertial lift forces in inertial microfluidic platforms [22]. These devices take advantage of micro-scale scale phenomena to provide a high-throughput platform for cell classification using cell deformability as a biomarker. Recently, Hydrodynamic stretching of single cells [40] and microcavity arrays [41] have also be used in high-throughput mechanical phenotyping [40, 41]. These devices have been proven to be useful for cell separation and high-throughput deformability measurements [22]. Although the throughput issue was addressed, long post-processing times and complexity of usage still exists.

Microfluidic deformability cytometry provides comparable statistical accuracies to traditional flow cytometry techniques, and also uses label-free biophysical biomarkers, opening opportunities for clinical diagnosis, stem cell characteristics and single-cell biophysics [40].

To conclude, cell deformability in microfluidics platforms can be used as a biomarker for identifying cells of different malignancies from a sample which proves that it is capable of being used in cancer diagnostic applications [24].

1.2 Cell as an Electrical Object

Single cells can be modeled as a dielectric shell, where each layer has its own permittivity and conductivity. The simplest model is the single-shell model, shown in Figure 1.5, which is useful for representing nucleus-free cells such as a red blood cell. The multi-shell model, shown in Figure 1.6, adds complexity to the model but better represents nucleated cells [42]. For example looking at the double shell model shown in Figure 1.7, starting from the inner to outer region the model represents the cell nucleus, nuclear envelope, cytoplasm, and plasma membrane, respectively. Each region also has its own respective dielectric properties such as permittivity and conductivity [43].

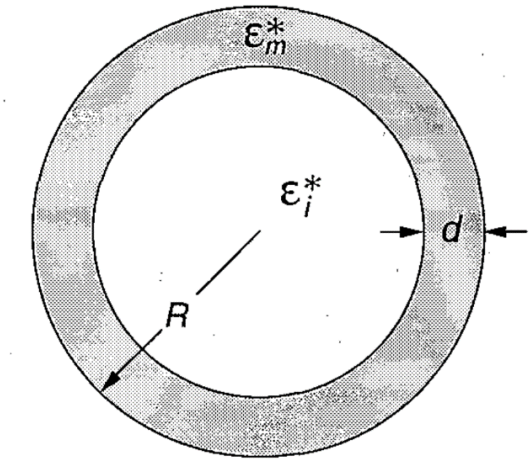

Figure 0.5: Single-shell model of cell [42].

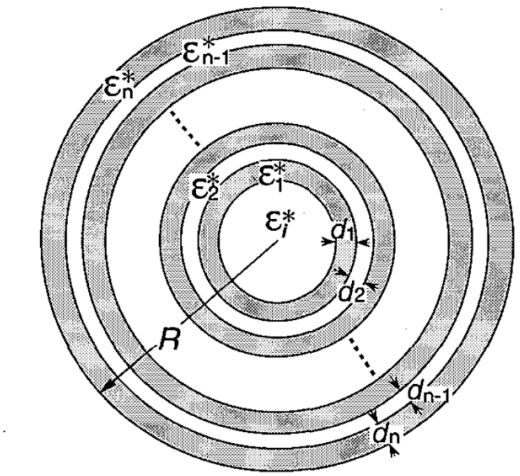

Figure 0.6: Multi-shell model of cell [42].

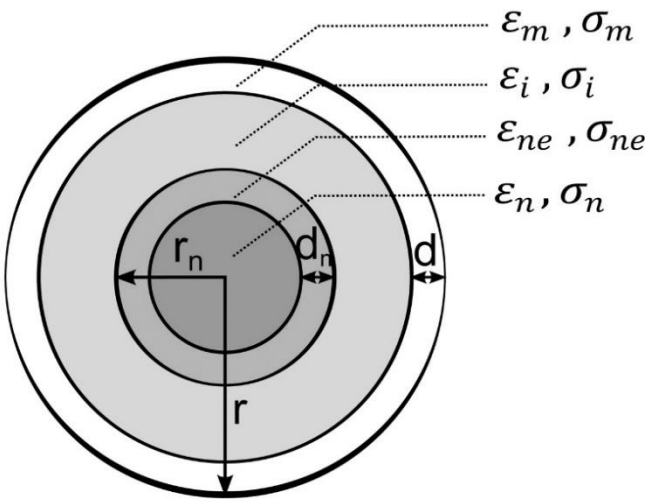

Figure 0.7: Double-shell model of a cell with corresponding dielectric and geometric parameters [43].

Impedance spectroscopy techniques can be used to measure the dielectric properties of single cells which can be modeled as a combination of linear components, such as a resistor and/or capacitor, in an electric circuit model (Figure 1.8) [44]. These electrical components can represent cell membrane resistance and capacitance, along with cytoplasm resistance.

Impedance spectroscopy can be used to obtain physiological properties from cells and has advantages that include simplicity, ease of use, non-invasive, and real-time capabilities. When an AC signal passes through the cell has a low frequency, the plasma membrane will act a barrier

to the flow of current, which can be measured as an impedance value. The impedance value has an amplitude and phase that is proportional to the cell's volume. At higher frequencies, the membrane is permeable to the electrical AC current and the measurements provide information about the intracellular contents. At intermediate frequencies the membrane acts less like a barrier and can provide information about the properties of the cell membrane. The current flow passing through cells at difference frequencies is shown in Figure 1.9. Different frequencies can provide different information about the cell, therefore multi-frequency measurements provide the capability to distinguish cells by size, membrane properties, and intracellular properties [45].

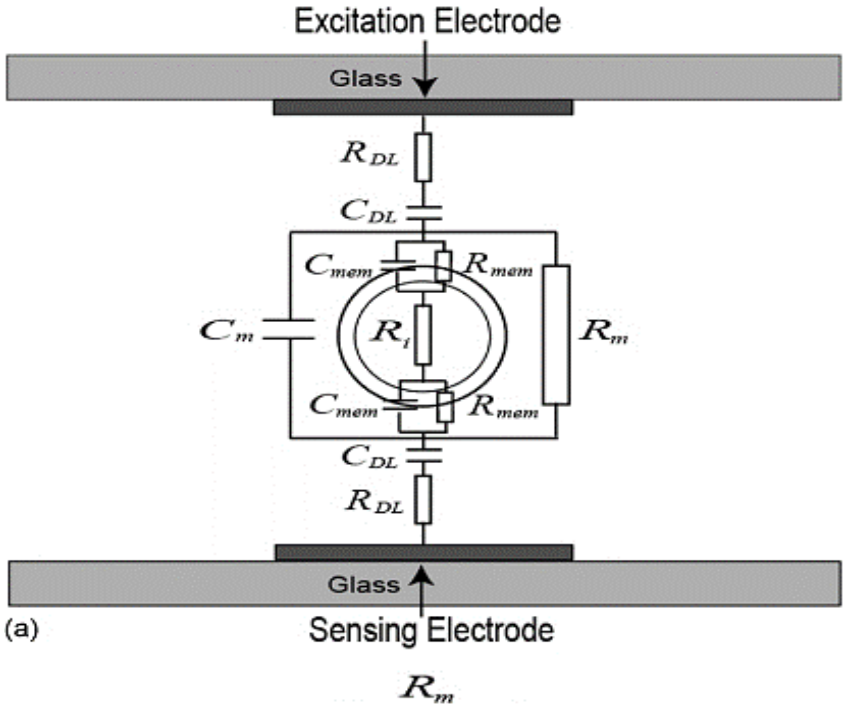

Figure 0.8: Electric circuit model for cell suspended between a pair of electrodes [44].

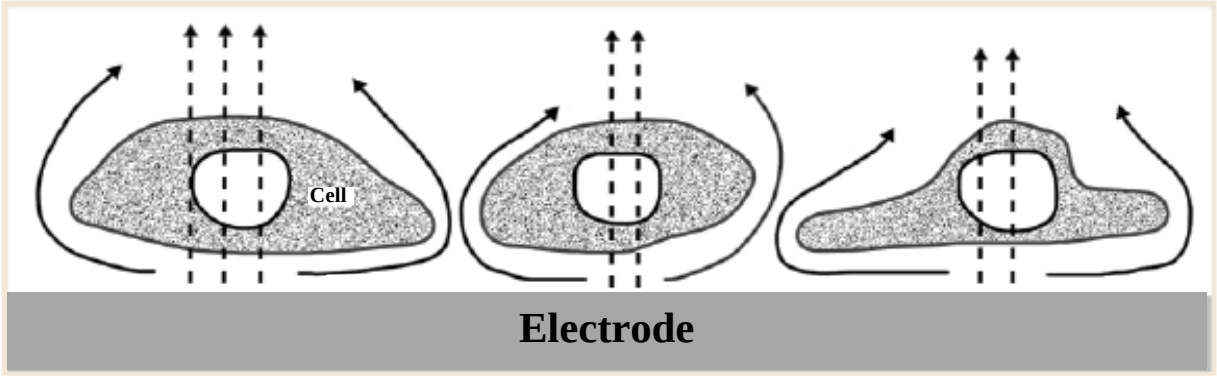

Figure 0.9: Diagram of current flow through cells at low (solid lines) and high frequencies (dotted lines) [46].

There are a variety of impedance spectroscopy techniques that can be used to extract these electrical properties of cells and cell populations. These techniques include Electrical Cell-Substrate Impedance Sensing (ECIS) and impedance spectroscopy in flow cytometry. ECIS involves measuring the change of the impedance of an electrode or across an electrode pair as an AC current passes through it. This technique is used to monitor the dynamic changes of biological cells that have adhered onto the typically gold electrodes. ECIS relies on the cells' ability to resist the flow of electric current and measurements can be taken at singular frequencies or a sweep across multiple frequencies[47]. The impedance is directly related to the adherence of the cells onto the electrodes, so it can be used to measure cell growth and proliferation. As cells begin to die the impedance will decrease because they will detach from the electrode surface. Due to this cellular behavior, other applications for ECIS device include measuring responses to chemical stimuli, which can be useful for evaluating the cytotoxicity of drugs and screening for optimal drug dosage in treatments. Although ECIS can be used in a wide variety of applications, it has restrictions due to its reliance on cell adherence. This technique is not suitable for single-cell analysis, but other methods such as impedance

spectroscopy in flow cytometry have that capability. Impedance spectroscopy in flow cytometry can also have a high-throughput, making it applicable for cell population studies as well.

Impedance spectroscopy in flow cytometry can be a tool for label-free cell characterization. Cell characterization is done by finding cell size, membrane capacitance, and cytoplasm conductivity as a function of frequency [48]. Dielectric spectroscopy has the potential to be used in the following applications: cell differentiation, mitosis/cell cycle monitoring, cytotoxicity and cell death, and as a drug screening platform. Cell differentiation is characterized by changes in cell morphology, aggregation, cell adhesion, ion channel activity or gene and protein expression, which are all changes that result in changes in the impedance spectrum of the cell [45].

Impedance spectroscopy in flow cytometry has also been used as a label-free method for quantifying the progression of cancer cells. Researchers have compared normal breast epithelial cells (MCF10A) to early stage breast cancer cell line (MCF-7), invasive human breast cancer cell line (MDA-MB-231), and metastasized human breast cancer cell line (MDA-MB-435). It was shown that the magnitude and phase had convincing differences from the cancer cell lines. This device could lead to development of diagnostic tools for cancer detection and drug therapy [49]. Wide microfluidic channels have been used to measure electrical properties of single cells and model the cell as an equivalent circuit. Using this model, they interpret the data measured at various frequencies in order to find cell cytoplasm conductivity and specific membrane capacitance [50]. Another application of impedance flow cytometry is pollen analysis where the robust and label-free method can provide reliable data estimating plant cell viability [51].

Impedance measurements can also be a viable non-invasive method to monitor cells during mitosis and their cell cycle. Dying cells experience change in impedance and can be used

to measure the effect of chemicals on cell mortality [45]. Additionally, flow cytometry combined with impedance measurements have been used to discriminate between live and dead cells [52]. Impedance also has a great deal of potential to screen for the cytotoxicity of various agents, including chemicals, drugs, and florescent tags and can also observe the stresses these reagents have on the cells. This technology can be implemented in point-of-care systems which can act as a biosensor for quick real-time measurements, replacing traditionally slow and invasive cytotoxicity assays [45]. Drug concentrations and drug incubation time have shown to have an inversely proportional effect on cell impedance values [53-56]. These systems can also have high-throughput due to their multiplexing capabilities. Therefore, these platforms have the ability to test different drugs and drug dosages in the same conditions simultaneously [45].

To conclude, impedance spectroscopy is a valuable tool in cell biosensing applications and there is great potential as a cost effective tool to replace conventional methods of cell analysis. Traditionally, extensive sample prep could include staining, labeling, and fixing of samples, all of which can be replaced using this label-free method. Impedance spectroscopy can be used in label-free analyzers for applications including: cell differentiation, cell cycle progression, cytotoxicity, and cell death detection. Implementation into microfluidic systems allows for the flexibility of devices to be incorporated into systems for cell monitoring, drug screening, flow cytometry and even point-of-care platforms. Impedance spectroscopy allows label-free, rapid, cost-effective and highly sensitive technique that holds great potential in becoming a standard in biological cell characterization for a wide array of applications [45].

1.3 Microfluidic Approach to deformability assays and impedance Spectroscopy

Microfluidics have been used to look at the behavior of breast cancer cells and have the ability to distinguish between non-malignant and malignant cells. The benefits of microfluidics includes the ability to study over the overall cell mechanical properties and they can better mimic in vivo conditions that the cells will experience [24]. Biomechanical properties of cells obtained in deformability assays can give information on cell health, for example cell stiffness changes when cells change from a healthy to unhealthy state [57]. Entry time and transit time can be used to distinguish between non-malignant and malignant cells. For example, when comparing normal and cancer breast cells, transit times of both are approximately equivalent but normal cells have much higher entry times [24]. Impedance measurements from frequencies 40 Hz to 1 GHz supply information about membrane capacitance, cytoplasm conductivity and cytoplasm permittivity as a function of frequency. Multi-frequency measurements applied to a single cell can give us ability to classify a cell by size, membrane properties, and intracellular properties [58].

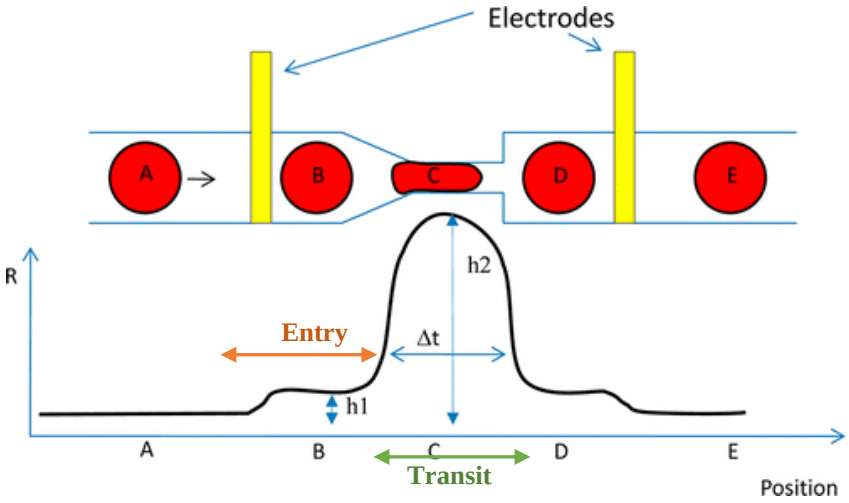

Figure 0.10: Illustration of cell passing through a constriction channel along with the corresponding impedance plot [57].

Electrodes embedded in a microfluidic device with a deformability channel enhances throughput and heavily reduces post-processing, which is shown below in Figure 1.10 [57]. Researchers have developed a device that monitors cell during the cell cycle and can detect the transition between different physiological states [59]. During the cell cycle (Figure 1.11), cell impedance increases while cell duplicates its contents and during DNA replication (G1 and S phase). In contrast, impedance decreases during mitosis (nuclear division) and cell division (G2 and M phases) [60]. These types of devices can be used as tools for cell cycle studies.

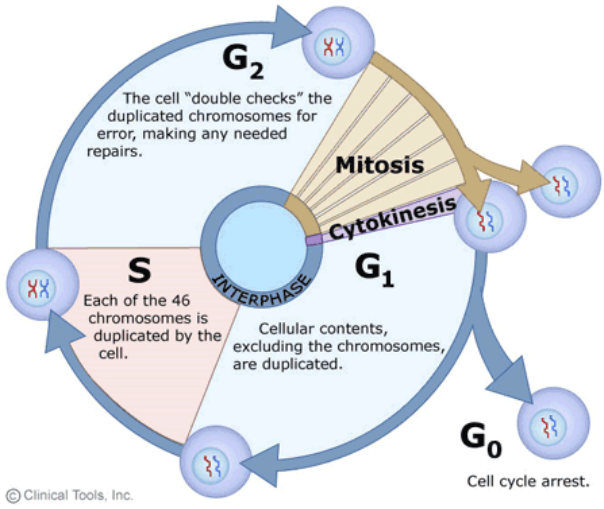

Figure 0.11: Description of the cell cycle [61].

Currently, one technique that combines impedance measurements in microfluidic deformability assays use micropillar traps to capture the cells and take impedance measurements [62, 63]. To improve impedance measurements, carbon nanotubes are being used as biosensors for cancer metastatic diagnosis with single-cell resolution. This tool was used for distinguishing cancerous stages of both breast and colon carcinoma cells [62]. Further research is being done for real-time monitoring of cells. In one case, cells' electrical responses have been measured during mechanical aspiration. This system was used for comparing healthy cells to malignant ones in

real-time. Results also showed that the remodeling of actin filaments decreased their electrical response and cancer cells did not change as much as healthy cells [63].

Previously at the VT MEMS Lab, others investigated mechanical response of cells using AFM [64]. It was shown that cancer cells with high metastatic potential are softer than their non-invasive counterpart. As an extension of that study, in order to replace the need of the high-costing and unrealistic deformation conditions, a microfluidic deformability assay was developed with a single deformation channel [65]. Another device was created to evaluate a single-cells' response to experiencing a series of iterative deformations and use their velocities in these deformation regions to discriminate metastatic cancer at the single-cell level [66]. These results exhibit the viability of using mechanical deformation in microfluidics as a trusted method of evaluating the biomechanical properties of cells.

1.4 Microfluidic Approach to Circulating Tumor Cell Enrichment and Detection

The main cause of cancer patient mortality is metastasis, where tumor cells detach from a primary tumor, traverse through the vascular system, and form secondary metastatic tumors (illustrated in Figure 1.12) [67-69]. Tumor cells traveling through the blood and lymphatic are called circulating tumor cells (CTCs). The study of CTCs in blood, categorized as a liquid biopsy, has proven to be a viable and minimally invasive replacement to standard invasive biopsies [70, 71]. CTC evaluation typically consists of molecular characterization or enumeration. Researchers have demonstrated that CTCs can be an informative biomarker for detecting cancer early, understanding cancer metastasis mechanisms, identifying tumor origin, determining prognosis, predicting response to natural progression or therapies, monitoring disease recurrence, and aiding diagnostic decisions [72-75]. The concentration of CTCs per mL

of blood is extremely low compared to white blood cells (WBCs) and red blood cells (RBCs). Their rarity causes several technical challenges as CTC counts range from about 1-10 cells compared to millions and billions of WBCs and RBCs, respectively. The development of technologies to enrich blood samples and isolate the tumor cells of interest attempt to alleviate this issue.

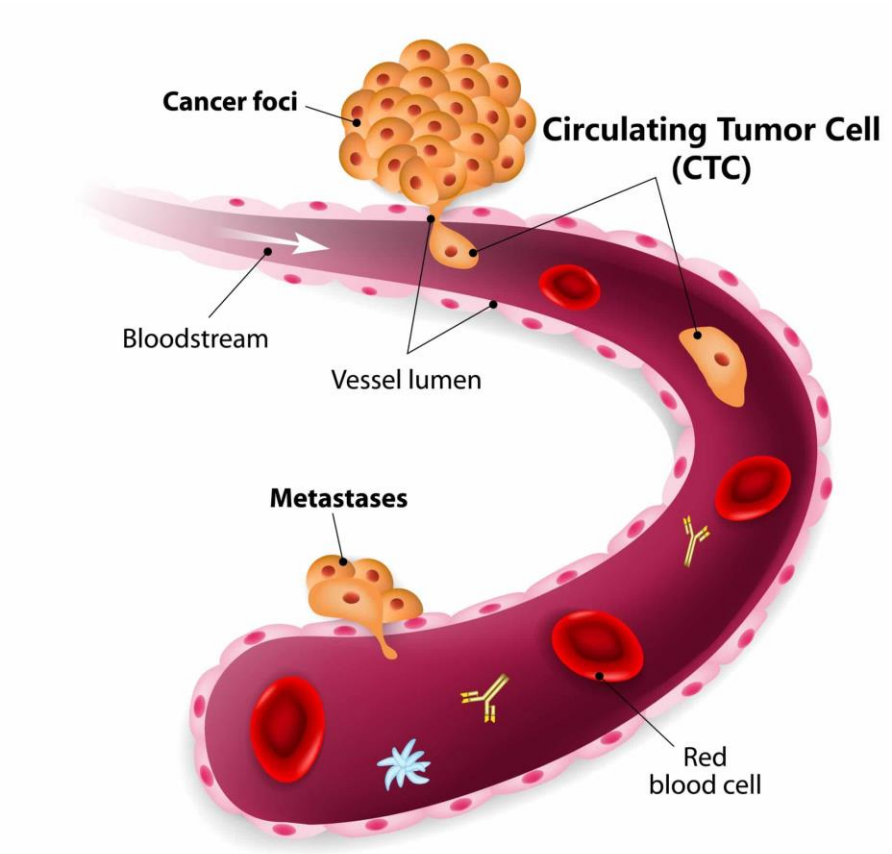

Figure 1.12: Cancer metastasis through circulating tumor cells [67].

CTC enrichment methods rely on either their biological or biophysical characteristics, shown in Figure 1.13, as they differ from the peripheral blood cells[76-79]. Biological differences include variations in gene and protein expression. Isolation through biological or label-based techniques typically rely on differences between surface antigen expression, which allows for the positive selection of CTCs and negative selection of WBCs. The epithelial cell adhesion molecule

(EpCAM) is the most used antigen for positive CTC selection as it is typically expressed in tumor cells derived from epithelial tissue. The Cellsearch platform is the only FDA-approved method of CTC analysis and it relies on the EpCAM surface marker[80, 81]. The main drawback of CTC analysis through label-based methods, such as Cellsearch, include the loss or diminished expression of EpCAM due to the epithelial-to-mesenchymal transition (EMT). Low capture efficiency can be detrimental to the reliability of liquid biopsies due to the scarcity of CTCs. Cocktails of antibodies have been used to solve the problem of the EMT, however the uncertainty of surface markers needed to be targeted and increased cost of the assay still hinder biologically based technologies[82].

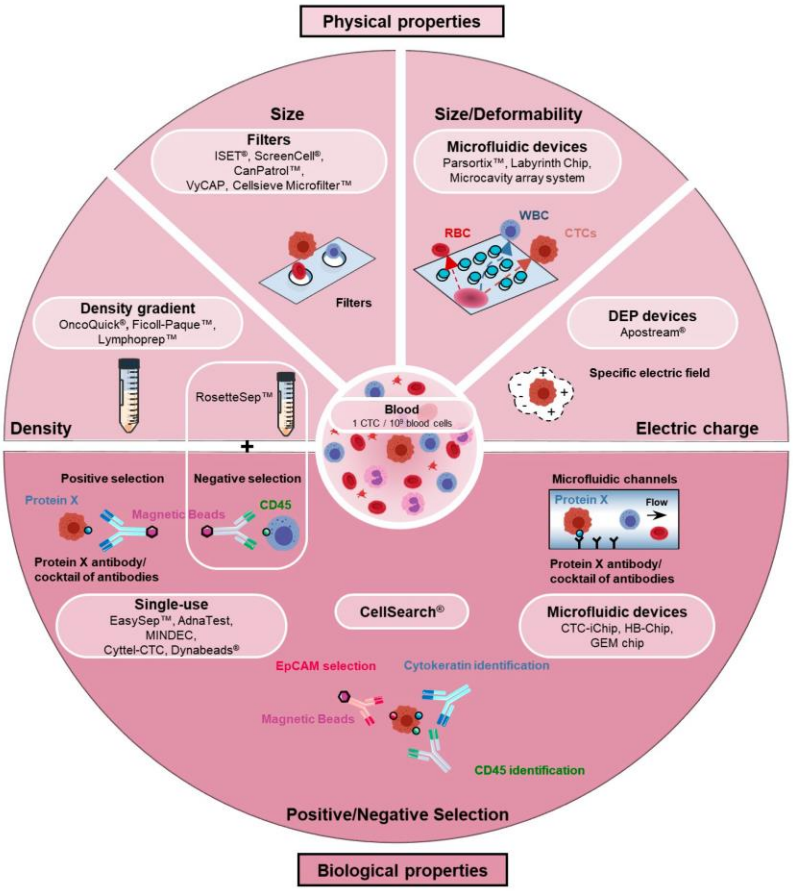

Figure 1.13: Overview and breakdown of circulating tumor cell enrichment technologies [76].

Label-free technologies alleviate issues that arise with loss of protein expression because they solely rely on biophysical properties such as their size, deformability, density, electrical properties (Figure 1.13)[76-79, 83]. In general, CTCs (10-25um) have much larger sizes than RBCs (6-8 um) and WBCs (5-13). Although an overlap in CTC and WBC sizes exists, the former tends to be less dense and more deformable than the latter. Density-based technologies, such as OncoQuick and Ficoll-Paque, utilize centrifugation to separate the CTCs from unwanted blood cells[84, 85]. Advantages of density gradient methods include extremely high throughput, lack of reliance on specific equipment, and typically preserves cell viability. However, downsides range from low specificity, poor efficiency, and low purity due to leukocyte contamination. Size-based filters such as FAST disc and CellSieve have high recovery rates and ultrafast enrichment, but also lack in purity depending on the geometry of the filter pores[85-87]. Size-based technologies that incorporates deformability as an additional factor for isolation, such as Celsee, improves on purity issues but introduce clogging problems which requires sample processing to be done within four hours for reliable results [88]. Dielectrophoresis (DEP) is an isolation technique that relies on the polarizability or electrical properties of cells. Commercial DEP technologies ApoStream and DEPArray have slow processing times and require expensive specialized equipment, but they can supplement CellSearch and other tools for a higher throughput isolation[89, 90]. Each biophysical-reliant approach has trade-offs, where the optimal solution would require a combination of these techniques, such as including newly developed methods involving acoustophoresis.

Microfluidics have demonstrated to be an effective platform for technology development of liquid biopsies as multiple cell properties can be probed and utilized for precise isolation. Microfluidic chips can facilitate the utilization of label-based and label-free technologies on the

same device. Additionally, due to their small footprint microfluidic devices are cost-efficient and can be easily mass produced for commercialization towards research and clinical settings. Parsortix, CTC-chip, and the HB-chip validated the compounding benefits of exploiting both biological and biophysical properties through size-based separation in combination with EpCAM+ and/or CD45- selection [79, 91]. Although combining label-dependent and label-independent solves the issues of low purity in addition to throughput, the pitfalls of cost and loss of surface expression still exists. Thus, there is a need for a label-free, low cost, and efficient method for processing blood samples to reliably study CTCs.

1.5 Research Objective and Overview

The long-term goal for this work is to utilize and exploit the biophysical properties of cells to develop a point-of-care system that can reliably analyze biological samples to assist cancer research. The work presented in this dissertation lays the groundwork for clinically relevant label-free microfluidic platforms in the form of single-cell analysis and liquid biopsy assays. **Chapter 2** demonstrates and compares the effects of constriction and relaxation channels in microfluidic deformability assays with the goal of evaluating cell health through their biomechanical properties. To evaluate the mechanical characteristics of single cells their velocities in the constriction channels were obtained. The assay demonstrated that cells have a non-linear response to deformation and subsequent relaxation. This response further exploits differing biomechanical properties that cancer cells and their normal counterparts. **Chapter 3** builds off the optimal multiconstriction channel that was evaluated from the work in Chapter 2. The biosensor is called the iterative mechano-electrical properties (iMEP) analyzer, which consists of a multi-constriction channel with embedded electrodes. The iMEP analyzer captures electronic signatures that represent the biomechanical and bioelectrical properties of single cells.

Additionally, the iMEP analyzer automates the post-processing of data using the same electronic signatures. The iMEP device was compared with standard biological assays that evaluate cell migratory behavior such as scratch wound healing and Boyden chamber assays. The multiparametric data set obtained using the iMEP device could distinguish between four different prostate cell lines, while the individual biological assays were unable to do so.

Chapter 4 presents a high-throughput microfluidic deformability assay consisting of an array of multiconstriction channels that can simultaneously capture single-cell biomechanical properties. Large datasets of cell transit velocities and size were utilized in conjunction with kernel-based machine learning methods to distinguish between three different breast cancer cell lines. Additionally, the biophysical signatures obtained were used to identify malignancy from tumor biopsy samples which demonstrates the clinical validity biomechanical markers. **Chapter 5** reports a microfluidic sensor with capabilities of simultaneously measuring biophysical properties of multiple cells in four parallel channels. Detailed information was collected from electronic signatures, which rely on cell biomechanical and bioelectrical characteristics. The combination of biomechanical and bioelectrical parameters demonstrate that this high-throughput device contains sufficient sensitivity for single-cell detection.

Chapter 6 introduces a liquid biopsy assay to capture CTCs using a high-throughput entrapment chip named CTC-HTECH. The microfluidic platform captures CTCs from murine blood through the exploitation of size and deformability differences of cancer cells compared to blood cells. **Chapter 7** reports a biosensor for the detection and enumeration of CTCs after enrichment of whole blood. The constriction-based microfluidic sensor detects all CTCs in a murine blood

sample using through bioelectrical signatures. Additionally, a cost-effective version of the device is reported and validated through two different cancer types in murine blood. The channels are separated from the electrode sensors through a thin glass slide so the electrode sensors can be re-used which consequently lowers the cost of the assay. **Chapter 8** presents a modular microfluidic platform called CTC-CARE; a Constriction Assisted Rapid Enrichment of Circulating Tumor Cells. Through the combination of multi-height delivery channels and an array of constriction channels, CTCs and CTC clusters are isolated via the combination of size, deformability, and density. The cost-effective modular device can be employed with a variety of configurations that improve the throughput, capture efficiency and purity of sample enrichment. The device is compatible with alternative enrichment and detection methods due to the continuous flow of the enriched sample out of the device. Whole human blood spiked with three different cancer cell lines validated the CTC-CARE device.

2. Single-cell Mechanical Characteristics Analyzed by Multiconstriction Deformability Assays

Ren, X., **Ghassemi, P**., Babahosseini, H., Strobl, J. S., & Agah, M. (2017). Single-cell mechanical characteristics analyzed by multiconstriction microfluidic channels. ACS sensors, 2(2), 290-299.

My contributions towards this body of work included device fabrication, sample preparation, experimentation, data collection and processing, and assisted with the manuscript writing.

2.1 Introduction:

Studies of the mechanical characteristics of single cells have been previously used in cancer research [1,2]. Different stages of cancer cells have significant mechanical differences due to the stiffness of their cell membrane [3]. Other well-developed methods and techniques based on cell membrane properties, the epithelial cell adhesion molecule (EpCAM) and fluorescence detection for the sorting of cancer cells require specific equipment, such as atomic force microscopy [3,4], costly antibody reagents [5,6] and flow cytometry setups [7-10]. Microfluidic chips bring new technologies and methods to both cancer cells analysis and circulating tumor cell (CTC) detection and sorting [11]. Size-based microfluidic channels for CTC cancer cell separation are broadly used in CTC studies which sense the different diameters of cancer cells, white blood cells and red blood cells [88, 92-96]. In order to analyze and sort different cancer cells with similar sizes, investigators have chosen to use constriction channels and study the dynamics of cells, usually accompanied by other methods sensitive to both biomechanical and bioelectrical properties to enable identification [18-22].

Characterization of the mechanical properties of cancer cells using a microfluidic device with constriction channels has been proven to be an accurate method to differentiate different cell lines [23-26]. Metastatic cancer cells have softer cell membranes, as well as deformation ability in microfluidic constriction channels. On the other hand, normal cells have a cytoskeleton with higher mechanical strength, including but not limited to actin filaments, intermediate filaments, and microtubules [27, 28]. Therefore, the deformation time of cancer cells and normal cells has been shown to differ due to their mechanical properties. Many studies have focused on the entry time and transit time of cells in a constriction channel, and analysis has defined criteria typifying specific cell lines [29]. By plotting the dynamic parameters of the single cells in constriction channel, different cell lines, including breast cancer cells [3, 18, 23], lung cancer cells [19, 30, 31] [97-99] [73-75] [7-9] [74-76], kidney tumor cells [32], and cervical cancer cell lines [33, 34], can be separated into groups in order to achieve cell characterization [35]. However, using a single constriction channel or adjustable constriction channels have limited capabilities to distinguish between cancer cells and normal cells. When differentiating various cell lines, scientists studying characterization of cancer cells have added an additional bioelectrical measurement along with the single constriction channel [2, 20]. At the same time, improvements in the methods used to induce cells' deformation using not only constriction channels, but also lateral displacement array or pillar array [17,36] in a microfluidic chamber [13, 14] have enhanced the resolution of characterizing cells.

This manuscript reports a multi-constriction multi-channel microfluidic device for analyzing velocity profiles of single-cells which provides greater single-cell resolution of normal and cancer cells than that afforded by a single constriction channel studies. Smartphone video-microscopy was used to capture the dynamic motions of cells as each passed through the series

of constriction channels. The result was a distinct velocity profile at each stage of deformation in the multiple constriction channels. Compared to single-constriction channels, multi-constriction channels divide the cell deformation into multiple stages, which effectively reveals the deformation process of each cell with higher resolution, and hence a new and simple way to observe the variations in individual cells' velocity profiles. The series of relaxation regions separating the constriction channels causes cells to experience multiple relaxations where cell membrane/shape recovery takes place. The length of relaxation regions are kept as 50 μm constantly, so that the results can focus on the effects of the constriction, the relaxation count and constriction length. The microfluidic channels device was designed with three different configurations to compare the ability to differentiate two different cell lines in each channel. We also compared the effect of adding one or multiple relaxation regions in the constriction channel. The velocity profiles analyses were focused on comparing the initial velocity change due to the deformation at the entrance of each channel and the exiting velocity at the last segment of the channel, where the cells have experienced sufficient deformations. The multiple deformation procedure increases the ability of deformation and recovery of the cells. Based on our experimental results, the ability to differentiate between cancer cells and normal cells in a multi-constriction channel is higher than that achieved with either a single constriction channel or two constriction channels with only one relaxation region. After establishing criteria to examine the difference between initial velocities and final velocities, we successfully differentiated ~94.3% of the cancer cells from normal cells. Then, four testing samples were used to verify our criteria. The results indicated that the selected criteria for the multi-constriction channels have an accuracy around 95% to tell the difference between cancer cells and normal cells.

2.2 Materials and Methods

Cell culture and sample preparation

We prepared the highly metastatic breast cancer cells MDA-MB-231 and benign breast epithelial cells MCF-10A to represent normal cells with the same concentration of ~50,000 cells/mL. Both MDA-MB-231 and MCF-10A cells were provided by the Tissue Culture Shared Resources of the Lombardi Comprehensive Cancer Center, Georgetown University in Washington, DC. MDA-MB-231 cells were grown in F12:DMEM (Lonza, Basel, Switzerland) with 10% fetal bovine serum (FBS), 4 mM glutamine and penicillin-streptomycin (100 units per mL). MCF-10A cells were grown in F12:DMEM with penicillin-streptomycin (100 units per mL), 2.5 mM L-glutamine, 20 ng/mL epidermal growth factor (EGF), 0.1 μg/mL cholera toxin, 10 μg/mL insulin, 0.5 μg/mL hydrocortisone, and 5% horse serum. The cells were grown in T-25 cm2 culture flasks at 37°C in a 5% CO2 in air atmosphere until cells were ready for subculture. The morphology of the cells was observed before trypsinization (Figure 2.1). The cells were then detached from the flask with Trypsin-EDTA solution (Trypsin-EDTA solution 10X, , Sigma); The MDA-MB-231 cells were trypsinized at 37°C for 2 min and MCF-10A cells were trypsinized at 37°C for 15 min. Before every experiment, the viability of the cells was observed under a microscope using trypan blue (Trypan blue solution (0.4%), Lot. 42K2360, Sigma) 37. Both trypan blue and culture medium were warmed to 37°C in a water bath before usage. The viability of the cells was 100%, as determined by the count using a hemocytometer.

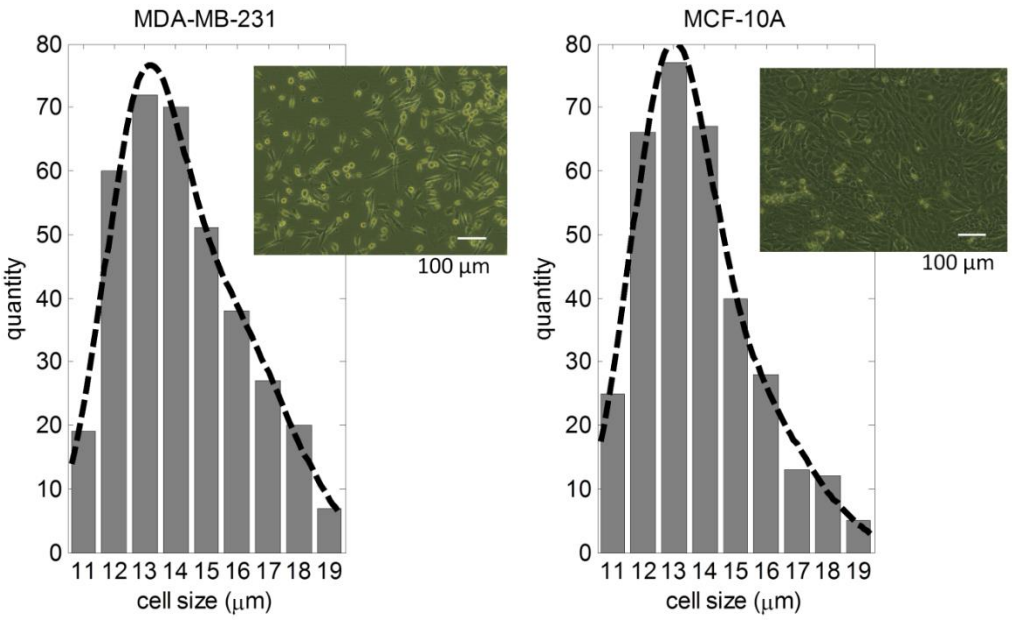

Figure 0.12: MDA-MB-231, MCF-10A cell size distribution; cell image before trypsinization.

Microfluidic channel fabrication

The multi-constriction channels devices were fabricated on a silicon wafer with two layers of SU-8 (SU-8 3005 and SU-8 3025, MicroChem, Newton, MA) photolithography and polydimethylsiloxane (PDMS) soft-lithography, followed by PDMS and glass bonding after plasma treatment. Three different configurations of channels were connected to a main delivery channel, as shown in the channel configurations in Figure 2.2. All the constriction channels had a cross-section of 8 μm by 8 μm. The first channel contains only one constriction channel with a length of 250 μm; the second channel contains two constriction channels with lengths of 125 μm each, and a relaxation section with a length of 50 μm; the third channel contains five constriction channels with a length of 50 μm each, and relaxation sections of 50 μm between every constriction channel.

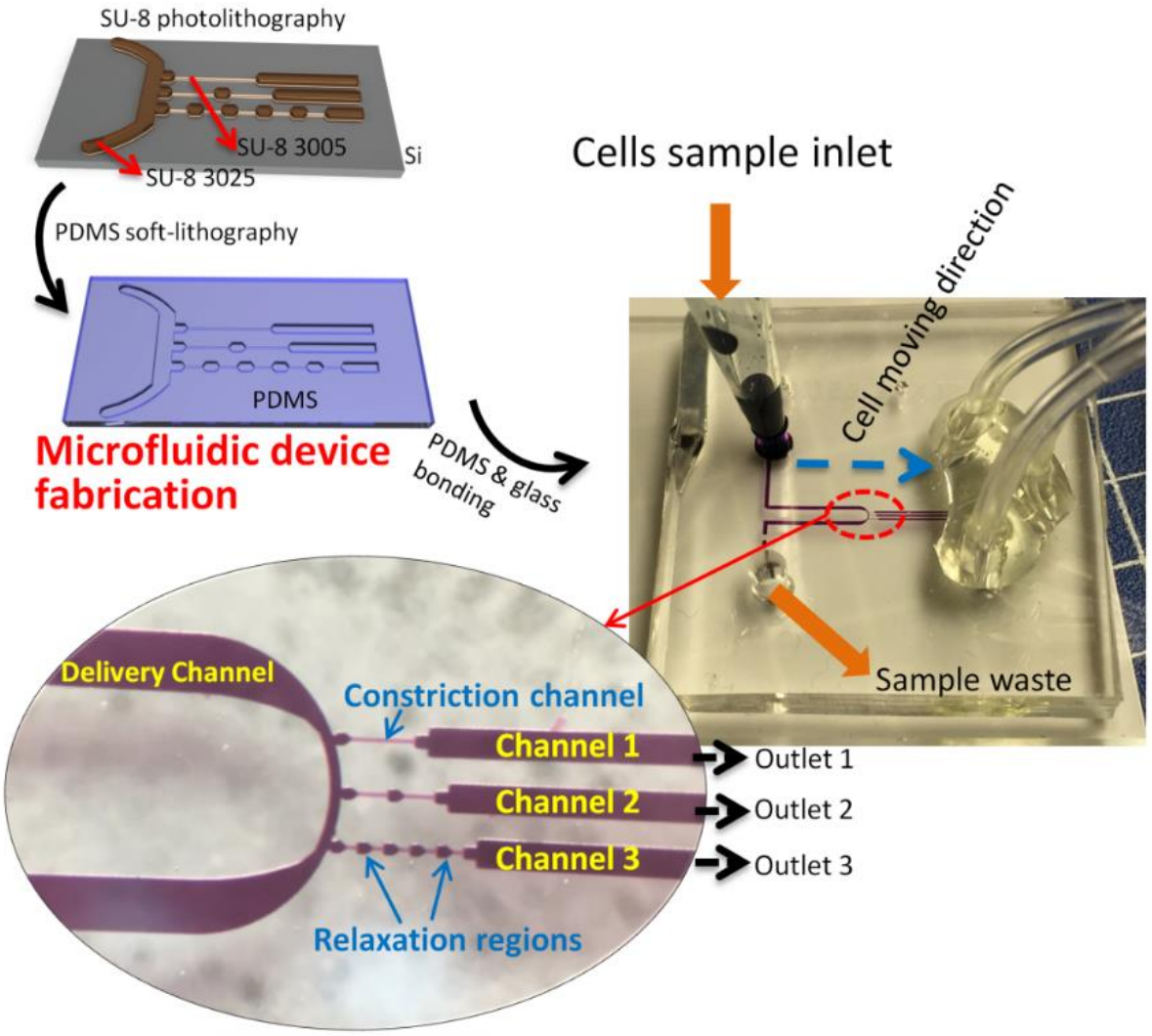

Figure 0.13: Microfluidic device fabrication processes.

The SU-8 mold consists of two layers with 8 μm of SU-8 3005 and ~25 μm of SU-8 3025, as illustrated in Figure 2.2. Tridecafluoro-1,1,2,2-tetrahydrooctyl-1-trichlorosilane (TFOCS, Fisher Scientific) was coated on the surface of the molds for the easy release of PDMS. After the mold was prepared, standard PDMS (SYLGARD® 184, Dow Corning, Midland, MI) replica molding was conducted to fabricate the microchannels. The PDMS channels were then bonded to a glass slide after air plasma treatment using plasma cleaner (Harrick Plasma, model PDC-001, Ithaca, NY).

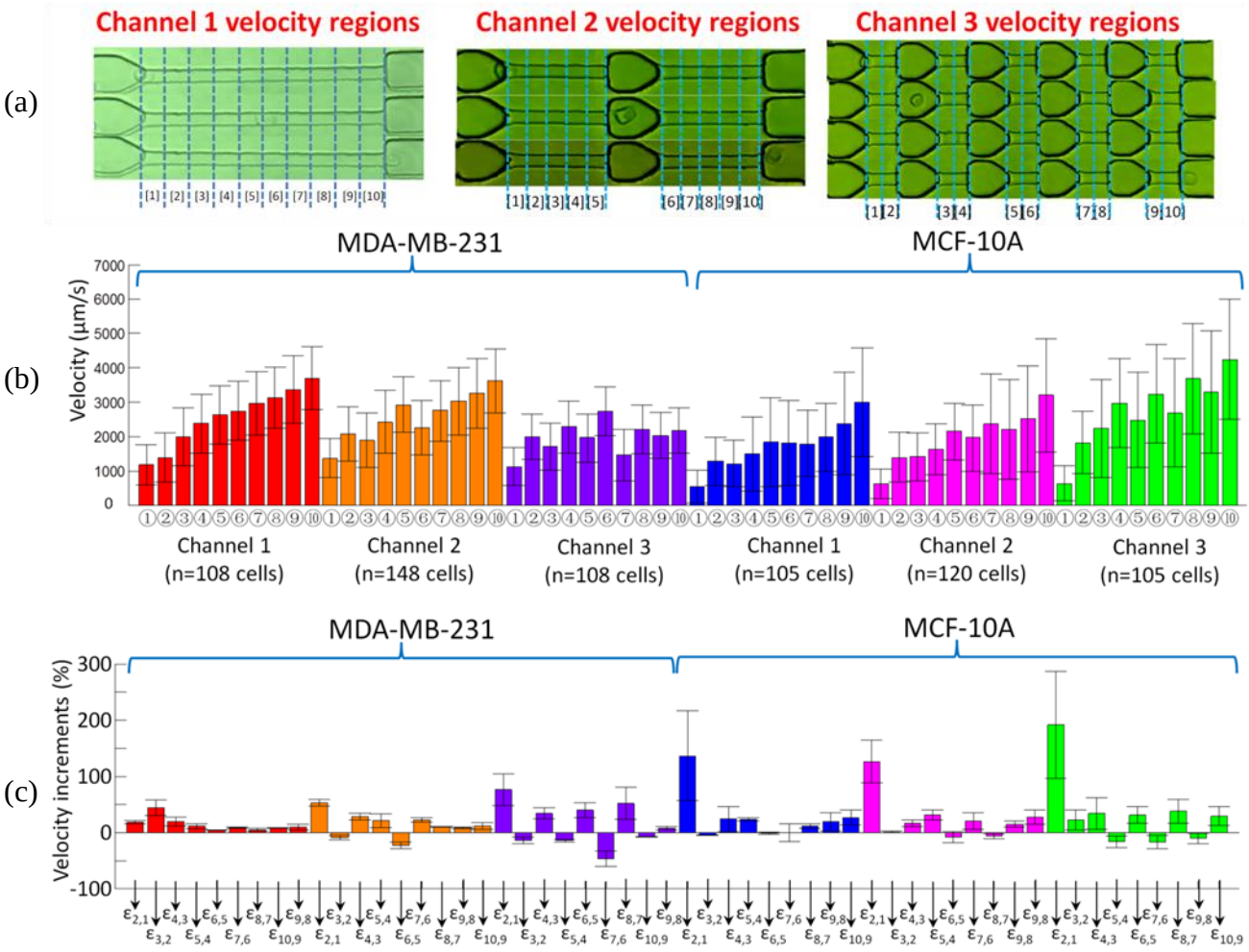

Figure 0.14: (a) Defining the velocity regions in three channel configurations using segment ①~⑩; The (b) velocity and (c) velocity increments of MDA-MB-231 cells and MCF-10A cells in three different microfluidic channels.

2.3 Experimental

Experimental setup

The microfluidic device was mounted on an inverted microscope (Zeiss Axio Observer, LSM-510, Thornwood, NY) with a lens magnification of 20×. One side of the delivery channel was connected to a reservoir with a cell sample. Three outlets were connected together to a syringe pump to create the same negative pressure. The cell delivery was initiated by applying a one-time negative pressure by another vacuum pump. The cell delivery was maintained by the

pressure difference between the cell sample reservoir and the opening of the other side of the delivery channel. This channel dimension is good for cell sizes from 11 μm to 19 μm. Normal cells (MCF-10A) with 25 μm or larger will completely clog the microchannel.

Instead of a high speed camera, a smartphone's slow motion function was applied to record videos of cell movement with a frame rate of 240 frames per second. The video can be analyzed to extract information about the motion of each cell traveling through the constriction channels. As shown in Figure 2.2, the single constriction channel was referred as channel 1; the middle channel with one relaxation at 125 μm was referred as channel 2; and the five-constriction and four relaxation channel was referred as channel 3.

Data collection

The data of the movement of the cells in the three different channels were collected from the smartphone videos. For analysis, only the constriction channels were considered, where all three channels have the same total length of 250 μm in constrictions. The velocity distribution for every 25 μm was plotted in Matlab. As shown in Figure 2.3, the velocity at each segment was represented as ① to ⑩. The velocities in segments ① to ⑩ were recorded as V1, V2, V3, … , V10, respectively. Next, the velocity increment between every 25 μm was calculated. The velocity increments between two segments are defined as: $\varepsilon_{m,n} = \frac{V_m - V_n}{V_n}$, where m = 1,2,3,…,8,9, 10, and n = 1,2,3,…,8,9, 10, representing ten segments in constriction channel.

2.4 Results

Velocity of the cells

The velocity and the increments of velocity between every 25 μm of both MDA-MB-231 and MCF-10A in three channels are demonstrated in Figure 2.3. Each cell line in every channel is represented by a color, and the same color will be used in the single cell analysis.

The initial entry velocity of MDA-MB-231 cells was similar regardless of the number of relaxation regions. This can be seen in Figure 2.3(b) by comparing the heights of the red bar ①, orange bar ① and purple bar ① into channel 1, channel 2, and channel 3 as shown in the channel configurations in Figure 2.3(b), respectively. Similarly, the initial entry velocity of MCF-10A cells was independent of the number of relaxation regions as can be seen by comparing the heights of blue bar ①, pink bar ① and green bar ①. These results serve to validate the measurement system because the aperture to each channel type (channel 1, channel 2, and channel 3) is identical. Due to the same dimension of the entrance of constriction channels, the same cell line had a similar entry velocity in channel 1~3.

As seen in Figure 2.3(b), the initial entry velocity measurement of MDA-MB-231 cells entered segment ① of each channel twice as fast as MCF-10A cells. Also shown in Figure 2.3(b), from the initial entry velocity of the MDA-MB-231 cells in channel 1, 2 and 3 (red bar ①, orange bar ①, and purple bar ①, respectively), the average velocity of MDA-MB-231 cells was measured as ~1.2×10^3 μm/s, with a standard deviation of ~0.6×10^3 μm/s. Also from Figure 2.3(b), from the initial entry velocity of the MCF-10A cells in channel 1, 2 and 3 (blue bar ①, pink bar ①, and green bar ①, respectively), the average velocity of MCF-10A cells was measured as 594.0 μm/s, with a standard deviation of 473.0 μm/s.

We assume the initial entry velocity

$$\overline{V_{CA}} = k \cdot \overline{V_{NR}}$$

where k represent how much times the velocity of cancer cells is compared to normal cells. Using α = 0.05, the t_k in t-test is 1.647; therefore, k=1.92. This means that the probability of the initial velocity of cancer cells is 1.92 times to normal cells is larger than 95%. If $k = 2$, which

means $\overline{V_{CA}} > 2 \cdot \overline{V_{NR}}$, the possibility p = 79.87%. Similarly, if $\overline{V_{CA}} > 1.86 \cdot \overline{V_{NR}}$, the possibility p = 99%.

Table 0.1: Velocity difference calculated by the velocity profiles in Figure 2.3.

	MDA-MB-231			MCF-10A		
channel	1	2	3	1	2	3
$\varepsilon_{2,1}$	1.36	1.26	1.91	0.18	0.53	0.76
channel		2			2	
$\varepsilon_{6,5}$		-0.23			-0.08	

It is well-recognized that metastatic cancer cells are softer than normal cells [2, 25, 26] and this has been correlated with faster deformation and transit times in constriction channels [3, 33, 31, 38] [99-102] [99-102] [99-102] [99-102] [99-102] [75-78] [9-12] [75-78] [76-79] [75-78] [76-79]. Here we have improved the resolution of such studies by analyzing velocity profiles. The initial velocity incremental difference between MDA-MB-231 cells and MCF-10A cells was further analyzed as illustrated by Figure 2.3c. $\varepsilon_{2,1}$ is defined by the equation: $\varepsilon_{2,1} = (V_2 - V_1)/V_1$. As calculated velocity difference (Table 2.1) from Figure 2.3c, the average $\varepsilon_{2,1}$ of the MCF-10A cells in channel 1 (blue), channel 2 (pink), and channel 3 (green) is 1.36, 1.26, 1.91, respectively (Table 2.1). This shows that after 25 μm of deformation, MCF-10A cells reach a much higher V2 compared to the initial entry velocity V1. However, the $\varepsilon_{2,1}$ of MDA-MB-231 cells was calculated to be 0.18, 0.53 and 0.76, respectively for channels 1, 2, and 3; these data indicated a slight decrease in the velocity of the MDA-MB-231 cells after their initial entry into the channel. This at first seems inconsistent with the “softer” biomechanical nature of the cancer cells, and we investigated this in greater depth.

The average velocity profiles can indicate the heterogeneity of the population of a cell-line. However, we need to analyze the detailed velocity differences in each segment to find the different mechanical characteristics. Channel 2 has one relaxation region between segment ⑤ and ⑥ (as illustrated in the "channel 2" in Figure 2.3(c)). The velocity has a drop for both MDA-MB-231 cells and MCF-10A cells at V6 compared to V5, as shown in segment ⑥ of the orange and pink in Figure 2.3(b). $\varepsilon_{6,5}$ is defined by the equation: $\varepsilon_{6,5} = (V_6 - V_5)/V_5$. As calculated velocity difference (Table 2.1) from Figure 2.3(c), the average $\varepsilon_{6,5}$ of the MDA-MB-231 cells and the MCF-10A cells in channel 2 (orange and pink), is -0.23 and -0.08, respectively. This indicated that the velocity of MDA-MB-231 cells had been reduced more than MCF-10A cells. In another word, MCF-10A cells inherited a higher more exiting velocity after the relaxation region between segment ⑤ and ⑥. Channel 3 contains five constriction channels, each 50 μm in length, separated by relaxation sections of 50 μm between every constriction channel. Cells deformed at the entrance of the first constriction channel (defined as segment ① in the "channel 3" in Figure 2.3(b)) and exited at the last segment of the final constriction channel (defined as segment ⑩ in the "channel 3" in Figure 2.3(b)), where the cells have experienced sequential deformations. Cancer cells recovered back to a round cell shape quicker than normal cells in each relaxation segment and we defined this as "deformation performance". Therefore, the cancer cells showed deformation performance at the entrance to each constriction channel, which resulted in a decreasing velocity.

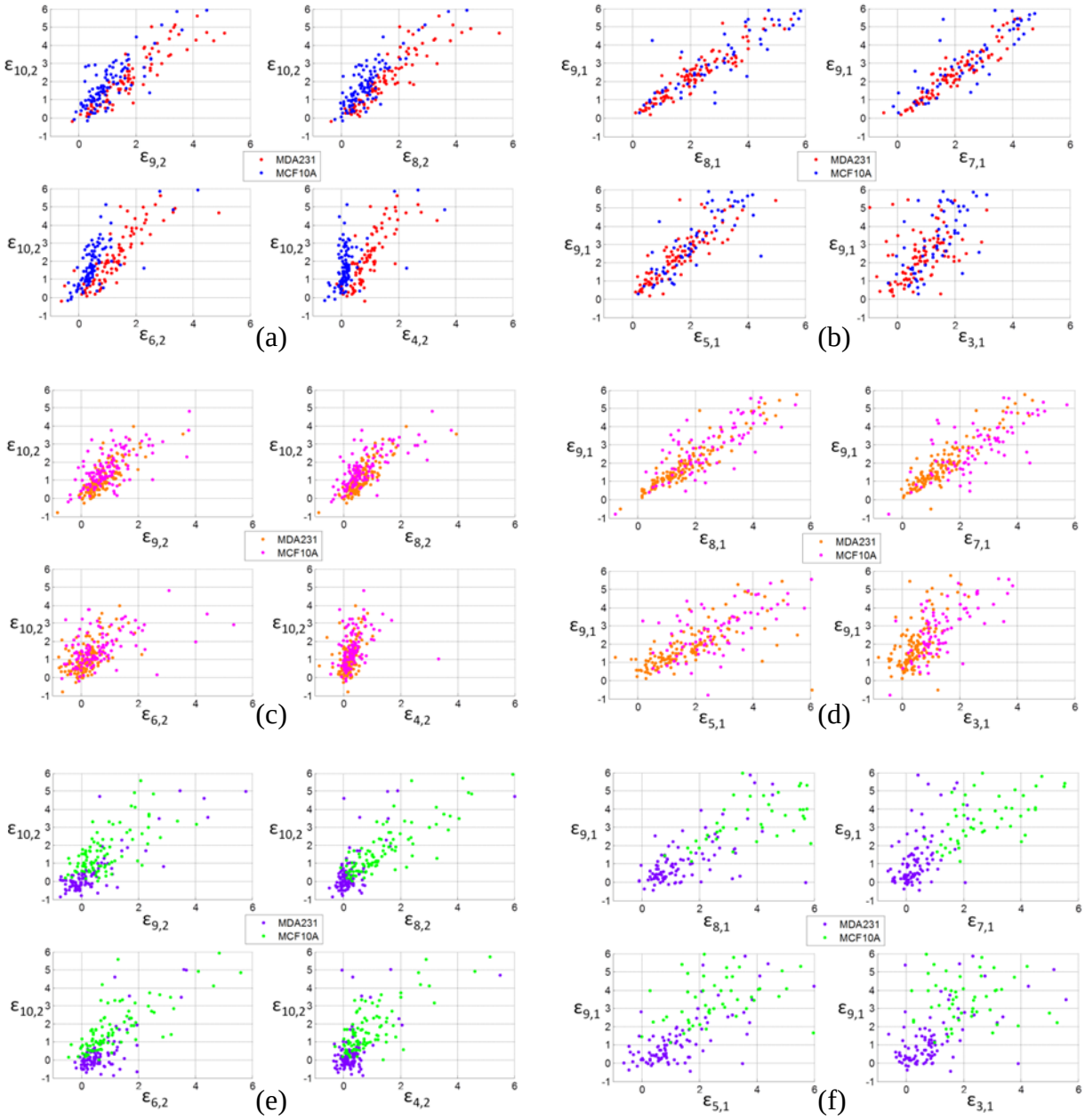

Figure 0.15: Scatter plot of MDA-MB-231 cells and MCF-10A cells velocity increments of comparing $\varepsilon_{10,2}$ to $\varepsilon_{9,2}$, $\varepsilon_{8,2}$, $\varepsilon_{6,2}$, and $\varepsilon_{4,2}$ in channel 1 (a), channel 2 (c), and channel 3 (e); and comparing $\varepsilon_{9,1}$ to $\varepsilon_{8,1}$, $\varepsilon_{7,1}$, $\varepsilon_{5,1}$, and $\varepsilon_{3,1}$ in channel 1 (b), channel 2 (d), and channel 3 (f).

As shown in Figure 2.3(a), the initial velocities (segment ①, 0~25 μm traveling distance in constriction channel) of MDA-MB-231 cells were ~1100 μm/s (purple bar ①), and exiting velocities (segment ⑩, 215~250 μm traveling distance in constriction channel) were ~2200

μm/s (purple bar ⑩). In contrast, normal cells deformed slower initially, but reached a relatively higher velocity after two or three deformations. Normal cells stay in a rod-like shape without fully recovering back to an original spherical shape. The initial velocities of MCF-10A cells were ~600 μm/s (green bar ①), and exiting velocities were ~4100 μm/s (green bar ⑩). The geometry shapes of normal cells were almost fixed when the normal cells entered the fourth and fifth constriction channels. The entrance time of cancer cells into the fourth and fifth channel was longer than the normal cells.

Single cell velocity analysis

In order to illustrate how well MDA-MB-231 and MCF-10A cells can be differentiated at the single cell level, Figure 2.4 presents the scatter plots of single cell velocity data in each channel using the same color legend as in Figure 2.3. Each dot represents the data of one cell.

The scatter plot of the MDA-MB-231 and MCF-10A cells' velocity differences in channel 1, 2, and 3 calculated at different regions within each channel are shown in Figure 2.4. The data from Channel 1 is the focus in Figure 2.4(a) and 2.4(b). Here it can been seen when comparing $\varepsilon_{10,2}$ and $\varepsilon_{9,1}$, (the ending velocity (V9 and V10), respectively) and the entry velocities (V1 and V2), the MDA-MB-231 (red dots) and MCF-10A cells (blue dots) had major overlaps in channel 1. The velocity profiling using the channel 1 configuration cannot distinguish between the cancer and normal cells at the single-cell level. About 95% of the cancer cells will be recognized as normal cells by the criterion $\varepsilon_{10,2} < 0$. Almost no cells have $\varepsilon_{10,2} > 0$, which means both MDA-MB-231 cells and MCF-10A cells have completely deformed and accelerated during passage through the single, 250 μm constriction channel. Compared to $\varepsilon_{8,2}$, and $\varepsilon_{6,2}$ in Figure 2.4(a), the criterion $\varepsilon_{4,2}$ showed a better segregation of red and blue dots into two separate regions. V1 and V2 represent the beginning of the constriction channel, where cells begin to

deform. MDA-MB-231 and MCF-10A cells showed a different deformation performance during the first 100 μm of the channel 1. MDA-MB-231 cells took a shorter time to reach a higher velocity than MCF-10A cells at V4. Therefore, the $\varepsilon_{4,2}$ of MDA-MB-231 cells had a higher value than MCF-10A cells in Figure 2.4(a). This phenomenon supports atomic force microscopy (AFM) data showing that MCF-10A cells were stiffer than MDA-MB-231 cells [2, 3, 38], which might account for inability of MCF10A cells to reach higher velocities in a continuous constriction channel of 250 μm.

Channel 2: As shown in Figure 2.4(c) and 2.4(d), the relaxation region between velocity segments ⑤ and ⑥ of the constriction channel 2 separated the channel into two 125 μm channels. The scatter plot of MDA-MB-231 cells (orange dots) and MCF-10A cells (pink dots) had major overlap at both in $\varepsilon_{10,2}$ and $\varepsilon_{9,1}$ regions, as well as in different velocity segments, such as $\varepsilon_{8,2}$, $\varepsilon_{7,1}$, $\varepsilon_{5,1}$ and $\varepsilon_{3,1}$. Because the complete deformation of MDA-MB-231 and MCF-10A cells was achieved by around the 100 μm mark within channel 2, the velocity differences were similar for both of these cell types within each velocity segment. The scatter plot in Figure 2.4(c) and 2.4(d) indicated that the channel 2 configuration was not useful in differentiating MDA-MB-231 and MCF-10A cells.

In channel 3, the short relaxation and constriction allowed the cells to continue experiencing a secondary deformation after the first relaxation. As shown in Figure 2.4(e) and 2.4(f), all of the MCF-10A cells (purple dots) had $\varepsilon_{10,2}>0$, and the majority of MDA-MB-231 cells (green dots) fell into $\varepsilon_{10,2}<0$. By further consideration of $\varepsilon_{7,1}$, more cancer cell dots fell into the region where $\varepsilon_{7,1}<2$. V7 was the velocity in the fourth constriction region in channel 3. Therefore, based on the scatter plots of MDA-MB-231 and MCF-10A cells, it is possible using the channel 3 configuration to accurately identify individual single cell from either the MDA-

MB-231 or MCF-10A cell line. The $\varepsilon_{4,2}$ in Figure 2.4(a) had a separation between MDA-MB-231 and MCF-10A cells. In channel 1, using criterion of $\varepsilon_{4,2}>0.5*\varepsilon_{2,1}$, the false negative (cancer cells observed as normal cells) rate is 7.4%, and the false positive (normal cells observed as cancer cells) rate is 19%. Using criteria of $\varepsilon_{4,2}> 0.5*\varepsilon_{2,1}$ and $\varepsilon_{4,2}>0.3$, the false negative rate is 7.4%, and the false positive rate is 19%, which means that the $\varepsilon_{4,2}$ does not further improve the differentiation rate. If we include more criteria, such as criterion II and III, the false negative rate decreased to 5.6%; however, it increases the false positive rate to 21%, so the differentiation results in channel 1 doesn't have a sufficient balance between false negative and false positive rates.

Using $\varepsilon_{10,2}$, $\varepsilon_{8,2}$, $\varepsilon_{6,2}$ and in Figure 2.4(a) had limitations in further improving the separation results. Some dots that cannot be separated by $\varepsilon_{10,2}$ or $\varepsilon_{8,2}$ but can be separated by $\varepsilon_{9,1}$ and $\varepsilon_{7,1}$. More mechanical alternation of the cells during constriction channels can bring variations in the cells' velocity profiles.

Differentiation criteria

To better define how normal cells and cancer cells can be differentiated in channel 3, specific criteria are established for separating the different cells based on their velocity profiles and their cell shape changes. Video observations revealed that MDA-MB 231 cells deformed faster than MCF-10A cells. In channel 3, MDA-MB-231 cells recovered their normal spherical shape while in the first and second relaxation regions; in contrast, here, MCF-10A tended to maintain the flattened shape they had acquired while passing through the constriction channels. When MDA-MB-231 cells continued deforming in the third and fourth constriction regions, by virtue of maintaining their flattened shape, MCF-10A cells had a smoother entry and transit in the fourth and fifth constriction regions. We propose that these differences in cell shape recovery

are reflective of differing mechanical properties and these contribute to the cell separation seen in the scatter plot of MDA-MB-231 and MCF-10A cells in channel 3, shown in Figure 2.4(e). By using the velocity at the last constriction channel and the first constriction channel we can differentiate the majority of the cancer cells from normal cells. Based on Figure 2.4(f), further decreasing of the overlapping areas between the MDA-MB-231 and MCF-10A cells can be achieved by adding the additional criteria of $\varepsilon_{7,1} < 2$. In channel 3, the entrance time of cancer cells into the fourth and fifth channel will take longer than the normal cells. Therefore, the $\varepsilon_{7,1}$ of normal cells will be larger than cancer cells. According to our experiments in channel 3, most MCF-10A cells have $\varepsilon_{7,1} > 2$, or $V7 > 3 \cdot V1$. In summary, we can further distinguish the contrasting mechanical properties between MDA-MB-231 and MCF-10A using the following criteria:

(1) Criterion I:

$$\begin{cases} \varepsilon_{10,2} = \dfrac{V_{10} - V_2}{V_2} \geq 0 \text{ (Normal cell)} \\ \varepsilon_{10,2} = \dfrac{V_{10} - V_2}{V_2} < 0 \text{ (Cancer cell)} \end{cases}$$

(2) Criterion II:

$$\begin{cases} \varepsilon_{10,2} = \dfrac{V_{10} - V_2}{V_2} \geq 0 \text{ (Normal cell)} \\ \varepsilon_{10,2} = \dfrac{V_{10} - V_2}{V_2} < 0 \text{ (Cancer cell)} \\ \varepsilon_{9,1} = \dfrac{V_9 - V_1}{V_1} \geq 2 \text{ (Normal cell)} \\ \varepsilon_{9,1} = \dfrac{V_9 - V_1}{V_1} < 2 \text{ (Cancer cell)} \end{cases}$$

(3) Criterion III:

$$\begin{cases} \varepsilon_{8,2} = \dfrac{V_8 - V_2}{V_2} \geq 0 \text{ (Normal cell)} \\ \varepsilon_{8,2} = \dfrac{V_8 - V_2}{V_2} < 0 \text{ (Cancer cell)} \\ \varepsilon_{7,1} = \dfrac{V_7 - V_1}{V_1} \geq 2 \text{ (Normal cell)} \\ \varepsilon_{7,1} = \dfrac{V_7 - V_1}{V_1} < 2 \text{ (Cancer cell)} \end{cases}$$

In order to evaluate the sensitivity of the criteria we listed, the receiver operating characteristic (ROC) curve was plotted in Figure 2.5. The sensitivities of cancer cells in channel 1, 2, and 3 were 0.69, 0.80, and 0.90, respectively; and the sensitivities of normal cells in channel 1, 2, and 3 were 0.76, 0.86, and 0.96, respectively. For channel 3 (green and purple) using criteria II & III listed above had the best differentiation results between cancer cells and normal cells.

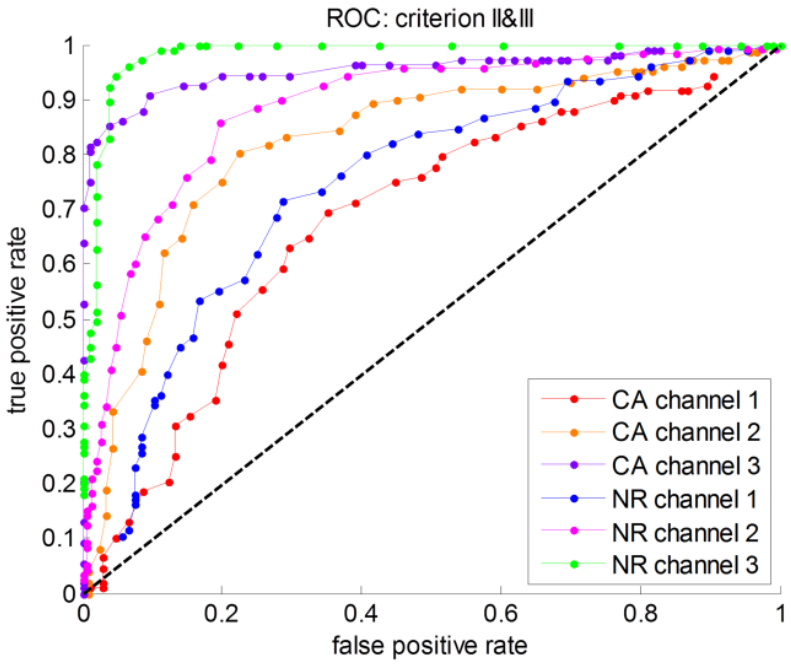

Figure 0.16: ROC curve of the cancer cells (CA) and normal cells (NR) in channel 1, 2 and 3, respectively.

Based on these differentiation criteria, scatter plots using criteria II, III, and the combination of both II & III was shown in Figure 2.6. Criteria I was able to differentiate all the

normal cells (purple dots with $\varepsilon_{10,2} < 0$). After labeling the dot of each cancer cell with sequence number 1~108 in scatter plot, we observed the sequence number of each cell. Criteria II with an additional term $\varepsilon_{9,1}$ was able to identify more cancer cells with $\varepsilon_{10,2} > 0$. Criteria III was similar to criteria II, except that we only used $\varepsilon_{8,2}$ and $\varepsilon_{7,1}$. Criteria III had some overlap of normal cells in $\varepsilon_{8,2} < 0$ and $\varepsilon_{7,1} < 2$. Therefore, we combined criteria II and III together, and used scatter plots, displayed in Figure 2.6(c), to help visualize the separation. The normal cells (purple dots) were further apart to the cancer cells (green dots).

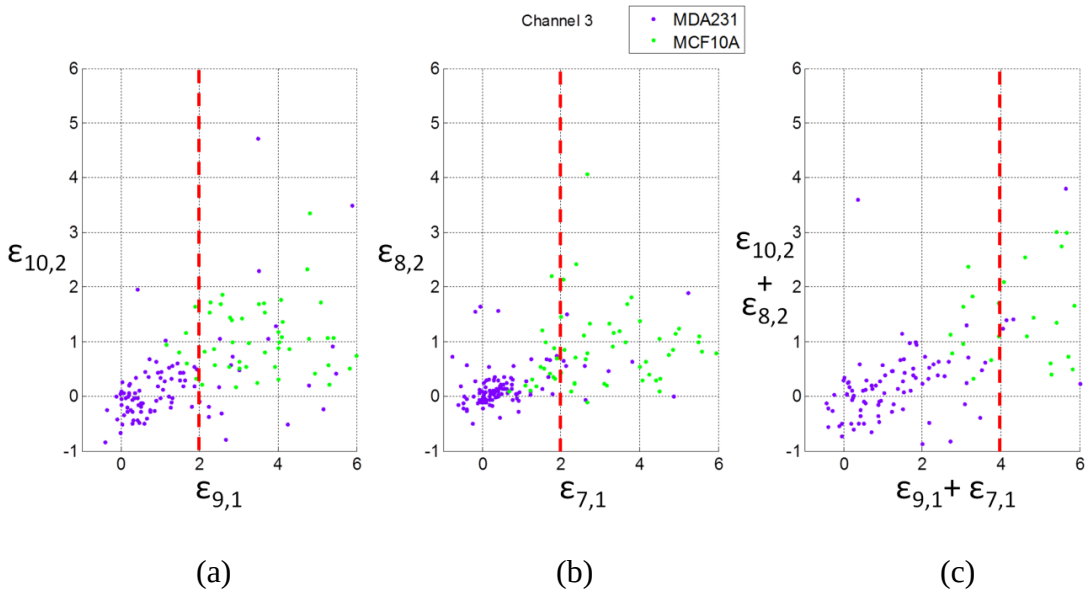

Figure 0.17: Scatter plot of using criteria II (a), III (b), and combining II & III (c) to differentiate MDA-MB-231 cells and MCF-10A cells in channel 3.

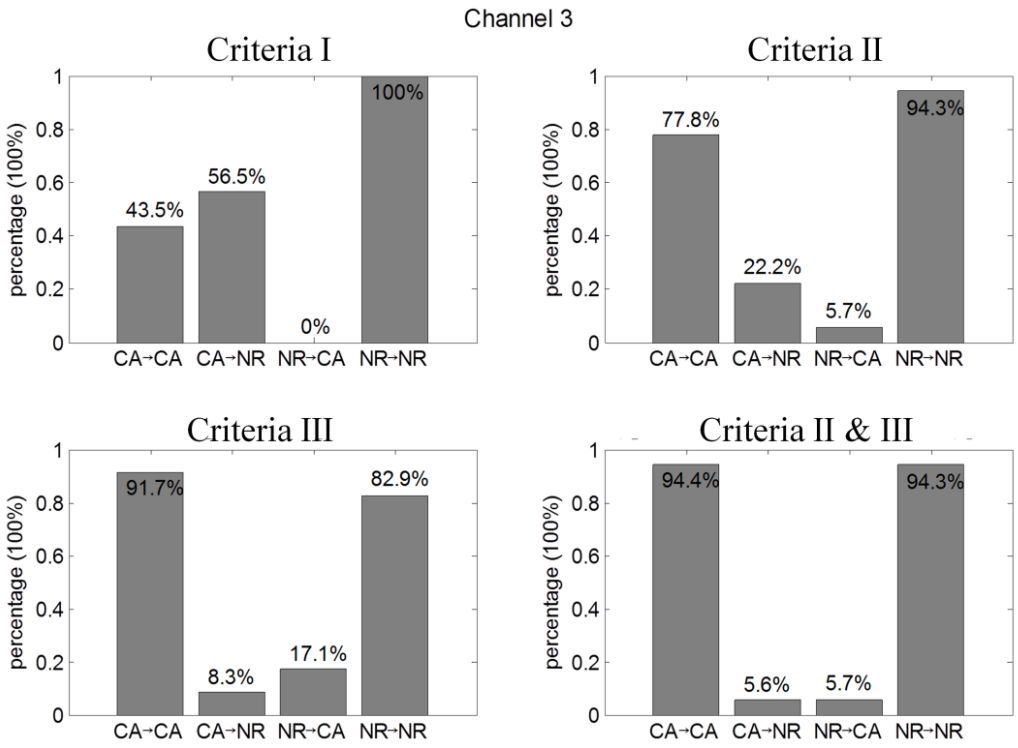

Figure 0.18: Differentiate rate of cancer cells (CA) and normal cells (NR) in channel 3 using different velocity analysis criteria.

By directly applying $\varepsilon_{10,2} > 0$, based on the scatter plot data in Figure 2.6(a) and bars in Figure 2.6(a), all of the normal cells can be recognized as normal cells (recorded as NR→NR); however, ~51% of the cancer cells were observed as normal cells (recorded as CA→NR) with $\varepsilon_{10,2} > 0$. Using criteria II and III, as shown in the scatter plot in Figure 2.6(a) and 2.6(b) and bars in Figure 2.7(b) and 2.6(c), the identification of normal cells were compromised in order to achieve higher likelihood of cancer cells being observed as either cancer cells (recorded as CA→CA) or as normal cells (CA→NR). After we applied both criteria II and III together, we achieved an acceptable ratio to differentiate cancer cells and normal cells.

Testing sample in Channel 3

In order to verify the quality of our differentiation criteria, four blind samples with either cancer cells or normal cells were tested. The data of velocity at each constriction increment in channel 3 was analyzed.

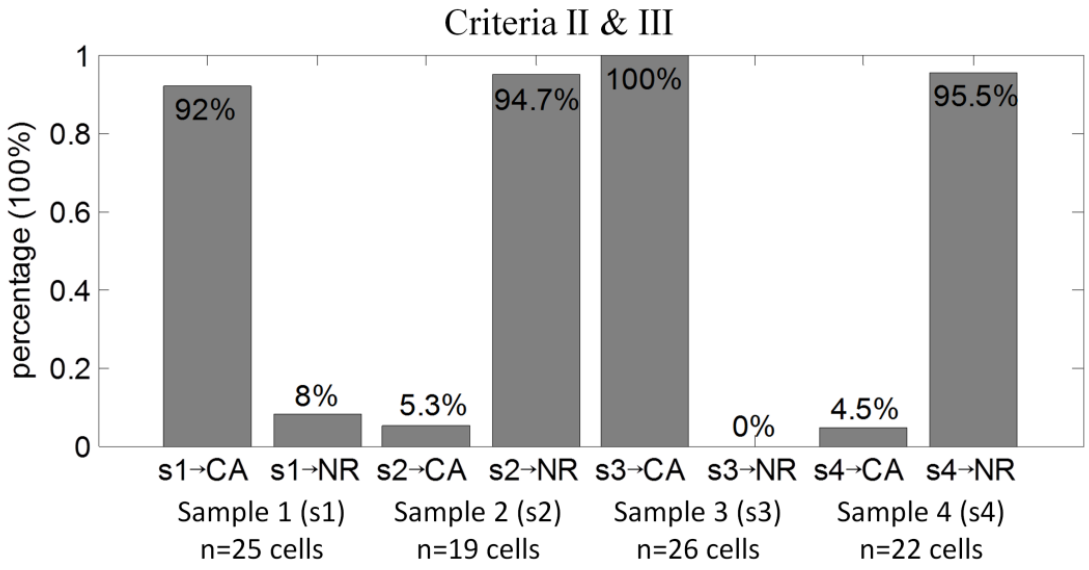

Figure 0.19: Differentiation ratio of cancer cells (CA) and normal cells (NR) using four blind-testing samples (s1, s2, s3, and s4) in channel 3.

The combination of criteria II & III was applied here to the blind-test samples (s1, s2, s3, and s4). As a result indicated in Figure 2.8, two samples were observed as cancer cells and the other two samples were observed as normal cells, which agreed to the predicted cells before testing.

2.5 Discussion

The initial deformation of the cells was affected by the mechanical properties of the cells, since the microfluidic channel geometries and experimental conditions were the same. The kinetic behaviors of the cells were directly related to the mechanical properties, such as Young's modulus, cell membrane stiffness, and tension stress of the membrane. These velocity profiles vary between normal cells and cancer cells, because cancer cells have lower membrane stiffness and cytoskeleton strength as documented by previous studies [3, 4, 39, 40] [100, 103-105] [100, 103-105] [100, 103-105] [100, 103-105] [100, 103-105] [76, 79-81] [10, 13-15] [76, 79-81] [77, 80-82] [76, 79-81] [77, 80-82]. The velocity of the cells depends on fluidic pressure, flow rate,

and the geometry of the cells. The cross-section of the microfluidic channels and flow rate are kept constant for both MDA-MB-231 and MCF-10A medium, so that the Reynolds number of both samples can be considered constant. The mechanical characteristics can be revealed by the dynamic behaviors of the cells. The stiffness of the cell membrane dominates the shear force and shear stress between the cell membrane and the microfluidic channel side wall. The Young's modulus of the cells affects the deformation of the cell membrane when the cross-section of the microfluidic channel changes. Both the stiffness of the cell membrane and the Young's modulus of the cells are typical bio-markers used to distinguish cancer cells from normal cells. By studying the average velocity at each segment and the velocity difference between different segments, we can differentiate the different cell types due to their different mechanical characteristics.

The first approaches that used microfluidics for differentiating cells were explored by using a single constriction channel like the channel 1 we presented in our device. The cells experienced a one-time deformation in a single constriction channel, which relied on both the cell size and stiffness. The differentiation merely based on velocity was not reliable due to the variability in cell size which is unavoidable due to at a minimum, cell cycle phase dependent variations in cell size. In a single constriction channel (channel 1), our experiments had a differential ratio of 52.9% for the cancer cells, which was similar to the results of others' experiments with single constriction channel with 8 μm × 8 μm cross-section [18]. Chen, et al., used the elongation and transit time of the cells in single constriction channel to characterize breast cancer cells, with a differential ratio about 57.5% [18]. This low recognition rate was another reason why scientists were encouraged to search for new methods to further differentiate different types of cells. Rather than adding electrodes to measure impedance to combine

biomechanical and bioelectrical parameters of the cells, we opted to add relaxation regions to separate the single constriction channel into multiple constriction channels to emphasize the biomechanical characteristics of the cells. Our differential ratio for both cancer cells and normal cells can reach more than 94%, which was also verified by four blind-testing samples.

From viewing images from the video microscopy, each cell, even within a cell line population, is different and unique. In the single-constriction channel (channel 1), the MDA-MB-231 cells have a higher velocity than the MCF-10A cells. The single-constriction channel with length of 250 μm was separated into 10 segments; however, the 10 segments of the velocity profiles in channel 3 included 5 velocities deformation regions. The two types of cells performed differently in velocity profiles with the five deformation regions, which was suitable in cell type differentiation. In channel 2, both cell types have a decreasing velocity at the relaxation region between 125~150 μm. In channel 3, due to the short constriction region and short relaxation region, MDA-MB-231 cells do not experience a full shape recovery process (deformation performance). Compared to channel 1, channel 3 distinguishes cell types by adding multiple deformation and relaxation regions, which make V7, V5, V3 more useful in differentiating different cell types. Channel 3 introduced more mechanical alternations for the cells, which increases the membrane mechanical differences between normal cells and cancer cells. Each time the cell deforms, a greater separation is obtained for cells of different metastatic potential. Therefore, based on the velocity profiles generated in constriction regions and relaxation regions, channel 3 had more opportunities to have varying velocity profiles, including velocity increments, for MDA-MB-231 cells and MCF-10A cells. MCF-10A cells in channel 3 have a long deformation time at the entrance, however, they kept the rod-like shape and moved into the succeeding constriction regions with a higher initial velocity. With the continuous acceleration,

MCF-10A cells reach a higher final velocity than MDA-MB-231 cells. In other words, once the MCF-10A cells deform, they retain the shape that facilitates their passage. MDA-MB-231 cells show more plasticity in their shape with a net retardation of their velocities.

In our experiments, the effect of multiple relaxation regions are studied in multiple-constriction channels (channel 3) in order to differentiate between cancer cells and normal cells. In future work, the length of relaxation regions can be modified and tested. The cancer cells and normal cells behave differently during the constriction and relaxation regions. The constriction time was determined by the constriction channel length, while the relaxation time was determined by relaxation position and relaxation length. With a longer relaxation region, the cancer cells can recover more after the constriction channels, which may have a recovery that behaves differently compared to the recovered normal cells.

2.6 Conclusions

After calculating the velocity increments in the fourth channel and fifth channel compared to the initial velocity in multiple-constriction channels (channel 3), the scatter plot of the single cell velocity data of each MDA-MB-231 (n= 108 cells) and MCF-10A (n= 105 cells) cells showed clear separation of the two cell lines into distinct regions, which successfully differentiated ~94.4% of the cancer cells from normal cells. Due to the fact that normal cells are stiffer than cancer cells, multiple relaxation regions gave cancer cells more chance to recover into its original shape, and enlarged the dynamic velocity increments along the constriction channels. Our measurement by smart phone video through microscope was reliable. Furthermore, this method has a potential to be developed into a convenient phone application of health examination. Our experimental results indicated that multi-constriction microfluidic channels can be used to differentiate metastatic MDA-MB-231 and MCF-10A cells at the single

cell level. For future studies, the quantity of parallel constriction channels can be increased to have higher throughput.

3. Comparative study of prostate cancer biophysical and migratory characteristics via iterative mechanoelectrical properties (iMEP) and standard migration assays

Ghassemi, P., Harris, K. S., Ren, X., Foster, B. M., Langefeld, C. D., Kerr, B. A., & Agah, M. (2020). Comparative study of prostate cancer biophysical and migratory characteristics via iterative mechanoelectrical properties (iMEP) and standard migration assays. Sensors and Actuators B: Chemical, 321, 128522.

3.1 Introduction

Chemotherapeutic treatment of cancer has focused on the inhibition of invasion and, consequently, metastasis. The scratch wound healing assay and Boyden chamber are common and well-established methods of evaluating cell migration *in vitro* [106-110]. The wound healing assay involves creating a gap within a cell monolayer and capturing time-lapse imagery of cell migration. The rate at which the cells travel to "heal" the wound is indicative of cell-matrix and cell-cell interactions during cell migration [107-110]. The Boyden chamber assay, also known as the transwell assay, consists of two compartments separated by a membrane with micropores, where pore sizes can range from 3-12 μm to suit cells of interest [106, 111]. The cells are seeded in the top region and the bottom region contains chemo-attractants. Using this method, migratory behavior is quantified using a plate reader or by staining cells and taking images of the cells [106, 109, 111]. Drawbacks of the wound healing method are lengthy experimentation time of the assay, the influence of cell proliferation, and lack of chemo-attractants. In contrast, the Boyden chamber method typically consumes less time, is independent of proliferation, and allows for the usage of chemotactic agents. Additionally, microfabricated

migration assays have also been developed using microfluidic platforms, where researchers have evaluated cell migratory behavior and kinetics of endothelial and cancer cells [112-115].

Deformability of cells in the presence of a compressive force is a mechanical property that can be used to phenotype cells with different sizes ranging from red blood cells to tumor cells [23, 57, 116, 117]. The deformability of a cell is influenced by its intracellular structures and is particularly dependent upon the cytoskeleton, the kinetic framework of the cell. The compliancy of a cell can be used to classify cells according to specific phenotypes, most notably, diseased versus healthy tissues. In this regard, phenotyping can provide information regarding the immune response, stem cell therapies, cancer diagnostics, etc. Deformability assays have become increasingly common in cancer research as it has been observed that in most cases more aggressive cancer cells exhibit decreased structural rigidity most likely benefitting cellular locomotion and metastasis [23, 57, 66, 118, 119].

In order to accommodate the urgency placed upon health-related diagnostic practices, a high-throughput method to analyze the compliance and migratory behavior of single cells is required. Methods of determining cell deformability already in practice are atomic force microscopy (AFM) [39, 120], micropipette aspiration [121], hydrodynamic stretchers [40], magnetic tweezers [27], and optical stretchers [23]; however, these techniques require specialized equipment and require time-consuming pre-processing, experimentation, and post-processing times. In addition, these procedures involve tools that can cause damage to the cells through contact or fixing and staining. Standard migration assays also share similar drawbacks, including time-consuming preparation and experimentation. To alleviate these issues, constriction-based microfluidic flow cytometry, which operates at a much greater throughput,

has proven to be a viable method of deformability and migratory analysis with the added benefits of cost-effectiveness and low-complexity [57, 66, 116, 118].

Flow cytometry is a versatile tool commonly employed to study cell surface markers and biophysical properties under laminar flow using optical scattering or fluorescent tags [122-125]. Deformability can be observed when a constriction slightly smaller than cell diameter is incorporated into the channel, which is the principle of constriction-based microfluidics. Data collected from these systems describe the passage time of single cells. Passage time is composed of entry time, the time required for a cell to deform and enter the constriction, and transit time, the time elapsed between the cell entering the constriction and exiting it. Transit time is influenced by friction between the cell and the channel wall, as well as fluid flow pressure [57, 66, 118]. Constriction-based technologies have been improved by employing a cyclic deformation assay, which involves sequential deformation regions separated by relaxation regions. Previously, our group has shown that cyclic deformations can improve the detection of breast cancer cells from their normal counterparts [66, 118, 119]. The traditional method of observing cell velocities as they pass through these constriction points is with a high-speed camera; however, this practice is time-consuming in data analysis and the equipment is expensive. The post-processing time is further amplified by incorporating multiple constriction microchannels as multiple time points need to be obtained for each constriction region. These disadvantages are improved through incorporation of electrode sensors embedded within the device. Electrodes can measure impedance within the constriction channel and impedance peak profiles can be utilized to measure transit times [58, 65, 126-130].

Bioelectrical properties of cells are emerging as label-free markers which allow for significant differentiation between similar cell types [131-135]. This is due to variations in

electrical properties of cells, such as membrane capacitance and cytoplasm resistance, attributed to differing physiologies between cells. Recently, research has emerged combining electrical analysis of cells with deformability microfluidics to produce microfluidic impedance devices [58, 65, 126-128]. In this study, it was hypothesized that measuring the impedance of single cells in combination with deformability, represented by transit times, allows for greater differentiation between similar prostate cancer cell types: LNCaP, LNCaP-C4-2, and LNCaP-C4-2B. These cell lines have clinical relevance as they represent the progression that human prostate cancer typically goes through, where the prostate cancer gains androgen-independence then metastasizes to bone. Thus, they provide a good model to help understand the mechanisms of androgen-independence and bone metastasis. Additionally, a normal/healthy prostate cell line, PWR-1E, has been included in the study to compare its biophysical attributes to those of various cancer cells.

The biosensor reported in this paper consists of five sequential constriction channels separated by relaxation regions where biomechanical and bioelectrical attributes of cells are obtained simultaneously. Yang et al. developed a multi-constriction microfluidic device with embedded 3D electrodes to obtain biomechanical and bioelectrical data of single cells [130]. Our work differs in terms of the device configuration, application and post-processing of data. The 3D electrode configuration is advantageous with respect to elimination of alignment and sensitivity, however they do not have the flexibility for an inexpensive off-chip device via planar electrodes [136]. Device configuration also differs as they do not have a built-in anti-clogging mechanism. Their work compared chemically treated MCF-7 cells, while our platform is used to compare various prostate cell lines with differing cancer progression. Lastly, their data analysis requires complex neural network post-processing compared to our quick and simple post-

processing. We report the first instance of studying biophysical attributes of the prostate progression model of LNCaP cell lines, and how it compares to a normal prostate cell line counterpart. Additionally, migratory behavior has been assessed through scratch wound healing and chemotaxis Boyden chamber assays, and results are compared to biophysical attributes obtained from our microfluidic sensor. The coupling of these assays provides a comprehensive analysis of cells at different stages of prostate progression model and how it compares to a healthy prostate cell line.

3.2 Materials and Methods

3.2.1. Cell lines

LNCaP is a human prostate cancer cell line; derived from a metastatic site- the left supraclavicular lymph node of a Caucasian 50-year-old male. The C4 cell line constitutes the in vitro cultured subline grown from the murine host's tumor. When the C4 sub-line was subsequently co-inoculated with MS osteosarcoma fibroblasts in a castrated athymic male nude mouse host for another 12 weeks, prostatic epithelial cells cultured from the resultant tumor in this host constituted the C4-2 subline which is androgen-independent. The LNCaP-C4-2B cell was obtained from bone metastatic C4-2 cells grown in a castrated mouse and is also androgen-independent [137]. LNCaP and LNCaP-C4-2B were gifts from Dr. Leland W.K. Chung via Dr. Simon W. Hayward and Dr. Magda M. Grabowska (Case Western Reserve University). LNCaP-C4-2 cells were a gift from Dr. Warren D. Heston (Cleveland Clinic). The PWR-1E cell line is prostate epithelial line derived from a Caucasian male at 67 years of age and was purchased and verified by ATCC. All lines have been confirmed negative for mycoplasma.

3.2.2. Sample Preparation

Human prostate cancer cell lines LNCaP, LNCaP-C4-2, and LNCaP-C4-2B were grown in RPMI-1640 with 10% fetal bovine serum and 1% Pen-Strep (100 U/mL penicillin and 100 ug/mL streptomycin)(GIBCO) . The human immortalized prostate epithelial cell line, PWR-1E, was cultured in keratinocyte serum-free medium (K-SFM) supplemented with 0.05 mg/mL of bovine pituitary extract and 5 ng/mL of human recombinant epidermal growth factor provided in the K-SFM kit (GIBCO). Cell monolayers were grown in T-25 cm^2 culture flasks at 37 °C in a combination of 95% air and 5% CO_2 until cells reached proper confluency. To process cell monolayers for experimentation, the cells were detached from the inner surface of the flask with a trypsin-ethylenediaminetetraacetic acid solution for ~5 minutes at 37 °C and gently aspirated to create a single cell suspension. Cell suspensions are spun down, rinsed, and resuspended in 1× PBS. Cell counts were ~ 10×10^4 cells/mL for each respective cell line. Cell diameters for LNCaP, LNCaP-C4-2, LNCaP-C4-2B, and PWR-1E ranged from 10-16 μm, 10-16 μm, 10-15 μm, and 10-15 μm, respectively [138].

3.2.3. Device Fabrication

Fabrication of the electrodes (Figure 1) starts with the patterning of a glass wafer with photoresist (S1813, MicroChem, Newton, MA) by means of photolithography. Using electron-beam (e-beam) evaporation, layers of chromium (~40 μm) and gold (~80 μm) are evaporated onto the patterned wafer and electrodes are created using standard metal lift-off techniques. To create the microfluidic channels (Figure 1), we patterned a silicon wafer with two layers of SU-8 (SU-8 3005 and SU-8 3025, MicroChem, Newton, MA) through photolithography to create a master mold. The SU-8 3005 was used to build the constriction channels with a height of 8 μm; and the SU-8 3025 was used to build the remaining microfluidic channels with a total height of ~30 μm. The mold is then coated with tridecafluoro-1,1,2,2-tetrahydrooctyl-1-tricholosilane

(TFOCS, Fisher Scientific) for easy release of polydimethylsiloxane (PDMS). Using soft-lithography techniques, we use the master mold to create the PDMS microchannel. Through plasma activated bonding we align and bond the PDMS microchannels onto the glass with electrodes. Each electrode has its own bond pad so that wires can be soldered in order to be connected to the impedance spectroscope.

3.2.4. Device Design

The sensor consists of two separate channels, delivery and constriction, to prevent cell accumulation at the constriction and clogging (Figure 1). The sample of single cells suspended in 1× PBS passes through the channel from an inlet to an outlet. Once cells have been introduced to the delivery channel, a vacuum pump applies a negative pressure at the outlet. Consequently, cells flow through the delivery channel due to pressure differences. The entrance of the constriction channel is located at the center of the delivery channel. A separate negative pressure applied at the end of the constriction channel, via a Harvard Apparatus syringe pump, in order to initiate flow through the constriction channel. Flow through the constriction channel is initiated by applying a constant negative pressure of $\Delta P = \sim$-100 Pa. Once a cell has entered the constriction channel, the flow coming from the delivery channel stops until the cell trapped in the constriction channel has passed through completely. The constriction channel consists of five constriction regions and four relaxation regions, where each region is 50 µm in length, 8 µm in height and 45 µm in width, respectively. The device also consists of a pair of two electrodes 20 µm-wide and 120 nm-tall with a spacing of 625 µm. The electrodes are aligned ~85-90 µm from the entrance and exit of the constriction channel.

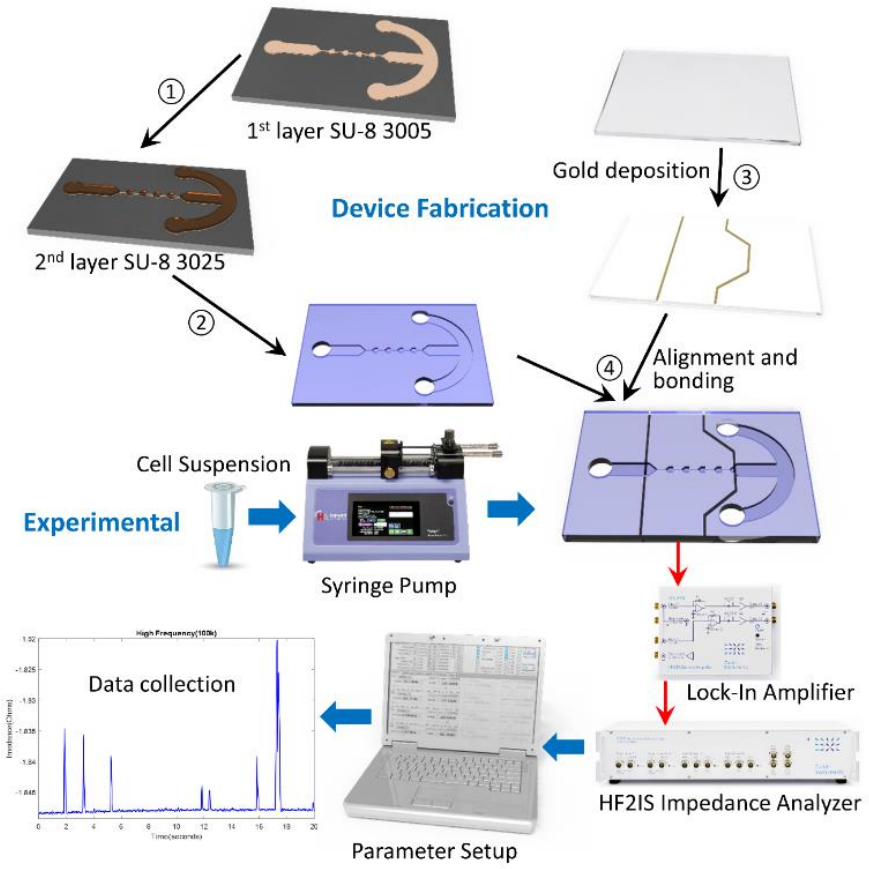

Figure 20. Overview of iMEP device fabrication and microfluidic experimental setup.

3.2.5. Experimental Setup

3.2.5.1. Scratch Wound Assay

Scratch wound migration assays were performed using the 96 well image lock plates (Sartorius) and the wound maker from IncuCyte ZOOM Live-Cell Analysis System (Sartorius). Cells were plated into each well at 4.5 x 10^4 - 7.5 x 10^4 in 100 µL of medium and allowed to adhere overnight. Cells were wounded using the wound maker, washed, and 200 µL of new media added. Plates were placed in the IncuCyte and scanned every two hours until wounds closed, media was changed every 2-4 days.

3.2.5.2. Chemotaxis Migration Assay

LNCaP, LNCaP-C4-2, LNCaP-C4-2B, and PWR-1E cells were plated, in ClearView 96-well chemotaxis plates (Sartorius) with 8 µm pore size, in biologically equivalent sextuplicates at 60-

120 cells per well using complete RPMI-1640 or complete K-SFM and incubated overnight to allow for adherence. To establish a chemical gradient, media was changed inside the upper reservoir from complete RPMI-1640 to serum-reduced RPMI-1640 supplemented with 1% FBS and complete K-SFM to growth factor-reduced K-SFM supplemented with 0.01 mg/mL BPE and 1 ng/mL. Cell migration towards complete media was monitored using the IncuCyte ZOOM Live-Cell Analysis System (Sartorius) by continuous imaging every 2 hours for 72 hours. Migrated cell count was quantified using IncuCyte software analysis (Sartorius) and normalized to the initial top value.

3.2.5.3. Microfluidic iMEP Assay

The iterative mechanoelectrical properties (iMEP) device is mounted on an inverted microscope (Zeiss Axio Observer LSM-510, Thornwood, NY) with a lens magnification of 20×. During experimentation, the electrical impedance across the channel was obtained by applying 1V AC signal at 8 different frequencies of 0.5, 1, 5, 10, 50, 100, 500, and 1000 kHz using the HF2IS Impedance Spectroscope (Zurich Instruments, Zurich, Switzerland). Two devices on separate days were used to obtain the biomechanical and bioelectrical results, where a minimum of three runs for each cell type was used on each individual device. Figure 2 shows a representation of the impedance peak collection for a single cell passing through the five constrictions. The electrical properties are represented by shifts in magnitude and phase, where the max peak is subtracted from the baseline. High-speed videos were obtained at 100 frames/sec via the Motion Xtra NX4-S3 high-speed camera (IDT, Tallahassee, FL) for cross-verification of cell transit through the constriction channels. Data was obtained from the impedance analyzer using Python 3.6.

3.2.5.4 Statistical Analysis

Statistical significance was determined by two-way or one-way analysis of variance (ANOVA) with Tukey post-test using the GraphPad Prism 7 software. For experiments over time, significance was confirmed using linear regression models to test for differences and test interactions between cell type and slope of the relationship with time with the SAS software. Error bars represent the SEM of experiments. * $p<0.05$, ** $p<0.005$, and *** $p<0.001$, and **** $p<0.0001$.

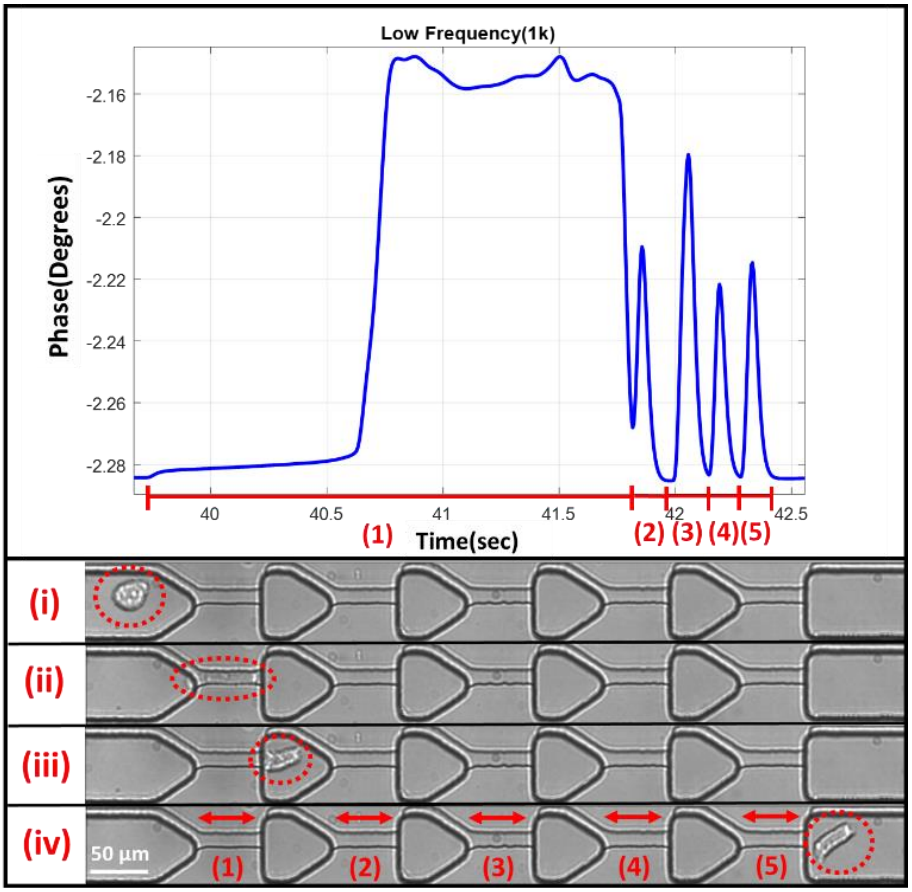

Figure 21. Representative impedance plot of a single cell passing through the sequential constriction channels. Each constriction results in its own peak, where timing and impedance information can be obtained. (i) Cell before deformation. (ii) Cell within the first deformation. (iii) Cell after first deformation. (iv) Cell after transit through all constriction channels.

3.3 Results

3.3.1 Scratch Wound Assay

To evaluate sheet migration behavior of normal prostate epithelial cells and androgen-dependent or independent prostate cancer cells, we performed a scratch wound healing assay. Results depicted in Figure 3 below indicate that the normal prostate cell line PWR1-E healed the wound the quickest out of all cell lines: 5-fold faster than LNCaP, 1.6-fold faster than LNCaP-C4-2, and 4.4-fold faster than LNCaP-C4-2B cells. However, comparing the prostate cancer cell lines show that the LNCaP-C4-2 heal the wound the quickest, followed by LNCaP-C4-2B (2.7-fold slower than LNCaP-C4-2) and LNCaP (3-fold slower than LNCaP-C4-2). Thus, the two-dimensional migration demonstrates altered migratory behavior dependent on the cell line tested with the normal epithelial cells healing the wound the fastest

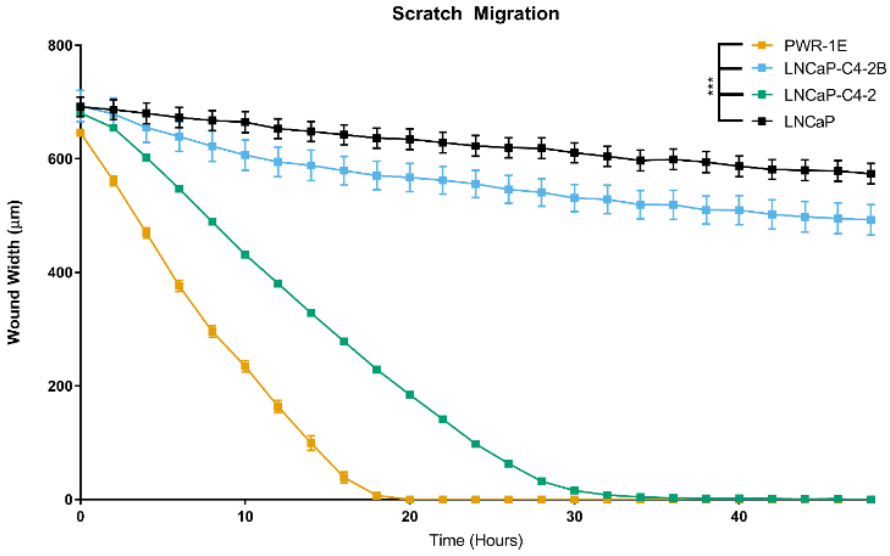

Figure 22. Normal prostate epithelial cells migrate quickly in two dimensions. Width of remaining wound after scratch represented as mean ± SEM. *** represents $p<0.001$ by two-way ANOVA with Tukey post-test.

3.3.2. Chemotaxis Migration Assay

To evaluate the chemotactic potential of normal prostate epithelial cells and androgen-dependent or independent prostate cancer cells, we performed a chemotactic migration assay using PWR-

1E, LNCaP, LNCaP-C4-2, and LNCaP-C4-2B (results are shown in Figure 4). LNCaP-C4-2 cells demonstrated the fastest migration through the pores: 3.5-fold faster than PWR-1E, 3-fold faster than LNCaP-C4-2B, and 4-fold faster than LNCaP cells. LNCaP-C4-2B and PWR-1E cells migrated more quickly than LNCaP cells, 1.4-fold, and 1.2-fold, respectively. Thus, in contrast to the two-dimensional migration, the normal epithelial cells and androgen-dependent prostate cancer cells migrated more slowly than the androgen-independent prostate cancer cell lines through the pores.

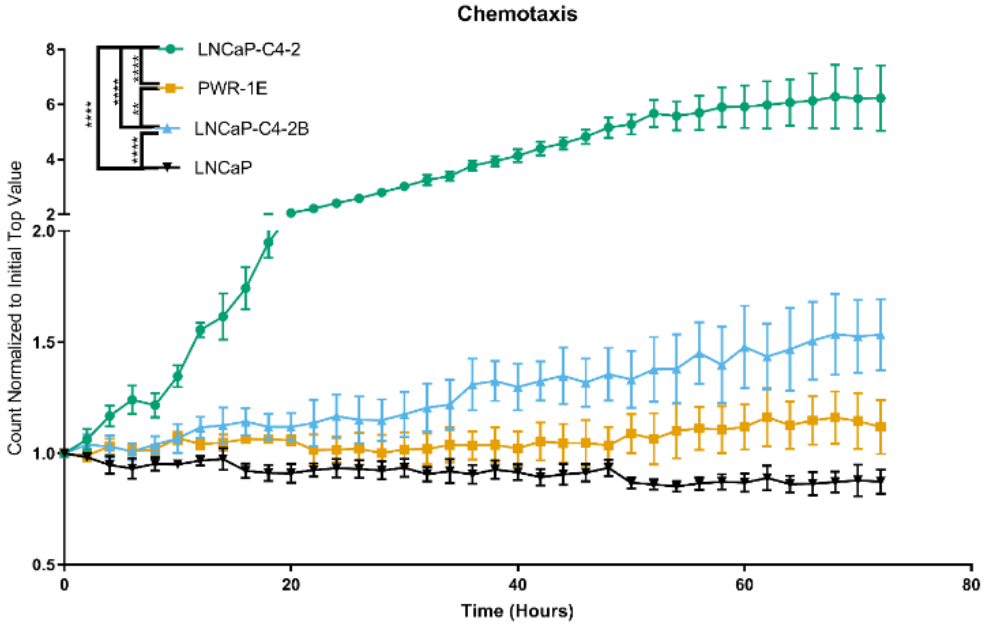

Figure 23. Androgen independent prostate cancer cell lines demonstrate higher chemotaxis compared with the normal epithelial cells and androgen-dependent prostate cancer cell lines. Number of cells in the bottom well normalized to the initial top well represented as mean ± SEM. * represents $p<0.05$, ** represents $p<0.005$, *** represents $p<0.001$, **** represents $p<0.0001$ by two-way ANOVA with Tukey post-test.

3.3.3. Microfluidic iMEP Assay

Cell timing information in the iMEP device was obtained in all 5 constriction regions in order to compare the four cells lines based on their response to the constriction channel. Average values

+/- standard error of the mean (SEM) are shown in Figure 5. Comparing the timing in constriction #1, which represents both entry and transit time, showed that the LNCaP and PWR1E cells are the most and least deformable, respectively. Additionally, the LNCaP-C4-2 and LNCaP-C4-2B have comparable constriction 1 values. Lower and higher timing in the first constriction are indicative of cells with more and less deformability, respectively. However, in the remaining four constriction channels, the cell's ability to regain its shape in the relaxation region and deformability both play a role. After experiencing the first constriction, LNCaP cells timing information approached those of the other LNCaP derivatives. The PWR-1E cells tended to have higher transit times regardless of the constriction region.

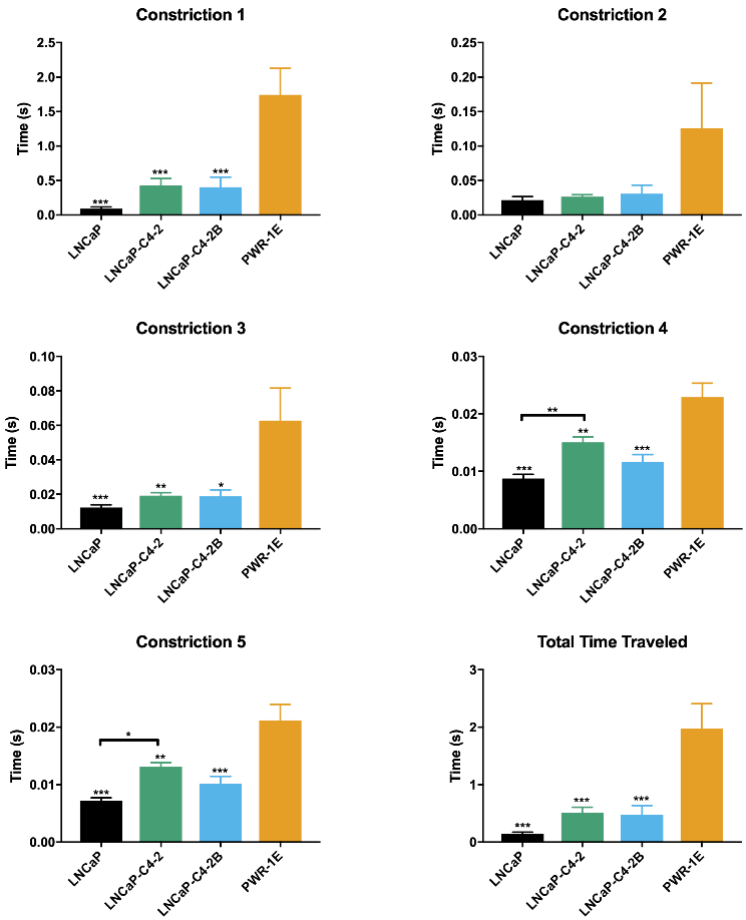

Figure 24. Passage time differentiates normal and cancerous cells. Average time traveled for single cells represented as mean ± SEM. * represents p<0.05, ** represents p<0.005, *** represents p<0.001 by one-way ANOVA with Tukey post-test. Cell count for each cell line is N = 60, 66, 41, and 48, respectively.

In addition to timing information, electrical properties were obtained for each cell line where the average +/- SEM of phase and magnitude, measured at respective frequencies of 50 kHz and 100 kHz, is shown in Figure 6. Although phase and magnitude were obtained for frequencies ranging from 0.5-1,000 kHz, we have included a single example of each due to redundancies in data and for the purpose of brevity. Looking at both mean values of phase and magnitude, it is clear that each cell line has a distinct difference in bioelectrical properties.

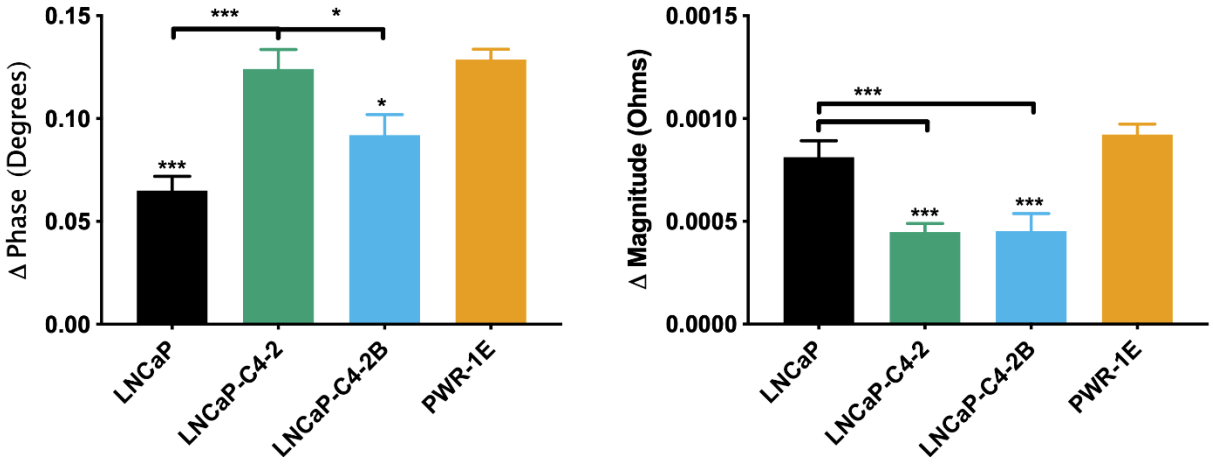

Figure 25. Bioelectrical measurements differentiate between all four cell lines with cell count N = 60, 45, 41, and 48, respectively. Phase shift and magnitude for single cells represented as mean ± SEM. * represents p<0.05, ** represents p<0.005, *** represents p<0.001 by one-way ANOVA with Tukey post-test.

3.4 Discussion

In vitro migration assays are proven techniques for evaluating cell motility, chemotherapeutic response, and metastatic potential of tumor cells [106-111]. Here, scratch wound, chemotaxis, and constriction-based microfluidic assays have been used to study prostate cancer cells of varying aggressiveness in addition to a healthy prostate cell line. Each assay provides both differing and overlapping information regarding the cells of interest. Scratch wound healing

assays operate by creating an opening in a cell monolayer and monitoring how long it takes for the cells to heal the wound. Here, cells maintain their cell-to-cell junctions and probe the collective cell migration called sheet migration [107, 110]. Our data demonstrate that normal prostate epithelial cells migrate faster than cancer cell lines in sheet migration. This is likely due to the role of epithelial cells in healing wounded tissues. In contrast, the chemotaxis and our constriction-based microfluidic assay probed the single cells by their movement through pores and microchannels where the cell is required to deform. This deformation is more relevant to the type of movement required for cancer progression. The chemotactic Boyden chamber assay, which relies on chemical stimuli to drive cell movement, measures the combination of the cells' response to the chemicals and its ability to deform and transit through the micropores [106, 111]. Our data show that the androgen-independent prostate cancer cell lines migrate more quickly through the pores and toward serum as a chemoattractant compared with androgen-dependent prostate cancer and normal prostate epithelial cells. Our microfluidic biosensor measures the ability of the cells to deform and transit through sequential constriction channels separated by relaxation regions that allow cells to have the opportunity to regain its original spherical-like shape from the rod-like shaped caused by the constriction channel. We demonstrate that normal prostate epithelial cells move slowly through the constriction channels, while the androgen-dependent prostate cancer cell line can deform and recover the most. Additionally, the electrical impedance of the cells is obtained, which relate to cell biophysical properties such as cell size, membrane capacitance, and resistance. These data were most effective in differentiating the different cell lines and when combined with constriction deformability in our iMEP device could differentiate among the metastatic cells. Figure S1 in the supplementary information illustrates an example of how a multi-parametric analysis can be utilized for single cell differentiation.

Additionally, this figure shows how combining biomechanical and bioelectrical parameters of cells can further distinguish cells. None of the standard techniques used in this study could provide this type of single cell differentiation.

The scratch wound healing and chemotaxis assay show that metastatic potential cannot be assessed using these methods. In brief, these methods are robust in terms of determining sheet migration behavior, response to chemo-attractants, and deformability; however, they cannot solely be used to study the metastatic potential of cancer cell lines. For the scratch wound assays, the results on the sheet migratory behavior do not correspond with aggressiveness in all cases. When comparing the LNCaP-C4-2 and LNCaP-C4-2B to the parental LNCaP cell line, the assay correctly indicates that the former cell lines are more aggressive than the parental cell line. However, it is not a good indicator of metastatic aggressiveness when comparing LNCaP-C4-2 and LNCaP-C4-2B; however, as these two cell lines are closely related their grouping together may be more indicative of their similarities as androgen-independent prostate cancer cell lines. Additionally, when comparing the normal PWR-1E and LNCaP cell lines, it shows that the normal cell line migrates much faster than all three cell lines. This is likely due to the role of epithelial cells in healing wounded tissues and their ability to migrate as a sheet. For the chemotaxis migration assay, we were not able to distinguish between the LNCaP and PWR-1E cell lines with statistical significance. The chemotaxis results also show that this assay is not always a good indicator of cancer aggressiveness, because the more bone-trophic LNCaP-C4-2B cell migrates at a much lower rate than the less aggressive LNCaP-C4-2 cells. We hypothesize that this could be due to changes in the cell generated by exposure to their metastatic niche: the bone microenvironment; however, further studies will be needed to tease out this association.

Cell stiffness and deformability have been used by our lab and other research groups to distinguish cancer cells from their non-tumorigenic counterparts, and untreated versus drug-treated cells [23, 65, 118, 129]. Cell deformability can be probed while attached to a surface such as in atomic force microscopy, or while suspended in liquid solution, such as microfluidic-based techniques. Microfluidic technologies are advantageous compared to alternative methods in terms of cost, throughput, and experimentation time. Researchers have commonly claimed that cell deformability is higher for cancer cells in comparison to normal cells and directly related to the aggressiveness of the cancer [139-145]. However, contradicting results have been presented, which counteract the narrative that cell stiffness is directly correlated to cell aggressiveness [146, 147]. For instance, Bastatas et al. compared stiffnesses of lowly and highly metastatic human prostate cancer cells via AFM, where the more metastatic cells were reported to be stiffer than the lowly metastatic counterpart [146]. Our iMEP results of prostate cells in some cases agree, and others disagree with this contradicting narrative, which proves that deformability or stiffness alone is not a reliable method of evaluating cell metastatic potential. More specifically, using the biomechanical properties manifested in cell transit times, we were not able to accurately predict the migratory behavior and metastatic potential of the cancer cells. However, we could clearly distinguish between the normal and cancerous populations. Furthermore, we could identify all four cell lines using the bioelectrical properties of deformed cells by combining the results of phase and magnitude shifts. The timing information was able to separate the androgen-dependent LNCaP and androgen-independent LNCaP-C4-2 cell lines providing prognostic information on cancer severity. The later constriction points demonstrated increasing separation between the androgen-dependent and independent cell lines indicating that additional constriction points may lead to an improved ability to separate these two cell lines.

The uniqueness of our proposed assay, when compared to the aforementioned standard techniques, is its multi-parametric output. Through a combination of cell mechanical modulatory behavior extracted by the deformation-relaxation transit times and the bioimpedance data of deformed cells, our assay is capable of not only distinguishing between normal and cancer cells but also between cancer cells having different metastatic potential. Further experimentation and analysis can be done to map these biophysical properties to cell attributes for other prostate cancer cells and other cancer types to determine if iMEP can be used as a standalone tool to analyze cancer cell invasiveness.

3.5 Conclusion

Each assay presented in this paper provides differing information about cell biological and biophysical properties. For instance, the chemotaxis assay provides information about how cell populations migrate through constrictive pores in response to a chemo-attractant gradient, while the scratch wound assay probes cell populations' sheet migration behavior. Although these two standard migration assays provide information about migratory behavior, they do not provide the whole story of the metastatic potential. The iMEP device provides information about the cell deformability and dielectric properties, but also cannot reliably predict metastatic potential. However, the iMEP device is advantageous over the other standard migration assays because we can obtain information about the single cells. Experimentation time is another advantage of our iMEP assay, as it can analyze a population of cells in a matter of minutes. To conclude, our iMEP device has the capability of identifying tumor cells from their normal counterparts, as well as distinguishing between closely related cancer cells using the average bioelectrical properties of the deformed cells. In contrast, the scratch wound assays showed significant differences between the normal and cancer cell lines, but the results with the three cancer cell lines did not

correspond to the cells' metastatic potential. Additionally, the chemotaxis assay results were not able to distinguish between the normal and cancer cell lines, and the results did not correspond to the metastatic potential for all cancer cell lines. Thus, the iMEP device presented here represents one method to differentiate between normal and cancerous cells and with additional development may be able to provide prognostic information on the metastatic potential of cancer cells.

4. Kernel-based microfluidic constriction assay for tumor sample identification

Ren, X., **Ghassemi, P**., Kanaan, Y. M., Naab, T., Copeland, R. L., Dewitty, R. L., ... & Agah, M. (2018). Kernel-based microfluidic constriction assay for tumor sample identification. ACS sensors, 3(8), 1510-1521.

My contributions towards this chapter included device fabrication, sample preparation, experimentation, data collection through image analysis, and assisted with manuscript preparation.

4.1 Introduction

The determination of risk for a patient with a primary tumor of the breast is of utmost interest to patients and clinicians alike. Clinical, pathological, biochemical, and most recently genetic tests have been developed in an attempt to inform treatment decisions based upon the risk for tumor metastasis and post-surgical recurrence rates. Tumors with aggressive markers will require adjuvant therapies, but in other primary tumors and conditions such as ductal carcinoma in situ (DCIS) more indolent markers are present. In such patients, there is still uncertainty what additional therapy beyond surgical resection is warranted or if no further therapy would be more appropriate in which case, physicians risk overtreatment of a non-aggressive condition.

Biomechanical properties of metastatic cancer cells provide a clue that the study of biomechanics of primary tumor cells might be of use as a marker of risk in primary breast cancer. Studies of cell lines derived from metastatic breast cancer show such cells have softer biomechanical strength, based on their cytoskeleton, microtubules and actin filaments, which result in a higher deformability in microfluidic constriction channels [66, 100, 148]. Microfluidic

devices utilizing constriction channels have been broadly applied to metastatic studies on different cell lines [101, 149-152]. Many studies have demonstrated the utility of circulating tumor cells as a minimally invasive cancer screening method for both the initial diagnosis of cancer and in monitoring patients for recurrent or metastatic cancer [153, 154]. An essential step in escape from the primary tumor is the epithelial-mesenchymal transition (EMT) that allows cancer cells to become more motile and more likely to survive in the patient circulation. Most of the studies on the mechanical properties of cell lines at single-cell level have been carried out in a single constriction microfluidic channel [99, 149, 150, 155]. Here, we show using an array of multi-constriction microfluidic channels a higher throughput is achieved. The multiple constriction channels can generate multiple deformations to cell structure, which increases the velocity-related variables for mechanical behavior analysis that can be correlated to metastatic characteristics [100, 104].

Multiple technologies have confirmed the biomechanical softness is most pronounced in the more metastatic prone cell lines. Such technologies include atomic force microscopy (AFM) [6, 33-35], micropipette aspiration [30-32], optical deformability [23, 37], and magnetic beads with selective antibodies assays [36]. For clinical applications, the high-throughput of microfluidic approaches and lab-on-chip technologies are more attractive. What is unknown is how the biomechanical properties of breast cells derived from primary tumors in patients and breast cells grown in long-term culture compare. Here, we show in a multi-constriction microfluidic device that patient-derived primary human breast tumor cells and breast cell lines show similar incremental velocity profiles, providing proof-of-concept that biomechanical properties of primary tumors can be assessed. Furthermore, the primary tumor tissue is biomechanically distinguishable from the patient's own adjacent normal breast tissue. This work

represents an important development in microfluidic analysis of breast biopsies and how cell biomechanical properties might contribute to the assessment of patient risk.

4.2 Experimental Section

Materials and Methods

Cell culture and sample preparation: MDA-MB-231 (passage #6, American Type Culture Collection (ATCC), Manassas, VA) was grown in F12:DMEM (Lonza, Basel,

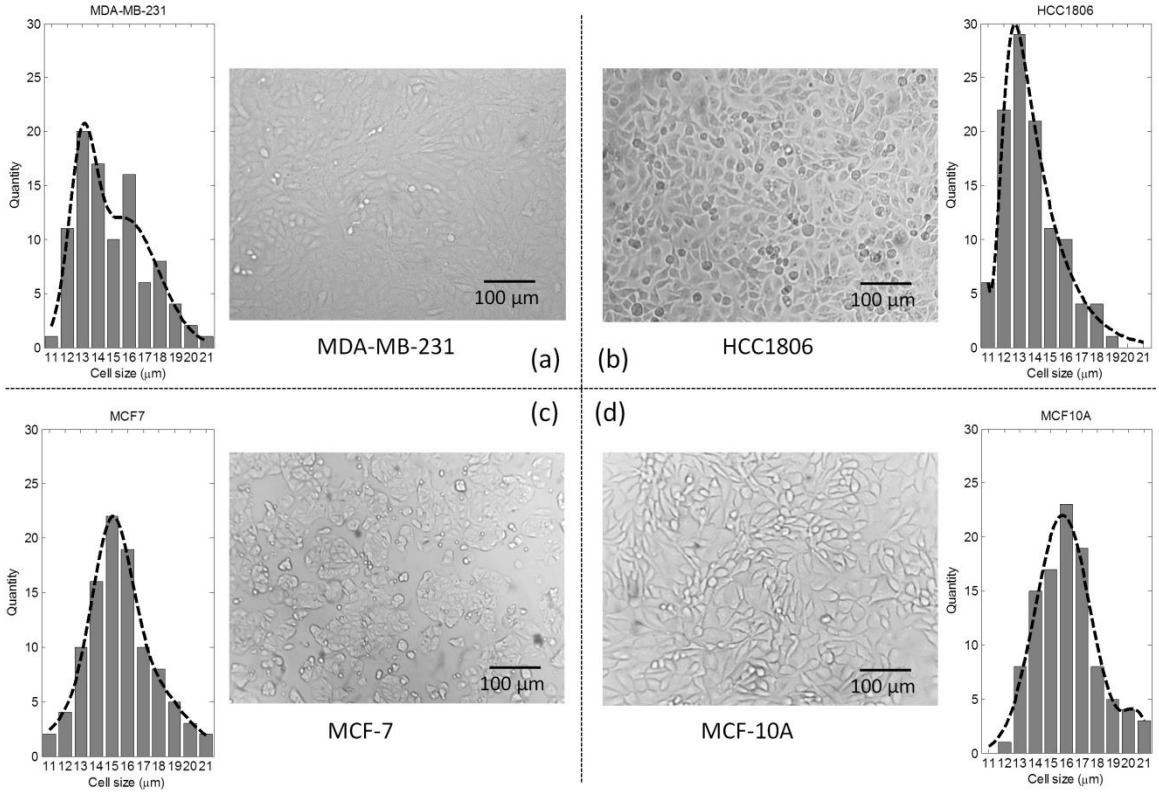

Figure 1. Cell morphology before trypsinization and cell size distribution (a) MDA-MB-231; (b) HCC-1806; (c) MCF-7; (d) MCF-10A.

Switzerland) with 10% fetal bovine serum (FBS), 4 mM glutamine and penicillin-streptomycin (100 units per mL). HCC-1806 (passage #5, ATCC) was grown in ATCC-formulated RPMI-1640 medium with 10% FBS. MCF-7 (passage #5, ATCC) was grown in EMEM with 10% FBS, and

2× L-glutamine. MCF-10A (passage #19, Lombardi Comprehensive Cancer Center, Georgetown University in Washington, D.C.) was grown in F12:DMEM with penicillin-streptomycin (100 units per mL), 2.5 mM L-glutamine, 20 ng/mL epidermal growth factor (EGF), 0.1 μg/mL cholera toxin, 10 μg/mL insulin, 0.5 μg/mL hydrocortisone, and 5% horse serum. All of the cells were grown in T-25cm^2 culture flasks at 37°C in a 5% CO_2 in air atmosphere until cells were ready for subculture. The morphology of the cells was observed before trypsinization. The cells were then detached from the flask with trypsin-EDTA solution (SigmaAldrich). The MDA-MB-231, HCC-1806, MCF-7, and MCF-10A cells were trypsinized at 37°C for 2 min, 8 min, 7 min, and 15 min, respectively. All of the cells were diluted to a final count of ~4×10^4cells/mL.

Human subjects and clinical data: For this study, two fresh breast tissue samples were collected along with clinical/pathological information with Institutional Review Board approval (IRB#2016-0601) from the Pathology Department at Providence Hospital and samples were coded to preserve patient confidentiality. Tumor diagnoses were confirmed by routine histopathological examination. (Detailed information available in Supporting Information)

Patient sample preparation and post-experiment collection: The patient samples were frozen and transported from Howard Cancer Center to Virginia Tech. The thawing procedure for patient samples was different from the thawing of cell lines. Unlike the quick thawing procedure for cell lines, the patient samples in vials needed to be thawed slowly. The frozen samples were transferred to an ice pack for 10-15 min, followed by 4°C fridge for 10 min, and to room temperature until the samples melt. Then the vials were moved to a 37°C water bath. The cancer samples were diluted with culture medium to reach the required cell concentration for microfluidic experiments.

After experiments, the patients' samples were collected from the sample collection outlet of the microfluidic device and stained for the epithelial markers (e.g., Pancytokeratin, CD45, CD68). (Detailed information available in Supporting Information)

Device fabrication: The microfluidic channels were fabricated by polydimethylsiloxane (PDMS) soft-lithography, followed by PDMS-glass bonding after plasma treatment. The molds for microfluidic channels were fabricated on a silicon wafer with two layers of SU-8 (SU-8 3005 and SU-8 3025, MicroChem, Newton, MA) photolithography. The detailed fabrication procedures were presented in the Supporting Information.

Experimental setup

The multi-constriction microfluidic channel array was treated with EDTA before experiment for 30 min to reduce the chance of cells attaching to the microchannel surfaces. Then, the device was washed by cell culturing medium to remove the residuals. The microfluidic device was mounted on an inverted microscope (Zeiss Axio Observer LSM-510, Thornwood, NY) with a 20× lens. The cell sample was connected to the inlet of the delivery channel. A constant pressure on the sample reservoir of 100 mbar was applied by a pressure pump. A negative pressure of 150 mbar was applied at the cell outlet collection channel. The pressure on the cell sample was kept constant during all the experiments on both cell lines and patient samples. Instead of using a high speed camera, a smartphone with slow motion function was used to record videos of the cell movement at a frame rate of 240 frames per second (fps). The overall magnification is 200× in smartphone video with a 1920×1080 resolution. The velocity information of the cells was extracted from the video using tracking software named "Tracker" (developed by "Open Source Physics", supported by National Science Foundation). An example of a cell passing through the device is demonstrated in Supporting Information Figure S1. After the experiment on patients' cancer and adjacent normal samples, the used cells were collected at

the outlet for secondary H&E staining studies. The cells were collected into vials, and 5%(v/v) DMSO was added into the vial for freezing purpose. The vials were frozen at -18°C for 1 hour before transferred into -80°C freezer. The following H&E staining was performed at Howard Cancer Center.

Statistical Analysis

We conduct variable selections and then obtain the prediction accuracy using 10-fold cross-validations. Three methods based on Ridge [156], Lasso [157], and NGK [158] methods are compared. Ridge and Lasso methods are popular variable selections methods based on multivariate linear and additive model, while NGK is a variable selection based on a nonlinear and nonparametric multivariate model. Ridge regression has been used the most popular when the data is not sparse, while Lasso has been used when the data is sparse. However, both methods are developed using multivariate linear and additive model. Hence, these two methods are not appropriate when variables are interacted and highly correlated. Since NGK is developed under the non-linear and non-additive model, it automatically built the complex interaction among variables using kernel function. The main advantage of this kernel-based approach is very flexible: (1) it can automatically identify what variables are most significant; (2) it can automatically model unknown and complicated interactions; (3) it provides flexibility for both additive and nonadditive nonparametric models; (4) it also provides flexibility for both parametric and nonparametric model. That is, if there are no complicated interactions or nonparametric model, it automatically becomes additive model or parametric model.

4.3 Results

Cell lines

The morphologies of two human triple-negative breast cancer (TNBC) cell lines, MDA-MB-231 and HCC-1806, the endocrine-responsive (ER+/PR+/Her2-) MCF-7 cell line, and the

immortalized breast epithelial cell line MCF-10A used in these studies were shown in Figure 1. Their cell sizes measured as the longest axial dimension were determined from video recorded images of the cells entering the microfluidic channel using a smartphone with slow-motion setting on an inverted microscope. The difference between the smartphone and a high-speed camera, such as IDT Redlake NX-3 (IDT vision, Pasadena, CA)[65, 66, 100, 159] that we have in the lab, is the available memory and the subsequent time we can record the videos without interrupting the experiment. A smartphone used in this work has an internal memory of 64GB while the high-speed camera provides only 5GB for video recording. Also, apps can be developed to perform all post-processing analysis of the videos taken on the smartphone. Using the videos taken by the smartphone, the distribution of cell sizes derived from ~100 cells for each cell line are shown in Figure 1 adjacent to the images of the cell monolayers. MDA-MB-231 (Figure 1a) cells exhibit a biphasic size distribution with peaks at 13 μm and 16 μm. HCC-1806 (Figure 1b), MCF-7 (Figure 1c), and MCF-10A (Figure 1d) cells have monophasic size distributions with peaks at 13 μm, 15 μm, and 16 μm, respectively.

(1) Multi-constriction channel array microfluidic chip

The microfluidic device contains two rows of multi-constriction channels, named sequential deformation channel (SDC) 1 and 2, referred as SDC1 and SDC2 in Figure 2a, respectively. Each row has six identical multi-constriction channels with four constriction regions (width: 8 μm, height: 8 μm, length: 50 μm) and three relaxation regions (width: 25 μm, height: 30 μm, length: 25 μm). A transition channel (TC) (center channel in blue, vertical to the multi-constriction channels) between SDC1 and SDC2 is created to function as a buffer for maintaining the constant pressure before the cells enter the SDC2. In addition, the width of 100 μm in the center channel allows the cells to relax longer and possibly recover to their original

spherical shape before entering SDC2. It is noteworthy that in this chip, we have separated the sensing channels and the delivery channel. This will minimize the possibility of channel clogging at the introduction of cells. We also treated the microchannel with EDTA before experiment for 30 min to reduce the chance of cells being stuck in the constriction channel. However, clogging may still be happening due to the small microchannel dimensions and the presence of larger and stiffer particles. We used 30 μm filters during the sample preparation. When large particles go inside the channel and disturb the flow, we reverse the negative pressure to push the large particles/cells back to the delivery channel, whose flow was kept constant during this procedure. We performed this operation as needed (not more than once per minute). We had 6 parallel channels and we did not have clogging on all channels. So, practically, we did not have to do this until all channels are clogged. The reason we did this though was to ensure that the videos and subsequent data analysis are being carried out while all channels are performing as normal and no very large particles have obstructed the flow. There are ways to address this in the future: by making more channels in parallel, using a finer filter, using a filter array as part of the chip to prevent the large particles from flowing, and even programming the pressure pump to reverse the pressure automatically for any possible clogging.

(2) Incremental velocity profiles of breast cell lines

Single cell suspensions were introduced to the delivery channel and the transit of individual cells through SDC1 and SDC2 were monitored by video imaging. In the case of both cell lines and patient samples, ~45-50% of the cells were passing through SDC1 and SDC2. Other cells were flowing along the delivery channel into the cell waste outlet. The data were collected from the videos of cells passing through the channels under a constant pressure. If a large particle/cell was clogging any part of SDC1 or SDC2, the data from that cell will not be

used in data analysis. Transit velocities were measured from the videos. To gain greater resolution in the velocity profile, we obtained two velocity measurements in each constriction segment (Figure 2b). For example, in SDC1, the transit velocity through the initial constriction segment was designated ① and ②. The velocities in segments ①–⑯ were recorded as v_1, v_2, …, v_{16}, respectively. The velocity increments between two different sections were defined as:

$$\alpha_{m,n} = (v_m - v_n)/v_n \ , (m = 1,2, \dots ,16; n = 1,2, \dots ,16; \quad (1)$$

where m and n were the sequence number to identify the velocities. It is noteworthy that our chip can provide other information including aspect ratio of each cell after going through SDC1 and SDC2 as well as the deformed length of each cell at each section of SDCs. However, collection of these data requires heavy image processing which is beyond the scope of this work. We only analyzed and included the velocity profiles as biomechanical properties as a simpler and faster technique. We can envision, however, that in future, by establishing automated image processing algorithms for more complex video analysis, we can include data from other parameters in our machine learning system.

The experiments on each cell line were repeated on more than 3 devices to prove the repeatability and reliability of this device. The velocity results of the three malignant cell lines,

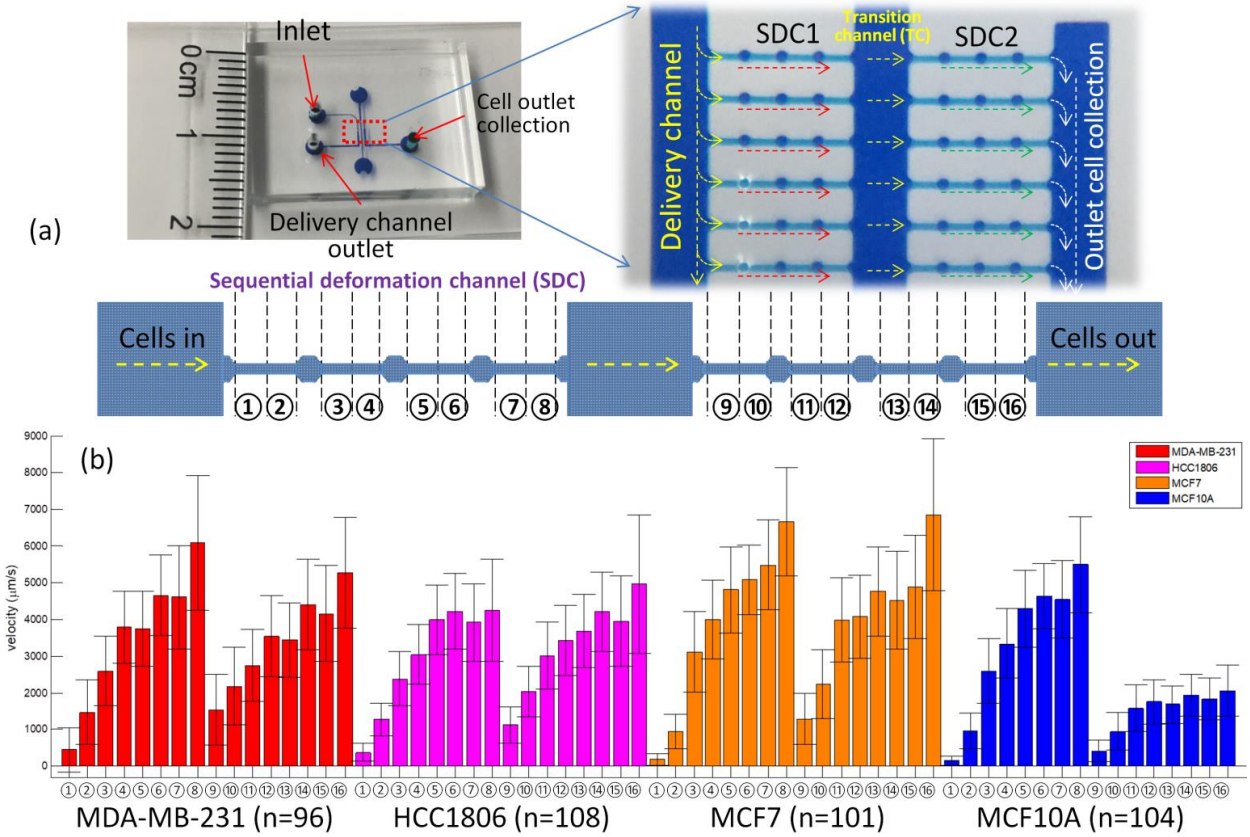

Figure 2. (a) high-throughput multi-constriction microfluidic channel device and the channel labeling; (b) the velocity at different segments of four cell lines; the error bars represent standard deviation.

illustrated in Figure 2b, all showed a characteristic profile in which the transit velocities through successive constriction segments in SDC1increase, then this repeats as cells enter SDC2. The nontumorigenic MCF-10A cells do not follow this pattern. The entry velocities of MDA-MB-231 (segment ① in red) and HCC-1806 (segment ① in pink) in SDC1 are higher than the entry velocities of MCF-7 (segment ① in orange) and MCF-10A (segment ① in blue). The initial velocities of the MDA-MB-231 and HCC-1806 are 457±598 μm/s (n=96) and 376±242 μm/s (n=108), respectively. The velocity profiles at population level and the trends of the velocity

variations of MDA-MB-231 and HCC-1806 are similar. The variations of velocities are related to cells' dynamic biomechanical properties which are functions of cells' cytoskeletal architecture, cell size, cell morphology and surface roughness, and possibly the mitosis cell cycles [103, 104, 160-164]. The microfluidic channels were treated with EDTA to minimize the cell stiffness to the surface of PDMS channel. The cell adhesion is an important component of the properties of the cells; however, the cell will not adhere to channel surface in the short time of cells passing through the microchannels. The cell requires a much longer time to adhere to the channel wall. The velocity profile reveals the biomechanical properties of the cell stiffness and cytoskeleton strength. To analyze the different cell lines by velocity profiles, we used kernel-based machine learning method to find the variables that represents the biomechanical properties of different cell lines. After passing through the SDC1, the cancer cell lines MDA-MB-231, HCC-1806, and MCF-7 show a higher entry velocity in SDC2 (segment ⑨ in red, pink and orange, respectively) than MCF-10A (segment ⑨ in blue). Based on the t-test results of velocities at segment ⑨, the velocity of MDA-MB-231 being higher than that of MCF-10A has a $t=11.1$, $p<0.0001$; even assuming the velocity of MDA-MB-231 being three times higher than that of MCF-10A has a $t=2.132$, $p=0.017$. The velocity of HCC-1806 being higher than that of MCF-10A has a $t=12.1$, $p<0.0001$; assuming the velocity of HCC-1806 twice higher than that of MCF-10A has a $t=3.65$, $p=0.0002$. The velocity of MCF-7 higher than than that of MCF-10A has a $t=11.5$, $p<0.0001$; assuming the velocity of MCF-7 2.5 times higher than that of MCF-10A has a $t=2.37$, $p=0.009$.

The cancer cell line MDA-MB-231 deformed faster at the segment ① of SDC1. After passing through SDC1, the MDA-MB-231 cells are recovered back to spherical geometry and become easier to deform at the entrance (segment ⑨) of SDC2. The normal cell line MCF-10A cells experience a different passing procedure. MCF-10A cells, which are stiffer than cancer cells

[24, 27, 33, 39, 103, 162, 163, 165], require a longer deformation time at the segment ① of SDC1. After passing through SDC1, the MCF-10A cells are not fully recovered back to spherical structure, which, due to cell rotation in TC, can result in a longer time to deform again and move into the entrance of SDC2 (segment ⑨). (Additional images available in Supporting Information Figure S1). However, when they deform completely and get into SDC2, their transit is generally slower compared to their velocities in SDC1. As illustrated in Figure 2(b), the average velocities of MCF-10A in SDC2 (segment ⑨-⑯ in blue) is lower than the three cancer cell lines. The three cancer cell lines show similar velocity profiles in SDC2 (segment ⑨-⑯ in red, pink, and orange) and SDC1.

The multi-constriction microfluidic device improves the resolution in distinguishing cancer cells from normal cells compared with single constriction channel microfluidic devices [24, 57, 148, 166]. The two rows of channels create 16 velocity segments in constriction regions for data analysis, which yields 120 variables using the definition in equation (1). We select eight velocity increments at the same segments of SDC1and SDC2 as variables:

$$\begin{cases} \alpha_{16,08} = (v_{16} - v_{08})/v_{08} \\ \alpha_{15,07} = (v_{15} - v_{07})/v_{07} \\ \alpha_{14,06} = (v_{14} - v_{06})/v_{06} \\ \alpha_{13,05} = (v_{13} - v_{05})/v_{05} \\ \alpha_{12,04} = (v_{12} - v_{04})/v_{04} \\ \alpha_{11,03} = (v_{11} - v_{03})/v_{03} \\ \alpha_{10,02} = (v_{10} - v_{02})/v_{02} \\ \alpha_{09,01} = (v_{09} - v_{01})/v_{01} \end{cases} \quad (2)$$

Together with the size information, 16 velocity segments, and eight additional velocity increments defined by equation (1), we can analyze 25 variables by three methods, Ridge [156], NGK [158], and Lasso [157], respectively. The kernel-based machine learning algorithm can be

applied on a group of cells with limited sample size. The key is to extract sufficient quantity of variables, which can be considered as high-dimensional variables combinations [158, 167].

Consider n observations for each cell type t, t=1,…,T, and p variables data set (y,X_t), where X_t=[x_{1t},x_{2t},…,x_{pt}], x_{jt}=[x_{j1t},x_{j2t},…,x_{jnt}]^T is an n×1 vector for the jth variable, j=1,…,p. Ridge and Lasso conduct variable selections based on the following generalized linear model for multinomial response,

$$\Pr(y = t|\, X_t) = H(\beta_0 + \beta_1 x_{1t} + \cdots + \beta_p x_{pt}) \tag{3}$$

where $H(\cdot)$ is a logit function and

$$\sum_{t=1}^{T} \Pr(y = t|X_t) = 1 \tag{4}$$

Ridge and Lasso conduct variable selection using L2 norm $||\beta||^2$ and using L1 norm $||\beta||$, respectively, where $\beta = (\beta_0, \beta_1, \ldots, \beta_p)^T$. Ridge's objective function is to minimize the following objective function,

$$\log[\prod_{t=1}^{T} \Pr(y = t|X_t)^t\ ] + \lambda||\beta||^2 \tag{5}$$

while Lasso is to minimize the following objective function

$$\log[\prod_{t=1}^{T} \Pr(y = t|X_t)^t\ ] + \lambda||\beta|| \tag{6}$$

However, NGK performed variable selection using nonparametric and nonlinear model using kernel function. According to the Representer theorem, the nonparametric regression model can be expressed as

$$\Pr(y = t|\, X_t) = H[f(X_t)] = H(K\alpha) \tag{7}$$

where $f(X_t)$ is the unknown nonparametric function, K is the kernel matrix corresponding to the function Hilbert space, and α is unknown parameter. Our kernel can be expressed in a nonlinear function form because the Gram matrix

$$K(\xi, X_t) = g(\sum_{j=1}^{p} \xi_j D^j) \tag{8}$$

where g is a known function (i.e., Gaussian form), D^j is the matrix with (k,l)th entry $d_{kl}^j = -(x_{jk} - x_{jl})^2$. We performed variable selection using $\xi = (\xi_0, \xi_1, \ldots, \xi_p)$. The objective function for NGK is to conduct the variable selection for minimizing the objective function,

$$\log[\prod_{t=1}^{T} \mathrm{H}\{K\alpha(\xi)\}^t] + \lambda||\xi|| \tag{9}$$

The prediction accuracy is calculated using 10-fold cross-validations (CV). This means that we have 10 training and 10 test data sets. Using a given training set, we perform variable selections. We then build the classifier and calculate the prediction accuracy using the test set. This procedure is repeated 10 times. The probability of correctly predicting the test group is named as the prediction value. Then, we are able to find the prediction value to distinguish between two different groups, either cell lines or patient samples. The full table of prediction values of different combinations of the selected variables is available in Supporting Information.

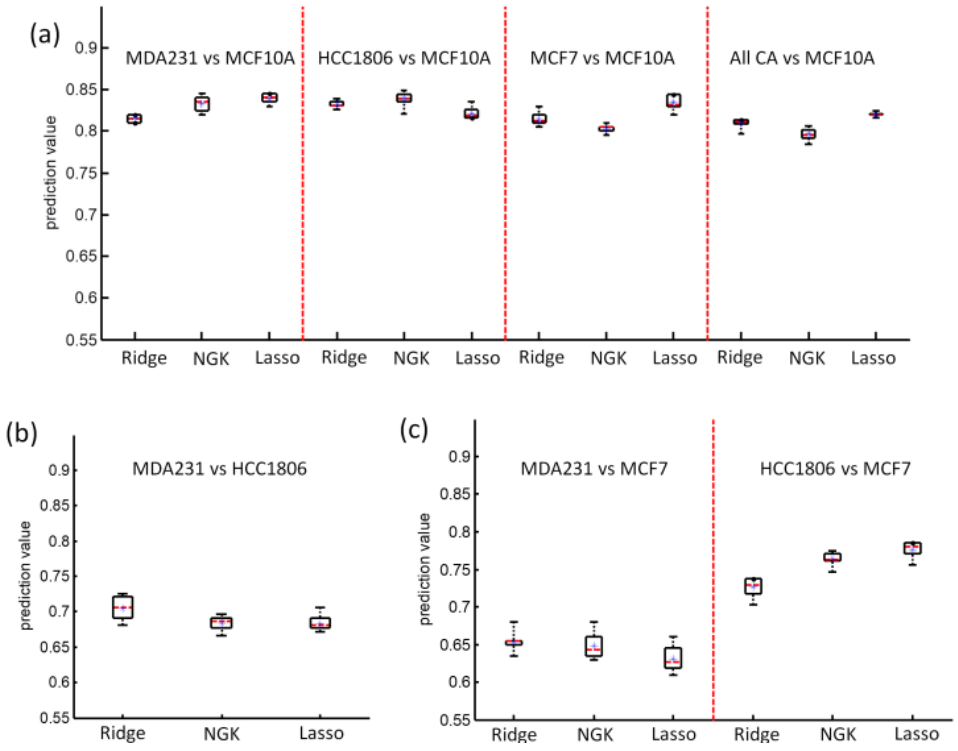

Figure 3. The prediction values of (a) comparing cancer cell lines MDA-MB-231, HCC-1806, MCF-7 to normal cell line MCF-10A; (b) comparing MDA-MB-231 and HCC-1806; (c) comparing TNBC cell lines MDA-MB-231 and HCC-1806 to ER+/PR+/Her2- cell line MCF-7.

One test of our approach is its reliability in distinguishing malignant and non-malignant breast cell lines. The prediction values (Figure 3) calculated by the Ridge, NGK, and Lasso methods show how well individual cell lines are distinguished based on their cell size and incremental transit velocities. All three statistical methods distinguished the malignant cell lines from the immortalized MCF-10A line with prediction values of 0.80-0.85 (Figure 3a).

Next individual malignant cell lines are compared. Here, there are some interesting

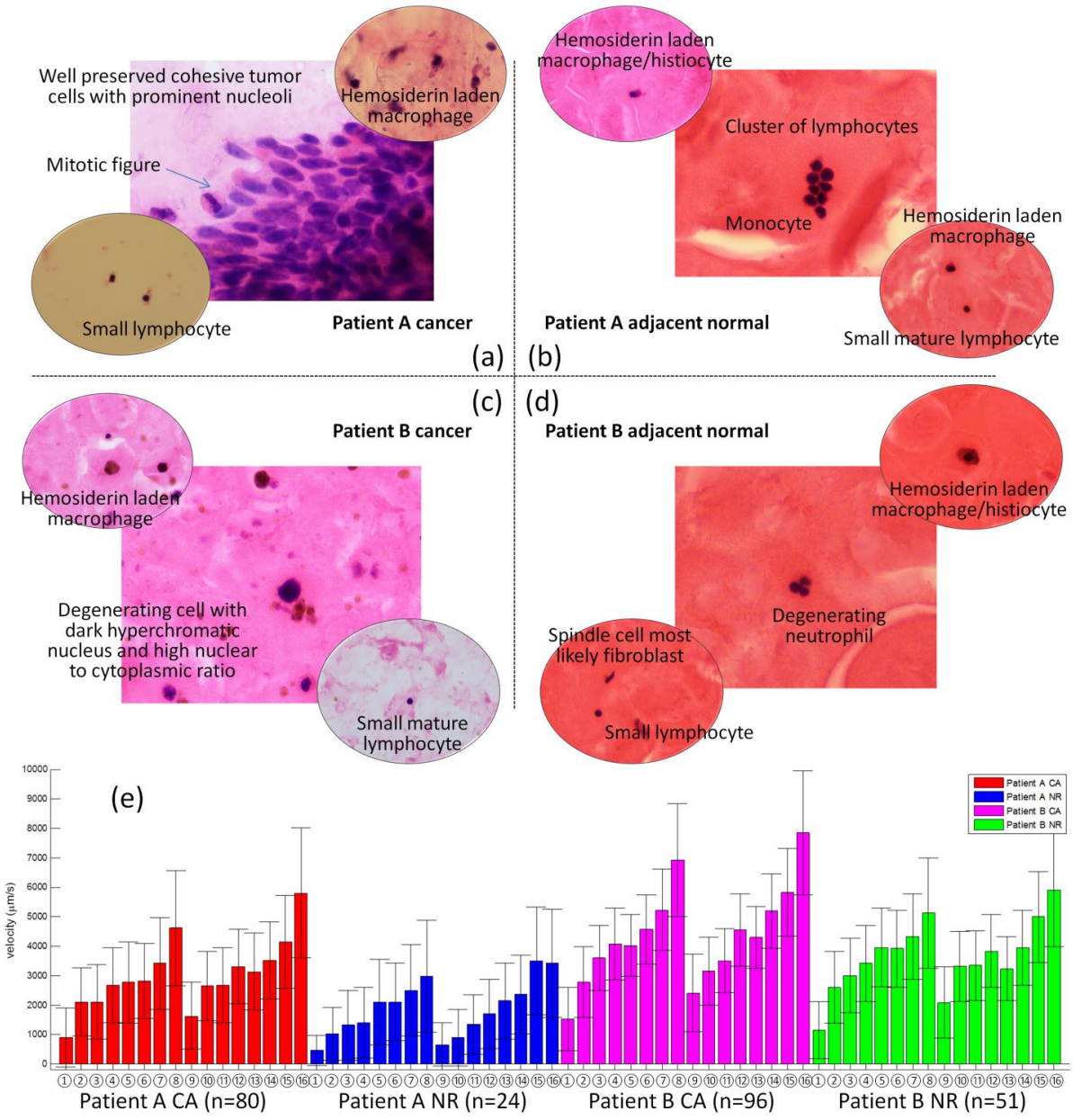

Figure 4. H&E stained slides of cell suspensions: (a) patient A cancer (CA) tissue; (b) patient A adjacent normal (NR) tissue; (c) patient B CA tissue; (d) patient B NR tissue; (e) velocity profiles for patient A (CA: red, NR: blue) and patient B (CA: violet, NR: lime).

observations. The two TNBC cell lines (MDA-MB-231 and HCC-1806) which are both metastatic in nude mice [168] exhibited differential biomechanical properties with predictive values between 0.65 and 0.7; thus even though both are TNBC, there is modest confidence (65-

70%) to distinguish between them (Figure 3b). The differences between breast cancer cell lines MDA-MB-231 and MCF-7 have been studied form both biochemical and biophysical [7, 127, 169] points. The biophysical differences were studied by impedance spectroscopy that focuses on the specific membrane capacitance and cytoplasm conductivity [65, 100, 126]. Surprising at first, there is even less confidence (between 0.6 and 0.65) in the ability to distinguish the MDA-MB-231 from the MCF-7 cell line which is not metastatic in nude mice [170] (Figure 3c). However, the Lasso method distinguished the HCC-1806 and MCF-7 cell lines with a high predictive value of 0.8 (Figure 3c). We conclude that the results in Figure 3b and 3c are more consistent with the patient origins of each of these cell lines rather than their metastatic behavior in nude mice or their hormone receptor status. This makes our multi-constriction channel approach unique, possibly more representative of metastatic risk in patients. By way of explanation, the HCC-1806 cell line is derived from a patient with a non-metastatic primary tumor classified as a grade II acantholytic squamous carcinoma of the breast (ATCC) with basal B characteristics [168]. In contrast, both the basal B TNBC MDA-MB-231 cell line and the hormone-responsive ductal adenocarcinoma line MCF-7 are derived from the pleural effusions of patients with metastatic breast cancer (ATCC). Thus, our approach might key on an as yet unidentified mechanical property characteristic of the metastatic, pleural effusion origin of MDA-MB-231 and MCF-7 cells. In support of this idea, even though studies have shown MCF-7 cells have a stiffer cytoskeleton structure with a higher Young's modulus [151, 171], others reported single constriction channel devices has limited capability in differentiating between MDA-MB-231 and MCF-7 [49].

Cell recovery from human breast biopsies

From patients undergoing partial or complete mastectomy, cancer cells (CA) and adjacent normal cells (NR) were collected separately and prepared identically by a method to enrich

epithelial organoids. Slides were prepared from each single cell suspension; epithelial cells (pancytokeratin +), lymphoid cells (CD45+), macrophages plus and histiocytes (CD68+) were enumerated after immunohistochemical (IHC). Slides were then stained with H&E. Representative images were shown in Figure 4(a-d). In the cancer samples, epithelial cells were cancer (CA) while in the adjacent normal samples, the epithelial cells were normal (NR) as assessed by a pathologist.

The nuclear-cytoplasmic ratio (N/C ratio) of normal epithelial cells is 1:4~1:6, while the N/C ratio of malignant carcinoma cells can reach 2:1. The epithelial cells in cancer samples show a larger nucleus in dark color. The large epithelial cells with hyperchromasia and increased N/C ratio represent carcinoma cells in patient A and patient B. Differential cell counts estimated the percentage of epithelial cells, lymphoid cells, and macrophage/histiocytes (M/H) in each of the patient samples. Individual cell sizes by cell type are measured in 1000× images. The average size of epithelial, lymphoid and M/H populations in each of the patient samples is presented in Table 1.

Table 1. The average size and cell type distribution in patient cancer samples.

Cell types	Patient A		Patient B	
	Cell size (μm)*	Cell counts (%, n**)	Cell size (μm)*	Cell counts (%, n**)
Epithelial	18.6 ± 7.1	37.6%, 34	16.0 ± 3.6	29.4%, 17
Lymphoid	10.5 ± 1.7	39.8%, 14	8.4 ± 3.5	32.4%, 34
M/H	14.3 ± 3.7	N/A***, 3	11.1 ± 1.7	25.0%, 12

* The error is one standard deviation. ** The n is cell counts. *** The sample size from patient A is limited (only 3 cells observed in IHC study).

Incremental velocity profile analysis of primary human tissue samples

Cell suspensions were passed through 30 μm filter screens to remove large cell clusters prior to velocity testing. The patient A, CA sample contained ~2.5×10^4 cells/mL; the patient A NR contained ~0.5×10^4 cells/mL. The patient B, CA sample was ~2.5×10^4 cells/mL; the patient B NR sample was ~1.5×10^4 cells/mL. The total number of cells in each velocity analysis is indicated by "n" in Figure 4e.

The velocity profile of CA and NR from both patient samples (Figure 4) exhibited the same incremental velocity profile as observed for the cell lines (Figure 2b). There was progressive increase in velocity with each segment in the first channel and then a repeat of this pattern in the second channel. These data largely reflect the epithelial cells in each sample. The small mature lymphocytes had a cell size around 8-10 μm, which was smaller than the dimensions of constriction channels. Without deformation in the constriction channels, the lymphocytes passed through all channels at the flow velocity of the medium.

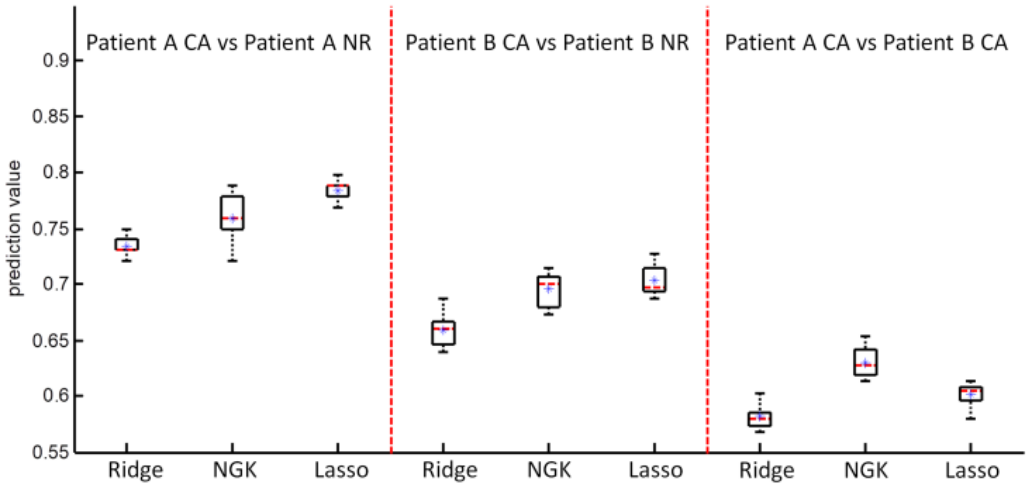

Figure 5. The prediction values of comparing the CA and adjacent NR cells in patient A, CA and adjacent NR cells in patient B, and comparing the CA cells in patients A and B.

The Lasso analysis yields the highest predictive value in discriminating CA and NR cells from patient samples (Figure 5). For patient A, CA and NR cells show a prediction value of 0.79 which approaches that achievable in the cell lines. The CA and NR cells from patient B show a less robust prediction value of 0.7. These results are obtained using patient biopsies that received minimal processing in order to retain all elements of tumor heterogeneity within the sample provided. We suggest that this high content microfluidic approach coupled with kernel based learning analysis has promise for distinguishing patient-derived cancer cells in small biopsy samples with less than a 24 hour assay turn-around time. The Lasso analysis also indicates that the two patient CA samples are more similar to each other (prediction value 0.6) than either CA compared to its patient-matched NR sample. This is of interest considering that patient A and B have undergone different therapeutic regimens prior to biopsy. Patient A has both chemotherapy and radiation therapy, while patient B does not receive any therapy. This suggests that prior treatment may not interfere with the ability of this microfluidic approach to identify cancer cells in patient biopsies. There is no gold standard for applying prediction values for clinical cancer diagnosis. Our results indicate that this device can be used in patient samples to reach a quantitatively comparison for clinical samples other than standard image reading in IHC studies.

4.4 Discussion

The evaluation of the risk of tumor recurrence and metastasis, and localized tumor infiltration status of breast cancer is a challenge. Typically, IHC technology is used in cancer diagnosis today to assess tumor grade and local infiltration status. These well-established IHC protocols are expensive, time-consuming and labor intensive, and still cannot definitively assess metastatic or recurrence risk in every patient [172-174]. With the assistance of machine learning methods, the analysis of IHC studies can be improved [175]. Genetic screens are available for

predicting cancer recurrence but are not widely available to all patients [176, 177]. One confounding factor in diagnosing risk is the heterogeneous nature of cells within patient biopsy samples [178]. As reviewed by Marjanovic et al., patient mastectomy samples collected at surgery usually contain a heterogeneous mixture of both cancerous and normal cells. When adjacent normal samples are dissociated into single cell suspensions, proliferating cancer cells are also seen [178]. Consequently, adjacent normal tissue is not commonly regarded as completely normal due to admixture with infiltrating cancerous cells. Here we demonstrated using heterogeneous patient breast tumor and normal tissue samples and a high-throughput microfluidic channel array device, cell biomechanical properties can be recorded at a rate of over 500 cells in 10 minutes with an inexpensive disposable microchip. In addition, we only analyzed ~45-50% of the cells passing through SDC1 and SDC2. This can also contribute to a reduction in prediction rate especially in patient samples containing a heterogeneous population of cells. Recycling the un-analyzed portion of the sample and performing the microfluidic analysis on those cells can enhance the prediction accuracy of our assay. The smartphone slow motion video can record sufficient velocity information as a replacement of expensive high-speed camera. This approach indicates that our device and method has a promising potential to be utilized in clinical applications with the development of smartphone technologies. Cell transit velocity data analysis using kernel learning-based statistical analysis identifies normal and tumor cells in very small biopsy samples based upon their biophysical traits which can augment current clinical diagnostic assessments.

Microfluidic technologies to study cancer cells have been carried out with a multitude of microfluidic platforms [101, 126, 150, 155, 179]. Single constriction channel technology with added impedance spectroscopy has shown promise in distinguishing between cancerous and

normal cells from multiple cell lines [49, 149, 180, 181]. However, characterization and separation of different subtypes of cancer cell lines are still challenging by microfluidic single constriction channel with impedance spectroscopy [101, 151, 182]. Single channel designs with multi-constriction regions were found to amplify the biomechanical differences between breast cancer cell lines and non-tumorigenic breast epithelial cell lines. The studies of channels with five constriction regions showed differentiation between breast cancer cell line MDA-MB-231 and normal cell line MCF-10A could be achieved with 95% accuracy [148]. Cells entering the constriction channel undergo dynamic cell deformation changes. Analysis of the constriction channel entry velocity versus the constriction channel exit velocity indicate that cells of the non-tumorigenic breast cell line has difficulty recovering from their deformed elliptical shape to their original spherical geometry. This differential recovery of shape plays a key role in differentiating the tumorigenic and non-tumorigenic breast cell lines. To scale up throughput towards use of this design in clinical applications, here we test a microchip design with parallel channels containing four constriction regions each. Combining the machine learning technology has attracted the attention of the lab-on-a-chip community on cell research. Starting from the American Association of Cancer Research (AACR) annual meeting 2017 in Washington, D.C. [183-185], the application of artificial intelligence and machine learning gained more progress in cancer research. Many approaches were made by involving many different machine learning algorithms in their cancer research [186-188]. K. Nyberg et al. presented a cancer invasion study by k-nearest neighbor machine learning algorithm in 2018 [189]. Nyberg, et al. [189] paper is based on short constriction channels they developed by Dr. Rowat's group [190, 191]. They developed their multiple constriction channels to detect the deformation parameters of different cell lines. The constriction channel they presented were short, which did not cause the full deformation of

the single cells. As presented in Nyberg, et al. [189], they studied the cell invasion by performing k-nearst neighbor (kNN) machine learning on six parameters from the multiple short constriction channels. The short constriction channel can collect the dynamic motions of the cell deformation as a model to study invasiveness. Rowat's paper, in fact, is a good method of using multi-parametric single cell analysis for predicting cell invasion behavior. Both their work and our work are a testimony that not just a single parameter but a collection of physical attributes are powerful to differentiate cells and to predict their disease status. Our work is different than Rowat as we use multi-constriction structures and collect different biophysical parameters when compared to Rowat. Rowat uses a single transition channel and then utilizes parameters such as size, elastic modulus, transit time, and maximum strain (some of these parameters are not directly measured by the microfluidic channel with kNN method to achieve 94-100% identification rate of 5 cell lines. The Rowat's paper extracted elastic modulus and cell fluidity parameters by pre-selecting the cell size population median ±1 μm. In our manuscript, we considered all cells sizes from 11 to 21 μm to guarantee the heterogeneity of the sample we used. The size distribution is presented in Figure 1. If we only analysis the cells by size median ±1 μm, we will lose 51.0% of the MDA-MB-231 cells, 33.3% of the HCC-1806 cells, 43.6% of the MCF-7 cells, and 42.3% of the MCF-10A cells. The elastic modules and cell fluidity parameter collection in Rowat paper requires post calculation and data fitting a rheology model with time dependent strain data. On the contrary, we can harvest parameters directly from velocity profiles to minimize the work load of data post processing. Consistent with our previous work [66, 192], we used our longer constriction channels to allow the cells to fully deform and transit through the channel, which is another model to study the tumor metastasis by biomechanical properties. The short channel in Rowat's work can only provide two time variables: entry time and transit time.

Based on their kNN method, the time variables provided 0.33-0.86 positive rates. Our multi-constriction channels provided more time variables. Together with kernel method, we can reach 81-85% prediction values. Our approach does not require the calculation of other biophysical parameters from the cells, which demonstrated an easier way to analyze dynamic motions of the cells. The Rowat paper concluded that a more sophisticated machine learning method can further improve the performance of study invasiveness. Our kernel-based algorithm is a significant improvement of the machine learning approach. It is also notable that the kNN classifiers used in K. Nyberg, et al. [189] is memory-based and require no model fit. This kNN approach is a nonparametric algorithm that does not assume the underlying data fits a particular model. It is a machine learning tool. The class assigned to new data points is determined by the most common class of the k number of nearest neighbors in the training set. These neighbors are determined using Euclidean distance. Hence this approach depends on the selection of k and distance measure; our NGK does not. Our NGK classifier is a nonparametric kernel machine based approach. Our NGK is not memory-based. We can consider NGK is a hybrid approach which is a mixed of nonparametric model and kernel machine tool. Using a training set, we built NGK classifier which is required to estimate nonparametric function but does not assume the particular function form. This nonparametric function is estimated via Gaussian process, which is known as a family of nonparametric functions. Unlike kNN, the class assigned to new data points is determined by the probability that new point is assigned to the certain class.

The TNBC MDA-MB-231 is representative of a highly invasive, rapidly proliferating basal breast malignancy expressing markers of cells, including P-cadherin and/or cadherin-11 [193] [194]. Both P-cadherin and cadherin-11 promote motility and invasiveness [195]. The MCF-7 cell line is a model of endocrine therapy responsive luminal A breast cancer expressing

both ER and progesterone (PR) receptors and also differentiation markers more typical of its epithelial cell origin such as E-cadherin [196] which is associated with lower motility and lower invasiveness. MDA-MB-231 express vimentin which makes them more mesenchymal in nature than HCC-1806 which exhibit a more epithelial morphology and do not express vimentin [197].

The TNBC cell lines MDA-MB-231 and HCC-1806 show similar velocity profiles in the high-throughput microfluidic channel array. The first deformation and secondary deformation indicate that both cells have similar deformation and transition times. The similar recovery ability to their original spherical shape indicates that both cells have similar biomechanical properties, such as cell membrane and cytoskeleton elasticity. The comparison of these two cell lines by the high-dimensional variables analysis of Ridge, NGK, and Lasso indicates that there are still differences between the two cell lines. Since all cells are breast cells, interactions among these variables within the same cell type and interactions between different cell types are not expressed as parametric models. The performance between Lasso and NGK is similar which means that the model for the data is more likely parametric model. NGK provides flexibility for both additive and nonadditive nonparametric models and it also provides flexibility for both parametric and nonparametric modeling. This kernel-based classifier is developed by connecting a kernel machine with the multivariate nonparametric regression model. This approach can simultaneously perform a variable selection in nonadditive multivariate nonparametric model for analyzing high-dimensional large data. Using NGK, we nonparametrically model unknown interaction terms among high dimensional variables. Especially in patient primary tumor samples, the heterogeneous status may include more nonlinear relationships among all the velocity-related variables we established.

The heterogeneous character of human tumors is commonly accepted [198]. We are able to distinguish cells isolated from biopsies of tumors and adjacent normal tissue based solely on their biomechanical properties with a prediction rate of 70.07%-75.96% considering that we processed only 50% of each sample. Therefore, in tests of two patients, the prediction rate, i.e., the ability to accurately identify a cell as tumor or normal was 5-10% less than that achieved with the cell lines. Considering the greater heterogeneity of the patient samples, this result is quite strong. Of note is the observation that the tumor cells removed from the patient A whose primary tumor has already metastasized conclude a higher prediction value than patient B with the non-metastatic tumor when compared to adjacent normal tissue. Clearly, the multi-constriction microfluidic channel is not a stand-alone assay for patient risk assessment at this point; many more patient samples need to be analyzed. Significantly, our patient population is primarily African American. As has been documented repeatedly, African Americans have much higher breast cancer mortality rates than Caucasian patients, and a substantial component lies in as yet unidentified differences in cancer biology [199-201]; thus a biomechanical diagnostic test might prove particularly of benefit to this patient population.

ABBREVIATIONS

NGK: non-malignant kernel machine; DCIS: ductal carcinoma in situ; EMT: epithelial-mesenchymal transition; AFM: atomic force microscopy; FBS: fetal bovine serum; EGF: epidermal growth factor; PDMS: polydimethylsiloxane; TNBC: triple-negative breast cancer; SDC: sequential deformation channel; TC: transition channel; IHC: immunohistochemical; N/C: nuclear-to-cytoplasmic; M/H: macrophage/histiocytes; kNN: k-nearest neighbor.

5. Biophysical phenotyping of cells via impedance spectroscopy in parallel cyclic deformability channels

Ren, X., **Ghassemi, P.,** Strobl, J. S., & Agah, M. (2019). Biophysical phenotyping of cells via impedance spectroscopy in parallel cyclic deformability channels. Biomicrofluidics, 13(4), 044103.

My contributions towards this chapter included conceptualization, device fabrication, sample preparation, experimentation, data collection through impedance analysis, and assisted with manuscript writing.

5.1 Introduction

Microfluidic technologies have enabled better understanding of cancer pathobiology by facilitating acquisition of novel biosignatures that are based on bioelectrical and biomechanical properties of cancer cells [7, 101, 149, 152]. These biosignatures prove useful as biomarkers of metastatic potential and therapeutic responsiveness. The biomechanical characteristics of cancer cells can be derived from velocity measurements as cells enter and then transit through constriction channels designed to impose mechanical deformation stress [57, 148, 151, 166, 180]. Bioelectrical properties are revealed through the use of impedance spectroscopy at the single-cell level either as cells are held in constriction channels or as cells pass through flow cytometry microchannels [65, 126, 202].

Multiple biophysical characteristics of cancer cells can be extracted from a microfluidic environment. Impedance spectroscopy measures the impedance amplitude ratio and phase shift that occurs over a wide frequency range and these data provide information on the specific membrane capacitance and cytoplasmic conductivity of single cells [49]. Most of the studies on

the mechanical properties of cell lines at the single-cell level have been carried out in a single constriction microfluidic channel, either with or without additional electrodes for impedance measurement [66, 99, 149, 150]. The impedance measurements obtained from cells within constriction channels can better identify the intrinsic biophysical properties of cancer cells [65, 101, 126] and can be used to distinguish cancer cell lines from normal cell lines at a single-cell level with an accuracy of >70-95% at the population level [126, 181]. Collection of biomechanical properties involves measuring transit times through video/image processing. Consequently, high-throughput analysis of single cells makes post-processing time consuming [57]. The parameters extracted from the images of the cells passing through the constriction channels are entry time, cell elongation, passing time, and cell sizes. The elongation of the cells is highly depending on the dimensions of the micro fabricated constriction channels. For example, C.T. Lim's group found that the elongation of the deformed breast cancer cells in a 10 μm by 10 μm constriction channel can vary from 20 μm to 35 μm [24]. The entry time, passing time, the elongation of the cells, and the cell sizes can differentiate 95% of the breast cancer cells (MCF-7) and normal cells (MCF-10A) [24]. However, the direct measurement of cell elongation from the optical microscope image can introduce measurement error. B. Fabry's group used image intensity to identify the different geometries of the cells undergoing deformation in a short constriction channel [203]. However, the intensity measurement requires staining processes of the nucleus and cytoskeleton, which increases sample preparation time. One way to increase the predication rate of cancer cells from normal cells through transit-time-based microfluidics is to perform cyclic deformation separated by relaxation regions. Our group has demonstrated that microchannels with cyclic deformation and relaxation regions can distinguish human breast cancer cell lines MDA-MB-231, HCC-1806, and MCF-7 from normal breast cells MCF-10A

with 81~85% confidence rate [119]. Video/image processing is commonly used to image cell movement in these constriction channels, which necessitates extensive image-processing time to obtain biomechanical information from the cell transit times [66, 148, 190].

Using the biomechanical and bioelectrical parameters directly measured from impedance spectroscopy can distinguish the cells with different dielectric properties. Y. Sun's group used a single constriction channel with two electrodes to detect different cells [101]. The parameters they selected were amplitude ratio, phase shift, and overall passing time of single cells. Directly using these three parameters, they were only able to distinguish the cells with significant different dielectric properties such as adult red blood cells without nucleus and early stage red blood cells with nucleus [181]. Distinguishing between two cell lines with comparable specific membrane capacitance and cytoplasm conductivity have proven to be challenging via impedance spectroscopy. Scientists tried different ways to add biomechanical characteristics in the impedance measurement results to increase the prediction rate. J. Chen's group found that the impedance information at 10 kHz and 100 kHz on two different microconstriction channels with cross-section of 6 μm by 6 μm and 8 μm by 8 μm reached 59.6% prediction accuracy on breast cancer cell line EMT6 [126]. The prediction rate can increase to 70.2% with additional transition time of the cells through a single-constriction channel [126]. The throughput of measuring the bioelectrical properties of single cells in a single constriction channel was limited. In addition, the possibility of measuring multiple cells simultaneously without interference between different impedance results of cells is a hindrance on the performance of a single constriction channel.

Here, we present a less time-consuming method using impedance spectroscopy as an alternative to image processing to monitor cell transit times through microchannels. By modifying the microfluidic constriction channel configurations, we are able to create time stamps

on time-domain impedance results that can be used to track cell velocity in the microchannel and to simultaneously evaluate the bioelectrical properties of cells. Compared to single constriction microfluidic channels for cell bioelectrical and biomechanical analysis, multi-parallel channels with relaxation regions have higher throughputs and provide additional information for cell sensing. This device was used to analyze breast cell line MDA-MB-231 and normal epithelial cell line MCF-10A.

5.2. Materials and Methods

5.2.1. Cell culture and sample preparation

To evaluate the performance of the microfluidic device with parallel constriction channels, a highly metastatic breast cancer cell line MDA-MB-231 (passage #29, American Type Culture Collection (ATCC), Manassas, VA) and a normal breast epithelial cell line MCF-10A (passage #17, ATCC, Manassas, VA) were used via impedance spectroscopy. MDA-MB-231 cells were grown in F12:DMEM (Lonza, Basel, Switzerland) with 10% fetal bovine serum (FBS), 4 mM glutamine and penicillin-streptomycin (100 units per mL). MCF-10A cells were grown in F12:DMEM with penicillin-streptomycin (100 units per mL), 2.5 mM L-glutamine, 20 ng/mL epidermal growth factor (EGF), 0.1 μg/mL cholera toxin, 10 μg/mL insulin, 0.5 μg/mL hydrocortisone, and 5% horse serum. The cells were grown in T-25cm^2 culture flasks at 37°C in a 5% CO_2 in air atmosphere until cells were ready for subculture. Figure 1 showed the optical microscope images of the cultured MDA-MB-231 and MCF-10A before trypsinization. After the cells were fully confluent, the MDA-MB-231 and MCF-10A cells were trypsinized (trypsin-EDTA, 1×) for 2 min and 10 min, respectively. Then the cells were diluted in culture medium to reach a final concentration ~4×10^4 cells/mL.

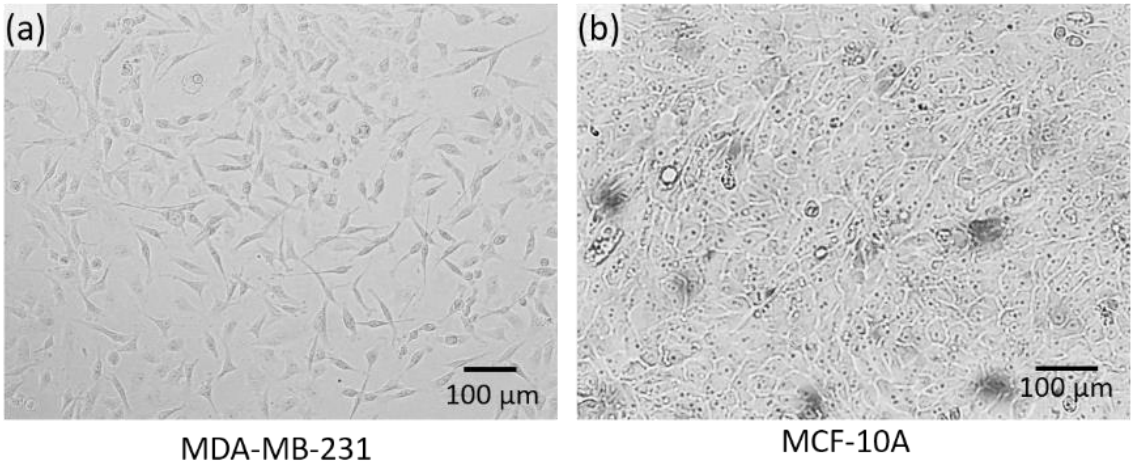

Figure 1. Micrographs depicting the morphology of (a) breast cancer cell line MDA-MB-231 and (b) normal epithelial cell line MCF-10A.

5.2.2. Device fabrication

We fabricated the microfluidic channels by polydimethylsiloxane (PDMS) soft-lithography, followed by PDMS-glass bonding after plasma treatment. As illustrated in Figure 2a, four microchannels with constriction (cross-section: 8 μm × 8 μm; length: 120 μm) and relaxation regions (cross-section: 20 μm × 30 μm; length: 40 μm) were connected in parallel. One electrode pair is shared across four channels. The microfluidic channels devices were fabricated on a silicon wafer with two layers of SU-8 (SU-8 3005 and SU-8 3025, MicroChem, Newton, MA) photolithography. Tridecafluoro-1,1,2,2-tetrahydrooctyl-1-trichlorosilane (TFOCS, Fisher Scientific) was coated on the surface of the molds for the easy release of PDMS. The detailed fabrication procedures are available in supplementary materials. The gold electrodes were deposited on glass by E-beam evaporation and lift-off. After plasma treatment, the PDMS microchannel was aligned and bonded to glass electrode under microscope without adding methanol. Wires were soldered on the gold electrode pads after bonding (Figure 2b) using solder paste [204].

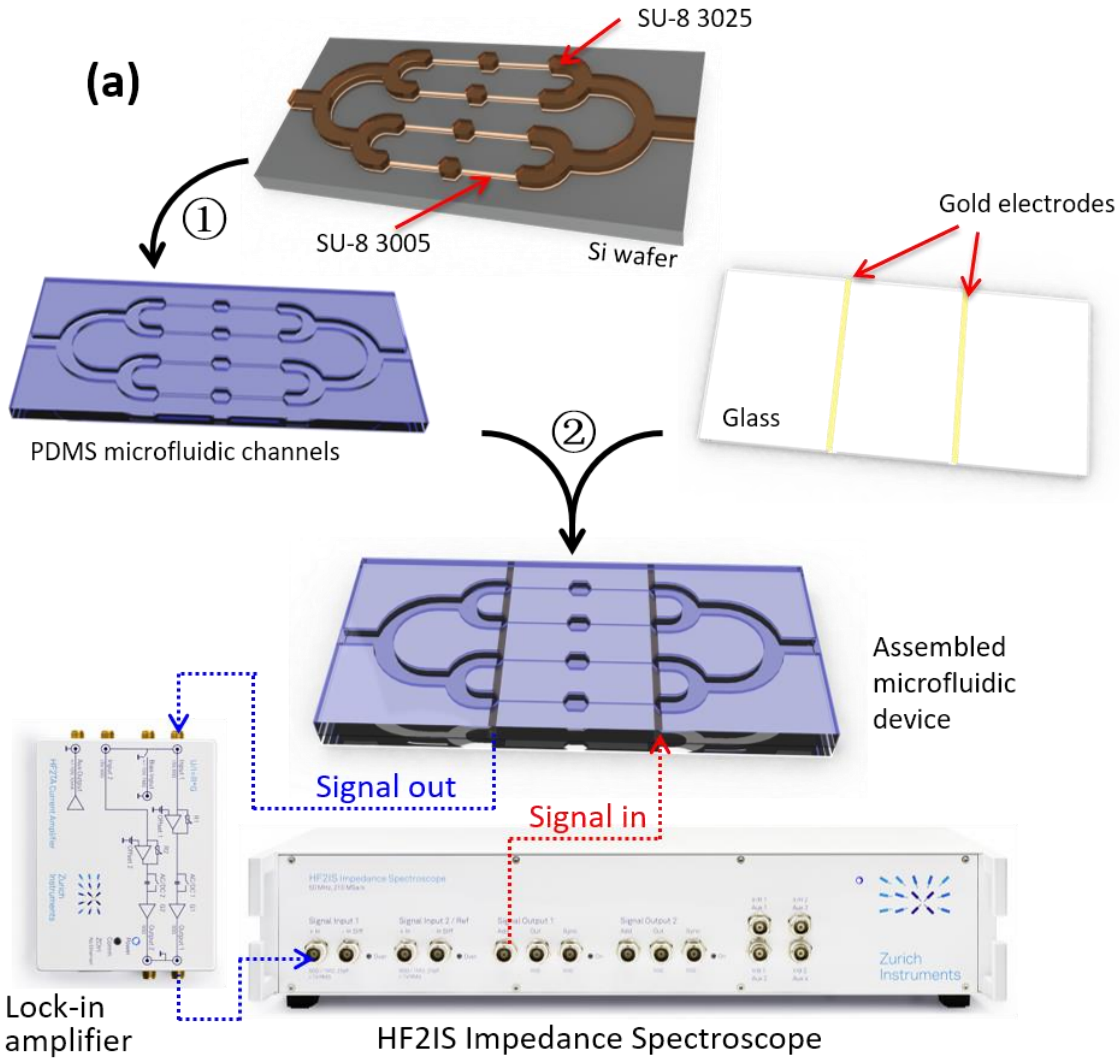
(a)
SU-8 3025
SU-8 3005
Si wafer
①
PDMS microfluidic channels
Gold electrodes
Glass
②
Assembled microfluidic device
Signal out
Signal in
Lock-in amplifier
HF2IS Impedance Spectroscope

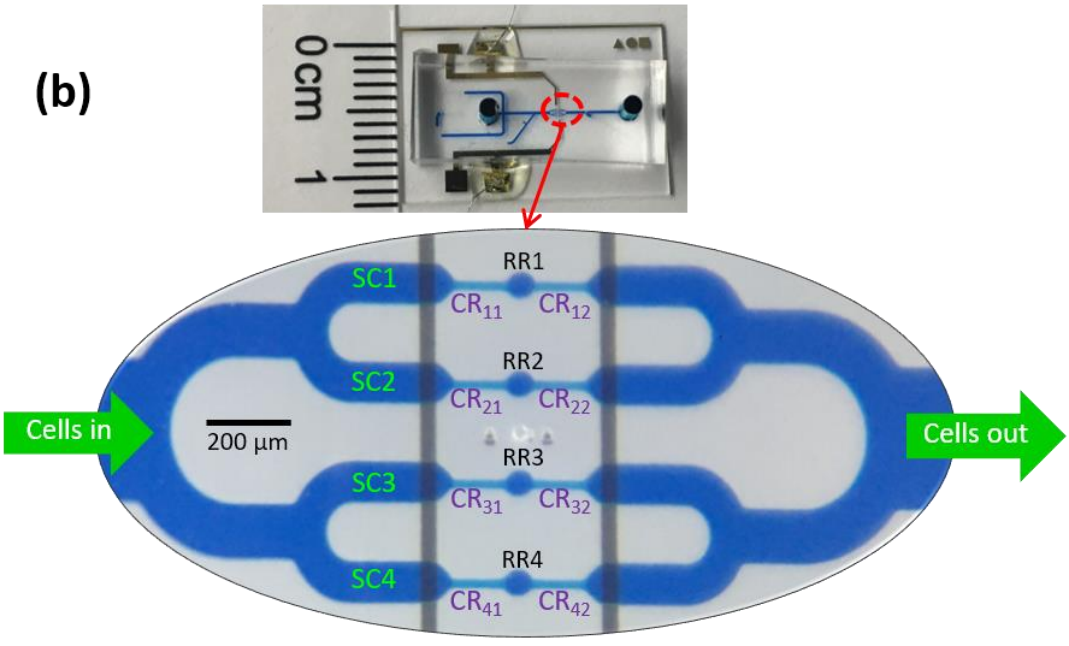
(b)
0 cm
1
SC1
SC2
SC3
SC4
RR1
RR2
RR3
RR4
CR11
CR12
CR21
CR22
CR31
CR32
CR41
CR42
Cells in
Cells out
200 µm

Figure 2. (a) Device fabrication processes and experimental setup: ① PDMS replica molding, ② PDMS to glass bonding after plasma treatment; (b) Illustration of the channels configurations; SC: sensing channel; CR: constriction region; RR: relaxation region; CRxy, x: row number (x=1,2,3,4), y: column number (y=1,2).

5.2.3. Experimental

The microfluidic device was mounted on an inverted microscope (Zeiss Axio Observer, LSM-510, Thornwood, NY). The cell suspension solution was injected into the inlet at a constant flow rate of 10 μL/min controlled by a syringe pump. The wires are connected to an impedance analyzer (HF2IS impedance spectroscope, Zurich Instruments, Zurich, Switzerland) with the affiliated lock-in amplifier. An AC signal with 1 V in amplitude, and four frequencies at 1 kHz, 10 kHz, 100 kHz, and 1 MHz was applied on the electrodes for impedance measurement. The impedance data was recorded through LabView® and processed by Matlab®. Simultaneously, videos of the cells travelling through the parallel microfluidic channel were recorded at 240 frames per second (fps). The movement of the cells was aligned with impedance measurement results to validate our assumption that impedance spectroscopy can recognize the location of the cells passing through the constriction channels and relaxation regions. According to our previous research and that of others on bioelectrical characteristics at single-cell level analysis, the amplitude ratio and phase shift are important biomarkers to distinguish different cell types [65].

As illustrated in Figure 2b, four parallel sensing channels (SC1, SC2, SC3, and SC4) share one pair of electrodes. In each sensing channel (SC), two sequential constriction regions (CR) are separated by one relaxation region (RR). Each constriction channel is named by the row number and column number. The first and second sequential constriction regions are labeled as CR_{x1} and CR_{x2}, where x is the SC sequential number 1~4. The relaxation regions in each SC are named as RR1, RR2, RR3, and RR4.

5.3. Results

5.3.1. Data collection and parameter definition

The shared pair of electrodes measures the overall impedance value of four channels in parallel. The impedance drops when the cell is in the RR because the impedance of the culture medium is lower than the cell. The time stamps generated by the RR helped identify the impedance shift of each cell. More importantly, the parallel SC allows more cells to pass through simultaneously. If one cell is deforming in one channel, other cells are still able to pass through other channels and be detected by the impedance variations. The impedance measurements were repeated on multiple devices with multiple samples (6 devices for MDA-MB-231 with 6 samples; and 5 devices for MCF-10A with 5 samples).

The location of a larger MDA-MB-231 (#1, red) and a smaller MDA-MB-231 cancer cell (#2, blue) in the microchannel with respect to time is plotted in Figure 3a. The impedance profile of the larger cancer cell #1 is well-resolved. As seen in Figure 3, six time stamps were collected from a single-cell passing through the channel SC4. By comparing the time stamps of the cell location and the impedance values, it can be seen that due to the deformation channel design, the impedance profile of this cell exhibits two peaks of roughly similar magnitude separated by a return to a baseline impedance value (Figure 3a). The impedance maxima at t = 9~13s and t = 16~20s correlated with the location of cell #1 in the CR41 and CR42, and the impedance dropped sharply as cell #1 entered the RR4 (t = 14~15s); here the impedance value returned to the original baseline typical of the medium solution. A smaller cancer cell #2, entered another channel SC2 as cell #1 was passing through the microchannel, which was detected by the electrode pair at t ≈ 6s (supplementary materials video “vv2.avi”).

The relaxation region in the middle of constriction channel causes a sharp drop in the impedance amplitude which can be correlated to the position of the cell in the relaxation region.

Once a cell enters the relaxation region, the medium starts to flow around the deformed cell and reduces the measured impedance value. This allows us to label time stamps to obtain velocity profiles of each cell. If the cell recovers to its original spherical shape, as illustrated in Figure 3a (14~15s), the impedance will reduce to its baseline as no cells traveling in SC. If the cell still keeps the deformed rod shape and travels to CR_{x2} without full recovery, as illustrated in Figure 3b (~16.5s), the impedance will show a drop in amplitude and continue to rise again at the entrance of CR_{x2}.

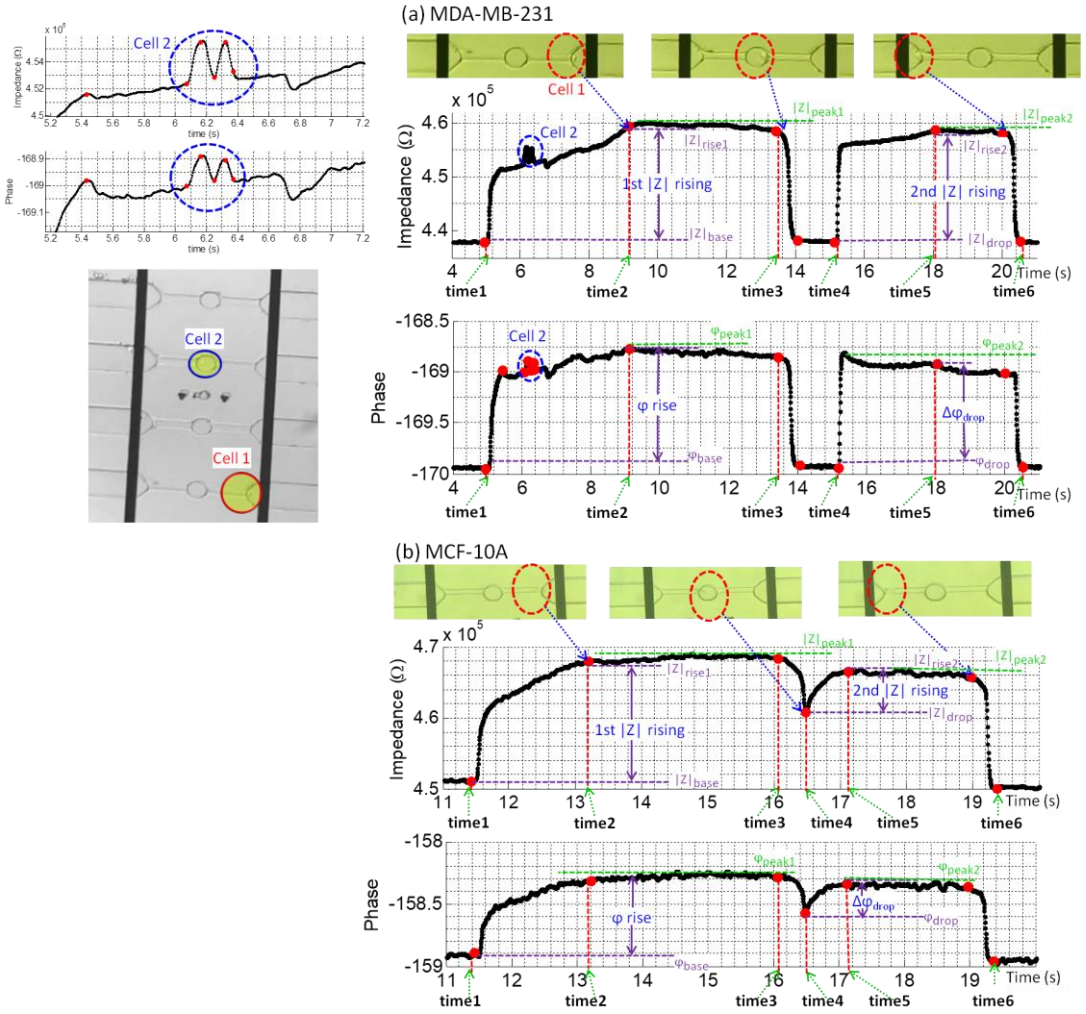

Figure 3. The impedance plot of an example cell through the device: (a) MDA-MB-231 (two cells); (b) MCF-10A (one cell).

Both the bioelectrical properties and biomechanical properties can be obtained from the impedance measurement results. The amplitude ratio, phase shift, and travel time of single-cells can be obtained directly from these impedance measurements as plotted in Figure 3. The variables that represent the velocity profiles of a single cell can be defined as follows: the rise time CRx1 channel $T_{rise1} = \text{time2} - \text{time1}$; the rise time in CRx2 channel $T_{rise2} = \text{time5} - \text{time4}$; and the overall travel time of the cell in the whole channel $T_{all} = \text{time6} - \text{time1}$. The amplitude rise in CRx1 is defined as: $\Delta|Z|_{rise1} = \frac{|Z|_{rise1} - |Z|_{base}}{|Z|_{base}}$; the amplitude in CRx2 channel is defined as: $\Delta|Z|_{rise2} = \frac{|Z|_{rise2} - |Z|_{drop}}{|Z|_{drop}}$, where $|Z|_{rise1}$ and $|Z|_{rise2}$ are the rising impedance when the cell deforms in the CRx1 and CRx2, respectively. The $|Z|_{base}$ is the baseline of the impedance value before the cell enters CRx1 channel. The $|Z|_{drop}$ is the impedance value when the cell enters the RR and causes an impedance drop. The $|Z|_{peak}$ is defined as the maximum value of impedance when the cell is traveling in either CRx1 or CRx2 channel. Similarly, the phase (φ) peak and baseline can also be collected at the same time points (supplementary materials video "vv1.avi", "vv2.avi", "vv3.avi"). Additionally, more combinations that reveal the bioelectrical and biomechanical properties of the cells can be obtained from the impedance plots in Figure 3. Comparing the deformation differences can be used as another parameter. The rise time ratio $\beta_{time} = \frac{T_{rise1}}{T_{rise2}}$ is defined as the ratio of the 1st rising time T_{rise1} and the 2nd rising time T_{rise2}. Another parameter we included is the impedance rise slope, which is defined as $\alpha_{1Z|t} = \frac{\Delta|Z|_{rise1}}{T_{rise1}}$ and $\alpha_{2Z|t} = \frac{\Delta|Z|_{rise2}}{T_{rise2}}$ for the impedance rise slope in CRx1 channel and CRx2 channel, respectively. In some cases, as illustrated in Figure 3a, the impedance can drop back to baseline if the cell relaxes in the RR and recovers back to its original shape. In other cases, as illustrated in Figure 3b, the cell enters CRx2 channel while maintaining

its rod shape, which does not allow the impedance to reach the baseline. Therefore, we can define the impedance drop ratio $\gamma_{Z\_drop} = \frac{|Z|_{peak} - |Z|_{drop}}{|Z|_{peak} - |Z|_{base}}$, as the ratio of the magnitude of impedance drop and the maximum impedance rise. Similar to the impedance drop, as shown in Figure 3, the phase will also drop when the cell reaches the RR1-4. Similar to the impedance drop ratio, the phase drop ratio is defined as $\gamma_{\varphi\_drop} = \frac{\varphi_{peak} - \varphi_{drop}}{\varphi_{peak} - \varphi_{base}}$. If the impedance magnitude drop of a cell reaches the baseline, the phase drop will also reach the baseline. If cells (whether similar size or not) are present at different channels at the same time and they cause blockage of the current (they deform and attach to walls), the baseline will be shifting to a new value. This will not affect the identification of rising, falling and dropping of impedance values.

5.3.2. Data analysis

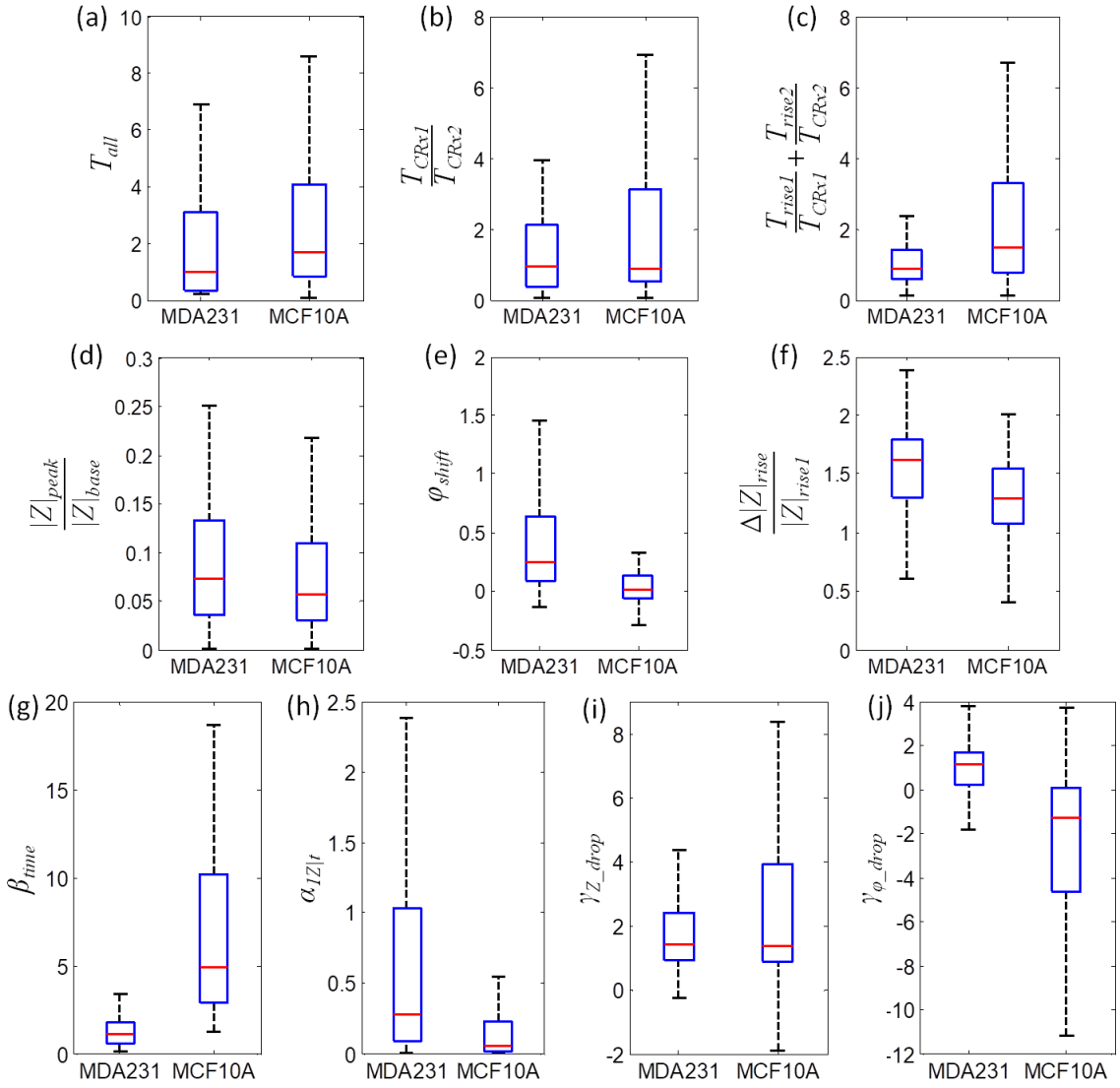

Figure 4. CA (cancer cells MDA-MB-231, n=101) and NR (normal cells MCF-10A, n=103) distinguished at population level with use of selected parameters: (a) total transit time; (b) transit time ratio of the passing time in CRx1 and CRx2; (c) the sum of rise time to passing time ratio in CRx1 and CRx2; (d) amplitude ratio: the ratio of relative impedance peak and impedance baseline; (e) phase shifts; (f) the ratio of the difference of impedance rise in CRx1 and CRx2 to the impedance rise in CRx1; (g) rise time ratio; (h) impedance rise slope in CRx1; (i) impedance drop ratio; (j) phase drop ratio. The blue box plot depicts the quantile numbers: maxima (upper dash whisker), Q75, Q50 (median, red bar), Q25, and minima (lower dashed whisker).

Many bioelectrical and biomechanical parameters can be extracted from the impedance measurement results. The total transit time T_{all} includes the travel time of cells through CRx1,

RR, and CRx2. T_{all} is broadly used in single constriction channels to characterize cancer cells [65, 205]. However, this chip with four parallel channels with RRs shows significant overlapping of cancer cells (CA) and normal cells (NR) in total transition time (Figure 4a). The travel time ratio in CRx1 and CRx2 also shows overlap with a similar median value (Figure 4b). If we select the rise time as a parameter, the ratio of rise time and travel time in each CR can better distinguish CA and NR cells at the population level (Figure 4c). Therefore, β_{time} can be a good parameter to represent the biomechanical properties of CA and NR cells. Researchers found that impedance spectroscopy is a useful tool in differentiating tumor cells from their normal counterparts based on the amplitude ratios and phase shifts [206, 207]. The bioelectrical parameters include impedance amplitudes and phase shifts. The commonly used amplitude ratio is defined as the ratio of the relative impedance amplitude peak to impedance baseline, when no cell is traveling in the constriction channel [101, 126]. The phospholipid abundance differs in human cancer cells (MDA-MB-231) and normal breast epithelial cells (MCF-10A) and leads to the impedance and phase shift differences [208]. The amplitude ratio shows a low differential rate between CA and NR cells (Figure 4d). The phase shifts of CA and NR shows a better separation at population level (Figure 4e); however, the Q75 line of MCF-10A is still higher than the Q25 line of MDA-MB-231, which means more than 25% of the cells cannot be distinguished by phase shifts only. A prediction accuracy of lower than 75% is not sufficient to distinguish CA and NR. Another bioelectrical parameter is the ratio of the impedance rise difference in CRx1 and CRx2 to the impedance rise in CRx1, which is defined as: $\frac{\Delta|Z|_{rise}}{|Z|_{rise1}} = \frac{||Z|_{rise1}-|Z|_{rise2}|}{|Z|_{rise1}}$ (Figure 4f). In the configuration of two sequential CR separated by one RR, the first deformation and second deformation can be compared and used as a biophysical marker for CA and NR cells. The impedance rise in CRx2 is directly affected by the biophysical status of the cells in RR. If the

cell recovers to its original spherical shape, the secondary deformation and impedance rise in CRx2 will be more similar to the deformation and impedance rise in CRx1. The different cell membrane stiffnesses and cytoskeleton strength of MDA-MB-231 and MCF-10A will behave differently in the RR, and result in different impedance rise in CRx2. The impedance drop ratio and phase drop ratio is used as a parameter to describe bioelectrical properties of cells in RR. The useful biomechanical and bioelectrical parameters for distinguishing CA and NR cells become β_{time}, $\alpha_{1Z|t}$, γ_{Z_drop}, and γ_{φ_drop}. The rise time ratio β_{time} shows a clear separation between the Q75 of CA cells and the Q25 value of NR cells (Figure 4g). The impedance rise slope $\alpha_{1Z|t}$ in CRx1 shows a wider distribution of CA cells than NR cells (Figure 4h). The impedance drop ratio γ_{Z_drop} shows a significant overlap between CA and NR cells (Figure 4i); however, the phase drop ratio γ_{φ_drop} has separated Q25 line of CA and Q75 line of NR, which may contribute more in prediction accuracy between the CA and NR cells.

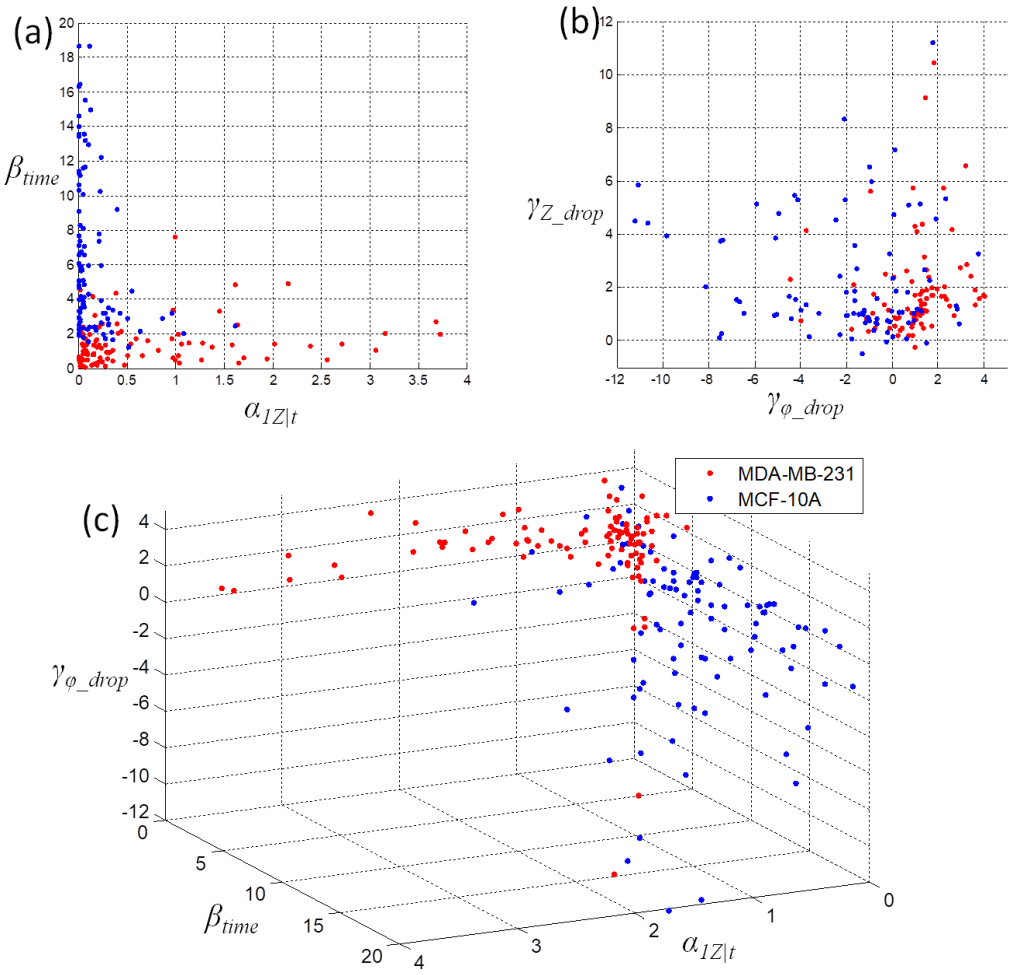

Figure 5. Scatter plot distinguishes at single cell level cancer cells (MDA-MB-231, n=101) and normal cells (MCF-10A, n=103): (a) biomechanical parameters of rise time ratio; (b) bioelectrical parameters of impedance drop and phase drop ratios; (c) combined biomechanical and bioelectrical properties.

Figure 5 shows the scatter plot at the single-cell level by using 3 parameters, β_{time}, $\alpha_{1Z|t}$, and γ_{φ_drop} to distinguish cancer cells (CA) and normal cells (NR). The vertical axis in Figure 5a is the rising time ratio β_{time}, which represents the biomechanical properties of the cells because it is a representation of how the cells behave in the relaxation region. In Figure 5a, using the vertical axis parameter, rising time ratio, a boundary between CA (red dots) and NR (blue dots) can be found to distinguish CA and NR at single cell level. This can be identified as the distinguish boundary between CA and NR using only the biomechanical properties. In Figure 5b,

both the impedance drop ratio and phase drop ratio can also be used to establish a boundary to distinguish CA and NR. The parameter $\alpha_{1Z|t}$ combines both the biomechanical and bioelectrical properties of the cells. The overall impedance includes the effect of both membrane capacitance and the cytoplasm resistance. We are not able to specify each parameter to a specific biological/biochemical property of a cell. The cancer cells have higher nuclear-cytoplasmic ratio (N/C ratio), which increased the membrane impedance of the cells. According to literature [208], the membrane of cancer cells shows higher impedance. In Figure 5c, together with three parameters selected, β_{time}, $\alpha_{1Z|t}$, and γ_{φ_drop}, we can further improve the prediction accuracy between CA and NR at single cell level.

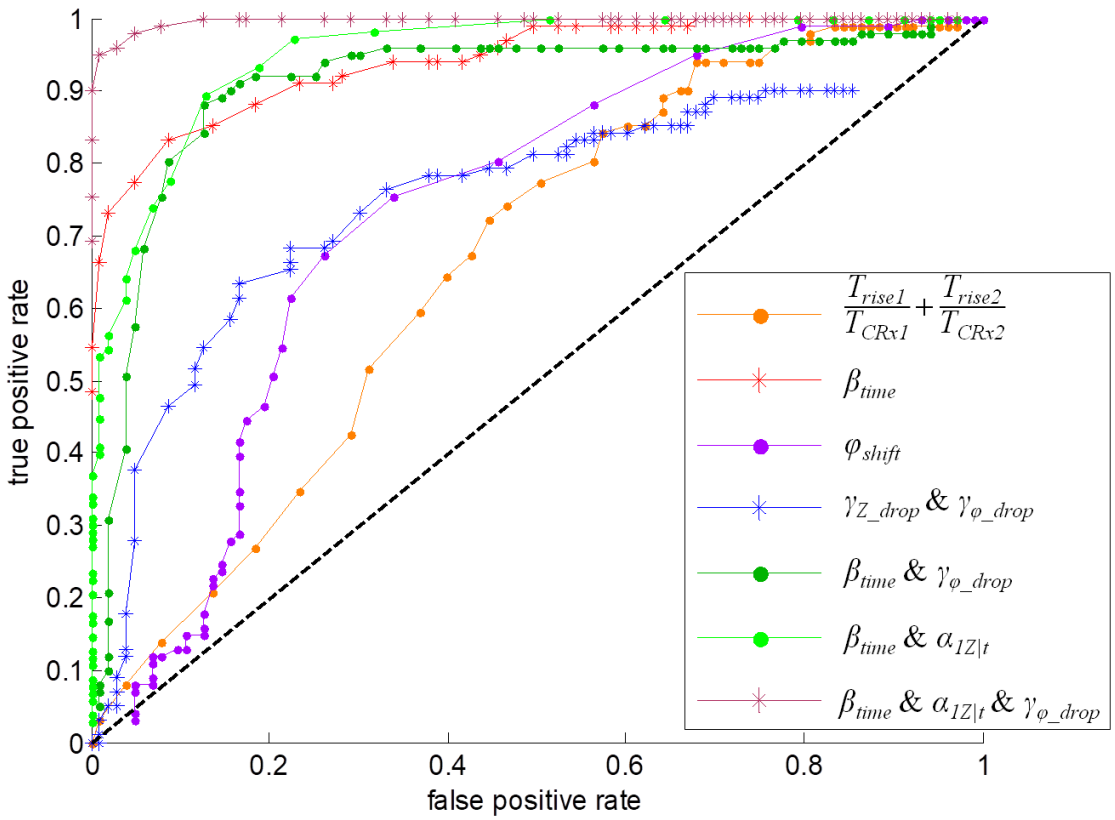

Figure 6. ROC curve depicting the ability to discriminate CA (MDA-MB-231) and NR (MCF-10A) using different biophysical parameters. (ROC curve of other parameters is available in supplementary materials)

Figure 6 indicates the receiver operating characteristic (ROC) curve for the best separation between MDA-MB-231 and MCF-10A at single-cell level. The area under curve (AUC) value can show the ability to differentiate cancer cells (MDA-MB-231) and normal cells (MCF-10A). The black line represents the boundary that CA and NR cannot be distinguished. The biomechanical parameter involving cells traveling time during impedance rise $\frac{T_{rise1}}{T_{CRx1}} + \frac{T_{rise2}}{T_{CRx2}}$ (orange curve in Figure 6) shows a separation rate of 63% between CA and NR cells. β_{time} (red curve in Figure 6) shows that the separation ratio between CA and NR can reach 85%. The phase shift only (purple curve in Figure 6) has a separation ratio of 63%; however, the false positive rate using φ_{shift} cannot be decreased below 16% unless the true positive rate is also lower than 41%. The rate of differentiation between CA and NR with γ_{Z_drop} and γ_{φ_drop} has only 62% (blue line in Figure 6). Combining the biomechanical parameter β_{time} and a bioelectrical parameter with higher prediction accuracy shown in Figure 4j, γ_{φ_drop}, the differentiation rate between CA and NR can reach 85% (dark green curve in Figure 6). If considering the combination of β_{time} and $\alpha_{1Z|t}$, a parameter with both of the bioelectrical impedance rise and the biomechanical travel time during the impedance rise, the differentiating rate between CA and NR can reach 92% (light green curve in Figure 6). When considering three parameters β_{time}, $\alpha_{1Z|t}$, and γ_{φ_drop}, the maroon curve in Figure 6 shows a low false positive rate and a high true positive rate. The rate at which between CA and NR can be identified reaches 97%.

5.4. Discussion

Cancer cell characteristics studied by label-free methods are focusing on the biophysical attributes, such as the abnormal nuclei, cell cytoskeleton strength, membrane stiffness and adhesion properties [24, 27, 33, 39, 165]. The biomechanical properties of cancer cells can be

measured and distinguished from normal cells by atomic force microscopy (AFM) [33-35, 100, 104]. The main issue with AFM measurement on cells is the extensive experimental procedures for both sample preparation and data acquisition. The biomechanical response time of cells to the cantilever stimulation is about 1 ms, while the mapping time for AFM on a cell can reach several minutes [209, 210]. Maintaining a survivable environment during the AFM measurement to keep the viability of the cells in culture medium is challenging. The uncertainty of the consistency of the cells during the AFM mapping can introduce error during experiments. Even with improved AFM stimulation on single cells, the data collection of cells at large population by AFM can reach over 2 hours for hundreds of cells [100], while our microfluidic chip presented in this paper can harvest the bioelectrical and biomechanical profile data within 20 s for a single cell. Meanwhile, probing for cells in aqueous environment by AFM cantilever tip with a spherical glass bead needs additional processes for fabrication and calibration [103, 104, 159]. Based on the principle of AFM, Bagnall's group have developed a microfabricated cantilever structure on chip can also be used to collect biomechanical data from cultured cells; however, using this method, the data acquisition requires extensive video/image processing [97, 211, 212]. To overcome the issues of AFM measurements for biomechanical properties of the cells, the microfluidic constriction channels become a superior tool for high throughput analysis of single cells. The time of data collection for both bioelectrical and biomechanical properties is also significantly reduced. The purpose of AFM and our microfluidic chip involve collecting biophysical properties from a large population of cells by studying single cells through a label-free technique. The CRs in our chip force the cells to deform and RRs allow the cells to recover, which has the similar function with the indentations by AFM cantilevers.

The use of parallel constriction channels for higher throughput cell analysis has been studied [213, 214]. However, capturing the biomechanical characteristics of cells directly from video analysis is difficult without proper time stamps from the constriction channel. Our device differs from existing devices by the addition of a RR within each constriction channel. This RR adds another crucial dimension to characterizing the biomechanical property of cells and also provides the means to assign time point labels for identifying the location of cells in the impedance measurement results. The six time points include the initial transit of CRx1 channel, followed by the transit through RR, and finally the transit through CRx2 channel. The CRx1 channel probed the deformation of the cell at a constriction channel, which is similar with other approaches of single cell biomechanical characterization with a single constriction channel. New to this device, the RR removes the mechanical stress which enables the cell to return to its original spherical shape. The CRx2 then re-imposes mechanical stress thus probing the cells' biomechanical properties during the secondary deformation. The CA and NR cells are differentiated by the secondary deformation process, specifically defined here as the impedance rise slope at the entrance of CRx2 channel. The entry time at CRx1 and CRx2 is related to the cytoskeleton strength and the cell membrane stiffness. The deformability is one of the differences in biomechanical properties between cancer and normal cells. The impedance rise slope includes the bioelectrical impedance properties and the rise time, which is one of the biomechanical parameters. The phase drop ratio is the bioelectrical parameter related to the capacitance of the cells, including the specific membrane capacitance and the capacitance from cytoskeleton and nucleus.

The impedance properties of normal and cancer cells are less well known. Here we incorporated electrodes to serve a dual role of providing time stamps on biomechanical changes

in single cells and analyzing impedance changes in response to mechanical stress. There are more ways to label time stamps on constriction channels. For example, a more direct way is to embed more electrodes on the constriction channels with individual or differential impedimetric measurement [215, 216]. Zhou, et al. added two sets of electrodes at the entrance and the exit of a single constriction channel to detect the passing time of MCF-7 [216]. The separation between MCF-7 and drug treated MCF-7 were distinguished by the impedance of cells entering and exiting the channel, as well as the passing time with $p<0.001$ at population level [216]. The time variables represent the velocity information and are indicative of the biomechanical properties of each cell. In our work, the presence of the RR amplified the difference of biomechanical behaviors between cancer and normal cells; the value of the RR here was predictable based upon on earlier findings of repetitive nano-indentation of cancer and normal cells [100]. We also showed in previous work that using the two sequential constriction channels with one RR can distinguish cancer and normal cells at a ratio of ~83% using selected biomechanical parameters [148]. Both of these studies confirmed that cancer cells are more deformable than normal cells, and that cancer cells recover their original spherical shape faster than the normal cells. Therefore, the cancer cells face the secondary deformation process at CRx2 channel in a different biomechanical condition than normal cells. Normal cells, less deformable than cancer cells, result in a smaller secondary entrance time T_{rise2} compared to the T_{rise1}. The timing parameter β_{time} shows the difference in biomechanical properties of the two cell lines. As a result, the β_{time} of the breast cancer cell line MDA-MB-231 is smaller than the β_{time} of the normal breast cell line MCF-10A. In the ROC curve, we showed similar conclusions to our prior work [66, 148]; we can reach a prediction ratio of 85.2% to identify cancer and normal cells if we rely only on the biomechanical properties.

The amplitude ratios and phase shifts represent the bioelectrical properties of each cell. Both the specific membrane capacitance and cytoplasm conductivity contribute to the bioelectrical data. Previous work on the bioelectrical characteristics of MDA-MB-231 and MCF-10A in single constriction channel, reported the membrane capacitance and cytoplasm conductivity of MDA-MB-231 are 1.63±0.17 μF/cm^2 and 24.9±1.12 MΩ [49]; and the membrane capacitance and cytoplasm conductivity of MCF-10A are 1.94±0.14 μF/cm^2 and 24.8±1.05 MΩ [49]. The dielectric parameters of MDA-MB-231 and MCF-10A cells are measured in constriction channels when the cells are deformed into rod shape. The key to improving discrimination between cancer and normal cells here is that both of the biomechanical and bioelectrical properties become the biosignatures of the cells. The phase drop ratio γ_{φ_drop} improves the prediction rate between CA and NR. MCF-10A is less deformable than MDA-MB-231, which causes a slower rod-to-spherical shape recovery in the RR. The impedance and phase drop will not reach the baseline if the cell retains the rod shape during the passing through RR. Based on the AUC, the ROC curve prediction rate between MDA-MB-231 and MCF-10A reaches 97% by combining both the biomechanical and bioelectrical properties.

We show that the shared pair of electrodes across four parallel channels can be used to measure bioelectrical parameters to increase the rate of cell identification. Even though multiple channels in parallel are added while still using a single electrode pair, the device is still sensitive enough to identify single cells or multiple cells passing through the parallel microchannels, which yields a 97% prediction rate between cancer and normal cell lines.

5.5. Conclusions

We developed a device with parallel constriction channels accompanied by a single sensor to improve the throughput and data collection of deformability assays. The two

constriction regions and one relaxation region in each channel served to establish time stamps for collecting the biomechanical variables of the cells, so that the biomechanical properties of the cells can be extracted from the time stamps in the impedance measurement. From the impedance measurement data, both biomechanical and bioelectrical properties were collected for data analysis. The potential for this device to effectively diagnose cancerous and normal breast cells is demonstrated. In the future, further refinements can be made. For example, embedding additional widths and lengths of the constriction channels and relaxation regions can potentially improve sensitivity to resolve more heterogeneous tissue samples. In addition, the acquisition of data and analysis of the increased variables such design features provide can also help understand the dynamic changes of cell biomechanical behaviors. We should add that this is first time we report this new bioassay. The throughput of our device is scalable allowing tens or hundreds of microchannels in array, which can process more than 2 mL of liquid sample within a few minutes. Doing so may require multiplexing between different electrode pairs or integrating more impedance analyzers with the system (electronics can be custom made). In this paper, we used one pair of electrodes for 4 channels. The impedance data can be collected from multi-electrodes at the same time, which can increase the throughput significantly. More work needs to be done to study the influence of the microfluidic chip parameters including the length of the constriction regions, the length and width of the relaxation region and the ratio of the two on the predication rate between normal and cancer cells. Also, the question remains to be answered if the more comprehensive biophysical attributes proposed here can be extended to other cancer cells and if they can be used to even distinguish between different cancer cells with different degrees of invasiveness.

6. Entrapment of prostate cancer circulating tumor cells with a sequential size-based microfluidic chip

Ren, X., Foster, B. M., **Ghassemi, P.,** Strobl, J. S., Kerr, B. A., & Agah, M. (2018). Entrapment of prostate cancer circulating tumor cells with a sequential size-based microfluidic chip. Analytical chemistry, 90(12), 7526-7534.

My contributions towards this chapter included device fabrication, sample preparation, experimentation, data collection through image analysis, and assisted with manuscript preparation.

6.1 Introduction

Measurement of circulating tumor cells (CTCs) represents a minimally invasive cancer screening method useful for initial staging of cancer patients and in monitoring recurrent or metastatic disease [153, 154, 217, 218]. The CTCs in peripheral blood play an important role in cancer metastasis. Considering the rare count of CTCs in blood with 1-100 cells/mL, the blood volume usually requires ~7.5 mL to achieve conclusive results for CTC detection and enrichment. The challenge of detecting and isolating the rare cells from peripheral blood encouraged scientists and engineers to develop many methods for CTC enrichment and enumeration. A limitation of the current CTC enumeration systems approved by the US Food and Drug Administration (FDA) namely CellSearch® and AdnaTest® is their reliance upon expression of the epithelial cell adhesion molecule (EpCAM) [219, 220]. Clinical studies show that CellSearch could detect CTCs in blood samples drawn from breast cancer, colorectal cancer, and prostate cancer patients [221-223]. While EpCAM is expressed on the majority of cells within primary epithelial tumors, its expression is often lost during tumor progression [224-226]. During epithelial-mesenchymal

transition (EMT), there is a loss of epithelial cell markers including EpCAM and an upregulation of mesenchymal surface proteins which corresponds to progression to more aggressive and metastatic cells [224-226]. The level of EpCAM expression also varies for different cancer types and among patients. Further, non-cancerous EpCAM+ epithelial cells can exist in the blood [227]. The same deficiency also applies to microfluidic chips that have been developed throughout the years that function based on such surface markers. A good example is the CTC-chip containing over 10,000 microposts in an array that uses anti-EpCAM or aptamers for cell capture. The CTC detection and capture rate using CTC-chip can reach 60% with approximately 50% purity [228, 229]. It is also notable that the surface markers used for CTC entrapment are fundamentally derived from cell lines and are based on primary tumor or metastatic tumor staining but very few have been validated on CTCs in patients [217, 224, 225].

The ideal method for CTC isolation and enrichment should have minimal sample pre-processing to avoid CTC loss, high throughput, high efficiency, high sensitivity, high purity, and low cost. These criteria along with the limitations associated with surface-marker-based approaches have motivated the microfluidics community to develop new CTC technologies that rely on biophysical attributes of CTCs. This is primarily based on the assumption that these properties such as size, deformability, permittivity, and conductivity in CTCs differ from those of blood cells. Size exclusion-based, deformability based, and dielectrophoresis based microchips have been explored and shown promising results in CTC collection[230-232]. Surface acoustic waves generating via tilted identical interdigital transducers on microfluidic channels also were used to collect CTCs from whole blood[233, 234].The development of microfluidic chip for CTC enrichment is finding the balance between throughput, capture efficiency and purity. Some existing technologies are listed in Table 1. In particular, separation of CTCs based on the

hypothesis that they have a larger size compared to other cells in blood have been broadly investigated. Several review articles have been published summarizing these efforts [235-238]. Some of the examples include using constriction channels [239], micro filter arrays [240], or fan-in-fan-out micro cavity arrays [241] to capture CTCs but these chips suffer from limitations in throughput and capture efficiency. Tai and Cote's groups developed 3D microfilters on chip to select CTCs [92]. The two layers filter structure with micro pores can capture ~85% of the spiked cancer cell lines LNCaP and MCF-7. The configuration and dimensions of the 3D microfilters needs to be customized for specific cell lines, which increase the complexity of fabricating the parylene-C microfilters on PDMS devices. Toner's group developed another type of microfilters with triangle barrier array to select single CTCs and CTC clusters [94]. The trapping efficiency for larger CTC clusters reached 41% for clusters formed by two CTCs. However, single CTC cells could deform and escape from the triangle barrier without being captured. Ventana Medical Systems, Inc. also developed a microchannel based filter for MCF-7 and MDA-MB-231 spiked blood sample with capture efficiency of ~75% [88]. Due to the limited volume of capturing cavity before the microchannel filter, the maximum quantity of the CTC captured by this device is limited. The capture efficiency increased to 84% if more than 1000 of the cancer cells were spiked in 1 mL of blood sample, which indicated a limited application of capturing rare CTCs with only 1-100 cells/mL. Di Carlo's group and the Vortex company demonstrated CTC isolation with generating rectangular reservoirs to form laminar vortices to isolate larger cancer cells from smaller blood cells [242-245]. The dimensions of the rectangular reservoirs can be modified in order to make the device suitable for different size distributions of CTCs in either different cancer types or different cancer subpopulations [245]. A recent report of using Vortex technique to isolate prostate CTCs with both cell line and patients

reached an average of 1.88-93.75 CTCs/7.5mL blood with purity of 1.74-37.59% [244], which had higher CTC detection than parallel CellSearch system comparison. The high-throughput Vortex (Vortex-HT) chip showed a capture efficiency of 51% and a purity of 55.2% after six cycles of sample screening with a high flow rate of 8 mL/min [244].

Table 1. Selected existing technologies on CTC enrichment.

Devices	Key observations (recovery rate, throughput, purity)	Reference
Micropillar chip; Herringebone chip	5-1281 CTCs/mL with 1 mL/h, detection rate 65%; 63 CTCs/mL with 1.2 mL/h, detection rate 91.8±5% for PC3; 50.3 CTCs/mL with 8 mL/h, detection rate 98% SKBR3;	M. Toner, [229, 246-248]
Micropillar chip	30 CTCs/mL with 1 mL/h, detection rate 97±3%	B.J. Kirby, [249]
Sinusoidal chip	53 CTCs/mL with 15 mL/h, detection rates are 98% MCF-7 and 82% MDA-MB-231	S.A. Soper, [250-253]
Microchannel array	10 CTCs/mL with 36 μL/min, recover rate >95%. Using additional grooved surface can achieve over 90% capture rate with >84% purity. Throughput: 3.6 mL/h.	Z. Fan, [254, 255]
μHall: antibody labeled magnetic nanoparticles	Recovery rate of MDA-MB-468 99%; purity 100%; throughput 3.25 mL/h; analyzing ovarian 7.6 CTCs/mL.	H. Lee, [256]
CellSearch® system	Positive selection to enrich tumor cells from whole blood. The enriched and stained cells are scanned and imaged on CellTrackersAnalyzer II®.	[222, 257-260]
Microfilter	0-12.5 CTCs/mL with 90 mL/h, detection rate 90%	M. Toner, [246, 261]
Portable filter	MCF-7, SK-BR-3: 5 CTCs/mL at 0.5 psi constant pressure, detection rate >90%	R.J. Cote, [262]
Microfilters	1-3 CTCs/mL with 2 mL/h, detection rate enhanced with antibody coating: 95% MCF-7; 97% MDA-MB-231	C.T. Lim, [263]
Microsieve filter with uniform pore structure	Undiluted whole blood with flow rate < 2 mL/min. MCF-7 recover rate >80%; accurately detected CTC from 8 patients.	M. Li, [264]
3D parylene-C microfilter	Selection by both size and deformability; collect >85% viable spiked MCF-7 cells.	Y. Tai, [92]
Suspended microchannel resonator	Flow rate: 45μL/h; analyze 500 cells per hour to reach 73% unhealthy cells. Healthy blood cells passage time <10 ms; CTC passage time >10 ms.	S. Manalis, [97, 212, 265]
Lab-on-disc: centrifugal microfluidic size selection	MCF-7: 61% capture rate; have the potential to high-throughput and easy detection by directly reading on disc. After collection, the MCF-7 still viable in 15 days cell culture. Detect 0-90 CTCs/7.5 mL. Throughput: >3mL/min; sensitivity: 95.9±3.1% recovery rate; selectivity: >2.5log WBCs depletion.	Y. Cho, [95, 266]

Vortex®	Capture CTC by fluidic vortex without having CTCs experience deformation. Throughput: 7.5 mL whole blood in 20 min. About 60-90 min on the system with no sample prep; No staining or any kind of affinity capture of the cells is required; efficiency of capture (60-80%).	D. Di Carlo, [242, 243, 267-269]

Here, we present our new size/deformability-based CTC high-throughput entrapment chip (CTC-HTECH) with multiple rows of micro constriction channels and trapping chambers that overcomes the limitations of inefficient capture observed with some existing size-dependent CTC capture designs. The single CTC can be captured in trapping chambers, while blood cells can pass through the microchannels with blood flow. The localized entrapment allows to determine the number of CTCs by scanning the trapping chambers, a unique feature that is not available in other size-based CTC microfluidic chips [88, 92, 262]. The following describes the chip design and fabrication along with the experimental results that are achieved by spiking blood samples with prostate cancer cells.

6.2 Experimental Section

6.2.1 Cell line selection and sample preparation

Prostate cancer is the second leading cause of cancer-related death in men. Prostate cancer cells are good candidates to represent CTCs in peripheral blood [252, 270]. Prostate cancer cell line LNCaP-C4-2 (passage #7, expressing green fluorescence protein (GFP) by lentiviral transduction) was grown in RPMI with 10% FBS and 1% PenStrep (100 U/mL Penicillin and 100 μg/mL Streptomycin). Cells were grown in T-25cm^2 culture flasks at 37°C in a 5% CO_2 in air atmosphere until cells were ready for subculture. The morphology of the prostate cancer cells was observed before trypsinization (Figure 1). The cells were then detached from the flask with trypsin-EDTA solution (Sigma Aldrich). The LNCaP-C4-2 cells were trypsinized at 37°C for 5 min, respectively. LNCaP-C4-2 cells were mixed with murine whole blood at about ~50 cells/mL. The white blood cells (WBCs) count in the murine whole blood is ~2-3×10^6/mL; the

lymphocytes count is ~1-2.5×10^6/mL; and the platelets count is ~10^9/mL.The size of blood cells including red blood cells (RBCs), WBCs, lymphocytes and platelets are below 8-10μm, while the prostate cancer cells are larger in size distributed mainly in the range of 10-15 μm according to previously published work[138].

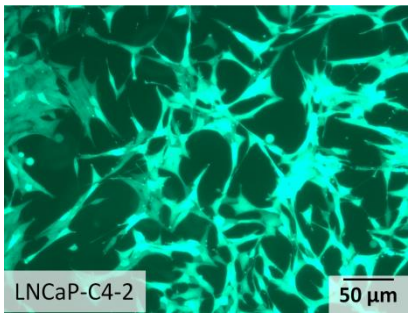

Figure 1. Micrographs depicting the morphology of prostate cancer cell line LNCaP-C4-2.

6.2.2 Device fabrication

The CTC-HTECH microfluidic channels were fabricated by polydimethylsiloxane (PDMS) soft-lithography, followed by PDMS-glass bonding after plasma treatment (Figure 2). Forty microchannels with constriction channels (width: 8 μm; height: 8 μm; length: 100 μm/each) and trapping chambers (width: 30 μm; height: 30 μm; length: 40 μm/each) were connected in parallel in each row. The molds for microfluidic channels were fabricated on a silicon wafer with two layers of SU-8 (SU-8 3005 and SU-8 3025, MicroChem, Newton, MA) photolithography on a clean and dehydrated silicon prime wafer.Tridecafluoro-1,1,2,2-tetrahydrooctyl-1-trichlorosilane (TFOCS, Fisher Scientific) was coated on the surface of the molds for the easy release of PDMS [148, 204]. The PDMS channels were then bonded to a glass slide after air plasma treatment using plasma cleaner. Detailed fabrication procedures are available in supplementary information.

6.2.3 Experimental setup

The CTC-HTECH device is mounted on an inverted microscope (Zeiss Axio Observer LSM-

510, Thornwood, NY). The blood sample is connected to the inlet and in all experiments with a constant pressure (500 mbar) applied to the sample reservoir by a pressure pump (Elveflow® OB1, Paris, France). The resultant flow rate of the blood sample was ~ 2.4 mL/hour. A smartphone with slow motion video function was positioned at the inlet and captured images at a rate of 240 frames per second (fps) which was sufficient to accurately count the number of cancer cells entering the chip. Only one inlet was open during each experimental run. As illustrated in Figure 2, cancer cells were deformed in multiple constriction channels arranged perpendicular to the inlet channel and cells recovered their shape within the cavities of the trapping chambers. RBCs, WBCs, platelets, and small lymphocytes passed through every constriction channel with the flow stream. The COMSOL® simulation results of flow through the channels with and without cells in the constriction channels are presented in supplementary information (Figure S1). When the cancer cells enter and deform within the constriction channel, the blood flow temporarily slows down. Once inside the cavity of the trapping chamber, the cancer cells recover their original spherical shape after the deformation created by their passage through the constriction channel and the flow rate resumes. An individual CTC either continues through the series of constrictions and trapping cavities or remains in the cavity region of the trapping chamber. When the CTC remains in the trapping cavity, this defines an equilibrium point where the impetus of the blood flow stimulating cell progress through a subsequent constriction channel is offset by a CTC's resistance to a subsequent deformation necessary to progress. Based on this principle, the CTCs are captured by this device. GFP prostate cancer cells diluted into whole mouse blood were visualized by their fluorescence. After 30 minutes the entire 1.2 mL sample passed through the device, then camera images were taken of the device to ascertain the capture of cancer cells. The trapped CTCs were counted from camera images and

the cancer cell trapping efficiency determined by comparing the number of trapped GFP+ cancer cells to the number of GFP+ cancer cells entering the device at the inlet.

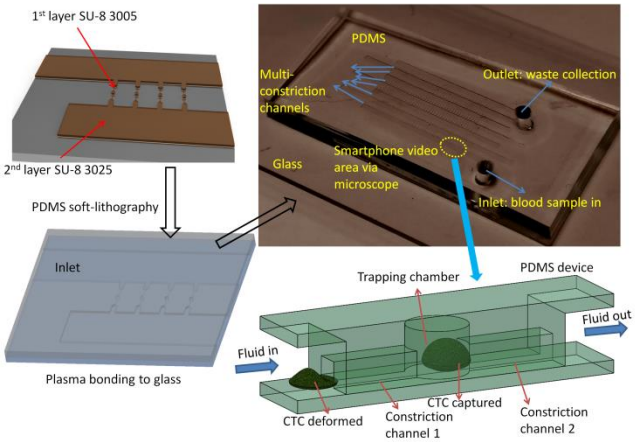

Figure 2. Illustration of high-throughput entrapment chip for CTC (CTC-HTECH).

It is important to note that both the constant pressure and constant flow rate modes are used in microfluidic experiments [65, 271]. The constant flow rate mode using syringe pump can guarantee the throughput for most microfluidic devices designed with a limited number of microchannels [271]. However, when a constant flow rate is applied to a device with a large quantity of microchannels in an array, the pressure will be redistributed as cells are trapped in the microchannels. The pressure redistribution causes varying mechanical drag forces on the trapped cells within different channels. If three or more channels contain trapped cells under constant flow rate conditions, for example, the local pressure in the middle channel will increase and attempt to force the trapped cells through the constriction channel. The increased pressure will cause these cells to undergo greater deformation that could lead to changes in their cytoskeleton and possible cell damage leading to poor recovery of viable cells [93, 94, 272]. A sudden change in pressure will alter the cytoskeleton strength, membrane stiffness, and the biomechanical properties [100, 192]. In contrast when a pressure pump is used in a constant pressure mode, the pressure supply is maintained constant by altering the back pressure. This results in a variation of

the flow rate as the cells become trapped in the microchannels but avoids excessive pressure that imposes additional mechanical stress on the cells. In a microfluidic system with a low Reynolds number, the constant pressure mode will apply constant mechanical force on the cell membrane. Since the capturing and enrichment is related to the biomechanical properties and metastatic properties of CTCs, a gentle variation in both pressure and flow rate is needed. We used a programmable pressure pump to provide constant pressure to the blood samples at the inlet of the CTC-HTECH device. Consequently, an advance in our methodology based on the constant pressure inlet mode is the provision of a low stress environment for CTC trapping and enrichment.

6.3 Results

6.3.1 Enrichment of prostate cancer cells from mouse whole blood

Figure 3a shows the CTC-HTECH device is comprised of 6 rows, ①-⑥ where row ①is closest to the blood inlet port. Figure 3b shows a GFP+ cancer cell at the blood inlet. The outlets 1-6 were defined as waste collection site terminals from rows 1-6, respectively. Only one outlet was opened and connected to waste collection during each trial. For example, when outlet 1 is open and all other outlets are not punched open, outlet 1 collects the cells which pass through row ① (Figure 3). When outlet 2 is opened, cells pass through rows ① and ②, and collect in outlet 2; when outlet 3 is open, cells pass through rows ①, ②, and ③ and collect in outlet 3, and so on.

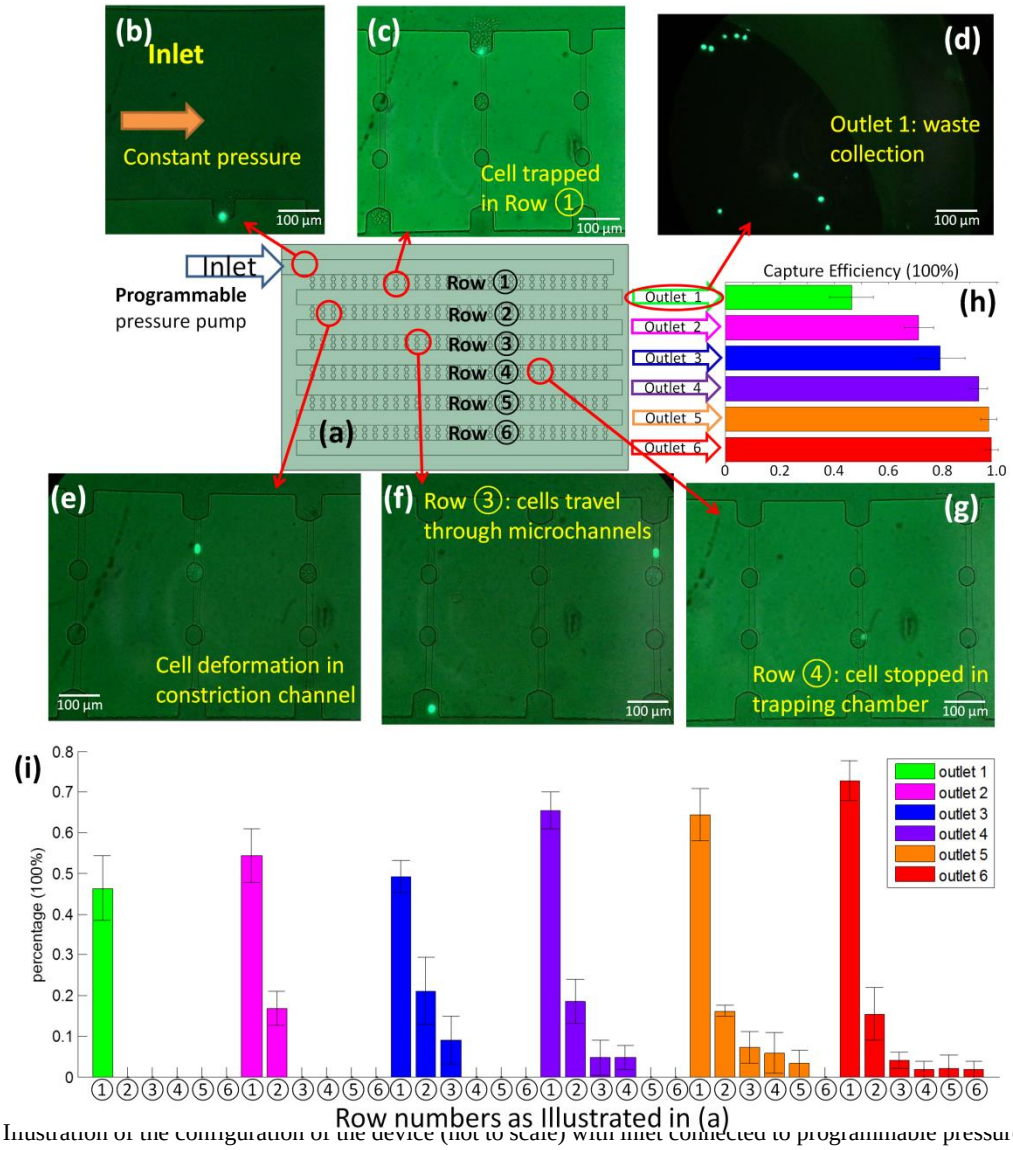

Figure 3. (a) Illustration of the configuration of the device (not to scale) with inlet connected to programmable pressure pump; each row and each outlet was assigned and labeled individually; (b-g) the GFP+ LNCaP-C4-2 prostate cancer cells; (b) image of inlet with a GFP+ cell starting to enter row ①; (c) a GFP+ cell trapped in row ① after the blood flow ceased; (d) image of the waste collection at outlet 1; (e) a GFP+ cell deforming and passing through row ②; (f) two GFP+ cells in row ③ with one cell still passing, and one cell exiting this row; (g) one GFP+ cell trapped in the trapping chamber of row ④; (h) the overall capture efficiency of each outlet. The data presented here is from 3 or 4 runs on CTC-HTECH device; (i) the percentage of the trapped GFP+ cells in every available row in the configuration where the indicated outlet was open (outlet 1 (green), outlet 2 (pink), outlet 3 (blue), outlet 4 (purple), outlet 5 (orange), and outlet 6 (red)).

To begin, GFP-labeled LNCaP-C4-2 cells were diluted into murine whole blood at a concentration of ~50 cells/mL. Outlet 1 was opened and the blood sample was video recorded at the inlet as cells entered row ①. Cells that do not exit row ① can be found in the constriction microchannels or in the trapping chambers. The blood flow passed through row ①and accumulated in the wider channel at outlet 1 waste collection. A GFP+ prostate cancer cell at the

entrance of one constriction channel in row ①surrounded by unlabeled blood cells is shown in Figure 3c. Cancer cells that escaped from row ①were visible at the outlet 1 waste collection (Figure 3d). Blood did not flow into row ② when only outlet 1 was open, due to the air remaining in the channels of rows ②-⑥. Figure 3e shows a GFP+ prostate cancer cell deformed in a constriction channel. Figure 3f shows two cells with one traveling in a constriction channel, and another escaped from the constriction channel and starting to enter the next row of microchannels. Figure 3g shows a GFP+ prostate cancer cell stopped and trapped in a trapping chamber in row ④. Once the GFP+ prostate cancer cell recovers its original spherical shape, the cell occupies the upper space in the trapping chamber, as illustrated in Figure 2. This allows the blood flow to resume through the constriction channels.

In preliminary trials, we observed that some GFP+ cancer cells were still able to deform and pass through the second constriction channel; therefore the CTC-HTECH design was adapted by duplicating the trapping chambers and increasing the quantity of microchannel rows to optimize trapping of the cancer cells. Figure 3h summarizes the results of sequentially selecting a different outlet (1-6) and monitoring the overall trapping efficiency of GFP+ cancer cells. When outlet 1 was open and only row 1 was used for capture, the trapping efficiency was 46.3% (Figure 3h green bar); when outlet 6 was open and rows 1-6 were used for capture, the trapping efficiency was 97.9% (Figure 3h red bar).

Figure 3i summarizes the GFP+ cell capture percentages for each outlet configuration. When only outlet 1 is open (green bar), cells transited only row ① and the capture efficiency of GFP+ prostate cancer cells was less than 50%. When outlet 2 was open (pink bars) cells transited both rows ① and ②. Here, the capture efficiency of row ① was ~55%, the number of captured GFP+ cells in row ② was somewhat less than 20%. We suggest that as the number of rows is

increased, the overall fluidic resistance is also increased and therefore, the trapping efficiency in each row varies. This said, the capture efficiency of row ① when either outlet 1, 2, or 3 was used was 45-55%. The capture efficiency of row ① when selecting either outlet 1, 2, or 3 was less than the capture efficiency of row ① when selecting either outlet 4, 5, or 6. However, the GFP+ cells that escape row ① can be captured by rows ② and ③ at a capturing ratio of ~20% and ~10%, respectively.

When the number of rows active in capture is ≤ 3, the flow rate at the outlet will be higher than when there are 6 active capture rows under the constant pressure mode. Therefore, a limiting factor for the capture efficiency in row ① appears to be the flow rate, with a slower flow rate resulting in more efficient cell capture in row ①. This could explain why the capture efficiency of row ① using outlets 1,2 or 3 was 45-55% (Figure 3i, green bar. row ①, pink bar, row ①, and blue bar, row ①). The configurations using either outlet 4 (Figure 3i, purple bars) or outlet 5 (Figure 3i, orange bars) had a higher capture efficiency of GFP+ cells in row ① of ~65%, while the capture efficiency in rows ② and ③ were similar to that of the configuration using outlet 3. The configuration using outlet 6 (Figure 3i, red bars) utilized all six rows and achieved the highest capture efficiency, ~70% in row ①. Row ② had a similar capture ratio of 15-20% when using outlets 2-6. The configuration using outlet 6 had more GFP+ cells captured in rows ② and ③ than rows ④, ⑤, and ⑥. The overall capture efficiency of all configurations is shown in Figure 3h. Using outlets 5 and 6 reached an overall capture ratio >95%.

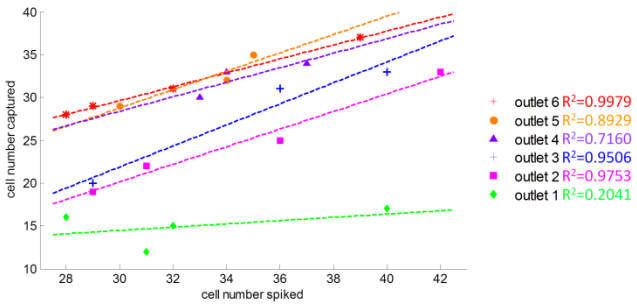

Figure 4. The number of cells captured compared to the number of cells spiked per 0.6-0.7 mL mouse whole blood in different outlet configurations. Results shown are the results testing n = 3-4 different devices at 6 different outlet configurations.

As shown in the results from multiple devices in Figure 4, in each configuration (either open or closed) of outlets 1-6, we plotted the captured cell counts and the spiked cell counts. Each data point represented one experimental result from one device. Opening outlet 6 (red) included all 6 rows of channels, which had the best capture rate. As illustrated by red stars in Figure 4, the outlet 6 overall capture efficiency almost reaches 100% with a high linear correlation value of R^2 = 0.9979. The outlet 5 and outlet 4 also achieved high capture efficiency by comparing the number of cells captured and the number of cells spiked in whole blood sample. The outlet 3 and outlet 2 capture efficiencies were reduced to 70-80%. The consistencies of outlets 2-6 were much better than outlet 1. Since outlet 1 only contained one row of micro constriction channel and trapping chambers, the uncertainty of cancer cells deformation and trapping in row ① caused low capture rate. Even though we used constant pressure mode at inlet, the flow rate will have higher variation if many cells trapped in the row ①. The local increasing flow rate dragged the trapped cancer cells through the trapping chambers. If using outlet 6, the overall pressure drop between the inlet and outlet will be smaller than using the outlet 1. The chance of driving trapped cancer cells from row ① using outlet 6 will be lower than using outlet 1.

Control group: blood cells observation through CTC-HTECH outlet 6

(1) Mouse whole blood without spiked LNCaP-C4-2

In order to estimate the trapping purities of the final CTC enrichment, we used mouse whole blood as a control group through the CTC-HTECH chip using outlet 6. The constant pressure was setup as same as the cancer cells spiked blood samples. As shown in Figure 5a, the RBCs and WBCs can pass through the micro channels and the trapping chambers freely. After ~0.8 mL

of mouse blood passed through the chip, in order to count the amount of the blood cells trapped in the CTC-HTECH device, we switched the inlet to LNCaP-C4-2 culture medium to remove the blood cells that did not trap in the chip. The flow pressure of culture medium was kept constant. After 15 min of rinsing, blood cells were not observed in most of the microchannels (Figure 5b &S2d). Only 17 out of 240 microchannels were found WBCs or lymphocytes trapped in the micro constriction channels as some RBCs were also blocked in the trapping chambers. As shown in Figure S2f, the fluid coming to the reservoir of the outlet 6 also contained littleblood cells. Most of the RBCs were removed in the CTC-HTECH chip.

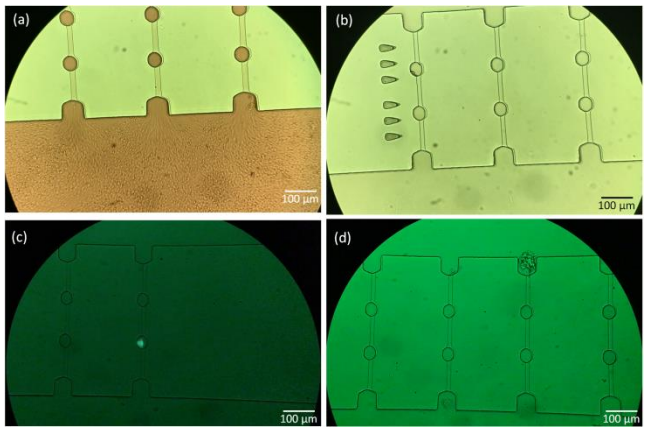

Figure 5. Image of the control group mouse whole blood without cancer cells spiked (a&b), and with cancer cells spiked (c&d) through the CTC-HTECH: (a) whole blood passing through the microchannels; (b) the inlet switched to LNCaP-C4-2 culture medium to remove the blood cells; (c) image of a trapped cancer cellafter 15 min rinsing by LNCaP-C4-2 medium; (d) image ofa microchannel with WBCs/lymphocytes trappedafter 15 min rinsing by LNCaP-C4-2 medium.

(2) Mouse whole blood with spiked LNCaP-C4-2

More control groups with mouse whole blood with spiked cancer cells were performed to estimate the amount of WBCs and lymphocytes remaining in the CTC-HTECH after rinsing with LNCaP-C4-2 culture medium. The LNCaP-C4-2 capture ratio again reached97.3±2.5% (repeated 3 times on 3 devices) after 15 min rinsing. Most of the trapped cancer cells stayed in the trapping

chambers (Figure 5c) while allowing the medium to freely flow through the channels. Similar to the control experiment, almost all blood cells passed through the microchannels. Only 19 out of 240 microchannels were observed with WBCs or lymphocytes trapped in the channel. Exact counting on these blood cells was difficult as they formed clusters. However, based on the size of the microchannels and trapping chambers, we estimated that no more than 100 WBCs or lymphocytes could trap in each microchannel. Therefore, the total numbers of blood cells trapped in these chips were calculated to be less than 2000. This is similar to what we observed when only blood cells were drawn through the chip in our control experiment. Nevertheless, compared to the total number of blood cells in the original sample (~2.4-4.4×10^6 cells of WBCs and lymphocytes), CTC-HTECH has been able to remove millions of blood cells and increase the concentration of CTCs from <1:10^6 to ~1:50.

6.4 Discussion

The CTC-HTECH provides a new size-based CTC entrapment microchip for low-cost and high-throughput analysis of cancer cells in whole blood samples. The CTC-HTECH device with six rows of constriction channels and trapping chambers captured over 95% of GFP+ LNCaP-C4-2 metastatic human prostate cancer cells used as surrogates for human CTCs. The sample preparation was minimal as these cancer cells were captured from whole blood; the microchip run time was ~30 min for a 1.2 mL blood sample. Compared to magnetic particles with antibody methods, such as FDA approved CellSearch system, our CTC-HTECH reduced the lengthy sample pre-processing and long analysis time of ~4-6 hours. There is no requirement for antibodies, a high-speed camera, or sophisticated image analysis; the data can be collected using the video features of a smartphone.

Size is one of the major biophysical attributes of cells that have been utilized to separate CTCs

from blood cells. Different microfluidic chips in PDMS, polycarbonate, parylene-C, and some other biocompatible polymers [273] have been designed and fabricated to isolate larger epithelial tumor cells from smaller blood cells. The geometry and dimension selection of the size-based trapping methods are key to achieve desired CTC trapping efficiency and purity. In microfilters, for example, an array of small holes with a size around 8 μm can capture CTCs while allowing the majority of blood cells to pass through [274]. Y. Chen's group developed a conical shaped hole to slightly increase the pressure once CTCs which are trapped in the small holes started to deform to enhance capture purity [275]. From their simulation and experiment results on MCF-7 cells captured in cone-shaped hole, the blood flow pressure facilitated leukocytes to escape from the holes, which resulted in an increased capture efficiency and purity with 6.5-8.0 μm diameter cone-shaped hole [275]. However, the results showed that the thickness of this microfilter also significantly affect the capture purity because more blood cells will accumulate and clog the cone-shaped holes if using a thicker microfilter. With this additional variable to the microfilter, finding the optimized parameters to achieve a balancing between capture efficiency and purity of the microfilter becomes challenging. A recent study from S. Lee's group demonstrated a flow-restricted microfluidic channel with an array of trapping cavities that reached 97% trapping rate with single MDA-MB-231 cells spiked in mouse blood [276]. The continuous blood flow in their delivery channel kept the spiked MDA-MB-231 cells staying in the trapping channel, which had less pressure to force the cancer cells passing through the constriction regions. However, the microchannel array still suffers from possible clogging when more CTCs are trapped in the same constriction. Therefore, a better CTC enrichment with micro constriction channels and trapping chambers requires proper selection size for CTCs with less chance of cells clogged in a single trapping cavity.

The CTC-HTECH device, presented here, operates on an enrichment principle whereupon large cancer cells are captured at an “equilibrium point” cavities (trapping chambers) positioned in between constriction microchannels, which allows the blood continue flowing through either the same channel or neighboring ones. It is also important to note that all 40 parallel channels between two adjacent rows experience the same pressure drop. The CTC-HTECH system is operated under constant pressure for all scenarios described earlier. As a result, the overall flow rate decreases as the more number of rows are utilized to trap CTCs. In each microchannel, the Reynolds number in constriction channel is around 2.77. Based on the dimension of each channel, including constriction channels and trapping chambers, the pressure drop across each channel is about 77 mbar. Assuming all channels are open and no large cell is trapped, the total fluid resistance across one row will be around 9×10^{3}Pa·s/(μL). In the case of using outlet 1, the low fluid resistance leads to higher flow rate which causes more cancer cells escape from the chip. Therefore, using only a couple of rows will significantly decrease the number of trapped CTCs. Also, when only one row is used and cell continue to trap, the flow rate in neighboring trapping chambers that are still open will experience a higher increase in flow rate when we compare this case to a 6 row configuration. In a 6 row configuration, the change in the flow resistance due to cell trapping has less effect on the overall flow rate compared to case that only one row is used. Furthermore, using less number of rows reduces the probability of experiencing to move through multiple trapping chambers which in turn causes loss in enrichment efficiency. Since more number of cell are trapped in the first row, one alternative design that can be explored in the future generations is to increase the number of parallel channels in the first row and decrease the number for the subsequent rows without changing the overall footprint of the chip.

6.5 Conclusions

This low-cost, label-free, size-based CTC-HTECH device is able to effectively enrich the CTC sample in prostate cancer cell line spiked blood samples. The chip was able to achieve a trapping efficiency of 96%. From out of 42 cancer cells only one was not captured. This is significant as the number of CTCs has been shown to be diagnostic or prognostic marker for tumor. The chip enables accurate enumeration of CTCs in blood and makes it a reliable tool for clinical settings for rapid CTC capture and subsequent counting. The difference between cancer cell line spiked in blood to patient CTC were discussed in previous publications [235, 277-279]. The blood cell size distribution, especially WBCs, lymphocytes, or other blood cells in peripheral blood from one patient or between different patients could vary from 8-20 μm[278, 280]. The deformability differences between cancer cells and blood cells can also be utilized in separating WBCs or lymphocytes [212]. It is likely that the chip once using patient samples could require some adjustment in design to ensure high efficient enrichment. However, out chip topography is very flexible and can be easily adopted to the clinical needs. We can envision new generations of this chip in which channels can be fabricated to have different sizes for both constriction regions and the trapping chambers. This may create a second degree of separation within the same chip. Also, more number of channels can be added to each row to make it more suitable for clinical samples where more number of CTCs may be present. We can also use CTC-HTECH chips in series whether having identical or different channel dimensions. CTC-HTECH has the potential to be connected in series as multi-stage multi-cycle CTC enrichment.

7. Post-enrichment circulating tumor cell detection and enumeration via deformability impedance cytometry

Ghassemi, P., Ren, X., Foster, B. M., Kerr, B. A., & Agah, M. (2020). Post-enrichment circulating tumor cell detection and enumeration via deformability impedance cytometry. Biosensors and Bioelectronics, 150, 111868.

7.1 Introduction

Cancer is a global health concern and one of the leading causes of death worldwide [281-283]. Mortality is dependent on how early one can detect the cancer and receive treatment. Current techniques for cancer detection and diagnosis are expensive, invasive, complex, and have slow response time, considering that they generally require specific equipment and trained experts to screen and diagnose cancer [284-288]. Therefore, there is a need for a simple, easy-to-use, and cost-effective techniques for early cancer diagnosis and monitoring treatment efficacy. Cancer progression is currently analyzed using tissue biopsies. Tissue biopsies are invasive and can be ineffective in terms of understanding the metastatic potential, disease progression, and treatment effectiveness. Additionally, biopsies require highly skilled personnel to conduct immunohistochemistry (IHC) studies, IHC staining, and readings. Recently, researchers have proven that analyzing circulating tumor cell (CTC) number is a viable substitute for tissue biopsies as a non-invasive diagnostic tool. CTCs are tumor cells that circulate throughout the body via the blood and lymphatic system and can potentially metastasize to form a secondary tumor at other distinct locations [289-292]. CTC count can be a good indicator of cancer prognosis, where decreasing CTC counts over time has shown to indicate a successful treatment or therapy [289-292]. The primary issue with CTC-related tests is their rarity as there are 1-100

CTCs in 1 mL of blood compared to about one billion blood cells in the same volume. Therefore, to count CTCs or to further analyze them, it is important to establish reliable enrichment and isolation methods.

Microfluidic technologies for cellular and bodily fluid analyses are advantageous in terms of cost, size, sample size requirement, and minimal reagent consumption [293-297]. Therefore, various microfluidic devices have been designed and fabricated for the study of CTCs [277, 298-300]. Research was done to enrich blood samples and isolate CTCs. CTC analysis can be divided into two main categories: label-based and label-free. Label-based methods rely on the binding of surface protein markers of CTCs and molecular markers such as antibodies, transferrin, and peptides. These techniques utilize nanoparticles to bind to CTCs for positive sorting/isolation and bind to leukocytes for negative sorting/isolation. The epithelial cell adhesion molecule (EpCAM) is the most commonly used biomarker but it cannot capture the entire CTC population in blood as some do not express EpCAM [298, 300-302]. CellSearch, which relies on the EpCAM biomarker to detect CTCs, is currently the only FDA-approved CTC isolation technique but has limitations because CTCs go through an epithelial-mesenchymal transition (EMT), which decreases the expression of EpCAM and other epithelial markers [222, 303, 304].

Label-free technologies rely on biophysical properties of cells such as size, density, deformability, and dielectric properties. Some label-free isolation techniques include size/deformability-based micropores [305], inertial microfluidics [269], acoustophoresis [306, 307], magnetophoresis [308], and dielectrophoresis [309, 310]. These techniques are advantageous because they do not rely on extensive pre-processing and incubation times, as well as being cost-effective. Label-free CTC isolation techniques have improved greatly over the last

decade and typically are tested by spiking beads, murine blood, or human blood samples with cancer cells. Antfolk et al., for instance, has shown that acoustophoresis technology can capture ~95% of spiked cancer cells in RBC-lysed whole blood with a purity of >97% at a flow rate of 100 μL/min [306]. Our group has also used a size-based microfluidic chip with sequential constriction channels separated by entrapment regions to capture ~96% of cancer cells spiked into whole murine blood at a flow rate of ~2.5 mL/hr [311]. Researchers have begun to create hybrid technologies too that include both label-free and label-based methods to improve efficiency. For example, Toner's group created the CTC-iChip that first uses deterministic lateral displacement to remove most blood cells, followed by negative filtration of the remaining WBCs through magnetophoresis utilizing anti-CD45 and anti-CD66 beads [308].

There is a wealth of knowledge demonstrating that the CTC count can be used to diagnose cancer and evaluate the prognosis and progression of tumors [221, 304, 312, 313]. For instance, Miller et al. evaluated CTC count by analyzing 7.5 mL of whole blood from breast, prostate, or colorectal cancer patients using CellSearch. They determined that for metastatic breast and prostate cancer, the cutoff value for favorable survival is 5 CTCs per mL, while in metastatic colorectal cancer patients it was 3 CTCs per 7.5 mL of blood [304]. The current practice of CTC enumeration, regardless of the enrichment technique, relies primarily on fluorescent microscopy where CTC-specific (such as EpCAM+/CK+/CD45-) antibodies conjugated to fluorescent dyes attach to cells of interest [264, 314-316]. As a result, even if the enrichment technique is label-free, postprocessing of CTCs is not. Microfluidic impedance cytometry, which relies on cellular bioelectric properties, can be an alternative approach to fluorescent microscopy for rapid enumeration of CTCs [317, 318]. Furthermore, blood cells are in general smaller than CTCs, indicating that CTCs and blood cells when passing through channels with dimensions less than 8

μm will generate two distinct timing profiles. The deformability of cells through such constriction channels has been used by our group and others to distinguish tumor cells from non-tumorigenic cells [66, 118, 119] as well as control and drug-treated tumor cells [65]. Integration of microfluidic impedance spectroscopy with constriction channels provides information on comprehensive biophysical attributes of cells such as size and mechanical and electrical properties of cells [58, 65, 126-128]. Here we, for the first time, demonstrate that such unique integrated platforms can be used to rapidly enumerate CTCs in blood samples and generate/process the data in less than one minute, thus eliminating fluorescent tagging and extensive video analysis. Both prostate and breast cancer cell lines were used in this study to see if the bioassay can be employed for more than one tumor type and if it can distinguish the type of tumor through biophysical properties. In this microfluidic CTC analyzer, postprocessing of the data is also automated to detect the presence of CTCs, their count, and their origin. Two different chips are presented. In one, the electrodes are part of the disposable chip providing more sensitivity. The other separates the electrodes from the disposable chip to reduce the fabrication cost while still allowing CTC enumeration.

7.2. Materials and Methods

7.2.1. Cell Culture and Sample Preparation

To test our microfluidic biosensor, we used single-cell suspensions of both breast and prostate cancer cell lines (MDA-MB-231 and LNCaP C4-2, respectively). Breast cancer cell line MDA-MB-231 (passage #8, American Type Culture Collection (ATCC), provided by Dr. Yasmine Kanaan, Howard University College of Medicine) was grown in F12:DMEM (Lonza, Basel, Switzerland) with 10% fetal bovine serum (FBS), 4 mM glutamine and penicillin-streptomycin (100 units per mL). Prostate cancer cell line LNCaP-C4-2 (passage #11, provided

by Dr. Bethany Kerr, Wake Forest School of Medicine) expressing green fluorescence protein (GFP) by lentiviral transduction, was grown in RPMI-1640 (L-glutamine) with 10% FBS and 1% PenStrep (100 U/mL penicillin and 100 μg/mL streptomycin). Both cell lines were grown in T-25cm^2 culture flasks at 37°C in a 5% CO_2 in air atmosphere until cells were ready for subculture. The morphology of the cells was observed before trypsinization. The cells were then detached from the flask with a trypsin-EDTA solution (Sigma Aldrich). After trypsinization, cells were spun down in the centrifuge and rinsed with phosphate-buffered silane 1x (PBS). The cells were then spun down and resuspended in PBS for experimentation. Before experimentation, cell viability was observed at 100% via trypan blue exclusion test. For experimentation with spiked blood samples, murine whole blood was diluted with PBS (1:5 ratio), and the blood sample is spiked with cancer cells at ~10^4 cells/mL. Murine whole blood was collected under Wake Forest School of Medicine IACUC approval #A15-221 from the vena cava of anesthetized mice into 1M ethylenediaminetetraacetic acid.

7.2.2. Device Fabrication

To fabricate the polydimethylsiloxane (PDMS) microfluidic channels, a master mold is fabricated onto a silicon wafer. Two layers of SU-8 (SU-8 3005 and SU-8 3025, MicroChem, Newton, MA) are patterned onto the wafer via photolithography (Figure 1A). SU-8 3005 was used to build the constriction channel with 8 μm height, while SU-8 3025 was used to build the remaining channel feature with a 25 μm height. The resulting mold is coated with tridecafluoro-1,1,2,2-tetrahydrooctyl-1-trichlorosilane (TFOCS, Fisher Scientific) to promote the easy release of PDMS. PDMS base and curing agent (10:1 weight ratio) are stirred generously and poured onto the master mold and cured at 65º C for 24 hours (Figure 1B and 1C). For the “on-chip” case, the resulting PDMS channels are then bonded directly onto the planar electrodes using

plasma-activated bonding (Figure 1E). The alternative "off-chip" device involves bonding the channel onto a 100 μm thick glass slide (#0, Electron Microscopy Sciences, USA), which acts as a passivation layer between the electrodes and microfluidic channel (Figure 1F). Details of the fabrication process have been previously published by our lab [319, 320] and is illustrated in Figure 1. The cross-section of the constriction across the length of the channel for both cases is depicted in Figure 1E and Figure 1G. To fabricate the electrode sensors, a pyrex glass wafer is patterned with photoresist (S1827, MicroChem, Newton, MA) through photolithography. Metal deposition through electron beam evaporation of chrome (40 μm), an adhesion layer, and gold (100 μm) is done onto the patterned glass wafer. The glass wafer is then submerged into acetone for metal liftoff and diced to create individual electrodes (Figure 1D).

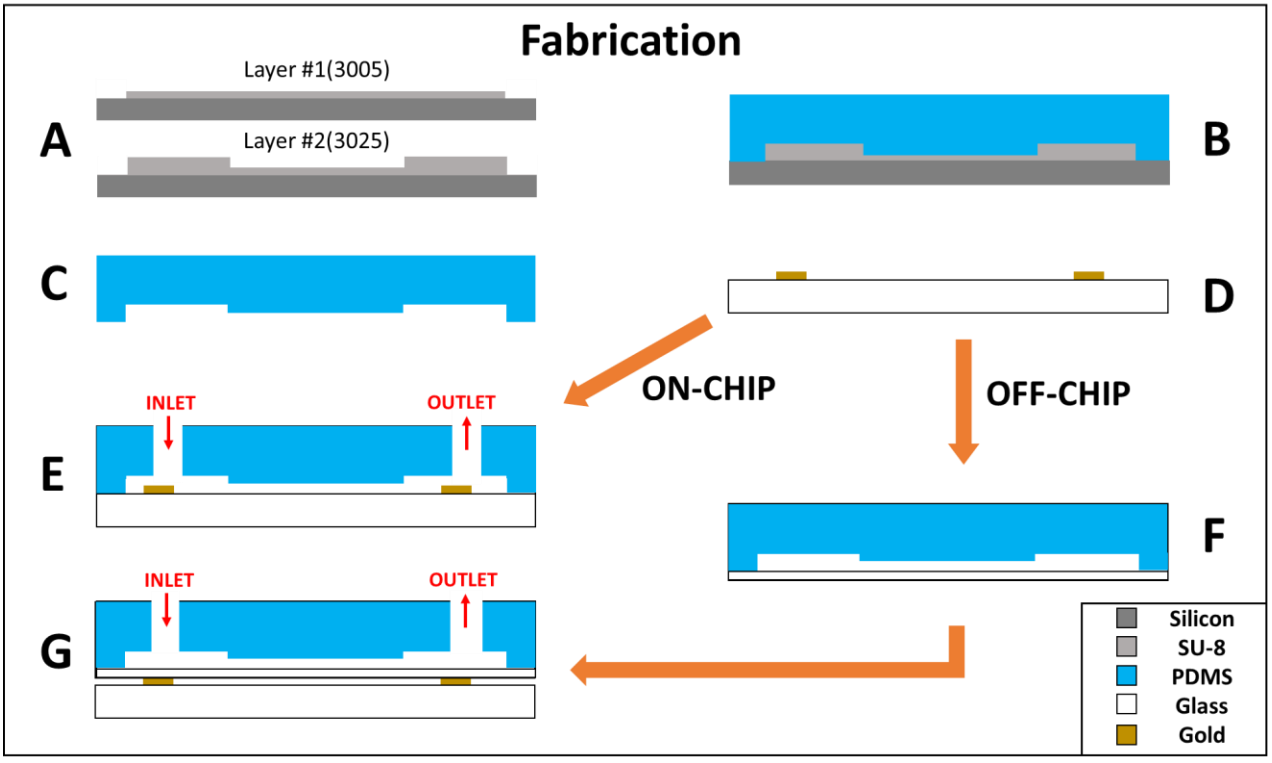

Figure 1. Fabrication steps(**A**-**G**) of both (**E**) ON-CHIP and (**G**) OFF-CHIP devices. Device perspective is the cross-section across the length of the constriction channel.

7.2.3. Channel Design and Experimental Setup

The microfluidic device consists of two main channels, delivery, and constriction, to prevent cell accumulation at the entrance of the constriction and prohibits clogging. The constriction channel has a 6 μm-width, 8 μm-height, and 500 μm-length. Both electrodes extend approximately 60 μm from the entrance and exit of the constriction channel.

The cell suspension is inserted in the delivery channel and flow is induced by applying a negative pressure, via a Harvard Apparatus syringe pump, at the other end of the delivery channel. A secondary negative pressure is applied using the syringe pump at the outlet of the constriction channel to create flow through the constriction. Once a cell has entered the constriction channel, the cell blocks the negative pressure the delivery channel experiences and prevents other cells from entering the channel until it has passed through the constriction. The device was able to collect impedance peaks of cells that can reach 100+ cells per minute.

As cells transit through the constriction channel, impedance information is obtained using a Zurich Instruments HF2IS Impedance Spectroscope. The impedance spectroscope inputs an AC voltage of 1V signal at eight different frequencies ranging from 500 Hz to 1 MHz simultaneously. To cross-verify the transit of cells in the constriction channel with the impedance data, we recorded high-speed videos at 100 frames/second.

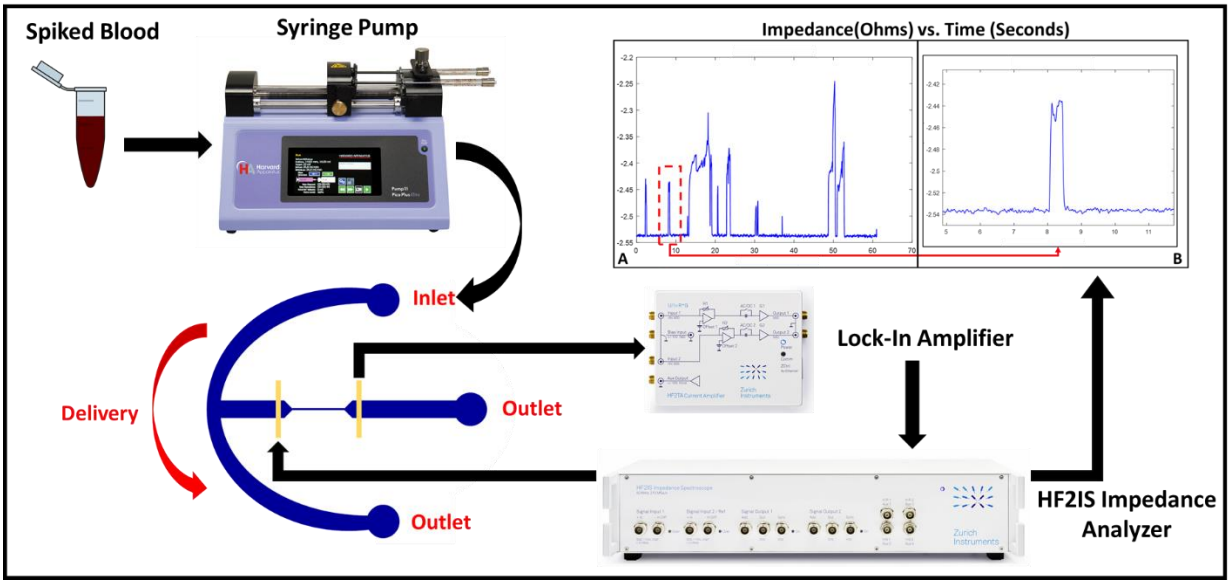

Figure 2. The experimental setup for CTC analysis by deformability impedance spectroscopy. The impedance results reflect the ON-CHIP device where we evaluate MDA-MB-231 cells spiked in murine blood.

7.3. Results

7.3.1. Data Collection

Figure 2 demonstrates the experimental setup where the sample enters the device and transits through the delivery, and consequently the constriction channel via a negative pressure applied at the outlet to initiate the flow. The device has an embedded pair of planar electrodes that extend outside the entrance and exit of the constriction channel. Therefore, impedance can be measured across the constriction channel, so when a cell enters the channel, we can obtain the impedance of the cell along with the surrounding medium (murine blood or PBS). CTCs within the constriction channel dominate the impedance in the channel compared to the surrounding medium, so we can obtain a clear peak that represents the CTC transiting through the channel. Figure 3A illustrates a sample run, where many (enriched) cells are observed within a minute. The transit of a single cell is shown in Figure 3B, where a cell is represented by a single peak. For the "on-chip" case, as PBS alone passes through the constriction, there is a constant baseline, which is shown by the red line in Figure 4A. However, for the sample of PBS spiked with

cancer cells (see Supplementary Video S1), once a cell enters and transits through the constriction channel, the impedance deviates from the baseline towards a peak and returns to the baseline after transit. This is illustrated by the blue line in Figure 4A. In the case of blood and blood spiked with cancer cells (see Supplementary Video S2 and S3, respectively), the resulting impedance profile is the same, but the baseline is noisier (shown in Figure 4B) because of the passage of blood cells through the constriction. Figure 5 shows the transit of a cancer cell from a spiked blood sample, where blood cells (circled in red) surround the cancer cell (circled in yellow), as it transits through the constriction channel. Figure 5 begins with the cancer cell before deformation (1), then the cell beginning to deform into constriction channel (2), followed by the cell transiting through the constriction channel (3), and lastly the cell after exiting the constriction (4). The blood cells impact the baseline and noise level of the signal, however, the impedance profile of cancer cells transiting through the constriction channel is robust.

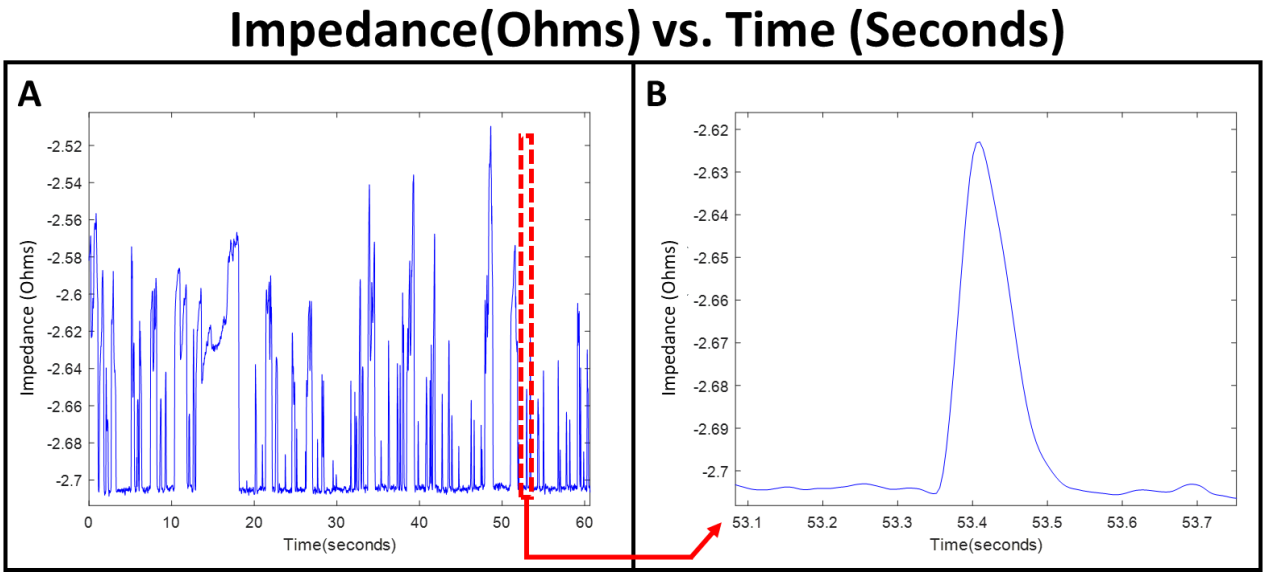

Figure 3. Sample impedance plot of the ON-CHIP configuration evaluating MDA-MB-231 cells spiked in murine blood during a single run (**A**) and an example of the impedance of a single cancer cell (**B**).

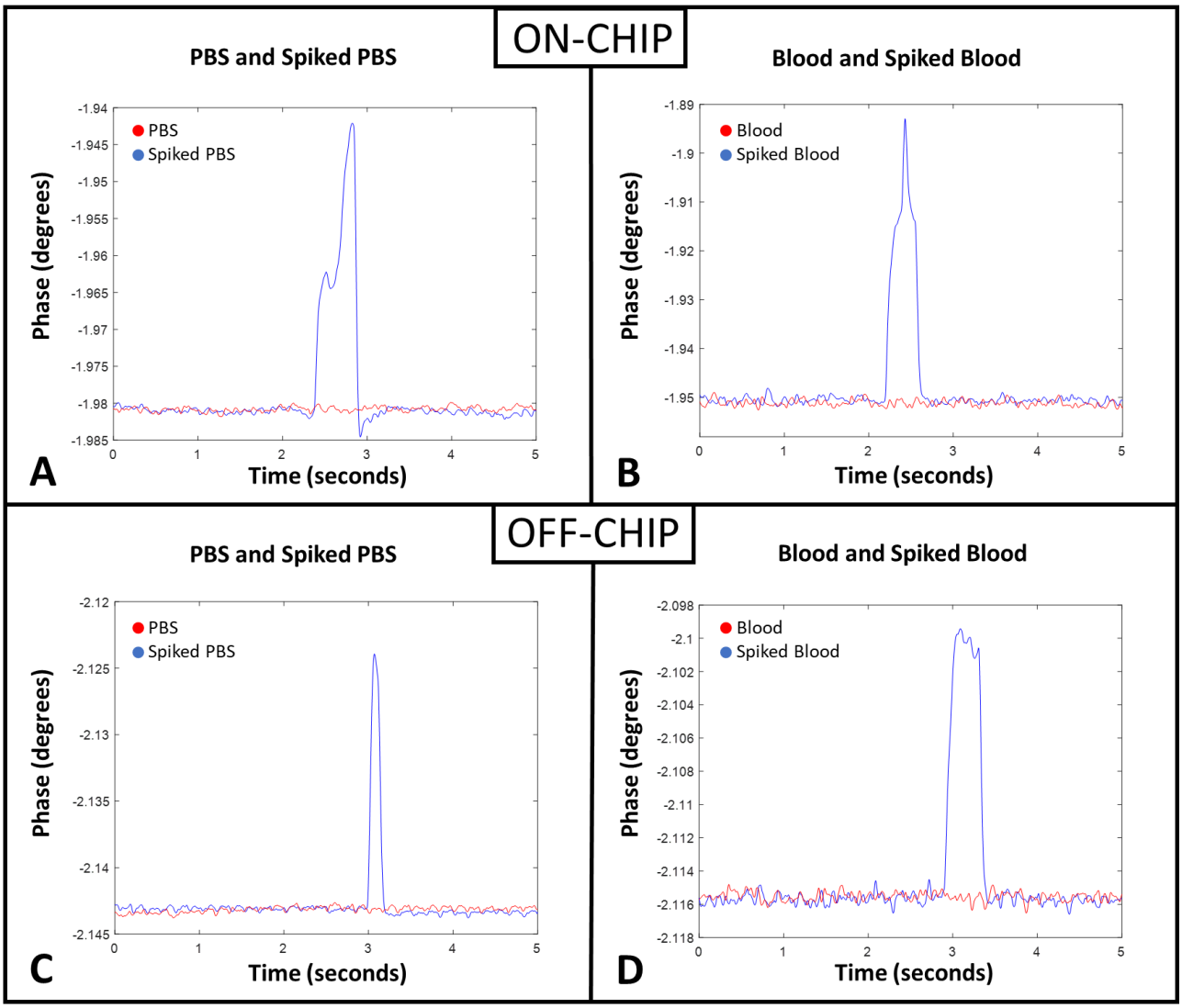

Figure 4. Representation of impedance measured across the constriction channel. (A) ON-CHIP and (C) OFF-CHIP sample of impedance (Phase at frequency = 50 kHz) with only PBS (red) and PBS spiked with MDA-MB-231 (blue). (B) ON-CHIP and (D) OFF-CHIP sample (Phase at frequency = 50 kHz) with only murine blood (red) and murine blood spiked with MDA-MB-231 (blue).

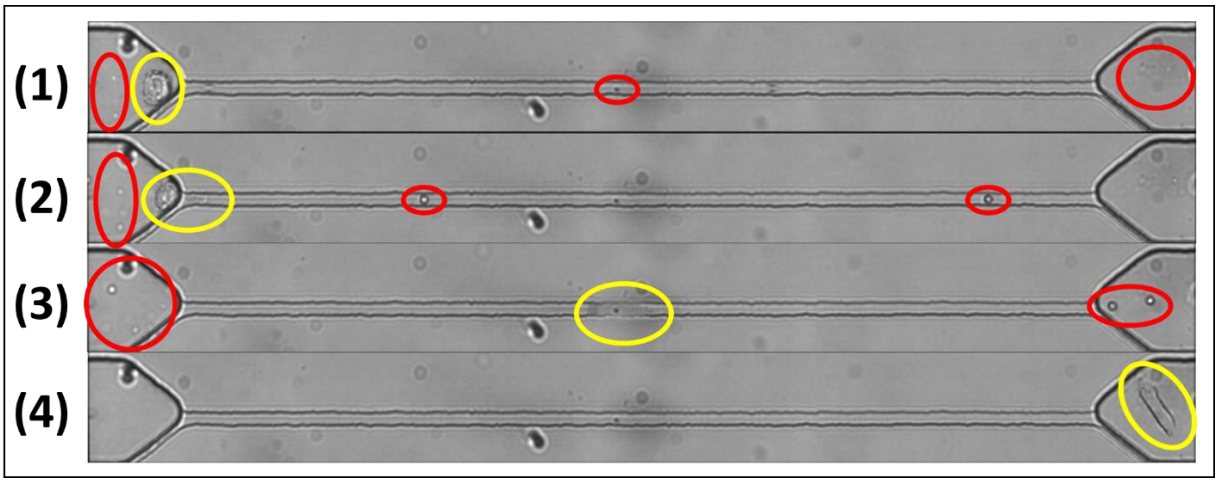

Figure 5. Transit of a MDA-MB-231 cell (circled in yellow) through the constriction region. (1) Cancer cell before deformation, (2) cell beginning to deform, (3) cell in constriction channel, and (4) cell after the constriction. The surrounding white and red blood cells indicated by the red circles.

The impedance profiles for the "off-chip" device are shown in Figure 4C and 4D, where the baseline is clearly noisier compared to the "on-chip" device. Despite the loss of sensitivity due to the passivation layer, the cells of interest are still easily detected for both PBS (Figure 4C) and blood (Figure 4D) spiked with cancer cells. Although the noise level has increased in the spiked blood sample, the biosensors were sensitive enough to detect 100% of the cancer cells that transit through the constriction channel in both "on-chip" and "off-chip" scenarios.

7.3.2. Data Analysis

The impedance peak is a representation of the electrical properties of the cell and can be used to count, evaluate, and distinguish these cells of interest. We obtained the impedance results of breast and prostate cancer cells individually spiked into PBS and whole murine blood for both the "on-chip" and "off-chip" cases. Each experiment was repeated on multiple devices to reduce the effects of device-to-device variation. Impedance data were collected in an automated fashion utilizing a MATLAB script to collect peaks with respect to the baseline. The threshold for determining peaks was any peak greater than two times the maximum noise variation of the sample without spiked cancer cells.

To evaluate the impedance data of the cell populations, we plotted histograms to show the distribution of magnitude and phase. Histograms were used to evaluate the cell population rather than the average/standard deviation since histograms illustrate the distribution of cells and reveal outliers that can influence the data. We have collected magnitude and phase data for different frequencies for every cell with redundant results, so we present data from one single frequency for each scenario for the purpose of brevity.

For the on-chip experiments, we evaluated the magnitude at a frequency of 5 kHz, which typically represents a combination of cell membrane properties and other biophysical properties such as cell size [44, 45, 48]. Figure 6A illustrates the histogram profile of magnitude for both MDA-MB-231 and LNCaP C4-2 spiked in PBS and murine blood. From these histogram plots, there is a clear difference between the two cell populations spiked in PBS and murine blood. For example, the cell magnitude of MDA-MB-231 and LNCaP C4-2 cells spiked into PBS at 5 kHz shows how the MDA-MB-231 cells have a bimodal distribution, where the LNCaP C4-2 cells have a unimodal distribution. This is also consistent with both cell lines spiked into the murine blood.

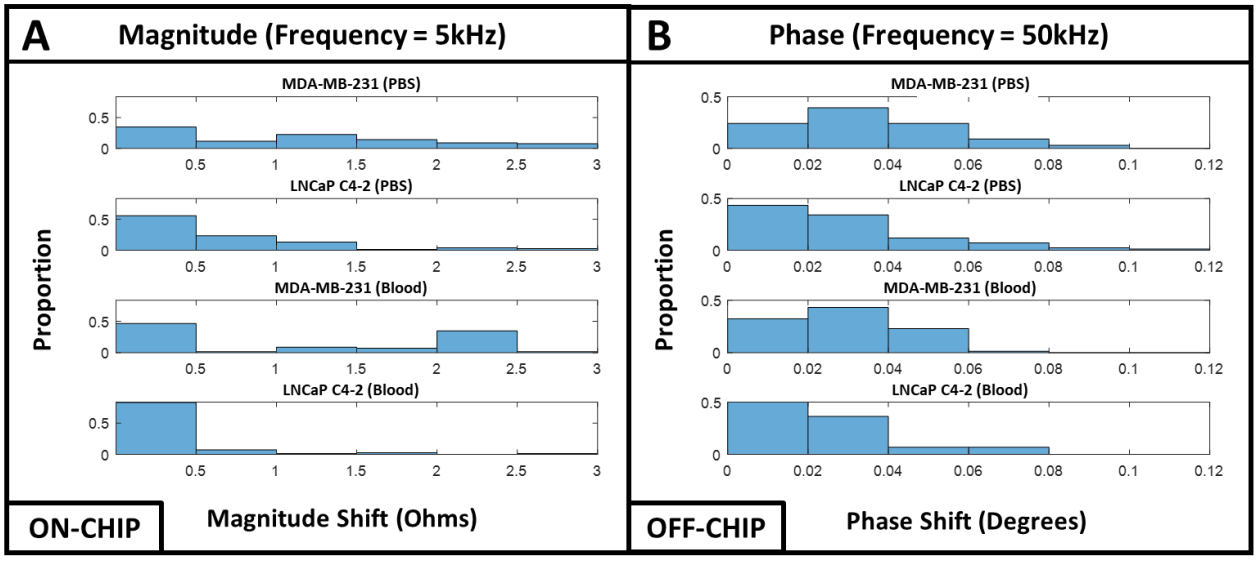

Figure 6. (A) ON-CHIP histogram representation of MDA-MB-231 and LNCaP C4-2 cells spiked in PBS and blood for magnitude measured at a frequency of 5kHz. (B) OFF-CHIP histogram representation of MDA-MB-231 and LNCaP C4-2 cells spiked in PBS and blood for phase measured at a frequency of 50kHz.

For the off-chip experiments, we evaluated the phase data at a frequency of 50 kHz for both cell lines spiked in PBS and murine blood, which is depicted in Figure 6B. Just as described for the on-chip experiments, the histograms reveal differences in the cell populations for this scenario too. For example, the phase values at 50 kHz show how the MDA-MB-231 cells and LNCaP C4-2 cells both have varying distributions. For the case of the MDA-MB-231 cells in PBS, there is a chi-squared distribution, however, the LNCaP C4-2 cells in the same scenario have a right-skewed distribution. Using the same frequency but spiked in blood, the MDA-MB-231 and LNCaP C4-2 cells maintain their normal and right-skewed distribution, respectively.

7.4. Discussion

CTC detection and enumeration are clinically important as it can be used to detect early cancer metastasis, predict prognosis, and monitor response to treatment. Typically, methods for enumerating CTCs rely on surface markers, such as the epithelial cell adhesion molecule (EpCAM), however, a sub-population of CTCs go through epithelial-mesenchymal transition (EMT) that changes the expression of cell surface markers [221, 304, 312, 313]. Thus, label-free methods are advantageous due to their reliance on biophysical characteristics rather than surface markers. Current label-free methods of enumeration cancer cells rely on fluorescent microscopy, but this method requires expensive pre-processing for fluorescent tagging and extensive post-processing of videos to observe and enumerate the cells [264, 314-316]. Impedance flow cytometry methods have been developed in research [58, 149, 321-323] and commercially by companies such as Amphasys [324]. Despite these current methods, no technologies have attempted to detect cancer cells of different origins within blood samples. We report a system

that can not only enumerate cells in blood samples but can also identify different types of cancer based on their bioelectrical properties.

Biophysical characteristics of cells extracted through label-free impedance analysis can be used to study cells in suspension for biological research and in blood for clinical applications [58, 149, 317, 318, 323]. Electrical properties of cells can be used as a powerful biomarker to identify cells, including CTCs because they provide a complex representation of cells by probing them at different frequencies. Higher frequencies provide information about the contents of the cells, while lower frequencies provide information about the cell membrane and surface properties. This technique has been widely used to identify and distinguish a variety of different cells, including healthy, diseased, and drug-treated cells [44, 45, 48].

Giaever and Keese first introduced electric cell-substrate impedance sensing (ECIS) and studied adherent mammalian fibroblasts by measuring their response to an AC signal [132]. ECIS techniques were then used as a label-free method to measure cell electrical properties, growth and proliferation, motility, and response to chemical compounds [131-135]. Throughput of ECIS sensing of cells was improved using microelectrode arrays, where an array of electrode pairs can measure impedance in up to hundreds of individual locations simultaneously [54, 325-327]. Our lab has utilized ECIS to study the effects of anti-cancer drug SAHA on two breast cell lines [328], to study various nano-scale coating of electrodes [329], and to distinguish basal and claudin-low subtypes of triple negative breast cancer cells [330]. Impedance spectroscopy has not only been used in research but also in commercialized settings to monitor cellular behavior as a replacement to more conventional fluorescence microscopy. For instance, commercial ECIS-based techniques developed by companies such as xCELLigence and Applied Biophysics have developed label-free assays to continuously monitor live cell proliferation, morphology,

and viability [331-334]. Limitations of ECIS render this method irrelevant for some clinical applications because ECIS requires the cells to be adherent for its electrical properties to be probed for their impedance values. Lengthy experimentation time is another issue, but even more limiting is the fact that ECIS is generally used for studying cell populations (thousands of cells) and CTCs that are isolated range from a few cells to up to one hundred, in rare cases, cells per mL of blood. To alleviate these issues, electrodes have been integrated into microfluidics to study the electrical properties of particles flowing through microchannels [58, 149, 321-324, 335]. Ayliffe et al. introduced the first microfluidic device with embedded electrodes to obtain bioelectrical information on single cells [335].

Constriction-based microfluidics for studying cell samples can provide mechanical properties of cells by studying transit times through the deformation channel. Cell mechanical proprieties are evaluated by observing the time it takes for a cell to enter (entry time) and transit (transit time) through the constriction channel [57, 116]. Our group has used constriction-based microfluidics to distinguish cancer and normal cells through repetitive deformation of cells [65, 66, 118, 119]. The approach was then extended to trap and enrich CTCs in whole blood [311]. Utilizing constriction-based microfluidics is advantageous compared to alternative label-free methods such as atomic force microscopy [120] and optical stretching [23, 117].

Embedding electrodes in constriction-based devices provides impedance data that can be used to both obtain and evaluate electrical and mechanical properties simultaneously. Impedance peaks represent cell electrical properties, and peak widths represent cell transit time, which is dependent on cell deformability, and both parameters are influenced by cell size [58, 65, 126-128]. Using impedance data to obtain cell timing information alleviates issues experienced when obtaining cell transit times through video analysis. Typically, extensive post processing is

needed to study high-speed videos frame-by-frame to capture timing data, whereas transit time can be simply obtained through peak widths. Obtaining this timing information from impedance can also be automated, which exponentially decreases post-processing times. In our control experiment where only blood sample was moving through the channel, the cells moving very fast without deformation and hence no considerable peak was generated beyond the noise level. We simply used a signal-to-noise ratio of 2-to-1, and we were able to detect all cancer cells without incorrectly identifying any blood cell as a tumor cell. Because we can detect all cancer cells regardless of origin in a blood sample, our biosensor can be used subsequently to established CTC isolation technologies that have a higher capture rate but lower purity. Also, an expanded higher throughput version of this device multiple constriction channels in parallel can be employed that further approaches a clinically-ready device.

This is the first system to use constriction-based impedance data to evaluate cancer cells in blood. Spencer et al. has previously conducted microfluidic impedance cytometry on tumor cells in blood, however, the samples they compared were blood spiked with beads, and breast cancer cells (MCF-7) spiked in varying counts of white blood cells yielded from lysed whole blood [318]. Although they were able to detect the cancer cells within a blood sample, their results have some false positives of MCF-7 cells, and they do not indicate the identification of different types of cancer cells. The ability to identify different types of cancer is valuable in clinical applications because it can potentially be used to replace the more invasive and potentially dangerous biopsies, and imaging tests, such as a computerized tomography scans, magnetic resonance imaging, positron emission tomography scans, or X-rays [336-339]. Our system identified cancer cells from two different origins spiked in murine blood samples; however, its clinical applicability needs to be verified by processing blood samples from patients with

different tumor types. Additionally, there is a potential for false positives when testing patient samples due to non-blood and non-tumor cells that circulate throughout the blood, such as circulating epithelial cells [313]. There may be cases that produce impedance peaks and phase shifts comparable to those of CTCs. If that occurs, we may need to combine the approach presented in this paper with our previous work in which we employed microfluidic chips with multiple constrictions. Our work has shown that we can distinguish between normal and cancer cells at the single cell level with more than 90% accuracy when using sectional cell transit velocities and bioimpedance information when cells move through repetitive deformations [65, 66, 118, 119, 129]. Nevertheless, the results presented here establishes the foundation that microfluidic deformability assay equipped with embedded electrodes can be used to monitor the presence of CTCs in blood samples. The measured sensitivity is high enough that allows the electrodes to be positioned off-chip and be reusable to lower the cost of the assay.

7.5. Conclusions

To conclude, we developed a label-free constriction-based CTC detection and enumeration assay coupled with sensors to conduct impedance spectroscopy on murine blood samples spiked with breast and prostate cancer cells. From the impedance data and the corresponding video analysis, we were able to determine that readily distinguishable electronic signals generated by our chips correlate with the passage of cancer cells through the constriction channel. Tumor cell transitioning through the constriction channel are represented by peaks that were collected using an automated peak detection script using MATLAB. In addition, we were able to distinguish breast and prostate cancer cells in murine blood samples, demonstrating that this system can potentially be used for a variety of cancer cell types. The current design dimensions can easily be modified to allow our system to be used on human blood samples. Throughput of this device

will be improved in future generations by adding multiple channels in parallel. If needed for more heterogeneous cell populations, information regarding the mechanical properties of cells, such as transit times, can also be extracted and employed for more accurate determination of CTCs, their clusters, or their origins. To conclude, the biosensors mentioned in this paper show promise for label-free detection and enumeration of CTCs after currently established CTC enrichment techniques.

Supplementary Materials: Video S1: MDA-MB-231 spiked in PBS, Video S2: Murine blood, Video S3: MDA-MB-231 spiked in murine blood.

8. CTC-CARE: Constriction Assisted Rapid Enrichment of Circulating Tumor Cells

8.1. Introduction

Circulating tumor cells (CTCs) are cells that have dissociated from a solid tumor and entered the vascular system. These cells circulate throughout the bloodstream and can form metastatic tumors elsewhere in the body. Assays evaluating CTCs in human blood have shown promise as a biomarker for early diagnosis, assessment of disease recurrence and as an indicator of cancer metastasis [72, 75, 340-343]. Also coined as a liquid biopsy, these assays are typically minimally invasive, rapid, and low-cost compared to the standard practice of tissue biopsies and other diagnostic tools [74, 75, 277, 341, 344]. CTC enumeration and analysis is a proven method to evaluate cancer prognosis, monitor progression, analyze therapeutic response and is a predictor of patient survival. Counting CTCs provides predictive prognostic information however downstream molecular characterization gives further insights into the tumor cell biology of patients [345-349]. Additionally, analysis of CTC biophysical and molecular properties can be useful for developing and assessing personalized therapies[346, 350-352].

Challenges exist for CTC-based assays due to their rarity, where there are typically 1-10 tumor cells per mL of blood compared to billions of surrounding blood cells in the same volume. In addition to their rarity, the heterogeneity of CTCs between patients of similar tumor origin as well as intra-patient tumor cell discrepancies make it more difficult to identify [72, 342-344]. To combat these issues, researchers have developed several technologies that enrich blood samples and isolate CTCs for further studies and analysis. Microfluidic-based technologies have commonly been utilized for these assays due to their low-cost, size and portability, minimal reagent requirement, rapid prototyping abilities, and advantageous fluidic physics that exist at the

micro-scale [235, 353-355]. CTC enrichment technologies in microfluidics can be broken down into label-based and label-free techniques, which is shown in Table S1. Label-based technologies rely on molecular surface markers, which differ for CTCs and blood cells. Although technologies relying on molecular markers are beneficial in terms of capture efficiency and purity, drawbacks include extensive and tedious sample preparation, and dynamic protein expression and cell heterogeneity results in loss of valuable CTCs [342, 356, 357].

In contrast, label-free technologies are advantageous for isolating CTCs as they eliminate bias that exist with affinity-based methods. Label-free techniques rely on the differences in biophysical properties of tumor cells and blood cells, where historically centrifugation of blood samples could isolate the cells of interest due to size and density compared to blood cells [77-79, 83]. However, centrifugation has a low purity and poor capture efficiency of CTCs. Microfilter technologies typically rely on CTC size or a combination of size and deformability. The benefits of this technology include high recovery-rate, preservation of cell viability, short processing times, and high throughput sample processing. However, microfilters are prone to clogging with cells, debris and other blood constituents while also losing CTCs due to their propensity to deform and pass through the pores of the filter [79, 83, 240, 358]. Thus, there is also a trade-off between throughput and capture purity. Parsortix utilizes cell size and deformability, however cells smaller than the cross-section of their cell traps and larger cells remain trapped limiting downstream harvesting for further investigation of the cells of interest [91, 359]. The FAST Disc has provided optimal results as they were able to achieve >95% CTC recovery rate with a flow rate of 180 mL/hr, however lacks the ability to remove the CTCs from their platform as analysis must be done on-chip [86, 87, 360]. Dielectrophoresis is the movement of particles or cells in

the presence of a non-uniform electric field based off their dielectric properties and has been utilized for CTC isolation in blood. Dielectrophoresis (DEP) is currently not a standalone solution to the problem of isolating CTCs in blood as it has low throughput, relatively low recovery rate, and requires multiple steps for operation in addition to specialized equipment [361-363]. DEP technologies can potentially provide value in isolating CTCs because it can be used in conjunction with higher-throughput technologies which can alleviate the throughput and low recovery rate that is dependent on CTCs and their surrounding media. Previously our research group has developed a microfluidic chip with sequential constriction channels that was able to entrap ~96% of cancer cells at 2.5 mL/hr of spiked murine blood [311]. The drawbacks of this device include its sole compatibility with murine blood, the difficulty of removing CTCs from entrapment chambers, and the issues that exist with microfilter technologies previously mentioned.

Our work aims to address the need for a low-cost rapid and efficient technique to enrich CTCs and CTC clusters in blood samples while maintaining viability for compatibility with continuous downstream analysis. Here, we present a new low-cost label-free microfluidic platform called CTC-CARE which can reliably process whole human blood at 100 μL/min while recovering >91% of spiked highly aggressive cancer cells and reducing the blood sample size by ~50-fold. The microfluidic device consists of a multi-height enrichment channel and an outlet channel which are separated by an array of constrictions. Due to the size, deformability and density of the cancer cells, the majority stay in the center collection channel while the majority (~98%) of other blood cells pass through the constriction array towards the waste channels. The CTC-CARE microsystem does not require any pre-processing and can directly process whole blood

without RBC lysis. An additional benefit of CTC-CARE is that the passive mechanism for CTC enrichment does not affect the viability of the enriched cancer cells. The cost of each CTC-CARE device is < $2, which is more than two orders of magnitude lower than the aforementioned FAST Disc which costs $220 per chip [86]. The device is compatible with capturing CTC clusters due to significant size differences compared to surrounding blood cells. CTC cluster enumeration and analysis can provide strengthened prognostic value in combination with studying CTCs. Further analysis can be done to isolate and evaluate the genetic information of CTCs and CTC clusters which can also help predict response to targeted therapies. The continuous flow of the enriched sample also makes the CTC-CARE device directly compatible with the majority of CTC detection methods as well as alternative CTC enrichment technologies.

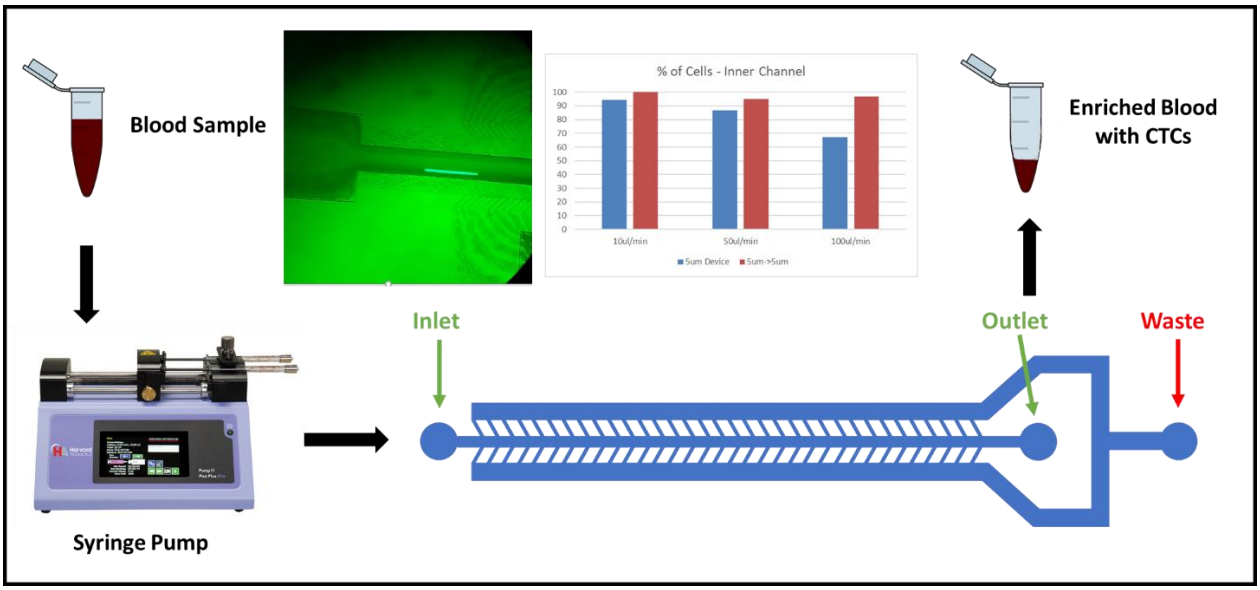

Figure 1: Overview of CTC-CARE device and microfluidic experimental setup

8.2. Materials and Methods

2.1. Cell lines/Cell Culture and Sample Preparation

To test our microfluidic platform we spiked a metastatic breast cancer cells into whole blood from healthy patients. Breast cancer cell line MDA-MB-231 (passage #8, American Type

Culture Collection (ATCC), provided by Dr. Yasmine Kanaan, Howard University College of Medicine) was grown in F12:DMEM (Lonza, Basel, Switzerland) with 10% fetal bovine serum (FBS), 4 mM glutamine and penicillin-streptomycin (100 units per mL). The MDA-MB-231 cells were grown in T-25cm^2 culture flasks at 37°C in a 5% CO_2 in air atmosphere until cells were ready for subculture. The morphology of cells were observed before trypsinization, where the cells detach from the flask via with a trypsin-EDTA solution (Sigma Aldrich). After trypsinization, cells were spun down in the centrifuge for 5 minutes at 400g and the culture media was removed. The cell pellet was covered with a 5 μM working solution of the Invitrogen CellTracker Green CMFDA Dye and incubated for 30 minutes at 37°C. The tagged cells were then spun down and resuspended in PBS 1x for spiking the whole blood sample. Tumor cell counts were ~ 10×10^3 cells/mL. The total volume of cell suspension is ~10μL which is negligible compared to the total volume of 1mL of blood. Healthy whole human blood was collected through the Wake Forest School of Medicine.

2.2. Device Fabrication

To fabricate the polydimethylsiloxane (PDMS) microfluidic channels, a master mold is fabricated onto a silicon wafer. Two layers of SU-8 (SU-8 3005 and SU-8 3025, MicroChem, Newton, MA) are patterned onto the wafer via photolithography. SU-8 3005 was used to build the constriction channel with ~10 μm height, while SU-8 3025 was used to build the remaining channel feature with a ~25 μm height. The resulting mold is coated with tridecafluoro-1,1,2,2-tetrahydrooctyl-1-trichlorosilane (TFOCS, Fisher Scientific) to promote the easy release of PDMS. PDMS base and curing agent (10:1 weight ratio) are stirred generously and poured onto the master mold and cured at 65°C for 24 hours. The PDMS channels are bonded onto glass slides through plasma-activated bonding.

2.3. Device Design and Operation

The CTC-CARE platform consists of a combination of enrichment modules, where each module consists of two main channels, the center CTC enrichment channel and the outer waste channels for unwanted peripheral blood cells. Device operation is demonstrated Video S1, where whole blood spiked with MDA-MB-231 transits through the entrance of the device. Between these two channels is an array of microconstrictions with a width of 5 μm and length of 100 μm. The channel heights of the constriction channels are ~10um while the height of the center and waste channel extends to ~25 μm. The outer waste channel combines into a single outlet, while the center CTC enrichment channel has a single outlet. For the series configuration of the enrichment modules, the enrichment outlet of one module feeds into the inlet of a second enrichment module. The parallel configuration consists of a microfluidic T-junction that evenly splits the sample to operate multiple enrichment modules simultaneously. The final sample of interest is collected at the center outlet channel(s) and all waste outlets are collected individually for further analysis.

2.4. Experimental Setup

The sample is injected into the CTC-CARE device inlet via a Harvard Apparatus syringe pump. As the sample transits through the center channel, some of sample also passes through the surrounding constriction channels which effectively operates as a dynamic blood filtration for CTC enrichment. To cross-verify the results, high-speed videos (Frame rate: 120-240 frames per second) were taken using a smartphone attached to a microscope lens which views the outlet of the devices. The videos were used to enumerate the spiked cancer cells that have been fluorescently tagged using Invitrogen CellTracker Green CMFDA Dye.

8.3. Results

3.1. Sample Reduction

To evaluate the reduction of blood volume, four different CTC enrichment module configurations were compared as shown in Figure 2. The original CTC-CARE platform consisted of a single height of 10μm at the enrichment channel as well as the constriction array. The current generation of the CTC-CARE platform introduced the multi-height aspect which exploits the differences in CTC density compared to surrounding blood cells. To improve the whole blood volume reduction an additional enrichment module is connected in series. The "series" configuration flow resistance increases at the center enrichment channel, thus increasing the reduction of the whole blood sample illustrated in Figure 2. Single height enrichment configurations clearly have a less efficient sample reduction compared to the multi-height configurations. Additionally, the series configuration for both single and multi-height devices have significant improvement. Thus, the multi-height series CTC-CARE device has the optimal reduction of blood.

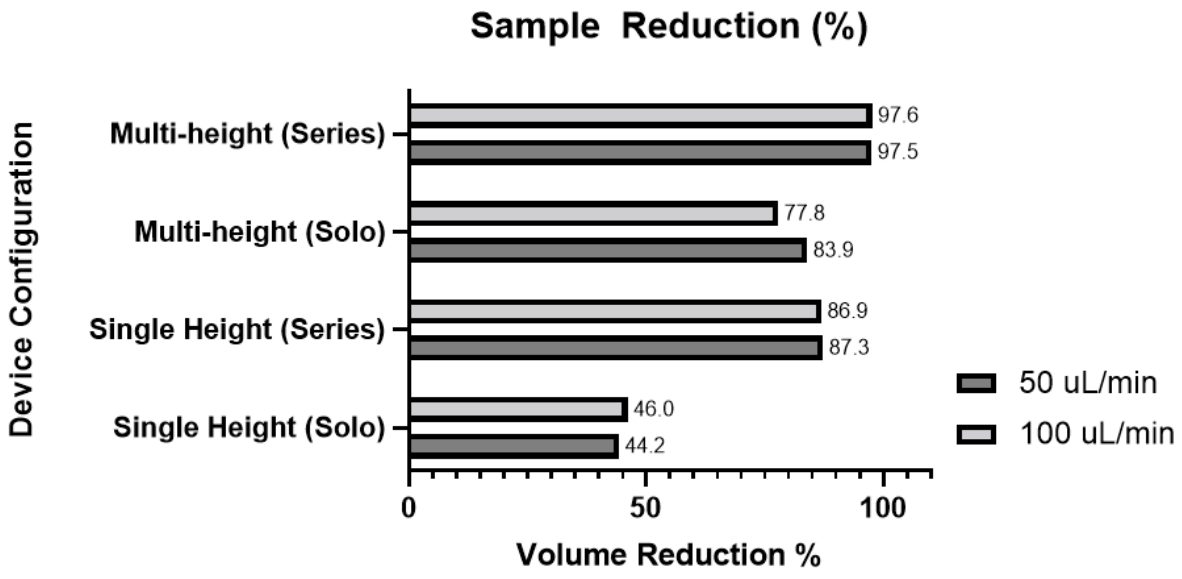

Figure 2: Comparison of different device configurations for blood sample volume reduction.

3.2. Sample Throughput Optimization

To optimize sample throughput, capture efficiency was evaluated at flow rates ranging from 10-100 μL/min for both the multi-height solo and series device configurations. Figure 3 demonstrates that the solo configuration is sensitive to increasing flow rates, while the series platform maintained ~95% capture efficiency regardless of flow rate. Flow rates above 100 μL/min were also examined, however the high flow rates diminished the robustness as it ocassionally led to disconnected tubing and leaking of the CTC-CARE enrichment modules.

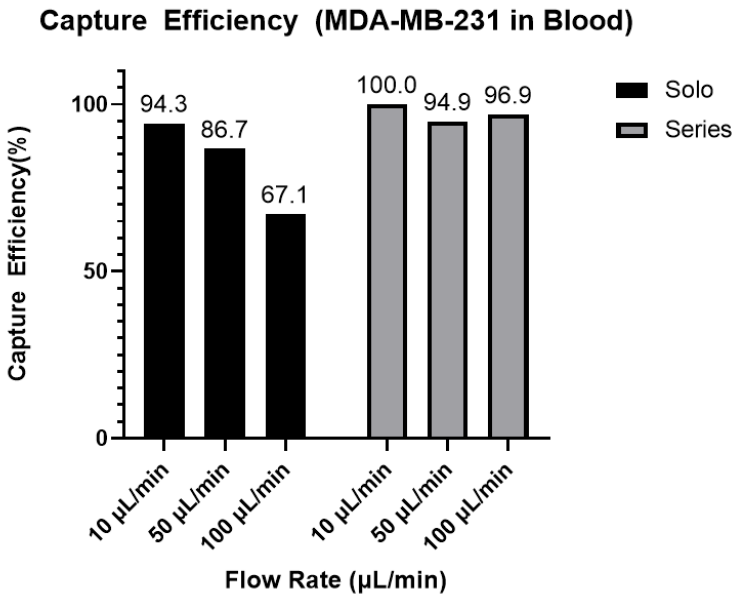

Figure 3: Flow rate comparison for the solo and series device configurations

3.3. Capture Efficiency Validation

To further validate the multi-height series CTC-CARE enrichment chip, we spiked whole healthy blood with two breast cancer cell lines (MDA-MB-231 and MCF-7) and a prostate cell

line (LNCaP C4-2). Figure 4 shows the average (n=3) capture efficiency for each cell line is greater than 90% in all experiments. Thus, the multi-height series configuration provided the optimal results for CTC enrichment that translates across different types of cancer. To prove the scalability of the CTC-CARE device throughput, two series configurations were put in parallel using a microfluidic T-junction. The parallel mode resulted in a 97.5% total volume reduction, while maintaining a capture efficiency of 99.01% and 97.51% for 100 μL/min and 200 μL/min, respectively. An important thing to note is that for all configurations of the CTC-CARE platform, 100% of the CTC clusters were captured in the enrichment channel.

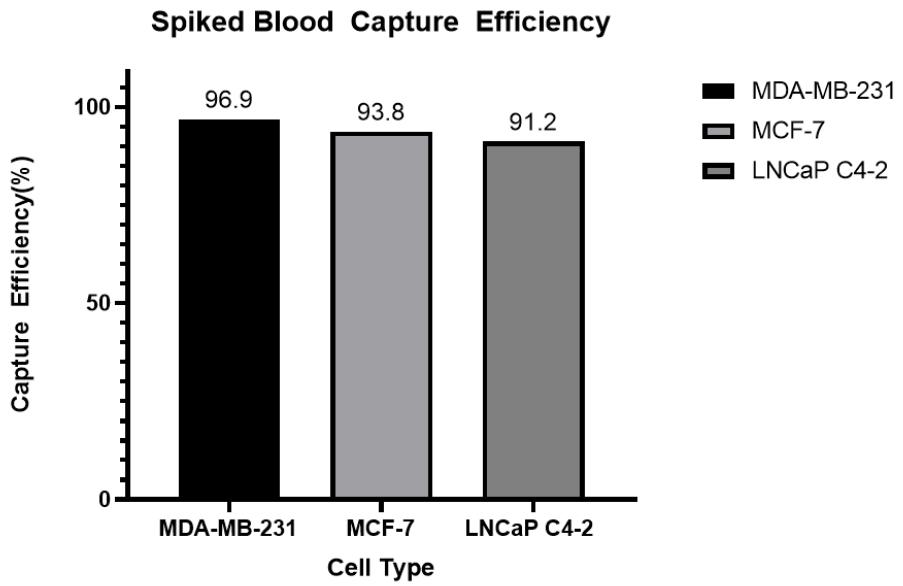

Figure 4: Capture efficiency comparison for different cell types.

8.4. Discussion

Recently, researchers have been developing a variety of platforms to study the clinical utility of CTCs including early detection, cancer prognosis, therapy monitoring, and personalized treatment. The rarity of CTCs in blood, ~1-10 cells per mL of blood compared to billions of

surrounding blood cells, is the main drawback for analyzing CTCs in liquid biopsies [72, 342, 343]. Researchers alleviated these issues by developing a wide range of technologies that can isolate and identify CTCs from blood samples. Label-based and label-free techniques, compared in Table S1, have various advantages in addition to undesired tradeoffs. Label-based techniques rely on molecular surface markers; however CTCs differ from patient-to-patient, cancer-to-cancer as well as intra-patient differences [342, 356, 357]. CTC clusters surrounded by blood cells will also be lost during isolation as they mitigate the interaction with surface markers[357, 364-366]. CTC enrichment and detection platforms, such as CellSearch and AdnaTest, typically rely on the expression of the EpCAM surface marker [80-82]. However, tumor cells can experience an epithelial-to-mesenchymal transition where they lessen or lose the expression of the EpCAM surface protein [367, 368]. Although the reliance on EpCAM+ expression has been addressed by the utilization of a cocktail of antibodies for CTC isolation, this increases the cost of the assay and typically requires previous information about tumor origin.

Label-free techniques typically rely on cell biophysical properties such size, deformability, density, and bioelectrical properties. These characteristics of cells are also intertwined and can be used in conjunction to further enrich the CTCs as their biophysical properties differ from surrounding blood cells. The CTC-CARE platform is a label-free assay that solely relies on cell biophysical This journal article describes different CTC-CARE configurations where a combination of enrichment modules was evaluated for throughput, capture efficiency and sample purity. The multi-height series configuration provided the best results for CTC enrichment as it allowed for a high throughput enrichment at 100 μL/min while maintaining a high capture efficiency of >90% for two breast cancer cell lines and one prostate cancer cell line.

The enrichment modules are easily scalable and can improve throughput (parallel configuration), improve capture efficiency, and increase purity via volume reduction (series configuration). The technology is essentially a tangential flow filtration relying on cell size and deformability in combination with density-based separation due to the multi-height aspect of the device. As the blood sample traverses through the enrichment channel the pressure difference across the array of constrictions allows for the smaller blood cells to pass through towards the waste channels. Additionally, the higher density blood cells experience a larger vertical movement downwards, which allows these cells unwanted cells to continuously pass through the constriction array for the length of the channel. The continuous flow of the CTC-CARE chip allows the resulting enriched sample to be easily collected for post-processing via flow cytometry or immunostaining or connected directly to a detection module for direct analysis. The device is also compatible with alternative enrichment technologies, such as DEP-based methods, for further purification as the 50-fold reduction of volume alleviates the issues of throughput-deficient methods.

Extensive research has been done to prove the importance of CTCs in clinical settings, however recent advances have indicated that CTC clusters may provide additional information on the mechanisms of cancer metastasis. Additionally, researchers have discovered that there may be a link between CTC clusters and resistance to treatments. For instance, Bithi et al. demonstrated in their droplet-based assay that the response of CTCs and CTC clusters, through multiple drug sensitivity assays, differ in terms of viability as CTC clusters tend to have a greater resistance to chemotherapeutic drug doxorubicin [369]. The CTC-CARE platform isolates 100% of the CTC clusters from whole blood, which make this tool advantageous for exploring their clinical utility.

The combination of CTC and CTC cluster analysis on a single low-cost and easy-to-use platform can be crucial for extensive and comprehensive studies, which can lead to further improvements in POC blood testing.

8.5. Conclusions

The CTC-CARE platform is a unique label-free, easy-to-operate, low-cost, highly efficient, and high throughput method of enriching CTCs and CTC clusters from whole blood that is widely compatible with alternative enrichment and detection methods. The device exploits several different biophysical attributes, including cell size, deformability, and density to isolate CTCs from peripheral blood cells. The label-free technology alleviates common issues that exist with surface protein dependent technologies. By combining series and parallel configurations the current processing time is 5 min/mL of whole blood with a capture efficiency >90% and a ~99% reduction in blood volume. The device was validated through whole human blood spiked with a breast cancer tumor cell lines MDA-MB-231 and MCF-7, in addition to prostate cancer cell line LNCaP-C4-2 and successfully isolated >91% of tumor cells while removing ~98% of the unwanted blood sample. The microfluidic assay also isolates 100% of the CTC clusters which have potential prognostic value that needs to be further explored. Direct use of whole blood eliminates the need for RBC lysis, which may negatively affect CTCs and increases the cost and complexity of the assay. To conclude, the CTC-CARE enrichment assay enables the rapid analysis of blood for high-throughput screening and counting of CTCs, which can be easily transportable and usable in clinical settings as an aide to point-of-care blood tests. Results of the low-cost enrichment assay can provide valuable information for cancer prognosis, monitoring progression, analyzing therapeutic response, and predicting patient survival.

9. Summary and Future Outlook

The research displayed in this dissertation aims to supplement cancer research through label-free microfluidic-based platforms by improving single-cell analysis and liquid biopsy technologies. The work presented improved on sensitivity, throughput, cost, ease-of-use, and cell identification efficiency for both types of assays. Below provides a summary of the research and significant outcomes that demonstrate the clinical utility of the assays developed.

9.1 Research Summary

a) Single-cell Mechanical Characteristics Analyzed by Multiconstriction Deformability Assays

A microfluidic-based deformability assay utilizes various constriction channels to analyze and evaluate the biomechanical dynamics of cells. Constriction channels have cross-sections smaller than the cells of interest, so cells need to deform in order to pass through the channel. Cell velocities in constriction channels represent their deformability and biomechanical characteristics. For instance, cancer cells are more deformable than their normal healthy counterpart, so they enter and pass through the channel more quickly. The introduction of relaxation channels, regions where channel geometries are larger than cells of interest, were discovered to further exploit the biomechanical differences between normal and cancer cells. Cancer cells regain their shape in relaxation regions while normal cells tend to keep their deformed shaped when introduced to constrictions. Thus, velocity ratios involving cell transit at the beginning and end of multiconstriction channels provide an improved ability for distinguishing between normal and cancer cells. Ten sequential cell velocities were collected for single cells using a smartphone camera attached to a microscope. After comparing three

different constriction channel configurations, our results indicated that five deformations separated by four relaxation regions provided better results than a standard single constriction and two constrictions separated by a single relaxation region. Through a series of blind studies with MDA-MB-231 (human breast cancer cell line) and MCF-10A (nontumorigenic human breast cell line), velocity profiles of cells can identify single cells with 94.4% differentiation accuracy.

b) Comparative study of prostate cancer biophysical and migratory characteristics via iterative mechanoelectrical properties (iMEP) and standard migration assays

Impedance spectroscopy is a label-free method of evaluating of cells and measuring variations in their electrical properties such as membrane capacitance, cytoplasm conductivity and nuclear resistance. A microfluidic biosensor coined the iterative mechano-electrical properties (iMEP) analyzer was developed to combine the benefits of multiconstriction channels described in Chapter 2 and bioimpedance analysis. The biosensor consists of the five consecutive constriction channels separated by four relaxation regions with a pair of embedded electrodes to capture electrical signatures of single cells that represent the biomechanical and bioelectrical properties of cells. The unique impedance profile of a single cell consists of five peaks that represent the transit of the cell in each sequential channel. The peak height represents the bioelectrical characteristics, while the peak widths represent the biomechanical properties of the cells as they indicate transit velocities. Additionally, impedance spectroscopy is conducted with eight different frequencies ranging from 0.5-1000 kHz. Different frequencies provide different bioelectrical information about the cells. For instance, low frequency AC signals travel around the cell so impedance depends on the size and cell membrane. In contrast, high frequency AC signals penetrate the cells which gives information about the contents of the cell such as the

cytoplasm and nucleus. The iMEP assay rapidly obtains a multiparametric dataset which was used to distinguish four different prostate cell lines that represent cancer progression and its normal counterpart. The iMEP assay was compared with standard migration assays, the Boyden chamber and scratch wound healing assays, to study the biophysical properties and migratory behavior of the prostate cell lines. Neither standard migration assay could completely distinguish all four cell lines, however utilizing solely the bioelectrical information the iMEP analyzer could distinguish between all four cell lines with p-value < 0.05. Although the biomechanical information was not required for distinguishing between the prostate cell lines, having a large dataset of information provides a wealth of knowledge of single cells that can be useful for alternative applications that are more challenging. Additionally, the iMEP analyzer greatly reduces the post-processing times that existed with the assay described in Chapter 2 because cell velocity acquisition can be automated using the electrical signatures.

c) Kernel-based microfluidic constriction assay for tumor sample identification

To build off the microfluidic deformability assay reported in Chapter 2, a higher throughput version of the chip was developed. The platform consists of eight sequential constrictions with six channels in parallel in contrast to the single channel with five sequential constrictions previously mentioned. Cell velocity and size information was extracted from the chips through video analysis and cell identification was done through machine learning methods. Kernel learning methods of Ridge, NGK, and Lasso utilized the large dataset to obtain prediction values ranging from ~81-85% for the breast cancer cell lines and their normal healthy counterpart. These methods were used to evaluate clinical relevance through comparing primary tumor and adjacent normal tissue collected. Primary tumor cells and adjacent breast cells from two patients were analyzed via the high throughput multiconstriction channels with the assistance of machine

learning algorithms. The prediction ratio using the NGK method ranged from 70-76% which demonstrates that this microfluidic device combine with kernel learning methods can identify malignancy. Thus, a low-cost and high throughput microfluidic chip can open the door for using biomechanical markers for patient risk assessment evaluation in clinical settings.

d) Biophysical phenotyping of cells via impedance spectroscopy in parallel cyclic deformability channels

The aforementioned assays describe how wealth of knowledge can be extracted through microfluidic deformability assays and impedimetric analysis. Clinical relevance is reliant on not only the efficiency of the data collection and analysis, but the throughput plays a large role in the usage of these assays in the medical field. A new biosensor was developed that can study single cell biophysical properties, both biomechanical and bioelectrical, at a high throughput. The biosensor consists of four parallel multiconstriction channels with a single pair of electrodes that measures impedance across all four channels. The individual constriction channels consist of two constriction channels separated by a relaxation region. Single cell impedance magnitude and phase was obtained using a 1V AC signal with four frequencies ranging from 1kHz-1MHz. Measuring impedance across all four channels decreases sensitivity, however this chip was still able to maintain sufficient sensitivity to capture impedance information when multiple cells transit through the sensing region simultaneously. Biosensor validation utilized biomechanical and bioelectrical properties to distinguish between breast cancer cells (MDA-MD-231) and normal breast cells (MCF-10A). Using solely the biomechanical attributes a prediction accuracy of 85% was achieved, however integrating the bioelectrical characteristics in the identification the prediction value reached 97%. The increased throughput of the impedimetric deformability

assay improves clinical relevance and applications can extend to assessing therapeutic response, metastatic potential, or liquid biopsies.

e) Entrapment of prostate cancer circulating tumor cells with a sequential size-based microfluidic chip

Circulating tumor cells (CTCs) are cells that circulate through the bloodstream and have recently shown promise as biomarker for early detection, evaluating disease recurrence and identify cancer metastasis. Due to the rarity of CTCs in whole blood, 1-100 CTCs compared to billions of blood cells in the same volume, blood enrichment typically needs to be done to isolate the cells for analysis. Label-free methods of CTC enrichment are advantageous because standard label-based technologies rely on surface markers that are not reliable due to heterogeneity of surface markers. The high throughput entrapment chip (CTC-HTECH) is a label-free microfluidic assay developed to enrich tumor cells in murine blood by utilizing biomechanical their differences with peripheral blood. The device consists of several rows where each row has an array of multiconstriction channels. The multiconstriction channels have two relaxation regions where the cell has the opportunity to regain their shape. Cancer cells tend to regain their shape and the peripheral blood usually travels around the cells while they become entrapped in the relaxation regions. The microfluidic chip had the flexibility to utilize one row and up to six rows. Experimentation demonstrated that for prostate cancer cells (LNCaP-C4-2) spiked in whole murine blood, the five and six row configurations provided optimal capture efficiency of >95%. The benefit higher row counts is the pressure drop across the constriction channels is decreased, which lessens the probability that these cells will deform and transit through the sequential constrictions. CTC-HTECH achieved a clinically relevant throughput of ~2.4 mL/hr, however the drawbacks of this enrichment platform are the channel geometries and unreliable removal of

CTCs. To improve the clinical utility of the chip, channel sizes need to be optimized for larger human cells and modifications need to be made so CTCs can be removed for further downstream analysis.

f) Post-enrichment circulating tumor cell detection and enumeration via deformability impedance cytometry

CTC count can be useful for cancer detection, diagnosis, and monitoring cancer progression. A CTC detection device was developed to enumerate the cells of interest through deformability impedance cytometry. The sensing region of the biosensor consists of a single constriction channel with single pair of embedded coplanar electrodes. Impedance signatures of cancer cells are significantly different than surrounding murine blood sample, so their peaks are utilized to automate the cancer cell detection. Two configurations of the assay are reported, where one is the standard direct contact (on-chip) electrodes and the second has a thin layer of glass between the electrodes and channels (off-chip). The off-chip mode is a cost-effective version of the assay, as the channels are disposable while the electrodes can be re-used. The devices were validated using murine blood samples spiked with breast (MDA-MB-231) and prostate cancer cells (LNCaP C4-2). Impedance spectroscopy is conducted with an AC voltage of 1V signal at eight different frequencies ranging from 500 Hz to 1 MHz simultaneously. For both electrode configurations 100% of tumor cells were detected and its sensitivity could detect differences in breast and prostate cancer cell populations. This study proves that low-cost off-chip devices is a robust method and throughput is scalable (reported in Chapter 4) which demonstrates clinical viability.

g) CTC-CARE: Constriction Assisted Rapid Enrichment of Circulating Tumor Cells

A cost-efficient microfluidic platform coined the constriction assisted rapid enrichment of CTCs (CTC-CARE) purifies whole human blood to aid the enumeration and analysis of CTCs and CTC clusters. The CTC-CARE assay is a modular platform, where each module consists of a multi-height delivery channel and an array of constriction channels. The device operates as a tangential flow filter where unwanted blood cells are exit the delivery channel through the constriction array due to differences in biophysical properties The multi-height channels in combination with the constriction array uniquely exploits differences in size, deformability, and density of the cells. The modules are small and low cost as they are fabricated with PDMS and glass which can be easily scalable to improve throughput, purity and capture efficiency of CTCs. CTC-CARE alleviates issues that CTC-HTECH (Chapter 5) experienced because the assay can process whole human blood and the enriched sample continuously flows out of the device for downstream analysis. Validation of the assay was done by spiking whole human blood with two different breast cancer cell lines (MDA-MB-231, MCF-7) and a prostate cancer cell line (LNCaP C4-2). CTC-CARE rapidly isolated >90% of tumor cells and 100% of CTC clusters, while purifying the sample by removing ~98% of the unwanted blood sample. The assay can process 1mL of blood in up to 5 minutes, which is clinically relevant as it processes the sample faster than the sole FDA-approved CTC enrichment technology. CTC-CARE is ready for clinical validation as it is compatible with standard methods of tumor cell identification such as flow cytometry and immunofluorescent image analysis.

9.2 Significance and Contribution

Label-free microfluidic platforms have contributed to the advancement of cancer research through single-cell analysis and liquid biopsies in the form of CTC evaluation in blood. This work aims to improve our understanding of the biomechanical dynamics through iterative microfluidic deformability assays. Biomechanical investigation in conjunction with impedimetric analysis of cells at the single cell level produces in-depth insight on the complexity cells for characterization. Additionally, bioimpedance collection in multi-constriction channels provide peak widths as time points for automated post-processing of cell response to iterative deformation. Throughput drawbacks were addressed in both deformability assays and mechano-electrical probing for single-cell analysis. The high-throughput deformability assay demonstrated clinical utility by distinguishing between normal and cancer cells with statistical significance. Mechano-electrical probing at a high-throughput maintained sensitivity to detect multiple cells passing through parallel channels simultaneously. Through a combination of biomechanical and bioelectrical attributes, this assay identified >97% of normal and cancer cells at the single-cell level. Liquid biopsy assays for CTC analysis that were developed improved upon both enrichment and detection aspects of the technology. The CTC-CARE modular enrichment platform for whole human blood allows for the cost-efficient optimization of technical parameters which include throughput, purity, and capture efficiency. CTC detection through constriction-based impedance spectroscopy could detect all cancer cells in murine blood. Furthermore, a low-cost version of the assay through an “off-chip” configuration proved to be sensitive enough to detect all cancer cells in murine blood, while also identifying differences in prostate and breast cancer cell lines. The work presented demonstrates the improvement of label-free microfluidic technologies towards an integrated systems that rapidly and reliably

processes biological samples for both research and clinical settings (illustrated in Figure 9.1). To conclude, the knowledge obtained can bridge the gap needed to develop clinically relevant assays that exploit the biophysical properties of cells to produce easy-to-use, cost-effective, robust, high-throughput, real-time capable, and efficient point-of-care technologies.

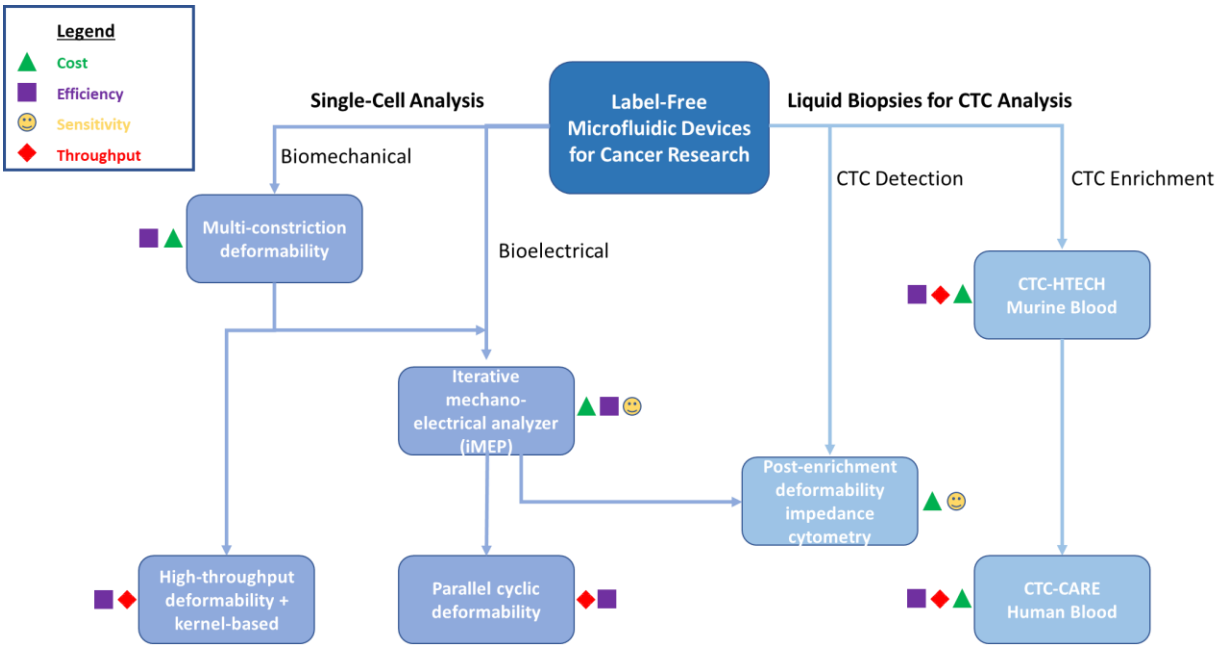

Figure 9.1: Overview of research contributions labeled with symbols that represent technical improvements.

9.3 Future Prospects

Microfluidic technologies have advanced greatly over the last decade in both research and commercial settings for cancer research. Label-free methods of evaluating biological samples in microfluidics has shown remarkable promise as viable technologies, however further developments are required in order for these technologies to be reliably used in clinical settings. Aspects of these devices that need improvement include sample throughput, cost, efficiency,

ease-of-use, robustness, integration of complete systems, and automation of data collection and processing for real-time feedback. The majority of current research-based and commercialized products have trade-offs in the aforementioned aspects that can be mitigated through combining different technologies.

The work published in this dissertation describes the significant advances made in single-cell analysis technologies in addition to liquid biopsies. However, there is a wide array of trajectories that can be pursued for technology improvement such as sample throughput, cost, efficiency, ease-of-use, robustness, system integration, and automation of data collection and processing for real-time feedback. Further development of the CTC isolation from whole blood and cancer cell detection from human blood samples or tissue. is required for a complete integrated low-cost, robust, and easy-to-use platform with clinical relevance. Improvements to the CTC enrichment technology can include an additional intermediate enrichment to further purify the sample for ease of detection. For instance, CTC-CARE can feed into an additional module that utilizes proven label-free technologies such as acoustophoresis, dielectrophoresis, and deterministic lateral displacement. A secondary purification not only be beneficial microfluidic-based detection methods but can better facilitate downstream analysis using standard biological characterization methods. Key issues with tumor cell detection technologies include throughput, sensitivity of sensors, and robustness. Throughput issues can be addressed through finer purification in liquid biopsy applications, parallelization of existing technologies and optimization of experimental parameters such as flow rate can further improve throughput. Sensitivity can be addressed through (1) different electrode types such as 3-dimensional or interdigitated electrodes, (2) varying orientation and operation through differential measurements, (3) modifying experimental parameters such as input voltage and frequencies,

and/or (4) modifying the channel geometries of the sensing region. Robustness can be improved through modifying the channel geometries to prevent clogging while maintaining sufficient sensitivity and incorporating complex data analysis through statistical and machine learning methods. Diminishing the drawbacks of current microfluidic technologies can lead to pathways that are vital for cancer research and clinical utility for patients.

10 References

1. *Cancer*. Available from: http://www.who.int/mediacentre/factsheets/fs297/en/.
2. *Metastatic Cancer.*
3. Chaffer, C.L. and R.A. Weinberg, *A perspective on cancer cell metastasis.* Science, 2011. **331**(6024): p. 1559-1564.
4. Siegel, R., et al., *Cancer statistics, 2014.* CA: a cancer journal for clinicians, 2014. **64**(1): p. 9-29.
5. Siegel, R.L., K.D. Miller, and A. Jemal, *Cancer statistics, 2016.* CA: a cancer journal for clinicians, 2016. **66**(1): p. 7-30.
6. Corbin, E.A., et al., *Biophysical properties of human breast cancer cells measured using silicon MEMS resonators and atomic force microscopy.* Lab on a Chip, 2015. **15**(3): p. 839-847.
7. Zheng, Y., et al., *Recent advances in microfluidic techniques for single-cell biophysical characterization.* Lab on a Chip, 2013. **13**(13): p. 2464-2483.
8. Ujihara, Y., M. Nakamura, and S. Wada, *A mechanical cell model and its application to cellular biomechanics*, in *Biomedical Engineering-From Theory to Applications*. 2011, InTech.
9. Elson, E.L., *Cellular mechanics as an indicator of cytoskeletal structure and function.* Annual review of biophysics and biophysical chemistry, 1988. **17**(1): p. 397-430.
10. *Microtubules and Filaments.* .
11. Satcher, R. and C.F. Dewey, *Theoretical estimates of mechanical properties of the endothelial cell cytoskeleton.* Biophysical journal, 1996. **71**(1): p. 109-118.
12. *Cytoskeleton.*
13. Nagayama, K. and T. Matsumoto. *EFFECTS OF ACTIN FILAMENTS AND MICROTUBULES ON QUASI-IN SITU TENSILE PROPERTIES AND INTRACELLULAR FORCE BALANCE OF CULTURED AORTIC SMOOTH MUSCLE CELLS (1A2 Micro & Nano Biomechanics II)*. in *The Proceedings of the Asian Pacific Conference on Biomechanics: emerging science and technology in biomechanics 2007.3*. 2007. The Japan Society of Mechanical Engineers.
14. Yu, C.-H., et al. *Morpho: A self-deformable modular robot inspired by cellular structure*. in *Intelligent Robots and Systems, 2008. IROS 2008. IEEE/RSJ International Conference on*. 2008. IEEE.
15. Ingber, D.E., *Tensegrity and Complex Systems Biology.*
16. Ingber, D.E., *Cellular tensegrity: defining new rules of biological design that govern the cytoskeleton.* Journal of Cell Science, 1993. **104**(3): p. 613-627.
17. Ingber, D.E., *Tensegrity I. Cell structure and hierarchical systems biology.* Journal of cell science, 2003. **116**(7): p. 1157-1173.
18. Ingber, D.E., *Tensegrity II. How structural networks influence cellular information processing networks.* Journal of cell science, 2003. **116**(8): p. 1397-1408.
19. Stamenović, D., et al., *Experimental tests of the cellular tensegrity hypothesis.* Biorheology, 2003. **40**(1, 2, 3): p. 221-225.
20. Wang, N., et al., *Cell prestress. I. Stiffness and prestress are closely associated in adherent contractile cells.* American Journal of Physiology-Cell Physiology, 2002. **282**(3): p. C606-C616.

21. *Cells, Biological.*
22. Hur, S.C., et al., *Deformability-based cell classification and enrichment using inertial microfluidics.* Lab on a Chip, 2011. **11**(5): p. 912-920.
23. Guck, J., et al., *Optical deformability as an inherent cell marker for testing malignant transformation and metastatic competence.* Biophysical journal, 2005. **88**(5): p. 3689-3698.
24. Hou, H.W., et al., *Deformability study of breast cancer cells using microfluidics.* Biomedical microdevices, 2009. **11**(3): p. 557-564.
25. Lincoln, B., et al., *Reconfigurable microfluidic integration of a dual-beam laser trap with biomedical applications.* Biomedical microdevices, 2007. **9**(5): p. 703-710.
26. Lincoln, B., et al., *Deformability-based flow cytometry.* Cytometry Part A, 2004. **59**(2): p. 203-209.
27. Swaminathan, V., et al., *Mechanical stiffness grades metastatic potential in patient tumor cells and in cancer cell lines.* Cancer research, 2011. **71**(15): p. 5075-5080.
28. Byun, S., et al., *Characterizing deformability and surface friction of cancer cells.* Proceedings of the National Academy of Sciences, 2013. **110**(19): p. 7580-7585.
29. Suresh, S., *Biomechanics and biophysics of cancer cells.* Acta Materialia, 2007. **55**(12): p. 3989-4014.
30. Hochmuth, R.M., *Micropipette aspiration of living cells.* Journal of biomechanics, 2000. **33**(1): p. 15-22.
31. Hoffman, R.M., *Imaging the role of the tumor microenvironment in tumor progression and metastasis.* Cancer Cell & Microenvironment, 2016. **3**(2).
32. Lee, G.Y. and C.T. Lim, *Biomechanics approaches to studying human diseases.* Trends in biotechnology, 2007. **25**(3): p. 111-118.
33. Cross, S.E., et al., *Nanomechanical analysis of cells from cancer patients.* Nature nanotechnology, 2007. **2**(12): p. 780-783.
34. Lekka, M., et al., *Elasticity of normal and cancerous human bladder cells studied by scanning force microscopy.* European Biophysics Journal, 1999. **28**(4): p. 312-316.
35. Rosenbluth, M.J., W.A. Lam, and D.A. Fletcher, *Force microscopy of nonadherent cells: a comparison of leukemia cell deformability.* Biophysical journal, 2006. **90**(8): p. 2994-3003.
36. Wang, N. and D.E. Ingber, *Probing transmembrane mechanical coupling and cytomechanics using magnetic twisting cytometry.* Biochemistry and Cell Biology, 1995. **73**(7-8): p. 327-335.
37. Suresh, S., et al., *Reprint of: connections between single-cell biomechanics and human disease states: gastrointestinal cancer and malaria.* Acta biomaterialia, 2015. **23**: p. S3-S15.
38. Darling, E.M. and D. Di Carlo, *High-throughput assessment of cellular mechanical properties.* Annual review of biomedical engineering, 2015. **17**: p. 35-62.
39. Xu, W., et al., *Cell stiffness is a biomarker of the metastatic potential of ovarian cancer cells.* PloS one, 2012. **7**(10): p. e46609.
40. Gossett, D.R., et al., *Hydrodynamic stretching of single cells for large population mechanical phenotyping.* Proceedings of the National Academy of Sciences, 2012. **109**(20): p. 7630-7635.
41. Yoshino, T., et al., *Evaluation of cancer cell deformability by microcavity array.* Analytical biochemistry, 2017. **520**: p. 16-21.

42. Irimajiri, A., et al., *Dielectric Modeling of Biological Cells: Models and Algorithm (Commemoration Issue Dedicated to Professor Tetsuya HANAI On the Occasion of His Retirement).* 1991.
43. Salimi, E., et al., *Dielectric model for Chinese hamster ovary cells obtained by dielectrophoresis cytometry.* Biomicrofluidics, 2016. **10**(1): p. 014111.
44. Morgan, H., et al., *Single cell dielectric spectroscopy.* Journal of Physics D: Applied Physics, 2006. **40**(1): p. 61.
45. Heileman, K., J. Daoud, and M. Tabrizian, *Dielectric spectroscopy as a viable biosensing tool for cell and tissue characterization and analysis.* Biosensors and Bioelectronics, 2013. **49**: p. 348-359.
46. Ducote M, V.B., Hogquist S, Riggs B, Saksena J, *Electrochemical Impedance Spectroscopy (EIS) as a Tool for Pathogen Detection.* Journal of Biosensors and Bioelectronics, 2016. **7**(224).
47. Wegener, J., C.R. Keese, and I. Giaever, *Electric cell–substrate impedance sensing (ECIS) as a noninvasive means to monitor the kinetics of cell spreading to artificial surfaces.* Experimental cell research, 2000. **259**(1): p. 158-166.
48. Cheung, K., S. Gawad, and P. Renaud, *Impedance spectroscopy flow cytometry: On-chip label-free cell differentiation.* Cytometry Part A, 2005. **65**(2): p. 124-132.
49. Han, A., L. Yang, and A.B. Frazier, *Quantification of the heterogeneity in breast cancer cell lines using whole-cell impedance spectroscopy.* Clinical cancer research, 2007. **13**(1): p. 139-143.
50. Wei, Y., et al., *Embedded silver PDMS electrodes for single cell electrical impedance spectroscopy.* Journal of Micromechanics and Microengineering, 2016. **26**(9): p. 095006.
51. Heidmann, I., et al., *Impedance Flow Cytometry: A Novel Technique in Pollen Analysis.* PloS one, 2016. **11**(11): p. e0165531.
52. David, F., et al., *Viability and membrane potential analysis of Bacillus megaterium cells by impedance flow cytometry.* Biotechnology and bioengineering, 2012. **109**(2): p. 483-492.
53. Asphahani, F., et al., *Single-cell bioelectrical impedance platform for monitoring cellular response to drug treatment.* Physical biology, 2011. **8**(1): p. 015006.
54. Liu, Q., et al., *Impedance studies of bio-behavior and chemosensitivity of cancer cells by micro-electrode arrays.* Biosensors and Bioelectronics, 2009. **24**(5): p. 1305-1310.
55. Schwarzenberger, T., et al., *Impedance sensor technology for cell-based assays in the framework of a high-content screening system.* Physiological measurement, 2011. **32**(7): p. 977.
56. Yu, J., et al., *Nanoporous membrane-based cell chip for the study of anti-cancer drug effect of retinoic acid with impedance spectroscopy.* Talanta, 2009. **80**(1): p. 189-194.
57. Adamo, A., et al., *Microfluidics-based assessment of cell deformability.* Analytical chemistry, 2012. **84**(15): p. 6438-6443.
58. Cheung, K.C., et al., *Microfluidic impedance-based flow cytometry.* Cytometry Part A, 2010. **77**(7): p. 648-666.
59. Ghenim, L., et al., *Monitoring impedance changes associated with motility and mitosis of a single cell.* Lab on a Chip, 2010. **10**(19): p. 2546-2550.
60. Wang, L., et al., *Real-time, label-free monitoring of the cell cycle with a cellular impedance sensing chip.* Biosensors and Bioelectronics, 2010. **25**(5): p. 990-995.
61. *The cell cycle, mitosis and meiosis.*

62. Jang, L.-S., et al., *Design and fabrication of microfluidic devices integrated with an open-ended MEMS probe for single-cell impedance measurement.* Microfluidics and Nanofluidics, 2010. **8**(4): p. 509-519.
63. Malleo, D., et al., *Continuous differential impedance spectroscopy of single cells.* Microfluidics and nanofluidics, 2010. **9**(2-3): p. 191-198.
64. Nikkhah, M., *Identification of Cell Biomechanical Signatures Using Three Dimensional Isotropic Microstructures*. 2010.
65. Babahosseini, H., et al., *The impact of sphingosine kinase inhibitor-loaded nanoparticles on bioelectrical and biomechanical properties of cancer cells.* Lab on a Chip, 2016. **16**(1): p. 188-198.
66. Babahosseini, H., J.S. Strobl, and M. Agah, *Microfluidic iterative mechanical characteristics (iMECH) analyzer for single-cell metastatic identification.* Analytical Methods, 2017. **9**(5): p. 847-855.
67. *Enumerating CTC in humans*. 2021 [cited 2021; Available from: https://www.vycap.com/application/circulating-tumor-cells/.
68. Cooperberg, M.R., J.M. Broering, and P.R. Carroll, *Risk Assessment for Prostate Cancer Metastasis and Mortality at the Time of Diagnosis.* JNCI: Journal of the National Cancer Institute, 2009. **101**(12): p. 878-887.
69. Steeg, P.S., *Tumor metastasis: mechanistic insights and clinical challenges.* Nature Medicine, 2006. **12**(8): p. 895-904.
70. Alix-Panabières, C. and K. Pantel, *Circulating Tumor Cells: Liquid Biopsy of Cancer.* Clinical Chemistry, 2013. **59**(1): p. 110-118.
71. Lim, S.B., et al., *Liquid biopsy: one cell at a time.* npj Precision Oncology, 2019. **3**(1).
72. Mentis, A.-F.A., et al., *Circulating tumor cells as Trojan Horse for understanding, preventing, and treating cancer: a critical appraisal.* Cellular and Molecular Life Sciences, 2020. **77**(18): p. 3671-3690.
73. Danila, D.C., et al., *Circulating Tumors Cells as Biomarkers.* The Cancer Journal, 2011. **17**(6): p. 438-450.
74. Kilgour, E., et al., *Liquid Biopsy-Based Biomarkers of Treatment Response and Resistance.* Cancer Cell, 2020. **37**(4): p. 485-495.
75. Casanova-Salas, I., et al., *Quantitative and Qualitative Analysis of Blood-based Liquid Biopsies to Inform Clinical Decision-making in Prostate Cancer*. European Urology, 2021. **79**(6): p. 762-771.
76. Genna, A., et al., *EMT-Associated Heterogeneity in Circulating Tumor Cells: Sticky Friends on the Road to Metastasis.* Cancers, 2020. **12**(6): p. 1632.
77. Murlidhar, V., L. Rivera-Báez, and S. Nagrath, *Affinity Versus Label-Free Isolation of Circulating Tumor Cells: Who Wins?* Small, 2016. **12**(33): p. 4450-4463.
78. Zeinali, M., et al., *High-Throughput Label-Free Isolation of Heterogeneous Circulating Tumor Cells and CTC Clusters from Non-Small-Cell Lung Cancer Patients.* Cancers, 2020. **12**(1): p. 127.
79. Ajanth, P., A. Sudeepthi, and A.K. Sen, *Microfluidics Technology for Label-Free Isolation of Circulating Tumor Cells.* Journal of The Institution of Engineers (India): Series C, 2020. **101**(6): p. 1051-1071.
80. Andree, K.C., G. Van Dalum, and L.W.M.M. Terstappen, *Challenges in circulating tumor cell detection by the CellSearch system.* Molecular Oncology, 2016. **10**(3): p. 395-407.

81. Müller, V., et al., *Prognostic impact of circulating tumor cells assessed with the CellSearch System™ and AdnaTest Breast™ in metastatic breast cancer patients: the DETECT study.* Breast Cancer Research, 2012. **14**(4): p. R118.
82. Andreopoulou, E., et al., *Comparison of assay methods for detection of circulating tumor cells in metastatic breast cancer: AdnaGen AdnaTest BreastCancer Select/Detect™ versus Veridex CellSearch™ system.* International Journal of Cancer, 2012. **130**(7): p. 1590-1597.
83. Miccio, L., et al., *Perspectives on liquid biopsy for label-free detection of "circulating tumor cells" through intelligent lab-on-chips.* View, 2020. **1**(3): p. 20200034.
84. Rawal, S., et al., *Identification and Quantitation of Circulating Tumor Cells.* Annual Review of Analytical Chemistry, 2017. **10**(1): p. 321-343.
85. Li, X., et al., *Strategies for enrichment of circulating tumor cells.* Translational Cancer Research, 2020. **9**(3): p. 2012-2025.
86. Kim, T.-H., et al., *FAST: Size-Selective, Clog-Free Isolation of Rare Cancer Cells from Whole Blood at a Liquid–Liquid Interface.* Analytical Chemistry, 2017. **89**(2): p. 1155-1162.
87. Lim, M., et al., *A lab-on-a-disc platform enables serial monitoring of individual CTCs associated with tumor progression during EGFR-targeted therapy for patients with NSCLC.* Theranostics, 2020. **10**(12): p. 5181.
88. Riahi, R., et al., *A novel microchannel-based device to capture and analyze circulating tumor cells (CTCs) of breast cancer.* International Journal of Oncology, 2014. **44**(6): p. 1870-1878.
89. Brown, H.K., et al., *Characterization of circulating tumor cells as a reflection of the tumor heterogeneity: myth or reality?* Drug Discovery Today, 2019. **24**(3): p. 763-772.
90. Gabriel, M.T., et al., *Circulating Tumor Cells: A Review of Non–EpCAM-Based Approaches for Cell Enrichment and Isolation.* Clinical Chemistry, 2016. **62**(4): p. 571-581.
91. Miller, M.C., et al., *The Parsortix™ Cell Separation System—A versatile liquid biopsy platform.* Cytometry Part A, 2018. **93**(12): p. 1234-1239.
92. Zheng, S., et al., *3D microfilter device for viable circulating tumor cell (CTC) enrichment from blood.* Biomedical microdevices, 2011. **13**(1): p. 203-213.
93. Mohamed, H., et al., *Development of a rare cell fractionation device: application for cancer detection.* IEEE transactions on nanobioscience, 2004. **3**(4): p. 251-256.
94. Sarioglu, A.F., et al., *A microfluidic device for label-free, physical capture of circulating tumor cell clusters.* Nature methods, 2015. **12**(7): p. 685-691.
95. Lee, A., et al., *All-in-one centrifugal microfluidic device for size-selective circulating tumor cell isolation with high purity.* Analytical chemistry, 2014. **86**(22): p. 11349-11356.
96. Loutherback, K., et al., *Deterministic separation of cancer cells from blood at 10 mL/min.* AIP advances, 2012. **2**(4): p. 042107.
97. Bagnall, J.S., et al., *Deformability-based cell selection with downstream immunofluorescence analysis.* Integrative Biology, 2016. **8**(5): p. 654-664.
98. Zhao, Y., et al., *Single-Cell Electrical Phenotyping Enabling the Classification of Mouse Tumor Samples.* Scientific reports, 2016. **6**.

99. Luo, Y., et al., *A constriction channel based microfluidic system enabling continuous characterization of cellular instantaneous Young's modulus.* Sensors and Actuators B: Chemical, 2014. **202**: p. 1183-1189.
100. Babahosseini, H., J.S. Strobl, and M. Agah, *Single cell metastatic phenotyping using pulsed nanomechanical indentations.* Nanotechnology, 2015. **26**(35): p. 354004.
101. Chen, J., J. Li, and Y. Sun, *Microfluidic approaches for cancer cell detection, characterization, and separation.* Lab on a Chip, 2012. **12**(10): p. 1753-1767.
102. Zhao, Y., et al., *Simultaneous Characterization of Instantaneous Young's Modulus and Specific Membrane Capacitance of Single Cells Using a Microfluidic System.* Sensors, 2015. **15**(2): p. 2763-2773.
103. Nikkhah, M., et al., *The cytoskeletal organization of breast carcinoma and fibroblast cells inside three dimensional (3-D) isotropic silicon microstructures.* Biomaterials, 2010. **31**(16): p. 4552-4561.
104. Babahosseini, H., et al., *Sub-cellular force microscopy in single normal and cancer cells.* Biochemical and biophysical research communications, 2015. **463**(4): p. 587-592.
105. Carmichael, B., et al., *The fractional viscoelastic response of human breast tissue cells.* Physical biology, 2015. **12**(4): p. 046001.
106. Chen, H.-C., *Boyden chamber assay*, in *Cell migration*. 2005, Springer. p. 15-22.
107. Jonkman, J.E., et al., *An introduction to the wound healing assay using live-cell microscopy.* Cell adhesion & migration, 2014. **8**(5): p. 440-451.
108. Liang, C.-C., A.Y. Park, and J.-L. Guan, *In vitro scratch assay: a convenient and inexpensive method for analysis of cell migration in vitro.* Nature protocols, 2007. **2**(2): p. 329.
109. Ramesh, A., A. Pattabhi, and M. Ravi, *Assays Used in vitro to Study Cancer Cell Lines.* Life Science Research, 2016. **1**(01): p. 19-24.
110. Rodriguez, L.G., X. Wu, and J.-L. Guan, *Wound-healing assay*, in *Cell Migration*. 2005, Springer. p. 23-29.
111. Kramer, N., et al., *In vitro cell migration and invasion assays.* Mutation Research/Reviews in Mutation Research, 2013. **752**(1): p. 10-24.
112. Chaw, K., et al., *Multi-step microfluidic device for studying cancer metastasis.* Lab on a Chip, 2007. **7**(8): p. 1041-1047.
113. Chung, S., et al., *Cell migration into scaffolds under co-culture conditions in a microfluidic platform.* Lab on a Chip, 2009. **9**(2): p. 269-275.
114. Hosseini, Y., et al., *A Silicon-Based Porous Thin Membrane as a Cancer Cell Transmigration Assay.* Journal of Microelectromechanical Systems, 2017. **26**(2): p. 308-316.
115. Zervantonakis, I.K., et al., *Three-dimensional microfluidic model for tumor cell intravasation and endothelial barrier function.* Proceedings of the National Academy of Sciences, 2012. **109**(34): p. 13515-13520.
116. Bow, H., et al., *A microfabricated deformability-based flow cytometer with application to malaria.* Lab on a Chip, 2011. **11**(6): p. 1065-1073.
117. Van Vliet, K., G. Bao, and S. Suresh, *The biomechanics toolbox: experimental approaches for living cells and biomolecules.* Acta materialia, 2003. **51**(19): p. 5881-5905.
118. Ren, X., et al., *Single-cell mechanical characteristics analyzed by multiconstriction microfluidic channels.* ACS sensors, 2017. **2**(2): p. 290-299.

119. Ren, X., et al., *Kernel-based microfluidic constriction assay for tumor sample identification.* ACS sensors, 2018. **3**(8): p. 1510-1521.
120. Kirmizis, D. and S. Logothetidis, *Atomic force microscopy probing in the measurement of cell mechanics.* International journal of nanomedicine, 2010. **5**: p. 137.
121. Guo, Q., S. Park, and H. Ma, *Microfluidic micropipette aspiration for measuring the deformability of single cells.* Lab on a Chip, 2012. **12**(15): p. 2687-2695.
122. Basiji, D.A., et al., *Cellular image analysis and imaging by flow cytometry.* Clinics in laboratory medicine, 2007. **27**(3): p. 653-670.
123. Huh, D., et al., *Microfluidics for flow cytometric analysis of cells and particles.* Physiological measurement, 2005. **26**(3): p. R73.
124. Khan, S.S., M.A. Solomon, and J.P. McCoy Jr, *Detection of circulating endothelial cells and endothelial progenitor cells by flow cytometry.* Cytometry Part B: Clinical Cytometry: The Journal of the International Society for Analytical Cytology, 2005. **64**(1): p. 1-8.
125. Spitzer, M.H. and G.P. Nolan, *Mass cytometry: single cells, many features.* Cell, 2016. **165**(4): p. 780-791.
126. Chen, J., et al., *Classification of cell types using a microfluidic device for mechanical and electrical measurement on single cells.* Lab on a Chip, 2011. **11**(18): p. 3174-3181.
127. Song, H., et al., *A microfluidic impedance flow cytometer for identification of differentiation state of stem cells.* Lab on a Chip, 2013. **13**(12): p. 2300-2310.
128. Zhao, Y., et al., *A microfluidic system enabling continuous characterization of specific membrane capacitance and cytoplasm conductivity of single cells in suspension.* Biosensors and Bioelectronics, 2013. **43**: p. 304-307.
129. Ren, X., et al., *Biophysical phenotyping of cells via impedance spectroscopy in parallel cyclic deformability channels.* Biomicrofluidics, 2019. **13**(4): p. 044103.
130. Yang, D., et al., *Biophysical phenotyping of single cells using a differential multiconstriction microfluidic device with self-aligned 3D electrodes.* Biosensors and Bioelectronics, 2019. **133**: p. 16-23.
131. Campbell, C.E., et al., *Monitoring viral-induced cell death using electric cell–substrate impedance sensing.* Biosensors and Bioelectronics, 2007. **23**(4): p. 536-542.
132. Giaever, I. and C.R. Keese, *Monitoring fibroblast behavior in tissue culture with an applied electric field.* Proceedings of the National Academy of Sciences, 1984. **81**(12): p. 3761-3764.
133. Szulcek, R., H.J. Bogaard, and G.P. van Nieuw Amerongen, *Electric cell-substrate impedance sensing for the quantification of endothelial proliferation, barrier function, and motility.* JoVE (Journal of Visualized Experiments), 2014(85): p. e51300.
134. Tran, T.B., et al., *Electrical dual-sensing method for real-time quantitative monitoring of cell-secreted MMP-9 and cellular morphology during migration process.* Biosensors and Bioelectronics, 2016. **77**: p. 631-637.
135. Zudaire, E., et al., *The aryl hydrocarbon receptor repressor is a putative tumor suppressor gene in multiple human cancers.* The Journal of clinical investigation, 2008. **118**(2): p. 640-650.
136. Ghassemi, P., et al., *Post-enrichment circulating tumor cell detection and enumeration via deformability impedance cytometry.* Biosensors and Bioelectronics, 2020. **150**: p. 111868.

137. Thalmann, G.N., et al., *LNCaP progression model of human prostate cancer: Androgen-independence and osseous metastasis.* The Prostate, 2000. **44**(2): p. 91-103.
138. Park, S., et al., *Morphological differences between circulating tumor cells from prostate cancer patients and cultured prostate cancer cells.* PloS one, 2014. **9**(1): p. e85264.
139. Alibert, C., B. Goud, and J.B. Manneville, *Are cancer cells really softer than normal cells?* Biology of the Cell, 2017. **109**(5): p. 167-189.
140. Faria, E.C., et al., *Measurement of elastic properties of prostate cancer cells using AFM.* Analyst, 2008. **133**(11): p. 1498-1500.
141. Ketene, A.N., et al., *The effects of cancer progression on the viscoelasticity of ovarian cell cytoskeleton structures.* Nanomedicine: Nanotechnology, Biology and Medicine, 2012. **8**(1): p. 93-102.
142. Lekka, M., *Discrimination between normal and cancerous cells using AFM.* Bionanoscience, 2016. **6**(1): p. 65-80.
143. Lekka, M. and J. Pabijan, *Measuring elastic properties of single cancer cells by AFM*, in *Atomic Force Microscopy*. 2019, Springer. p. 315-324.
144. Lekka, M., et al., *Cancer cell recognition–mechanical phenotype.* Micron, 2012. **43**(12): p. 1259-1266.
145. Park, S. and Y.J. Lee, *AFM-based dual nano-mechanical phenotypes for cancer metastasis.* Journal of biological physics, 2014. **40**(4): p. 413-419.
146. Bastatas, L., et al., *AFM nano-mechanics and calcium dynamics of prostate cancer cells with distinct metastatic potential.* Biochimica et Biophysica Acta (BBA)-General Subjects, 2012. **1820**(7): p. 1111-1120.
147. Liu, C.-Y., et al., *Vimentin contributes to epithelial-mesenchymal transition cancer cell mechanics by mediating cytoskeletal organization and focal adhesion maturation.* Oncotarget, 2015. **6**(18): p. 15966.
148. Ren, X., et al., *Single-Cell Mechanical Characteristics Analyzed by Multi-Constriction Microfluidic Channels.* ACS Sensors, 2017. **2**(2): p. 290-299.
149. Chen, J., et al., *Microfluidic impedance flow cytometry enabling high-throughput single-cell electrical property characterization.* International journal of molecular sciences, 2015. **16**(5): p. 9804-9830.
150. Xue, C., et al., *Constriction channel based single-cell mechanical property characterization.* Micromachines, 2015. **6**(11): p. 1794-1804.
151. Hu, S. and R.H. Lam, *Characterization of viscoelastic properties of normal and cancerous human breast cells using a confining microchannel.* Microfluidics and Nanofluidics, 2017. **21**(4): p. 68.
152. TruongVo, T., et al., *Microfluidic channel for characterizing normal and breast cancer cells.* Journal of Micromechanics and Microengineering, 2017. **27**(3): p. 035017.
153. Siravegna, G., et al., *Integrating liquid biopsies into the management of cancer.* Nature Reviews Clinical Oncology, 2017.
154. Hegemann, M., et al., *Liquid biopsy: ready to guide therapy in advanced prostate cancer?* Bju international, 2016.
155. Babahosseini, H., J.S. Strobl, and M. Agah, *Microfluidic Iterative Mechanical Characteristics (iMECH) Analyzer for Single-Cell Metastatic Identification.* Analytical Methods, 2017.
156. Hoerl, A.E. and R.W. Kennard, *Ridge regression: Biased estimation for nonorthogonal problems.* Technometrics, 1970. **12**(1): p. 55-67.

157. Tibshirani, R., *Regression shrinkage and selection via the lasso.* Journal of the Royal Statistical Society. Series B (Methodological), 1996: p. 267-288.
158. Fang, Z., I. Kim, and P. Schaumont, *Flexible variable selection for recovering sparsity in nonadditive nonparametric models.* Biometrics, 2016. **72**(4): p. 1155-1163.
159. Babahosseini, H., J.S. Strobl, and M. Agah, *Using nanotechnology and microfluidics in search of cell biomechanical cues for cancer progression.* Nanomedicine, 2015. **10**(17): p. 2635-2638.
160. Babahosseini, H., et al., *Bioactive sphingolipid metabolites modulate ovarian cancer cell structural mechanics.* Integrative Biology, 2013. **5**(11): p. 1385-1392.
161. Nikkhah, M., J.S. Strobl, and M. Agah, *Attachment and response of human fibroblast and breast cancer cells to three dimensional silicon microstructures of different geometries.* Biomedical microdevices, 2009. **11**(2): p. 429.
162. Nikkhah, M., et al., *Cytoskeletal role in differential adhesion patterns of normal fibroblasts and breast cancer cells inside silicon microenvironments.* Biomedical microdevices, 2009. **11**(3): p. 585.
163. Nikkhah, M., et al., *MCF10A and MDA-MB-231 human breast basal epithelial cell co-culture in silicon micro-arrays.* Biomaterials, 2011. **32**(30): p. 7625-7632.
164. Nikkhah, M., et al., *Isotropically etched silicon microarrays for rapid breast cancer cell capture.* IEEE Sensors Journal, 2013. **13**(3): p. 1125-1132.
165. Agus, D.B., et al., *A physical sciences network characterization of non-tumorigenic and metastatic cells.* Scientific reports, 2013. **3**: p. 1449.
166. Guan, G., et al., *Real-time control of a microfluidic channel for size-independent deformability cytometry.* Journal of Micromechanics and Microengineering, 2012. **22**(10): p. 105037.
167. Fang, Z. and I. Kim, *Bayesian Ising Graphical Model for Variable Selection.* Journal of Computational and Graphical Statistics, 2016. **25**(2): p. 589-605.
168. Volk-Draper, L.D., et al., *Novel model for basaloid triple-negative breast cancer: behavior in vivo and response to therapy.* Neoplasia, 2012. **14**(10): p. 926IN13-942.
169. Berezin, M.Y. and S. Achilefu, *Fluorescence lifetime measurements and biological imaging.* Chemical reviews, 2010. **110**(5): p. 2641-2684.
170. Shafie, S.M. and L.A. Liotta, *Formation of metastasis by human breast carcinoma cells (MCF-7) in nude mice.* Cancer letters, 1980. **11**(2): p. 81-87.
171. Dokukin, M.E., N.V. Guz, and I. Sokolov, *Mechanical properties of cancer cells depend on number of passages: Atomic force microscopy indentation study.* Japanese Journal of Applied Physics, 2017. **56**(8S1): p. 08LB01.
172. Ihemelandu, C.U., et al., *Molecular breast cancer subtypes in premenopausal and postmenopausal African-American women: age-specific prevalence and survival.* Journal of Surgical Research, 2007. **143**(1): p. 109-118.
173. Canas-Marques, R. and S.J. Schnitt, *E-cadherin immunohistochemistry in breast pathology: uses and pitfalls.* Histopathology, 2016. **68**(1): p. 57-69.
174. Vrekoussis, T., et al., *Image analysis of breast cancer immunohistochemistry-stained sections using ImageJ: an RGB-based model.* Anticancer research, 2009. **29**(12): p. 4995-4998.
175. Fakoor, R., et al. *Using deep learning to enhance cancer diagnosis and classification*. in *Proceedings of the International Conference on Machine Learning*. 2013.

176. Albain, K.S., et al., *Prognostic and predictive value of the 21-gene recurrence score assay in postmenopausal women with node-positive, oestrogen-receptor-positive breast cancer on chemotherapy: a retrospective analysis of a randomised trial.* The lancet oncology, 2010. **11**(1): p. 55-65.
177. Paik, S., et al., *A multigene assay to predict recurrence of tamoxifen-treated, node-negative breast cancer.* New England Journal of Medicine, 2004. **351**(27): p. 2817-2826.
178. Marjanovic, N.D., R.A. Weinberg, and C.L. Chaffer, *Cell plasticity and heterogeneity in cancer.* Clinical chemistry, 2013. **59**(1): p. 168-179.
179. Jeon, J.S., et al., *Human 3D vascularized organotypic microfluidic assays to study breast cancer cell extravasation.* Proceedings of the National Academy of Sciences, 2015. **112**(1): p. 214-219.
180. Zheng, Y., et al., *Microfluidic characterization of specific membrane capacitance and cytoplasm conductivity of singlecells.* Biosensors and Bioelectronics, 2013. **42**: p. 496-502.
181. Zheng, Y., et al., *High-throughput biophysical measurement of human red blood cells.* Lab on a Chip, 2012. **12**(14): p. 2560-2567.
182. Wang, K., et al., *Specific membrane capacitance, cytoplasm conductivity and instantaneous Young's modulus of single tumour cells.* Scientific Data, 2017. **4**: p. 170015.
183. Turkki, R., et al., *Exploration of tissue morphologies in breast cancer samples using unsupervised machine learning*. 2017, AACR.
184. Ramarajan, N., et al., *Abstract P1-14-01: Building an experience engine to make cancer treatment decisions using machine learning*. 2017, AACR.
185. Saib, W.B., et al., *Abstract A11: A deep learning approach for extracting clinically relevant information from pathology reports*. 2017, AACR.
186. Malta, T.M., et al., *Machine learning identifies stemness features associated with oncogenic dedifferentiation.* Cell, 2018. **173**(2): p. 338-354. e15.
187. Yala, A., et al., *Using machine learning to parse breast pathology reports.* Breast cancer research and treatment, 2017. **161**(2): p. 203-211.
188. Bahl, M., et al., *High-Risk Breast Lesions: A Machine Learning Model to Predict Pathologic Upgrade and Reduce Unnecessary Surgical Excision.* Radiology, 2017: p. 170549.
189. Nyberg, K.D., et al., *Predicting cancer cell invasion by single-cell physical phenotyping.* Integrative Biology, 2018. **10**(4): p. 218-231.
190. Nyberg, K.D., et al., *Quantitative Deformability Cytometry: Rapid, Calibrated Measurements of Cell Mechanical Properties.* Biophysical journal, 2017. **113**(7): p. 1574-1584.
191. Hoelzle, D.J., et al., *A microfluidic technique to probe cell deformability.* Journal of visualized experiments: JoVE, 2014(91).
192. Babahosseini, H., et al., *Biomechanical profile of cancer stem-like/tumor-initiating cells derived from a progressive ovarian cancer model.* Nanomedicine: Nanotechnology, Biology and Medicine, 2014. **10**(5): p. e1013-e1019.
193. Lyon, C., et al., *Bristol Heart Institute, University of Bristol, Research Floor Level Seven, Bristol Royal Infirmary, Upper Maudlin St, BRISTOL, BS2 8HW, United Kingdom.* Frontiers in Bioscience, 2011. **16**: p. 644-673.

194. Sarrió, D., et al., *Epithelial-mesenchymal transition in breast cancer relates to the basal-like phenotype.* Cancer research, 2008. **68**(4): p. 989-997.
195. Nieman, M.T., et al., *N-cadherin promotes motility in human breast cancer cells regardless of their E-cadherin expression.* The Journal of cell biology, 1999. **147**(3): p. 631-644.
196. Subik, K., et al., *The expression patterns of ER, PR, HER2, CK5/6, EGFR, Ki-67 and AR by immunohistochemical analysis in breast cancer cell lines.* Breast cancer: basic and clinical research, 2010. **4**: p. 35.
197. Chavez, K.J., S.V. Garimella, and S. Lipkowitz, *Triple negative breast cancer cell lines: one tool in the search for better treatment of triple negative breast cancer.* Breast disease, 2010. **32**(1-2): p. 35.
198. Meacham, C.E. and S.J. Morrison, *Tumor heterogeneity and cancer cell plasticity.* Nature, 2013. **501**(7467): p. 328.
199. DeSantis, C.E., et al., *Breast cancer statistics, 2017, racial disparity in mortality by state.* CA: A Cancer Journal for Clinicians, 2017.
200. Ellis, L., et al., *Racial and Ethnic Disparities in Cancer Survival: The Contribution of Tumor, Sociodemographic, Institutional, and Neighborhood Characteristics.* Journal of Clinical Oncology, 2017: p. JCO. 2017.74. 2049.
201. Jemal, A., et al., *Factors That Contributed to Black-White Disparities in Survival Among Nonelderly Women With Breast Cancer Between 2004 and 2013.* Journal of Clinical Oncology, 2017: p. JCO. 2017.73. 7932.
202. Song, H., et al., *Identification of mesenchymal stem cell differentiation state using dual-micropore microfluidic impedance flow cytometry.* Analytical Methods, 2016. **8**(41): p. 7437-7444.
203. Lange, J.R., et al., *Microconstriction arrays for high-throughput quantitative measurements of cell mechanical properties.* Biophysical journal, 2015. **109**(1): p. 26-34.
204. Ren, X., et al., *Stability of free-standing tetraether planar membranes in microchips.* Journal of Membrane Science, 2017. **540**: p. 27-34.
205. Apichitsopa, N., A. Jaffe, and J. Voldman, *Multiparameter cell-tracking intrinsic cytometry for single-cell characterization.* Lab on a Chip, 2018. **18**(10): p. 1430-1439.
206. Mulhall, H., et al., *Cancer, pre-cancer and normal oral cells distinguished by dielectrophoresis.* Analytical and bioanalytical chemistry, 2011. **401**(8): p. 2455-2463.
207. Liang, X., et al., *Human oral cancer cells with increasing tumorigenic abilities exhibit higher effective membrane capacitance.* Integrative Biology, 2014. **6**(5): p. 545-554.
208. Dória, M.L., et al., *Lipidomic analysis of phospholipids from human mammary epithelial and breast cancer cell lines.* Journal of cellular physiology, 2013. **228**(2): p. 457-468.
209. Heu, C., et al., *Glyphosate-induced stiffening of HaCaT keratinocytes, a Peak Force Tapping study on living cells.* Journal of structural biology, 2012. **178**(1): p. 1-7.
210. Deng, X., et al., *Application of atomic force microscopy in cancer research.* Journal of nanobiotechnology, 2018. **16**(1): p. 102.
211. Arntz, Y., et al., *Label-free protein assay based on a nanomechanical cantilever array.* Nanotechnology, 2002. **14**(1): p. 86.
212. Bagnall, J.S., et al., *Deformability of tumor cells versus blood cells.* Scientific reports, 2015. **5**.
213. Huang, S., et al., *Dynamic deformability of Plasmodium falciparum-infected erythrocytes exposed to artesunate in vitro.* Integrative Biology, 2013. **5**(2): p. 414-422.

214. Rosenbluth, M.J., W.A. Lam, and D.A. Fletcher, *Analyzing cell mechanics in hematologic diseases with microfluidic biophysical flow cytometry.* Lab on a Chip, 2008. **8**(7): p. 1062-1070.
215. Reale, R., et al., *Electrical measurement of cross-sectional position of particles flowing through a microchannel.* Microfluidics and Nanofluidics, 2018. **22**(4): p. 41.
216. Zhou, Y., et al., *Characterizing Deformability and Electrical Impedance of Cancer Cells in a Microfluidic Device.* Analytical chemistry, 2017. **90**(1): p. 912-919.
217. Kerr, B.A., et al., *CD117+ cells in the circulation are predictive of advanced prostate cancer.* Oncotarget, 2015. **6**(3): p. 1889.
218. Harris, K.S. and B.A. Kerr, *Prostate Cancer Stem Cell Markers Drive Progression, Therapeutic Resistance, and Bone Metastasis.* Stem Cells International, 2017: p. 8629234.
219. Thalgott, M., et al., *Detection of circulating tumor cells in different stages of prostate cancer.* Journal of cancer research and clinical oncology, 2013. **139**(5): p. 755-763.
220. Josefsson, A., et al., *Circulating Tumor Cells as a Marker for Progression-free Survival in Metastatic Castration-naïve Prostate Cancer.* The Prostate, 2017. **77**(8): p. 849-858.
221. De Bono, J.S., et al., *Circulating tumor cells predict survival benefit from treatment in metastatic castration-resistant prostate cancer.* Clinical cancer research, 2008. **14**(19): p. 6302-6309.
222. Riethdorf, S., et al., *Detection of circulating tumor cells in peripheral blood of patients with metastatic breast cancer: a validation study of the CellSearch system.* Clinical cancer research, 2007. **13**(3): p. 920-928.
223. Cohen, S.J., et al., *Relationship of circulating tumor cells to tumor response, progression-free survival, and overall survival in patients with metastatic colorectal cancer.* Journal of clinical oncology, 2008. **26**(19): p. 3213-3221.
224. Schilling, D., et al., *Isolated, disseminated and circulating tumour cells in prostate cancer.* Nature Reviews Urology, 2012. **9**(8): p. 448-463.
225. Lowes, L.E., et al., *Epithelial-to-mesenchymal transition leads to disease-stage differences in circulating tumor cell detection and metastasis in pre-clinical models of prostate cancer.* Oncotarget, 2016. **7**(46): p. 76125.
226. Rycaj, K. and D.G. Tang, *Chapter 12 - Metastasis and Metastatic Cells: A Historical Perspective and Current Analysis A2 - Liu, Huiping*, in *Cancer Stem Cells*, J.D. Lathia, Editor. 2016, Academic Press: Boston. p. 317-340.
227. Punnoose, E.A., et al., *Molecular biomarker analyses using circulating tumor cells.* PloS one, 2010. **5**(9): p. e12517.
228. Maheswaran, S., et al., *Detection of mutations in EGFR in circulating lung-cancer cells.* New England Journal of Medicine, 2008. **359**(4): p. 366-377.
229. Nagrath, S., et al., *Isolation of rare circulating tumour cells in cancer patients by microchip technology.* Nature, 2007. **450**(7173): p. 1235-1239.
230. Shim, S., et al., *Dielectrophoresis has broad applicability to marker-free isolation of tumor cells from blood by microfluidic systems.* Biomicrofluidics, 2013. **7**(1): p. 011808.
231. Shim, S., et al., *Antibody-independent isolation of circulating tumor cells by continuous-flow dielectrophoresis.* Biomicrofluidics, 2013. **7**(1): p. 011807.
232. Moon, H.-S., et al., *Continuous separation of breast cancer cells from blood samples using multi-orifice flow fractionation (MOFF) and dielectrophoresis (DEP).* Lab on a Chip, 2011. **11**(6): p. 1118-1125.

233. Li, P., et al., *Acoustic separation of circulating tumor cells.* Proceedings of the National Academy of Sciences, 2015. **112**(16): p. 4970-4975.
234. Chen, Y., et al., *Rare cell isolation and analysis in microfluidics.* Lab on a Chip, 2014. **14**(4): p. 626-645.
235. Qian, W., Y. Zhang, and W. Chen, *Capturing Cancer: Emerging Microfluidic Technologies for the Capture and Characterization of Circulating Tumor Cells.* Small, 2015. **11**(32): p. 3850-3872.
236. Wu, J., Q. Chen, and J.-M. Lin, *Microfluidic technologies in cell isolation and analysis for biomedical applications.* Analyst, 2017.
237. Guo, Q., S.P. Duffy, and H. Ma, *Microfluidic Technologies for Deformability-Based Cell Sorting*, in *Microtechnology for Cell Manipulation and Sorting*. 2017, Springer. p. 225-254.
238. Huang, L., et al., *Microfluidics cell sample preparation for analysis: Advances in efficient cell enrichment and precise single cell capture.* Biomicrofluidics, 2017. **11**(1): p. 011501.
239. Nora Dickson, M., et al., *Efficient capture of circulating tumor cells with a novel immunocytochemical microfluidic device.* Biomicrofluidics, 2011. **5**(3): p. 034119.
240. Fan, X., et al., *A microfluidic chip integrated with a high-density PDMS-based microfiltration membrane for rapid isolation and detection of circulating tumor cells.* Biosensors and Bioelectronics, 2015. **71**: p. 380-386.
241. Shen, F.-M., et al., *A high throughput micro-chamber array device for single cell clonal cultivation and tumor heterogeneity analysis.* Scientific reports, 2015. **5**.
242. Hur, S.C., A.J. Mach, and D. Di Carlo, *High-throughput size-based rare cell enrichment using microscale vortices.* Biomicrofluidics, 2011. **5**(2): p. 022206.
243. Lee, W., P. Tseng, and D. Di Carlo, *Microfluidic Cell Sorting and Separation Technology*, in *Microtechnology for Cell Manipulation and Sorting*, W. Lee, P. Tseng, and D. Di Carlo, Editors. 2017, Springer International Publishing: Cham. p. 1-14.
244. Renier, C., et al., *Label-free isolation of prostate circulating tumor cells using Vortex microfluidic technology.* npj Precision Oncology, 2017. **1**(1): p. 15.
245. Haddadi, H., H. Naghsh-Nilchi, and D. Di Carlo, *Separation of cancer cells using vortical microfluidic flows.* Biomicrofluidics, 2018. **12**(1): p. 014112.
246. Stott, S.L., et al., *Isolation of circulating tumor cells using a microvortex-generating herringbone-chip.* Proceedings of the National Academy of Sciences, 2010. **107**(43): p. 18392-18397.
247. Yu, M., et al., *RNA sequencing of pancreatic circulating tumour cells implicates WNT signalling in metastasis.* Nature, 2012. **487**(7408): p. 510-513.
248. Ozkumur, E., et al., *Inertial focusing for tumor antigen–dependent and–independent sorting of rare circulating tumor cells.* Science translational medicine, 2013. **5**(179): p. 179ra47-179ra47.
249. Gleghorn, J.P., et al., *Capture of circulating tumor cells from whole blood of prostate cancer patients using geometrically enhanced differential immunocapture (GEDI) and a prostate-specific antibody.* Lab on a chip, 2010. **10**(1): p. 27-29.
250. Dharmasiri, U., et al., *High-throughput selection, enumeration, electrokinetic manipulation, and molecular profiling of low-abundance circulating tumor cells using a microfluidic system.* Analytical chemistry, 2011. **83**(6): p. 2301-2309.

251. Jackson, J.M., et al., *UV activation of polymeric high aspect ratio microstructures: ramifications in antibody surface loading for circulating tumor cell selection.* Lab on a Chip, 2014. **14**(1): p. 106-117.
252. Dharmasiri, U., et al., *Highly efficient capture and enumeration of low abundance prostate cancer cells using prostate-specific membrane antigen aptamers immobilized to a polymeric microfluidic device.* Electrophoresis, 2009. **30**(18): p. 3289-3300.
253. Adams, A.A., et al., *Highly efficient circulating tumor cell isolation from whole blood and label-free enumeration using polymer-based microfluidics with an integrated conductivity sensor.* Journal of the American Chemical Society, 2008. **130**(27): p. 8633-8641.
254. Sheng, W., et al., *Aptamer-enabled efficient isolation of cancer cells from whole blood using a microfluidic device.* Analytical chemistry, 2012. **84**(9): p. 4199-4206.
255. Sheng, W., et al., *Capture, release and culture of circulating tumor cells from pancreatic cancer patients using an enhanced mixing chip.* Lab on a Chip, 2014. **14**(1): p. 89-98.
256. Issadore, D., et al., *Ultrasensitive clinical enumeration of rare cells ex vivo using a micro-hall detector.* Science translational medicine, 2012. **4**(141): p. 141ra92-141ra92.
257. Van der Auwera, I., et al., *Circulating tumour cell detection: a direct comparison between the CellSearch System, the AdnaTest and CK-19/mammaglobin RT–PCR in patients with metastatic breast cancer.* British journal of cancer, 2010. **102**(2): p. 276-284.
258. Peeters, D., et al., *Semiautomated isolation and molecular characterisation of single or highly purified tumour cells from CellSearch enriched blood samples using dielectrophoretic cell sorting.* British journal of cancer, 2013. **108**(6): p. 1358.
259. Miller, M.C., G.V. Doyle, and L.W. Terstappen, *Significance of circulating tumor cells detected by the CellSearch system in patients with metastatic breast colorectal and prostate cancer.* Journal of oncology, 2009. **2010**.
260. Schwed Lustgarten, D.E., et al., *Use of circulating tumor cell technology (CELLSEARCH) for the diagnosis of malignant pleural effusions.* Annals of the American Thoracic Society, 2013. **10**(6): p. 582-589.
261. Au, S.H., et al., *Clusters of circulating tumor cells traverse capillary-sized vessels.* Proceedings of the National Academy of Sciences, 2016. **113**(18): p. 4947-4952.
262. Lin, H.K., et al., *Portable filter-based microdevice for detection and characterization of circulating tumor cells.* Clinical Cancer Research, 2010. **16**(20): p. 5011-5018.
263. Tan, S.J., et al., *Microdevice for the isolation and enumeration of cancer cells from blood.* Biomedical microdevices, 2009. **11**(4): p. 883-892.
264. Lim, L.S., et al., *Microsieve lab-chip device for rapid enumeration and fluorescence in situ hybridization of circulating tumor cells.* Lab on a Chip, 2012. **12**(21): p. 4388-4396.
265. Grover, W.H., et al., *Measuring single-cell density.* Proceedings of the National Academy of Sciences, 2011. **108**(27): p. 10992-10996.
266. Kim, T.-H., et al., *FAST: Size-Selective, Clog-Free Isolation of Rare Cancer Cells from Whole Blood at a Liquid–Liquid Interface.* Analytical chemistry, 2016. **89**(2): p. 1155-1162.
267. Cruz, I., et al., *Evaluation of multiparameter flow cytometry for the detection of breast cancer tumor cells in blood samples.* American journal of clinical pathology, 2005. **123**(1): p. 66-74.

268. Di Carlo, D., *A mechanical biomarker of cell state in medicine.* Journal of Laboratory Automation, 2012. **17**(1): p. 32-42.
269. Sollier, E., et al., *Size-selective collection of circulating tumor cells using Vortex technology.* Lab on a Chip, 2014. **14**(1): p. 63-77.
270. Paris, P.L., et al., *Functional phenotyping and genotyping of circulating tumor cells from patients with castration resistant prostate cancer.* Cancer letters, 2009. **277**(2): p. 164-173.
271. Ren, X., et al., *Porous Polydimethylsiloxane as a Gas-Liquid Interface for Microfluidic Applications.* Journal of Microelectromechanical Systems, 2017. **26**(1): p. 120-126.
272. Mohamed, H., et al., *Isolation of tumor cells using size and deformation.* Journal of Chromatography A, 2009. **1216**(47): p. 8289-8295.
273. Zheng, S., et al., *Membrane microfilter device for selective capture, electrolysis and genomic analysis of human circulating tumor cells.* Journal of chromatography A, 2007. **1162**(2): p. 154-161.
274. Vona, G., et al., *Isolation by size of epithelial tumor cells: a new method for the immunomorphological and molecular characterization of circulating tumor cells.* The American journal of pathology, 2000. **156**(1): p. 57-63.
275. Tang, Y., et al., *Microfluidic device with integrated microfilter of conical-shaped holes for high efficiency and high purity capture of circulating tumor cells.* Scientific reports, 2014. **4**: p. srep06052.
276. Yoon, Y., et al., *Deterministic Capture of Individual Circulating Tumor Cells Using a Flow-Restricted Microfluidic Trap Array.* Micromachines, 2018. **9**(3): p. 106.
277. Dong, Y., et al., *Microfluidics and Circulating Tumor Cells.* The Journal of Molecular Diagnostics, 2013. **15**(2): p. 149-157.
278. Allard, W.J., et al., *Tumor cells circulate in the peripheral blood of all major carcinomas but not in healthy subjects or patients with nonmalignant diseases.* Clinical Cancer Research, 2004. **10**(20): p. 6897-6904.
279. Wan, Y., et al., *Velocity effect on aptamer-based circulating tumor cell isolation in microfluidic devices.* The Journal of Physical Chemistry B, 2011. **115**(47): p. 13891-13896.
280. Krombach, F., et al., *Cell size of alveolar macrophages: an interspecies comparison.* Environmental health perspectives, 1997. **105**(Suppl 5): p. 1261.
281. Bray, F., et al., *Global cancer statistics 2018: GLOBOCAN estimates of incidence and mortality worldwide for 36 cancers in 185 countries.* CA: a cancer journal for clinicians, 2018. **68**(6): p. 394-424.
282. Torre, L.A., et al., *Global cancer statistics, 2012.* CA: a cancer journal for clinicians, 2015. **65**(2): p. 87-108.
283. Torre, L.A., et al., *Global cancer incidence and mortality rates and trends—an update.* Cancer Epidemiology and Prevention Biomarkers, 2016. **25**(1): p. 16-27.
284. Berry, D.A., et al., *Chapter 6: Modeling the Impact of Treatment and Screening on US Breast Cancer Mortality: A Bayesian Approach.* JNCI Monographs, 2006. **2006**(36): p. 30-36.
285. Bleyer, A. and H.G. Welch, *Effect of three decades of screening mammography on breast-cancer incidence.* New England Journal of Medicine, 2012. **367**(21): p. 1998-2005.

286. Siegel, R., et al., *Cancer treatment and survivorship statistics, 2012.* CA: a cancer journal for clinicians, 2012. **62**(4): p. 220-241.
287. Tabar, L., et al., *Mammography service screening and mortality in breast cancer patients: 20-year follow-up before and after introduction of screening.* The Lancet, 2003. **361**(9367): p. 1405-1410.
288. Weir, H.K., et al., *Annual report to the nation on the status of cancer, 1975–2000, featuring the uses of surveillance data for cancer prevention and control.* Journal of the National Cancer Institute, 2003. **95**(17): p. 1276-1299.
289. Pantel, K. and M. Speicher, *The biology of circulating tumor cells.* Oncogene, 2016. **35**(10): p. 1216.
290. Wu, S., et al., *Classification of circulating tumor cells by epithelial-mesenchymal transition markers.* PLoS One, 2015. **10**(4): p. e0123976.
291. Alix-Panabières, C. and K. Pantel, *Clinical applications of circulating tumor cells and circulating tumor DNA as liquid biopsy.* Cancer discovery, 2016. **6**(5): p. 479-491.
292. Aceto, N., et al., *En route to metastasis: circulating tumor cell clusters and epithelial-to-mesenchymal transition.* Trends in cancer, 2015. **1**(1): p. 44-52.
293. Crane, M.M., et al., *Microfluidics-enabled phenotyping, imaging, and screening of multicellular organisms.* Lab on a Chip, 2010. **10**(12): p. 1509-1517.
294. Jahn, A., et al., *Preparation of nanoparticles by continuous-flow microfluidics.* Journal of Nanoparticle Research, 2008. **10**(6): p. 925-934.
295. Ohno, K.i., K. Tachikawa, and A. Manz, *Microfluidics: applications for analytical purposes in chemistry and biochemistry.* Electrophoresis, 2008. **29**(22): p. 4443-4453.
296. Situma, C., M. Hashimoto, and S.A. Soper, *Merging microfluidics with microarray-based bioassays.* Biomolecular engineering, 2006. **23**(5): p. 213-231.
297. Yun, H., K. Kim, and W.G. Lee, *Cell manipulation in microfluidics.* Biofabrication, 2013. **5**(2): p. 022001.
298. Hajba, L. and A. Guttman, *Circulating tumor-cell detection and capture using microfluidic devices.* TrAC trends in analytical chemistry, 2014. **59**: p. 9-16.
299. Li, P., et al., *Probing circulating tumor cells in microfluidics.* Lab on a Chip, 2013. **13**(4): p. 602-609.
300. Myung, J. and S. Hong, *Microfluidic devices to enrich and isolate circulating tumor cells.* Lab on a Chip, 2015. **15**(24): p. 4500-4511.
301. Alunni-Fabbroni, M. and M.T. Sandri, *Circulating tumour cells in clinical practice: Methods of detection and possible characterization.* Methods, 2010. **50**(4): p. 289-297.
302. Yu, M., et al., *Circulating tumor cells: approaches to isolation and characterization.* The Journal of cell biology, 2011. **192**(3): p. 373-382.
303. Andree, K.C., G. van Dalum, and L.W. Terstappen, *Challenges in circulating tumor cell detection by the CellSearch system.* Molecular oncology, 2016. **10**(3): p. 395-407.
304. Miller, M.C., G.V. Doyle, and L.W. Terstappen, *Significance of circulating tumor cells detected by the CellSearch system in patients with metastatic breast colorectal and prostate cancer.* Journal of oncology, 2010. **2010**: p. 617421.
305. Asghar, W., et al., *Electrical fingerprinting, 3D profiling and detection of tumor cells with solid-state micropores.* Lab on a Chip, 2012. **12**(13): p. 2345-2352.
306. Antfolk, M., et al., *A single inlet two-stage acoustophoresis chip enabling tumor cell enrichment from white blood cells.* Lab on a chip, 2015. **15**(9): p. 2102-2109.

307. Augustsson, P., et al., *Microfluidic, label-free enrichment of prostate cancer cells in blood based on acoustophoresis.* Analytical chemistry, 2012. **84**(18): p. 7954-7962.
308. Karabacak, N.M., et al., *Microfluidic, marker-free isolation of circulating tumor cells from blood samples.* Nature protocols, 2014. **9**(3): p. 694.
309. Alshareef, M., et al., *Separation of tumor cells with dielectrophoresis-based microfluidic chip.* Biomicrofluidics, 2013. **7**(1): p. 011803.
310. Gascoyne, P. and S. Shim, *Isolation of circulating tumor cells by dielectrophoresis.* Cancers, 2014. **6**(1): p. 545-579.
311. Ren, X., et al., *Entrapment of prostate cancer circulating tumor cells with a sequential size-based microfluidic chip.* Analytical chemistry, 2018. **90**(12): p. 7526-7534.
312. Budd, G.T., et al., *Circulating tumor cells versus imaging—predicting overall survival in metastatic breast cancer.* Clinical Cancer Research, 2006. **12**(21): p. 6403-6409.
313. Paterlini-Brechot, P. and N.L. Benali, *Circulating tumor cells (CTC) detection: clinical impact and future directions.* Cancer letters, 2007. **253**(2): p. 180-204.
314. Lu, Y.-T., et al., *NanoVelcro Chip for CTC enumeration in prostate cancer patients.* Methods, 2013. **64**(2): p. 144-152.
315. Sonn, C.H., et al., *Detection of circulating tumor cells in patients with non-small cell lung cancer using a size-based platform.* Oncology letters, 2017. **13**(4): p. 2717-2722.
316. Swennenhuis, J.F., et al., *Characterization of circulating tumor cells by fluorescence in situ hybridization.* Cytometry Part A: The Journal of the International Society for Advancement of Cytometry, 2009. **75**(6): p. 520-527.
317. Choi, H., et al., *A label-free DC impedance-based microcytometer for circulating rare cancer cell counting.* Lab on a Chip, 2013. **13**(5): p. 970-977.
318. Spencer, D., V. Hollis, and H. Morgan, *Microfluidic impedance cytometry of tumour cells in blood.* Biomicrofluidics, 2014. **8**(6): p. 064124.
319. Soltanian-Zadeh, S., et al., *Breast cancer cell obatoclax response characterization using passivated-electrode insulator-based dielectrophoresis.* Electrophoresis, 2017. **38**(16): p. 1988-1995.
320. Zellner, P., et al., *Off-chip passivated-electrode, insulator-based dielectrophoresis (OπDEP).* Analytical and bioanalytical chemistry, 2013. **405**(21): p. 6657-6666.
321. Emaminejad, S., et al., *Microfluidic diagnostic tool for the developing world: Contactless impedance flow cytometry.* Lab on a Chip, 2012. **12**(21): p. 4499-4507.
322. Gawad, S., L. Schild, and P. Renaud, *Micromachined impedance spectroscopy flow cytometer for cell analysis and particle sizing.* Lab on a Chip, 2001. **1**(1): p. 76-82.
323. Sun, T. and H. Morgan, *Single-cell microfluidic impedance cytometry: a review.* Microfluidics and Nanofluidics, 2010. **8**(4): p. 423-443.
324. Kaufmann, S., et al., *CHARACTERIZATION OF CANCER CELLS BY IMPEDANCE FLOW CYTOMETRY.*
325. Anh-Nguyen, T., et al., *An impedance biosensor for monitoring cancer cell attachment, spreading and drug-induced apoptosis.* Sensors and Actuators A: Physical, 2016. **241**: p. 231-237.
326. Robilliard, L., et al., *The Importance of Multifrequency Impedance Sensing of Endothelial Barrier Formation Using ECIS Technology for the Generation of a Strong and Durable Paracellular Barrier.* Biosensors, 2018. **8**(3): p. 64.

327. Tran, T.B., C. Baek, and J. Min, *Electric cell-substrate impedance sensing (ECIS) with microelectrode arrays for investigation of cancer cell–fibroblasts interaction.* PloS one, 2016. **11**(4): p. e0153813.
328. Srinivasaraghavan, V., J. Strobl, and M. Agah, *Bioimpedance rise in response to histone deacetylase inhibitor is a marker of mammary cancer cells within a mixed culture of normal breast cells.* Lab on a Chip, 2012. **12**(24): p. 5168-5179.
329. Srinivasaraghavan, V., et al., *A comparative study of nano-scale coatings on gold electrodes for bioimpedance studies of breast cancer cells.* Biomedical microdevices, 2014. **16**(5): p. 689-696.
330. Srinivasaraghavan, V., J. Strobl, and M. Agah, *Microelectrode bioimpedance analysis distinguishes basal and claudin-low subtypes of triple negative breast cancer cells.* Biomedical microdevices, 2015. **17**(4): p. 80.
331. Bird, C. and S. Kirstein, *Real-time, label-free monitoring of cellular invasion and migration with the xCELLigence system.* Nature methods, 2009. **6**(8): p. 622.
332. Daza, P., et al., *Monitoring living cell assays with bio-impedance sensors.* Sensors and Actuators B: Chemical, 2013. **176**: p. 605-610.
333. Ke, N., et al., *The xCELLigence system for real-time and label-free monitoring of cell viability*, in *Mammalian Cell Viability*. 2011, Springer. p. 33-43.
334. Shih, S.C., et al., *Digital microfluidics with impedance sensing for integrated cell culture andanalysis.* Biosensors and Bioelectronics, 2013. **42**: p. 314-320.
335. Ayliffe, H.E., A.B. Frazier, and R. Rabbitt, *Electric impedance spectroscopy using microchannels with integrated metal electrodes.* Journal of Microelectromechanical systems, 1999. **8**(1): p. 50-57.
336. Chappy, S.L., *Women's experience with breast biopsy.* AORN journal, 2004. **80**(5): p. 885-901.
337. Harnden, P., et al., *The clinical management of patients with a small volume of prostatic cancer on biopsy: what are the risks of progression? A systematic review and meta-analysis.* Cancer: Interdisciplinary International Journal of the American Cancer Society, 2008. **112**(5): p. 971-981.
338. Loeb, S., et al., *Systematic review of complications of prostate biopsy.* European urology, 2013. **64**(6): p. 876-892.
339. Smith, R.A., V. Cokkinides, and O.W. Brawley, *Cancer screening in the United States, 2012: a review of current American Cancer Society guidelines and current issues in cancer screening.* CA: a cancer journal for clinicians, 2012. **62**(2): p. 129-142.
340. Jin, K.T., et al., *Current progress in the clinical use of circulating tumor cells as prognostic biomarkers.* Cancer Cytopathology, 2019. **127**(12): p. 739-749.
341. Li, J., et al., *Clinical applications of liquid biopsy as prognostic and predictive biomarkers in hepatocellular carcinoma: circulating tumor cells and circulating tumor DNA.* Journal of Experimental & Clinical Cancer Research, 2018. **37**(1).
342. Lin, D., et al., *Circulating tumor cells: biology and clinical significance.* Signal Transduction and Targeted Therapy, 2021. **6**(1).
343. Thiele, J.A., et al., *Circulating Tumor Cells: Fluid Surrogates of Solid Tumors.* Annual Review of Pathology: Mechanisms of Disease, 2017. **12**(1): p. 419-447.
344. Green, B.J., et al., *Beyond the Capture of Circulating Tumor Cells: Next-Generation Devices and Materials.* Angewandte Chemie International Edition, 2016. **55**(4): p. 1252-1265.

345. Larsson, A.-M., et al., *Longitudinal enumeration and cluster evaluation of circulating tumor cells improve prognostication for patients with newly diagnosed metastatic breast cancer in a prospective observational trial.* Breast Cancer Research, 2018. **20**(1).
346. Toss, A., et al., *CTC enumeration and characterization: moving toward personalized medicine.* Annals of translational medicine, 2014. **2**(11).
347. Wallwiener, M., et al., *Serial enumeration of circulating tumor cells predicts treatment response and prognosis in metastatic breast cancer: a prospective study in 393 patients.* BMC Cancer, 2014. **14**(1): p. 512.
348. Yan, W.-T., et al., *Circulating tumor cell status monitors the treatment responses in breast cancer patients: a meta-analysis.* Scientific Reports, 2017. **7**(1): p. 43464.
349. Yang, Y.-P., T.M. Giret, and R.J. Cote, *Circulating Tumor Cells from Enumeration to Analysis: Current Challenges and Future Opportunities.* Cancers, 2021. **13**(11): p. 2723.
350. Agashe, R. and R. Kurzrock, *Circulating Tumor Cells: From the Laboratory to the Cancer Clinic.* Cancers, 2020. **12**(9): p. 2361.
351. Alimirzaie, S., M. Bagherzadeh, and M.R. Akbari, *Liquid biopsy in breast cancer: A comprehensive review.* Clinical Genetics, 2019. **95**(6): p. 643-660.
352. Li, Y.-Q., et al., *Rational Design of Materials Interface for Efficient Capture of Circulating Tumor Cells.* Advanced Science, 2015. **2**(11): p. 1500118.
353. Cho, H., et al., *Microfluidic technologies for circulating tumor cell isolation.* The Analyst, 2018. **143**(13): p. 2936-2970.
354. Myung, J.H. and S. Hong, *Microfluidic devices to enrich and isolate circulating tumor cells.* Lab on a Chip, 2015. **15**(24): p. 4500-4511.
355. Pei, H., et al., *Recent advances in microfluidic technologies for circulating tumor cells: enrichment, single-cell analysis, and liquid biopsy for clinical applications.* Lab on a Chip, 2020. **20**(21): p. 3854-3875.
356. Bailey, P. and S. Martin, *Insights on CTC Biology and Clinical Impact Emerging from Advances in Capture Technology.* Cells, 2019. **8**(6): p. 553.
357. Habli, Z., et al., *Circulating Tumor Cell Detection Technologies and Clinical Utility: Challenges and Opportunities.* Cancers, 2020. **12**(7): p. 1930.
358. Rawal, S., et al., *Microfilter-Based Capture and Release of Viable Circulating Tumor Cells*. 2017, Springer New York. p. 93-105.
359. Hvichia, G.E., et al., *A novel microfluidic platform for size and deformability based separation and the subsequent molecular characterization of viable circulating tumor cells.* International Journal of Cancer, 2016. **138**(12): p. 2894-2904.
360. Kim, H., et al., *Circulating Tumor Cells Enumerated by a Centrifugal Microfluidic Device as a Predictive Marker for Monitoring Ovarian Cancer Treatment: A Pilot Study.* Diagnostics, 2020. **10**(4): p. 249.
361. Balasubramanian, P., et al., *Antibody-independent capture of circulating tumor cells of non-epithelial origin with the ApoStream® system.* PLOS ONE, 2017. **12**(4): p. e0175414.
362. Di Trapani, M., N. Manaresi, and G. Medoro, *DEPArray™ system: An automatic image-based sorter for isolation of pure circulating tumor cells.* Cytometry Part A, 2018. **93**(12): p. 1260-1266.
363. Peeters, D.J.E., et al., *Semiautomated isolation and molecular characterisation of single or highly purified tumour cells from CellSearch enriched blood samples using dielectrophoretic cell sorting.* British Journal of Cancer, 2013. **108**(6): p. 1358-1367.

364. Amintas, S., et al., *Circulating Tumor Cell Clusters: United We Stand Divided We Fall.* International Journal of Molecular Sciences, 2020. **21**(7): p. 2653.
365. Costa, C., et al., *Analysis of a Real-World Cohort of Metastatic Breast Cancer Patients Shows Circulating Tumor Cell Clusters (CTC-clusters) as Predictors of Patient Outcomes.* Cancers, 2020. **12**(5): p. 1111.
366. Wang, C., et al., *Improved Prognostic Stratification Using Circulating Tumor Cell Clusters in Patients with Metastatic Castration-Resistant Prostate Cancer.* Cancers, 2021. **13**(2): p. 268.
367. Hyun, K.-A., et al., *Epithelial-to-mesenchymal transition leads to loss of EpCAM and different physical properties in circulating tumor cells from metastatic breast cancer.* Oncotarget, 2016. **7**(17): p. 24677-24687.
368. Lowes, L.E. and A.L. Allan, *Circulating tumor cells and implications of the epithelial-to-mesenchymal transition.* Advances in clinical chemistry, 2018. **83**: p. 121-181.
369. Bithi, S.S. and S.A. Vanapalli, *Microfluidic cell isolation technology for drug testing of single tumor cells and their clusters.* Scientific Reports, 2017. **7**(1): p. 41707.